

ION-SURFACE INTERACTIONS AND LIMITS TO SILICON EPITAXY
AT LOW TEMPERATURES

Thesis by

M.V. Ramana Murty

In Partial Fulfillment of the Requirements

for the Degree of

Doctor of Philosophy

California Institute of Technology

Pasadena, California

1995

(Submitted August 5, 1994)

© 1995

M.V. Ramana Murty

All rights reserved

ACKNOWLEDGEMENTS

I have benefitted tremendously from interacting with the students and faculty during my several years at Caltech. It will be difficult to thank everyone, but I will make an effort. I apologize if I have failed to mention anyone.

I would like to thank Cho Jen Tsai for showing me the operation of the MBE system and the X-ray rocking curve system, and Jimmy Yang for managing the computers and making it a pleasure to write programs and manuscripts. I was pleased to have colleagues like Jung Shin who gave many a company in my late night endeavours and Imran Hashim who showed me cross section TEM specimen preparation and use of the X-ray diffractometer. I would like to thank Shouleh Nikzad who also showed me many details of the MBE system. Thanks to Gang He and Selmer Wong for asking me all kinds of questions, some of which I am still searching for an answer. Thanks, Sue Melnik and Renato Camata for being kind and patient while helping me set up the elastic recoil spectrometry system. I also thank John Nagel for showing me the operation of the AFM. It is also a pleasure to acknowledge many other fellow students, Howard Lee, Mike Albert, Jim Im, Byungwoo Park, Kirill Shcheglov, Hyun Joo, Heather Frase, Maggie Taylor, Ruth Brain, Aimee Smith, Lawrence Anthony, Donald Lie, Jen Sue Chen, Winston Saunders and Pete Sercel for expressing interest in my work and clarifying any problem I had.

I wish to specially thank our secretary, Rosalie Rowe, for handling all the paperwork and making travel arrangements to Conferences.

Setting up the ERS system was a big job and would not have proceeded far without the help of Mike Easterbrook and Rob Gorris. I would like to thank Mike Easterbrook for setting up the Pelletron, and for lending a hand on the ERS system whenever asked and Rob Gorris for machining or fixing jobs on short notice. I have to thank Joe Fontana at the Keck machine shop for machining jobs on short notice and fixing what seemed like hopeless pieces.

I am obliged to Carol Garland for teaching me all the operations in the TEM lab – from specimen preparation to use of the electron microscope. I really enjoyed working in the lab which is one reason why you will see a lot of TEM images in this thesis. I am thankful to Ian Hutcheon and Alan Rice for doing SIMS and XPS analysis, respectively, on my samples.

I found many of the graduate courses extremely useful. I enjoyed learning statistical mechanics from Dr. Corngold. The three courses on diffraction and TEM by Dr. Fultz and Dr. Ahn showed me the power of TEM. I would like to thank Dr. Nicolet for teaching me the use of RBS. I am obliged to both Dr. Nicolet and Dr. Goodwin for helpful suggestions on the ERS system. I would also like to thank Dr. J.E.E. Baglin and Dr. A.J. Kellock at IBM, Almaden for the experiments done at their place, and for ideas, and material support during the building of the ERS system.

I would like to thank the Institute Proofreader, Natalie Gilmore, and Dr. Atwater for indicating the many grammatical and punctuation errors in the manuscript.

In doing research and learning new things, I have found Dr. Atwater an extremely enthusiastic advisor. He showed me how to communicate effectively, had a great belief in what I was doing, and was a great motivator through good times and especially through hard times. He also gave me complete independence in choosing an approach to a problem. He was also the first to credit me for any results that were obtained. He always found time to discuss any problem, whether of a technical nature or in personal life.

Science today is advancing through highly specialized disciplines. The wide ranging research interests of Dr. Atwater has shown me that it is possible to make contributions in several fields, and that one must make an effort to explain the relevance of one's results to people studying closely related subjects. These are some the things that I take with me as I look forward toward my career.

Finally, I have to thank my parents and my sister who have always urged me to reach my dreams and aspirations. It is through their encouragement and commitment that I have reached so far.

ABSTRACT

Low temperature ($T \lesssim 400^\circ\text{C}$) deposition of Si on Si(001) proceeds epitaxially up to a finite thickness followed by a crystal-state—amorphous-state transition. An atomistic model, the twin-boundary/facet (TBF) mechanism, has been proposed for this transition. The increase in surface roughness during film growth has been directly tied to the breakdown of epitaxy. The mechanism involves the nucleation of a twin boundary on a $\{111\}$ facet (produced by roughening). When the twinned region meets a different part of the perfect crystal, it inevitably leads to the formation of five- and seven-member rings. These act as nucleation sites for amorphous silicon. Adsorbates such as carbon and oxygen can dramatically increase the surface roughness even at small coverages (~ 0.01 ML). They thus play an indirect role by accelerating the surface roughening rate.

Films with improved crystalline quality were deposited by ion beam-assisted molecular beam epitaxy. Atomic force microscopy revealed that the main effect of low energy Ar^+ ion irradiation was surface smoothing.

Molecular dynamics simulations suggest that epitaxy on hydrogen-terminated silicon surfaces (at high hydrogen coverage) proceeds by subplantation of the incident Si atom and segregation of SiH_x units. The remarkable success of sputter deposition in growing epitaxial films on a dihydride-terminated Si(001) surface is explained by the very rapid rise in the subplantation probability with the incident Si atom energy.

An empirical interatomic potential has been developed to describe Si-H interactions. This can be used, with caution, for classical molecular dynamics investigations of hydrogen-terminated silicon surfaces, chemical vapor deposition of silicon and hydrogenated amorphous silicon.

A technique for low temperature Si(001)-2×1 substrate preparation was developed to complement the various low temperature processes that are being developed for device fabrication. This was achieved by low energy noble gas ion (Ar^+ or He^+) irradiation of a nominally dihydride-terminated Si(001)-1×1 surface. Reconstructed Si(001)-2×1 surfaces were prepared at temperatures as low as 100°C. Silicon films deposited on such surfaces were epitaxial.

LIST OF PUBLICATIONS

Parts of this thesis have been published, or will be published under the following titles:

Crystal-state — Amorphous-state Transition in Low Temperature Silicon Homoepitaxy, M.V. Ramana Murty and H.A. Atwater, Phys. Rev. B **49**, 8483(1994).

Very Low Temperature ($< 400^{\circ}\text{C}$) Silicon Molecular Beam Epitaxy: The Role of Low Energy Ion Irradiation, M.V. Ramana Murty, H.A. Atwater, J.E.E. Baglin and A.J. Kellock, Appl. Phys. Lett. **62**, 2566(1993).

Defect Generation and Morphology of (001) Si Surfaces During Low Energy Ar Ion Bombardment, M.V. Ramana Murty and H.A. Atwater, Phys. Rev. B **45**, 1507(1992).

Empirical Interatomic Potential for Si-H Interactions, M.V. Ramana Murty and H.A. Atwater, submitted for publication.

Low Temperature Ion Beam-Induced Si(001)-2×1 Surface Reconstruction, M.V. Ramana Murty and H.A. Atwater, in preparation.

Epitaxy on Hydrogen-Terminated Silicon Surfaces, M.V. Ramana Murty and H.A. Atwater, in preparation.

Empirical Interatomic Potential for Si-H interactions, M.V. Ramana Murty and H.A. Atwater, Mat. Res. Soc. Symp. Proc. **317**(1993).

Low Energy Ar Ion Bombardment of (001) Si: Defects and Surface Morphology, M.V. Ramana Murty and H.A. Atwater, Mat. Res. Soc. Symp. Proc. **223**, 21(1991).

Surface and Near-Surface Atom Dynamics During Low Energy Xe Ion Bombardment of Si and fcc Surfaces, M.V. Ramana Murty, H.S. Lee and H.A. Atwater, Mat. Res. Soc. Symp. Proc. **193**, 301(1990).

Contents

1	INTRODUCTION	1
1.1	Low Temperature Silicon Homoepitaxy	1
1.2	Silicon Epitaxy in VLSI Technology	4
1.3	The Silicon Surface	6
1.4	Molecular Beam Epitaxy of Silicon	8
1.5	Kinetic Roughening	11
1.6	Hydrogen	13
1.7	Low Energy Ion Irradiation	14
1.8	Outline of the Thesis	16
	Bibliography	17
2	LOW TEMPERATURE SILICON MOLECULAR BEAM EPI- TAXY	26
2.1	The Molecular Beam Epitaxy System	26
2.2	Sample Preparation	31
2.3	Silicon Molecular Beam Epitaxy – A Reflection High-Energy Electron Diffraction Study	32
2.4	Conventional Molecular Beam Epitaxy – A Transmission Elec- tron Microscopy Study	39

2.5	The Breakdown of Epitaxy at Low Temperatures	43
2.6	Ion Beam-Assisted Molecular Beam Epitaxy	46
2.7	Other Thin Film Characterization Techniques	53
2.7.1	Rutherford Backscattering and Channeling	53
2.7.2	Secondary Ion Mass Spectrometry	54
2.7.3	Atomic Force Microscopy	58
2.8	Annealing Experiment	65
2.9	Voids in Low Temperature MBE Grown Silicon	66
2.10	Beam-Induced Desorption of Surface Hydrogen	68
2.11	Temperature Ramp Experiments	70
2.12	The Crystal-state—Amorphous-state Transition	73
	Bibliography	80

3	LOW ENERGY ION IRRADIATION OF SILICON – A	
	MOLECULAR DYNAMICS INVESTIGATION	87
3.1	Introduction	87
3.2	Interatomic Potential for Silicon	89
3.2.1	The Tersoff Potential	89
3.2.2	Description of Silicon	91
3.3	Numerical Methods	93
3.3.1	The Algorithm	93
3.3.2	The Runge-Kutta-Nyström Method	96
3.3.3	The Link Cell Method	100
3.3.4	The Cutoff Function	100
3.3.5	Boundary Conditions	101

3.4	Low Energy Ar^+ Ion Irradiation of Smooth and Rough Silicon Surfaces	102
3.4.1	Energy Loss of Ions	102
3.4.2	Simulation Description	103
3.4.3	Simulation Results	106
	Bibliography	115
4	EPITAXY ON HYDROGEN-TERMINATED SILICON SURFACES	120
4.1	Introduction	120
4.2	An Empirical Interatomic Potential for Si-H Interactions . . .	122
4.3	Epitaxy on a Dihydride-Terminated $\text{Si}(001)\text{-}1\times 1$ Surface . . .	134
4.4	Epitaxy on a Monohydride-Terminated $\text{Si}(001)\text{-}2\times 1$ Surface .	143
4.5	Discussion	147
	Bibliography	149
5	LOW TEMPERATURE ION BEAM-INDUCED $\text{Si}(001)\text{-}2\times 1$ SURFACE RECONSTRUCTION	155
5.1	Introduction	155
5.2	Beam-Induced Reconstruction of Silicon	157
5.2.1	Sample Preparation	157
5.2.2	Reflection High-Energy Electron Diffraction	158
5.2.3	Transmission Electron Microscopy of Silicon Films . . .	159
5.3	Molecular Dynamics Simulations of the Beam-Induced Reconstruction	163
5.4	Discussion	169

Bibliography	172
6 SUMMARY	174
6.1 Silicon Molecular Beam Epitaxy	174
6.2 Summary of Results	175
6.3 The Crystal-state—Amorphous-state Transition	177
6.3.1 The Role of Surface Roughness	177
6.3.2 The Role of Low Energy Ion Irradiation	179
6.3.3 The Role of Adsorbates	181
6.4 Other Results	184
6.4.1 Surface Cleaning of Silicon	184
6.4.2 Empirical Si-H Interatomic Potential	185
Bibliography	187
A Chemical Cleaning of Silicon Wafers	191
Bibliography	193
B Elastic Recoil Spectrometry	194
B.1 Introduction	194
B.2 The Elastic Recoil Spectrometry System	196
B.3 Calibration	203
B.4 Error Analysis	205
B.5 Hydrogen on Silicon Surface	206
B.6 Conclusion	209
Bibliography	212
C Algorithm for Molecular Dynamics Simulations	214

List of Figures

1.1	(a) The various geometric features on a vicinal surface. (b) The terrace and step structure of a vicinal Si(001) surface. The two different types of monatomic steps, S_A and S_B , are indicated and the arrow marks the direction of fast diffusion of adatoms.	9
2.1	The molecular beam epitaxy system.	29
2.2	A schematic of the molecular beam epitaxy system. The drawing is not to scale.	30
2.3	The surface net of the (a) unreconstructed Si(001), and (b) (2×1) reconstructed Si(001). The (2×1) reconstruction is shown in the x-direction.	34
2.4	The reciprocal lattice corresponding to the (a) unreconstructed Si(001), and (b) (2×1) reconstructed Si(001) in the previous figure.	34
2.5	The RHEED pattern of a Si(001)- 2×1 surface along the $\langle 110 \rangle$ azimuth with the electron beam incident at (a) 0.6° , (b) 1.5° , and (c) 2.1° grazing angle.	36

- 2.6 A sequence of RHEED patterns illustrating substrate preparation and Si MBE at high and low temperatures. RHEED pattern after (a) chemical cleaning; and (b) complete hydrogen desorption at 550°C. *High temperature buffer layer*. RHEED patterns after (c) 0.5 nm; (d) 30 nm; and (e) 110 nm deposition at 550°C. *Low temperature growth*. RHEED patterns after (f) 60 nm deposition; (g) identification of diffraction spots (only twin spots) in (f); and (h) 200 nm deposition at 300°C. 38
- 2.7 Bright field image of a 220 nm film deposited by conventional MBE at 370°C. The image was taken under multibeam conditions in the $\langle 110 \rangle$ projection. The epitaxial thickness, h_{epi} , is estimated to be 83 nm. 41
- 2.8 (a) High resolution image of a twinned region. (b) A planar defect believed to be a “hydrogen-platelet.” 42
- 2.9 High resolution image of a 110 nm film deposited by conventional MBE at 240°C. The image was taken in the $\langle 110 \rangle$ projection. The epitaxial thickness, h_{epi} , is estimated to be 25 nm. 44

- 2.10 A possible pathway to the breakdown of epitaxy. (a) Low temperature growth results in three-dimensional islanding with some $\{111\}$ -oriented facets. (b) A wireframe model illustrating the pathway to amorphous silicon. It is postulated that a $\Sigma 3$ coherent twin boundary is formed on a (111) plane. When this twinned region grows and meets a different plane, say $(\bar{1}11)$, the atoms do not line up. This necessarily leads to the formation of five- and seven-member rings and acts as a nucleation site for amorphous silicon. 47
- 2.11 (a) High resolution TEM image of an IAMBE film deposited at 370°C and 0.09 nm/s . The Ar^+ ion energy was 50 eV and the ion-to-atom flux was about 0.06 . The image was taken in the $\langle 110 \rangle$ projection. (b) An enlarged view of the surface showing a $\{311\}$ facet. Both $\{311\}$ and $\{111\}$ facets were observed on the growing front. 50
- 2.12 Epitaxial thickness vs. inverse temperature for conventional MBE films measured by (a) • cross section transmission electron microscopy, and (b) ○ RHEED observations. 51
- 2.13 Epitaxial thickness vs. inverse temperature for (a) • Conventional MBE, (b) ◇ 50 eV Ar^+ IAMBE, and (c) △ 70 eV Ar^+ IAMBE. The epitaxial thickness was measured by cross section transmission electron microscopy. 52

2.14 Rutheford backscattering/channeling spectra from (a) a 50 nm film deposited by conventional MBE at 370°C, and (b) an 80 nm film deposited by IAMBE. The substrate temperature was 370°C for both films. The minimum yield $\chi_{\min} = 0.03$ for the (001) aligned spectra in both cases. It is noted that about (a) 75% and (b) 50% of the signal from the low temperature film falls within the surface peak. 55

2.15 The SIMS profiles of H, C and O in (a) conventional MBE film and (b) IAMBE film. Both films were deposited at 370°C and 0.09 nm/s. C and O profiles were obtained with a 14.5 keV Cs⁺ beam; the H profile was obtained with a 10.5 keV O₂⁺ beam. Note that the background levels of H and O are different for (a) and (b). 59

2.16 AFM images after (a)20, (b)40, (c)60, and (d)80 nm film deposited at 325°C by conventional MBE. The growth rate was 0.09 nm/s. (e) AFM image of an IAMBE film after 40 nm deposition at 325°C. The Ar⁺ ion energy was 50 eV and the ion-to-atom flux ratio was about 0.06. The horizontal and vertical scales are 100 nm/division and 2.5 nm/division, respectively. 60

2.17 RHEED patterns after (a)20, (b)40, (c)60, and (d)80 nm film deposited at 325°C. (a) RHEED pattern from an IAMBE film after 40 nm deposition at 325°C. These RHEED patterns correspond to the AFM images in the previous figure. 61

2.18 The rms surface roughness vs. film thickness for different growth conditions. The roughness was measured over a $300 \times 300 \text{ nm}^2$ area at three separate points on each specimen. Conventional MBE at (a) \triangle , 240°C , (b) \bigcirc , 325°C , and IAMBE at (c) \diamond , 325°C . The arrows indicate the epitaxial thickness estimated from the RHEED patterns. The dashed line is the measured roughness of a high-temperature buffer layer. 62

2.19 RHEED pattern along $\langle 110 \rangle$ azimuth. (a) After depositing 50 nm at 325°C , and (b) after 10 min. anneal at 450°C 67

2.20 (a) Bright field image of a 140 nm buffer layer deposited at 530°C followed by a 340 nm film at 410°C . The image was taken under multibeam conditions in the $\langle 110 \rangle$ projection. A trail of voids can be seen in the film. (b) The diffraction pattern shows twin spots. (c) An enlarged view (high resolution) of a defect at the buffer layer/substrate interface. 69

2.21 RHEED pattern showing low energy Ar^+ ion beam-induced reconstruction. The substrate temperature was 190°C 71

2.22 HRTEM image of a film deposited by He^+ IAMBE. The temperature was dropped at a rate of 9 K/min. starting at 500°C and the growth rate was 0.02 nm/s. The ECR source was operated at 130 W and 0.07 Pa He pressure. 74

2.23 HRTEM image of a film deposited by conventional MBE in a background (0.07 Pa) of He gas. Temperature was dropped at a rate of 9 K/min. starting at 500°C and the growth rate was 0.02 nm/s. 75

3.1	The (2×1) reconstructed Si(001) surface viewed along the <110> axis according to the Tersoff potential.	93
3.2	Flow chart showing the major steps in the molecular dynamics code.	94
3.3	The variation in step size during a simulation of a 10 eV Si atom incident on a dihydride-terminated Si(001) surface. . . .	99
3.4	The three defect structures placed on the Si(001) surface. The rectangles drawn around each structure indicate the area in which the ions were incident. All ions were incident at 45° with respect to the surface normal and the arrows indicate the azimuths.	108
3.5	The time evolution of displacement yield for argon ions incident on smooth Si(001)-2×1 surface. The lines are spline fits to guide the eye.	109
3.6	The total displacement yield vs. energy for the defect structures. The lines are spline fits to guide the eye.	112
3.7	The distribution of displacements in the substrate at (a) 10 eV, (b) 20 eV, (c) 35 eV, and (d) 50 eV. The four symbols refer to smooth Si(001) (○), dimer pair (△), dimer string edge (◊), and dimer string center (●). Displacements in layer 0 are those from the defect placed on the surface.	113

- 3.8 (a) The surface-to-bulk displacement ratio R and (b) the average number of broken dimers per incident ion (only from the placed dimers) for the different defect structures. The results are for the dimer pair (\triangle), dimer string edge (\diamond), and dimer string center (\bullet). 114
- 4.1 The combination of the potentials used for different triples. I is the Si-Si potential, IIa and IIb are parts of the Si-H potential and III is the H-H potential. 125
- 4.2 The different hydrogen-induced reconstructions of the silicon surface. (a) The (2×1) monohydride structure with a hydrogen coverage $\theta = 1$ ML, (b) the (3×1) structure with alternate monohydride and dihydride units at $\theta = 1.33$, and (c) the (1×1) dihydride structure with $\theta = 2$ ML. The dimensions and angles are according the Si-H potential. 132
- 4.3 HRTEM image of a silicon film deposited on an initially dihydride-terminated Si(001)- 1×1 surface. The substrate temperature was 190°C and the growth rate was 0.09 nm/s . The film is amorphous. 136
- 4.4 Molecular dynamics simulation of a 0.25 eV Si atom (blue) incident on a dihydride-terminated Si(001)- 1×1 surface. The atomic positions are at (a) 0 ps , i.e., start of the simulation, (b) 0.15 ps , (c) 0.30 ps , and (d) 1 ps into the simulation. Only the top layer of silicon atoms (green) and hydrogen atoms (red) in the region of interest are shown. 137

4.5	Molecular dynamics simulation of a 4 eV Si atom (blue) incident on a dihydride-terminated Si(001)-1×1 surface. The atomic positions are at (a) 0 ps, i.e., start of the simulation, (b) 0.05 ps, (c) 0.10 ps, and (d) 1 ps into the simulation. Only the top layer of silicon atoms (green) and hydrogen atoms (red) in the region of interest are shown.	138
4.6	The subplantation probability P_s versus incident silicon atom energy.	141
4.7	Epitaxial silicon film deposited on an initially monohydride-terminated Si(001)-2×1 surface. The substrate temperature was 380°C and the growth rate was 0.02 nm/s.	145
4.8	The atomic positions after 1 ps of simulation for two different impact points of the incident silicon atom. The incident atom (blue) is subplanted in (a) but remains at the level of hydrogen atoms in (b). The incident atom had a kinetic energy of 0.25 eV. Only the top layer of silicon atoms (green) and hydrogen atoms (red) in the region of interest are shown.	146
5.1	RHEED pattern (a) immediately after HF dip; after 50 eV Ar ⁺ ion irradiation at (b) 190°C, and (c) 100°C; and after exposure to He ⁺ ions at (d) 190°C, and (e) 50°C.	160
5.2	HRTEM image of a silicon film deposited after beam-induced reconstruction using 50 eV Ar ⁺ ions incident at 45° with respect to the substrate normal. The substrate temperature was 190°C and the growth rate was 0.09 nm/s.	161

5.3	HRTEM image of a silicon film deposited after beam-induced reconstruction using He^+ ions. The substrate temperature was 190°C and the growth rate was 0.03 nm/s	162
5.4	Silicon film deposited after beam-induced reconstruction using 50 eV Ar^+ ions incident at 65° with respect to the substrate normal. The substrate temperature was 100°C and the growth rate was 0.03 nm/s	164
5.5	Silicon film deposited after beam-induced reconstruction using He^+ ions. The substrate temperature was 50°C and the growth rate was 0.03 nm/s . The thin oxide at the surface is also visible.	165
5.6	The sputtering yield of hydrogen versus Ar ion energy from (a) \circ dihydride-terminated $\text{Si}(001)\text{-}1\times 1$ surface, and (b) \bullet monohydride-terminated $\text{Si}(001)\text{-}2\times 1$ surface. The lines are spline fits to guide the eye.	167
5.7	The implantation of surface hydrogen atoms versus Ar ion energy from (a) \circ dihydride-terminated $\text{Si}(001)\text{-}1\times 1$ surface, and (b) \bullet monohydride-terminated $\text{Si}(001)\text{-}2\times 1$ surface. The lines are spline fits to guide the eye.	168
5.8	The silicon sputtering yield from (a) \circ dihydride-terminated $\text{Si}(001)\text{-}1\times 1$ surface, and (b) \bullet monohydride-terminated $\text{Si}(001)\text{-}2\times 1$ surface. The lines are spline fits to guide the eye.	168
B.1	A schematic of the elastic recoil spectrometry system. The line-of-sight port to the substrate is marked by the letter A. A Kaufman ion source is shown connected at this port. The drawing is not to scale.	198

B.2	The electronics used for the detection of alpha particles and protons. Both RBS and ERS spectra can be collected simultaneously on a single computer.	199
B.3	The scattering geometry used in the experiments.	200
B.4	The (a) backscattering and (b) forward scattering spectra from a 100 nm film of $(C_8H_8)_n$ (polystyrene) on Si. The background subtracted carbon peak is also shown in the RBS spectrum. Both spectra were collected simultaneously. The incident He^+ ion energy was 2.0 MeV.	204
B.5	The (a) backscattering and (b) forward scattering spectra from a Si(001) wafer after a dilute ($\sim 5\%$) HF dip. Both spectra were collected simultaneously. The incident He^+ ion energy was 2.0 MeV.	208
B.6	(a) The ERS spectrum from a Si(001) wafer dipped in a $\sim 1\%$ HF + D_2O solution for two minutes followed by an overnight anneal at $200^\circ C$. The hydrogen coverage is about 3.0 ML and the deuterium coverage is about 0.26 ML. (b) The ERS spectrum after a 1 ML dose of 50 eV Ar^+ ions at a substrate temperature of $200^\circ C$. The hydrogen coverage is about 3.3 ML and the deuterium coverage is about 0.11 ML. The spectra in (a) and (b) are normalized with respect to the incident He^+ dose. The incident He^+ ion energy was 2.0 MeV.	210

List of Tables

2.1	The results of temperature ramp experiments.	73
3.1	The speed of operation of molecular dynamics codes.	95
3.2	Impact parameters used with different surface defect structures.	106
4.1	The parameters used in the Si-H interatomic potential along with the Si-Si and H-H potentials.	127
4.2	Properties of some Si_mH_n molecules. Vibrational wave num- bers in cm^{-1} . The bond energy of H_2 includes the zero- point energy. Asterisk (*) indicates a theoretically calculated value. The Si-H potential was explicitly fitted to the proper- ties marked by the † sign.	129
4.3	The energy differences ΔH for disilane decomposition. The asterisk (*) indicates a theoretically estimated value.	130
4.4	Hydrogen sputtering events during energetic silicon atom de- position on a dihydride-terminated Si(001) surface.	142
B.1	Hydrogen coverage after annealing a dilute HF dipped Si(001) wafer.	207

Chapter 1

INTRODUCTION

My life is spent in one long effort to escape from the commonplaces of existence. These little problems help me to do so.

– *Sherlock Holmes*, The Red-headed League

Sir Arthur Conan Doyle

1.1 Low Temperature Silicon Homoepitaxy

Anyone who has practiced semiconductor epitaxy must have asked the question, “Why does one grow epitaxial films at high temperatures but amorphous films at low temperatures?” The usual response is to draw attention toward the limited adatom mobility at low temperatures. While such an answer is essentially correct, it is a macroscopic view of the phenomenon. A more complete description would include the microscopic view — the atomic arrangements that lead to the breakdown of epitaxy. Such a description is essential particularly in light of the fact that the crystalline phase is the ther-

modynamically favored phase. The understanding so gained can be used to develop techniques to prevent the nucleation of the amorphous phase.

The crystal-state—amorphous-state transition during low temperature epitaxy is a fundamental phenomenon in semiconductors. Growth at low temperatures proceeds epitaxially up to a finite thickness followed by a locally abrupt transition to amorphous film deposition. It has now been observed in Si, Ge, GaAs and InP. Although semiconductor films have been fabricated and studied for more than three decades, the discovery of the crystal-state—amorphous-state transition in physical vapor deposition is a relatively recent one [1, 2]. Earlier it was believed that growth of semiconductor films always proceeds epitaxially above a certain temperature, T_{epi} (with a weak dependence on growth rate), whereas amorphous films would be obtained below T_{epi} [3]. In this view, when the diffusion length of an adatom was less than the nearest neighbor distance on the surface, the adatoms would just stick where they land. This would lead to an amorphous film in materials with strongly directional bonds [3]. Applying this criterion to Si on Si(001), we find $T_{\text{epi}} \approx 300$ K using the surface diffusion coefficient (activation energy 0.67 eV and prefactor 10^{-3} cm²/s [4]) and a growth rate of one monolayer (ML) per second. For Si on Si(001), the transition to amorphous film deposition is observed at temperatures as high as 400°C. Thus the loss of lattice periodicity occurs even with a large adatom mobility and this has been a challenge in formulating the growth mechanisms in low temperature epitaxy.

Silicon molecular beam epitaxy (MBE), or vacuum evaporation as it was called in the early days, has been studied for over three decades. A review of most of the work done until 1973 can be found in Ref. [5]. Early work

focussed on epitaxy on Si(111). The films were frequently deposited under high vacuum conditions [6]. Even films deposited at high temperatures ($T > 1000^\circ\text{C}$) contained defects such as twins and stacking faults [7]. When ultrahigh vacuum conditions were used, single crystal films were obtained at 550°C on Si(111) [8]. In a transmission electron microscopy study of silicon films grown on Si(111)- 7×7 using a silane beam, it was observed that deliberate carbon contamination changed the growth mode from layer-by-layer to three-dimensional islanding [9, 10]. With the increasing use of MOS transistors, epitaxy on Si(001) began to be studied in more detail. Silicon MBE, as it began to be called in the 1970s, was studied with scrupulous attention to every aspect of thin film growth — *ex situ* and *in situ* surface cleaning, substrate orientation and vicinality, temperature, growth rate and effects of doping and ion irradiation. The importance of a clean starting surface was recognized and the influence of various chemical pre-treatments (*ex situ* methods) and ion beam sputtering (*in situ* methods) were studied. Surface analytical tools such as X-ray photoelectron spectroscopy (XPS), Auger electron spectroscopy (AES), low energy electron diffraction (LEED) and reflection high-energy electron diffraction (RHEED) were employed to characterize the efficacy of the surface cleaning procedures. The observation of intensity oscillations of the specular beam in reflection high-energy electron diffraction, or RHEED oscillations, provided a way to control growth at the sub-monolayer level [11]. Scanning tunneling microscope (STM) images revealed a host of phenomena at the silicon surface. The various surface reconstructions, the terrace and step structure of vicinal surfaces, anisotropic surface diffusion on Si(001), anisotropic island shapes and the adsorption

sites of foreign elements were some of the features observed/revealed by the STM. Many phenomena on silicon are now known at the atomic scale. There remain, however, many problems that are still being addressed such as the improvement in surface smoothness of silicon wafers after chemical cleaning and growth of lattice-mismatched films on silicon substrates.

Low temperature silicon homoepitaxy has received a lot of attention in recent years and is the central issue in this thesis. A brief description of the many features closely related to low temperature silicon epitaxy is given in the following sections.

1.2 Silicon Epitaxy in VLSI Technology

The ability to grow crystalline semiconductor films at low temperatures has been considered an important step in the development of future integrated-circuit technology. Currently, epitaxial silicon films are deposited by chemical vapor deposition (CVD) from chlorosilane precursors at $T > 900^{\circ}\text{C}$. Dopant redistribution and reaction of predeposited layers is quite rapid at such high temperatures. This has limited the use of epitaxial silicon films in very large scale integrated (VLSI) circuits. Today, metal-oxide semiconductor (MOS) devices are frequently fabricated within epitaxial silicon films deposited on Czochralski wafers. An epitaxial silicon film is also deposited after creating the buried collector layer for bipolar junction transistors (BJT) [12]. These films are deposited quite rapidly (several $\mu\text{m}/\text{min}$) to prevent contaminant accumulation. The main reason for this is the high background pressure

($> 10^{-6}$ Pa) in the deposition systems. Lower growth rates can be tolerated by going to ultra-high vacuum (UHV) systems and this has been a topic of intense research during the past decade. Silane (SiH_4) has been frequently used as the gas precursor in ultra-high vacuum chemical vapor deposition (UHVCVD) systems. Excellent epitaxial films can be deposited at $T \sim 500^\circ\text{C}$. Heterojunction bipolar transistors (HBT), both discrete and in integrated circuits, have been fabricated [13, 14].

Low temperature epitaxial growth of semiconductor films also generates a number of new possibilities. One application is the ability to grow delta-doped structures. The mobility of electrons and holes degrades rapidly as the doping concentration increases due to the disruption of the periodic potential. This can be minimized by depositing atomically abrupt dopant layers. This requires growth at extremely low temperatures to kinetically suppress the surface segregation of dopant atoms. The deposition temperature must be less than 300°C for the n-type dopant Sb [15]. Boron delta-doped layers can be deposited at 400°C [16]. Delta-doped layers with almost unity activation of the dopant have been demonstrated [17, 18]. Delta-doped layers can be used to improve the performance of a number of devices such as MOS transistors, BJTs and ohmic contacts [19].

The prevention of strain relaxation in heterostructures is another motivation. Deposition of group IV alloys and III-V semiconductors on silicon has received much attention due to the possibility of integrating devices with different functions on a single chip. The large lattice mismatch between silicon and other semiconductors has made it difficult to grow thick films without defects. However, pseudomorphic films exceeding the equilibrium

critical thickness for misfit dislocation formation can be readily prepared. Once such films have been deposited, thermal cycling of the wafer must be minimized to prevent strain relaxation.

1.3 The Silicon Surface

The structure and energetics of silicon surfaces have been studied in great detail. A clean, low index surface of silicon reconstructs to reduce the number of dangling bonds. Atoms on a semiconductor surface move a significant distance to reconstruct. The Si(001) surface usually reconstructs to form a (2×1) structure. The Si(111) surface forms many reconstructions such as the (2×1) , (5×5) and (7×7) structures. The (2×1) surface of Si(001) was first observed in 1959 [20]. The reconstructions on the Si(111) surface have a similar history, but the actual atomic arrangements for the (2×1) and the (7×7) structures were reported in 1981 [21] and 1985 [22], respectively.

Silicon wafers are usually made by cutting an ingot with a diamond saw and chemo-mechanical polishing with silica particles and sodium hydroxide. This usually produces wafers with a small miscut, i.e., the surfaces are oriented away from a low index crystallographic plane by a small angle. Scanning tunneling microscopy [23] and low energy electron microscopy (LEEM) [24, 25] images have shown detailed atomic arrangements and the shapes of steps on such vicinal surfaces. They are characterized by a terrace and step structure as shown schematically in Fig. 1.1. The average terrace size is given by $h/\tan \theta$ where h is the step height and θ is the angle

of miscut. Tight-binding calculations have shown that a double step is energetically more favorable than two single steps on the Si(001) surface [26, 27]. Indeed, double steps are found for vicinal angles greater than about 3° [28]. However, for vicinal angles less than about 2° , the surface is dominated by monatomic steps [28]. This splitting of the double step into two single steps was explained in Ref. [29] as being due to the surface stress induced by the dimerization. With double steps, the dimers are all oriented in one direction whereas with single steps, the dimer direction rotates by 90° at a step. This relieves some of the strain in the crystal.

The rotation of the dimers at a monatomic step gives rise to two different types of steps (labeled S_A and S_B [27]) as shown schematically in Fig. 1.1. The dimers on the top terrace are oriented perpendicular (parallel) to the step edge in the S_A (S_B) step. The double steps D_A and D_B are defined similarly. Experimentally, it is found that S_B step edges meander a lot but S_A and D_B step edges are relatively smooth and this has its origin in the kink formation energies [28]. The step energies in the order of increasing energy are S_A , D_B , S_B and D_A [27]. Kinks on a S_A step are of S_B type and vice versa (similarly for D_A and D_B steps) which explains the roughness of the step edges.

Despite the large number of studies of the silicon surface, the surface energy as a function of orientation is not known. This is due to the inability to access non-equilibrium orientations and the large amount of mass transport required to bring a macroscopic crystal into equilibrium. Such knowledge could be used to determine the equilibrium crystal shape as a function of temperature [30] and the surface roughening temperature. It would also

facilitate the study of surface morphology in low temperature epitaxy. The surface energy for the $\langle 100 \rangle$ and $\langle 111 \rangle$ orientations was determined in two recent studies [31, 32]. Both studied the geometry of internal cavities generated by ion irradiation. The surface energies for the $\langle 100 \rangle$ and the $\langle 111 \rangle$ surfaces were estimated to be 1.36 and 1.23 J/m² respectively. The reconstruction of the internal surfaces in the cavity was not known.

The surface diffusion of adatoms on Si(001) has been studied both experimentally and theoretically. The adatom diffusion has been shown to be highly anisotropic with the fast direction being along the dimer rows as indicated in Fig. 1.1. The activation energy and prefactor for diffusion have been estimated as 0.67 ± 0.08 eV and 10^{-3} cm²/s respectively [4]. This corresponds to ~ 1 and $\sim 10^6$ jumps/s at room temperature and 300°C respectively. A number of computational studies based on the local density approximation [33] and empirical potentials [34, 35] have produced similar numbers for the diffusion constant.

1.4 Molecular Beam Epitaxy of Silicon

Steps on the surface play an important role in epitaxy. This was recognized early in the development of the theory of crystal growth [36]. The fact that crystal growth occurs even at small supersaturations was explained by the diffusion and incorporation of adatoms at steps.

The magnitude of the Péclet number $P = jL^2/D$ provides a way to classify the different growth regimes in molecular beam epitaxy [30, 37]. Here, D is

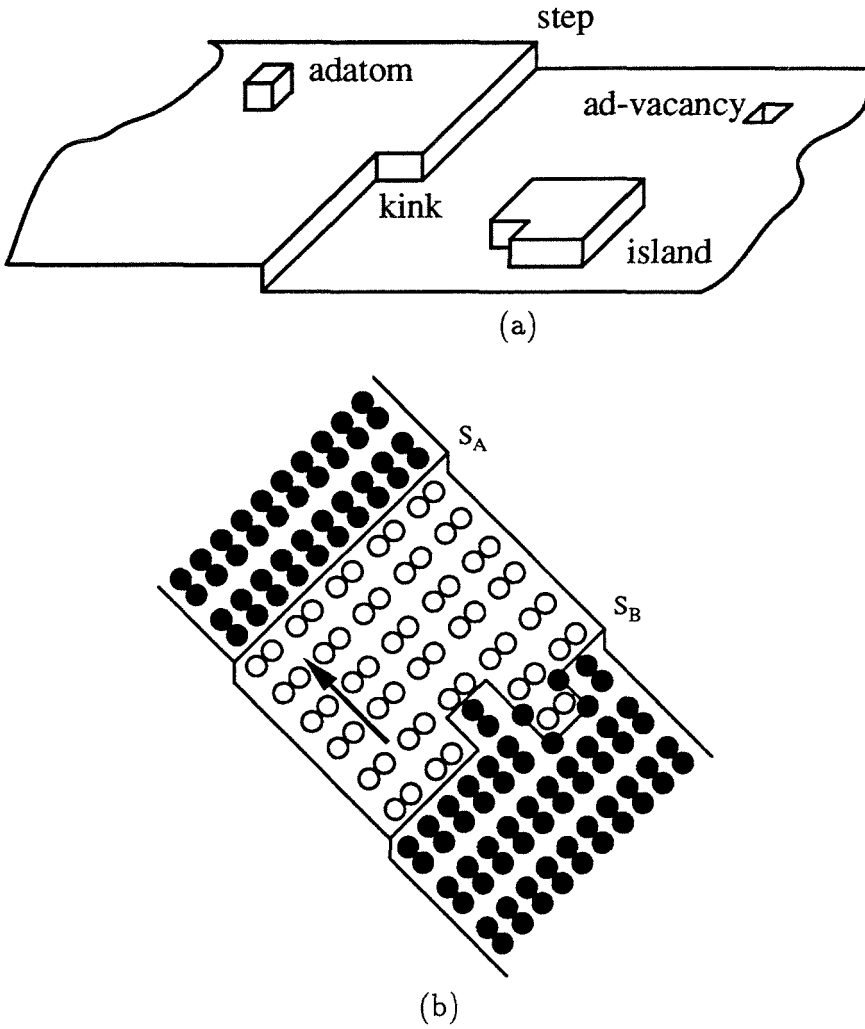


Figure 1.1: (a) The various geometric features on a vicinal surface. (b) The terrace and step structure of a vicinal Si(001) surface. The two different types of monatomic steps, S_A and S_B , are indicated and the arrow marks the direction of fast diffusion of adatoms.

the diffusion constant, j is the growth rate in monolayers (ML) per second and L is the terrace width. When $P \ll 1$, the adatoms are able to diffuse to a step edge and growth proceeds by step flow. There are no RHEED oscillations. For typical growth rates (~ 1 ML/s) on Si(001), this occurs for $T \gtrsim 650^\circ\text{C}$.

For $P \approx 1$, many atoms diffuse to the step but a significant fraction also form two-dimensional (2-D) islands on the terrace. The step velocity alternately rises and falls as it consumes islands until a steady state is reached and growth is said to occur by convective diffusion. The adatom coverage and step velocity are fairly well described by an analytical theory [30, 37, 38]. There are a few oscillations of the specular beam intensity in RHEED before it settles to a steady value. This occurs in the temperature range of $500 \lesssim T \lesssim 600^\circ\text{C}$.

At lower temperatures ($400 \lesssim T \lesssim 500^\circ\text{C}$) for which $P > 1$, most of the adatoms nucleate 2-D islands on the terrace. The critical size for a stable cluster is two [39]. This is the regime of 2-D cluster nucleation and growth where one observes RHEED intensity oscillations [11]. The island shapes are highly anisotropic due to differences in the step energies. This high anisotropy greatly reduces the nucleation of islands on top of islands and there are never more than ~ 3 incomplete layers [40]. One can grow crystalline silicon almost indefinitely and persistent RHEED oscillations have been observed for thousands of cycles [11].

At very low temperatures ($T \lesssim 400^\circ\text{C}$ and $P \gg 1$), three-dimensional (3D) islands are formed. This occurs when the diffusion length of an adatom is less than the size of a typical island. This is the regime where a crystalline-

to-amorphous transition is observed after a certain thickness. The RHEED intensity oscillations damp out after the deposition of a few layers [11]. A phenomenological or Monte Carlo model to describe the crystal growth would have to include a number of parameters and rates, many of which are not known. These include surface diffusion on a flat surface, rate of diffusion along a step, energy barriers to incorporation at a step, attachment and detachment rates from a step, surface energies and diffusion rates on various non-equilibrium orientations, etc. The modification of some of these rates by adsorbates will further complicate matters. It is these features which have made the study of low temperature epitaxy an open and challenging problem.

1.5 Kinetic Roughening

When the free energy to create a step at the surface vanishes, islands are created spontaneously. This is thermodynamic roughening and the roughening temperature has been most recently estimated as 1200°C for Si(001) [41].

Film growth from the vapor phase occurs under highly non-equilibrium conditions. Since the atoms are not deposited as a sheet, the surface tends to roughen. Counteracting this roughening are factors like surface diffusion and desorption which tend to smooth the surface. In this regime, kinetic roughening dominates, and the surface morphology evolves as a net result of these different factors. The rate of roughening is frequently expressed (on long length scales) by $w \sim h^\beta$ where w is the interface width (rms roughness) and h is the film thickness (for a uniform growth rate, $h \sim t$, the time of

film growth). The exponent is calculated for $(d + 1)$ dimensions (d lateral dimensions plus one vertical dimension) by either performing a Monte Carlo simulation or solving analytical equations (continuum models). The random arrival of the incident atoms is expressed by a Poisson distribution (noise term) [42]. In a simple model, the surface diffusion term is proportional to $\nabla^4 h$ where the gradient is taken with respect to the lateral dimensions [42, 43]. Desorption of adatoms is negligible in the case of molecular beam epitaxy. In the case of no surface diffusion, the exponent $\beta = 1/2$. Introduction of a smoothing term reduces the value of β , i.e., the surface roughens more slowly. For example, for the Kardar-Parisi-Zhang equation, the exponent $\beta = 1/3$ for $d = 1$ and $\beta = 0.24$ for $d = 2$ [44, 45]. If surface diffusion is the only smoothing term, the exponent has been calculated to be $\beta = 0.375$ for $d = 1$ and $\beta = 0.25$ for $d = 2$ [46, 47].

The study of kinetic roughening during film growth is a very active field today. It is particularly relevant to low temperature silicon epitaxy because surface roughness plays a crucial role. As mentioned in the previous Section, there are a large number of parameters affecting film growth and this has made even a qualitative description difficult. A combination of experimental and theoretical work is needed to make progress toward application to semiconductors.

1.6 Hydrogen

Silicon is the prototypical semiconductor and hydrogen is the simplest element [48]. The interaction of these two elements is important in many processes in VLSI technology. Chemical vapor deposition from silane, an HF dip, and hydrogenated amorphous silicon are some examples where hydrogen plays a crucial role.

Hydrogen as an adsorbate has many interesting effects in silicon homoepitaxy. Hydrogen-termination of the silicon surface causes a remarkable change in its reactivity. A bare silicon surface exposed to atmosphere will immediately form a thin oxide. If the surface Si atoms are terminated with hydrogen atoms (commonly performed by an HF dip), the oxidation rate is reduced by several orders of magnitude. Such surfaces are stable in a laboratory atmosphere for hours [49]. Recently, it was discovered that dipping a Si(111) wafer in a high pH solution ($\text{pH} \geq 5$) of HF and NH_4F produces atomically smooth surfaces [50]. Most of the surface is covered with monohydride species with very few dihydride and trihydride species. The analogous process with Si(001) wafers, however, produces relatively rough surfaces. This is believed to be due to the strong repulsion of H atoms on neighboring dihydride units. Although the surface is nominally dihydride-terminated, significant amounts of monohydride and trihydride species may be present [51]. Silicon surfaces can also be hydrogen-terminated by exposing a clean surface to atomic hydrogen, but molecular hydrogen does not adsorb on silicon. Depending on the hydrogen coverage, the Si(001) surface can exhibit a (2×1) , (3×1) or (1×1) reconstruction [52].

Complete hydrogen desorption occurs above 500°C on both Si(001) and Si(111) [53]. The desorption product is molecular hydrogen. On Si(001), a dihydride-to-monohydride transition occurs at 350 – 400°C which transforms the surface from a (1×1) to a (2×1) structure. The desorption of hydrogen from the monohydride follows first order kinetics on the Si(001) [54]. It is hydrogen desorption which limits the growth rate in low temperature chemical vapor deposition with silanes [55].

Introduction of hydrogen during Si MBE can cause a premature breakdown of epitaxy [56, 57]. It has been shown that even a small coverage of hydrogen can drastically increase the Si island density during Si epitaxy [58]. At the same time, epitaxy is possible even with a uniform coverage of hydrogen [59, 60, 61]. These very interesting observations led us to examine the influence of hydrogen on the growth process.

1.7 Low Energy Ion Irradiation

Exposure to ions or energetic particles is not an unusual event in device fabrication. Examples include ion implantation to create doped regions, reactive ion etching to open regions for contacts, sputter deposition of metals, and plasma-enhanced chemical vapor deposition of amorphous silicon.

Ion beam-assisted deposition has been used to modify thin film microstructure and properties in a number of materials [62]. Energetic beams of dopants have been used to deposit heavily doped silicon films by MBE [63]. The surface segregation of dopants is overcome by incorporating them in sub-

surface sites. Ion beam sputtering is frequently used to create clean surfaces in vacuum. A novel phenomenon in sputtering is the layer-by-layer removal of silicon with 200 eV Xe^+ ions [64]. Low energy ion irradiation has also been used to suppress 3-D island formation during the initial stages of growth of Ge [65], and GaAs [66] on Si(001). This was attributed to the reduction of surface amplitude fluctuations during the early stages of growth.

The motivation for using ion irradiation in conjunction with silicon homoepitaxy comes from their ability to modify surface kinetics [67]. This could be used to favor the growth of a crystalline film. Such an approach has indeed met with success and thick epitaxial films have been deposited at temperatures as low as 200°C [61]. Silicon films have been deposited by direct ion beam deposition [68, 69, 70] and sputter deposition [60, 71]. Ion damage is an important consideration since electrical properties are very sensitive to beam-induced defects. This limits the maximum ion energy that can be used to irradiate a growing silicon film [72] and motivates the use of ion energies below 20 eV. The generation and transport of such ions has proved difficult due to space charge effects and there have been relatively few investigations of low energy ion beam-assisted silicon homoepitaxy.

Despite the success with the use of energetic particles, the influence of ion irradiation on a growing film are relatively unknown. The observation of ion beam enhanced epitaxial growth of Ge(001) was explained as a balance of ion-induced vacancy-like defects and growth-induced adatoms and islands [73]. Ion beam-assisted molecular beam epitaxy provides a way to independently control ion energy, flux and the growth rate. This was used to investigate the effects of ion irradiation on the surface morphology, film microstructure

and surface hydrogen.

1.8 Outline of the Thesis

The contents in this thesis are arranged as follows. Chapter 2 describes an experimental investigation of low temperature silicon molecular beam epitaxy. The influence of surface roughness, adsorbates and low energy ion irradiation on the crystal-state—amorphous-state transition is discussed. Chapter 3 describes the methods of molecular dynamics and the simulations of low energy ion irradiation of smooth and rough silicon surfaces. Chapter 4 begins with the development of an empirical interatomic potential to describe Si-H interactions. This is followed by a molecular dynamics investigation of epitaxy on hydrogen-terminated silicon surfaces. A new technique for preparing Si(001)- 2×1 surfaces at low temperatures is described in Chapter 5. Finally, Chapter 6 summarizes the main results of this thesis.

There are three appendixes. Appendix A contains a description of the chemical cleaning procedure for silicon wafers. The computer program SIH used for molecular dynamics simulations is listed in Appendix B. Lastly, Appendix C contains the details of an elastic recoil spectrometry system to measure hydrogen concentrations in thin films and substrates.

Bibliography

- [1] H. Jorke, H.J. Herzog, and H. Kibbel, ‘Kinetics of ordered growth of Si on Si(100) at low temperatures,’ Phys. Rev. B **40**, 2005(1989).
- [2] D.J. Eaglesham, H.-J. Gossmann, and M. Cerullo, ‘Limiting thickness h_{epi} for epitaxial growth and room temperature Si growth on Si(100),’ Phys. Rev. Lett. **65**, 1227(1990).
- [3] J.A. Venables and G.L. Price in *Epitaxial Growth*, ed. J.W. Matthews, Academic Press, New York, 1975.
- [4] Y.W. Mo, J. Kleiner, M.B. Webb, and M.G. Lagally, ‘Activation energy for surface diffusion of Si on Si(001) – a scanning tunneling microscopy study,’ Phys. Rev. Lett. **66**, 1998(1991).
- [5] B.A. Joyce, ‘The growth and structure of semiconducting thin films,’ Rep. Prog. Phys. **37**, 3639(1974).
- [6] See, for example, B.A. Unvala, ‘Epitaxial growth of silicon by vacuum evaporation,’ Nature **194**, 966(1962).
- [7] See, for example, B.A. Unvala and G.R. Booker, ‘Growth of epitaxial silicon layers by vacuum evaporation I. Experimental procedure and initial assessment,’ Phil. Mag. **9**, 691(1964).

- [8] H. Widmer, 'Epitaxial growth of Si on Si in ultra high vacuum,' Appl. Phys. Lett. **5**, 108(1964).
- [9] B.A. Joyce, J.H. Neave, and B.E. Watts, 'The influence of substrate surface conditions on the nucleation and growth of epitaxial silicon films,' Surf. Sci. **15**, 1(1969).
- [10] J.M. Charig and D.K. Skinner, 'Carbon contamination of Si(111) surfaces,' Surf. Sci. **15**, 277(1969).
- [11] T. Sakamoto, N.J. Kawai, T. Nakagawa, K. Ohta, and T.Kojima, 'Intensity oscillations of reflection high-energy electron diffraction during silicon molecular beam epitaxial growth,' Appl. Phys. Lett. **47**, 617(1985).
- [12] B.G. Streetman, *Solid State Electronic Devices*, Prentice Hall, New Jersey, 1990.
- [13] B.S. Meyerson, 'UHV CVD growth of Si and Si-Ge alloys – chemistry, physics, and device applications,' IEEE Proc. **80**, 1592(1992).
- [14] B.S. Meyerson, 'High-Speed silicon-germanium electronics,' Sci. Am. **270**, 62(1994).
- [15] H. Jorke, H. Kibbel, F. Schäffler, A. Casel, H.-J. Herzog, and E. Kasper, 'Properties of Si layers grown by molecular beam epitaxy at very low temperatures,' Appl. Phys. Lett. **54**, 819(1989).
- [16] N.L. Matthey, M. Hopkinson, R.F. Houghton, M.G. Dowsett, D.S. McPhail, T.E. Whall, E.H.C. Parker, G.R. Booker, and J. Whitehurst, 'P-type delta doping in silicon MBE,' Thin Sol. Fi. **184**, 159(1990).

- [17] H.-J. Gossmann and E.F. Schubert, 'Delta doping in silicon,' *Crit. Rev. Sol. St. Mat. Sci.* **18**, 1(1993).
- [18] R.L. Headrick, B.E. Weir, A.F.J. Levi, D.J. Eaglesham, and L.C. Feldman, 'Si(100)-(2×1) boron reconstruction: self-limiting monolayer doping,' *Appl. Phys. Lett.* **57**, 2779(1990).
- [19] H.-J. Gossmann, E.F. Schubert, D.J. Eaglesham, and M. Cerullo, 'Low-temperature Si molecular beam epitaxy: solution to the doping problem,' *Appl. Phys. Lett.* **57**, 2440(1990).
- [20] R.E. Schlier and H.E. Farnsworth, 'Structure and adsorption characteristics of clean surfaces of germanium and silicon,' *J. Chem. Phys.* **30**, 917(1959).
- [21] K.C. Pandey, 'New π -bonded chain model for Si(111)-(2×1) surface,' *Phys. Rev. Lett.* **47**, 1913(1981).
- [22] K. Takayanagi, Y. Tanishiro, S. Takahashi, and M. Takahashi, 'Structure analysis of Si(111)-7×7 reconstructed surface by transmission electron diffraction,' *Surf. Sci.* **164**, 367(1985).
- [23] B.S. Swartzentruber, N. Kitamura, M.G. Lagally, and M.B. Webb, 'Behaviour of steps as a function of vicinality,' *Phys. Rev.* **B47**, 13432(1993).
- [24] W. Telieps, 'Surface imaging with LEEM,' *Appl. Phys.* **A44**, 55(1987).
- [25] R.M. Tromp and M.C. Reuter, 'Wavy steps on Si(001),' *Phys. Rev. Lett.* **68**, 820(1992).

- [26] D.E. Aspnes and J. Ihm, 'Biatomic steps on (001) silicon surfaces,' *Phys. Rev. Lett.* **57**, 3054(1986).
- [27] D.J. Chadi, 'Stabilities of single-layer and bilayer steps on Si(001) surfaces,' *Phys. Rev. Lett.* **59**, 1691(1987).
- [28] See, for example, J.E. Griffith and G.P. Kochanski, 'The atomic structure of vicinal Si(001) and Ge(001),' *Crit. Rev. Sol. St. Mat. Sci.* **16**, 255(1990).
- [29] O.L. Alerhand, A.N. Berker, J.D. Joannopoulos, D. Vanderbilt, R.J. Hamers, and J.E. Demuth, 'Finite-Temperature phase diagram of vicinal Si(100) surfaces,' *Phys. Rev. Lett.* **64**, 2406(1990).
- [30] J.Y. Tsao, *Materials Fundamentals of Molecular Beam Epitaxy*, Academic Press, Boston, 1993.
- [31] D.J. Eaglesham, A.E. White, L.C. Feldman, N. Moriya, and D.C. Jacobson, 'Equilibrium shape of Si,' *Phys. Rev. Lett.* **70**, 1643(1993).
- [32] D.M. Follstaedt, 'Relative free-energies of Si surfaces,' *Appl. Phys. Lett.* **62**, 1116(1993).
- [33] G. Brocks, P.J. Kelly, and R. Car, 'Binding and diffusion of a Si adatom on the Si(100) surface,' *Phys. Rev. Lett.* **66**, 1729(1991).
- [34] C. Roland and G.H. Gilmer, 'Epitaxy on surfaces vicinal to Si(001). 1. Diffusion of silicon adatoms over the terraces,' *Phys. Rev. B* **46**, 13248(1992).

- [35] D. Srivastava and B.J. Garrison, 'The dynamics of surface rearrangements in Si adatom diffusion on the Si(100)-(2×1) surface,' J. Chem. Phys. **95**, 6885(1991).
- [36] W.K. Burton, N. Cabrera, and F.C. Frank, 'The growth of crystals and the equilibrium structure of their surfaces,' Phil. Trans. Roy. Soc. (Lond.) **A243**, 299(1951).
- [37] R. Ghez and S.S. Iyer, 'The kinetics of fast steps on crystal surfaces and its application to the molecular beam epitaxy of silicon,' IBM J. Res. Develop. **32**, 804(1988).
- [38] R.L. Schwoebel, 'Step motion on crystal surfaces. II,' J. Appl. Phys. **40**, 614(1969).
- [39] M.G. Lagally, in *Kinetics of Ordering and Growth at Surfaces*, ed. M.G. Lagally, Plenum, New York, 1990.
- [40] J.Y. Tsao, E. Chason, U. Koehler, and R. Hamers, 'Dimer strings, anisotropic growth, and persistent layer-by-layer epitaxy,' Phys. Rev. **B40**, 11951(1989).
- [41] R.M. Tromp, E.D. Williams, and J. Tersoff, presented at the 12th International Summer Institute of Surface Science, Milwaukee, 1994.
- [42] J. Villian, 'Continuum models of crystal growth from atomic beams with and without desorption,' J. Phys. I **1**, 19(1991).
- [43] W.W. Mullins, 'Flattening of a nearly plane solid surface due to capillarity,' J. Appl. Phys. **30**, 77 (1959).

- [44] M. Kardar, G. Parisi, and Y.-C. Zhang, 'Dynamic scaling of growing interfaces,' *Phys. Rev. Lett.* **56**, 889(1986).
- [45] K. Moser, J. Kertész, and D.E. Wolf, 'Numerical solution of the Kardar-Parisi-Zhang equation in one, two and three dimensions,' *Physica A* **178**, 215(1991).
- [46] Z.-W. Lai and S. Das Sarma, 'Kinetic growth with surface relaxation: continuum versus atomistic models,' *Phys. Rev. Lett.* **66**, 2348(1991).
- [47] D.E. Wolf and J. Villain, 'Growth with surface diffusion,' *Europhys. Lett.* **13**, 389(1990).
- [48] C.G. Van de Walle, P.J.H. Denteneer, Y. Bar-Yam, and S.T. Pantelides, 'Theory of hydrogen diffusion and reactions in crystalline silicon,' *Phys. Rev. B* **39**, 1079(1989).
- [49] T. Takahagi, I. Nagai, A. Ishitani, H. Kuroda, and Y. Nagasawa, 'The formation of hydrogen passivated silicon single-crystal surfaces using ultraviolet cleaning and HF etching,' *J. Appl. Phys.* **64**, 3516(1988).
- [50] G.S. Higashi, Y.J. Chabal, G.W. Trucks, and K. Raghavachari, 'Ideal hydrogen termination of the Si(111) surface,' *Appl. Phys. Lett.* **56**, 656(1990).
- [51] Y.J. Chabal, G.S. Higashi, K. Raghavachari, and V.A. Burrows, 'Infrared spectroscopy of Si(111) and Si(100) surfaces after HF treatment: hydrogen termination and surface morphology,' *J. Vac. Sci. Technol. A* **7**, 2104(1989).

- [52] J.J. Boland, 'Scanning tunneling microscopy of the interaction of hydrogen with silicon surfaces,' *Adv. Phys.* **42**, 129(1993).
- [53] G. Schulze and M. Henzler, 'Adsorption of atomic hydrogen on clean cleaved silicon (111),' *Surf. Sci.* **124**, 336(1983).
- [54] K. Sinniah, M.G. Sherman, L.B. Lewis, W.H. Weinberg, and J.T. Yates, 'Hydrogen desorption from the monohydride phase on Si(100),' *J. Chem. Phys.* **92**, 5700(1990).
- [55] S.M. Gates and S.K. Kulkarni, 'Hydrogen coverage during Si growth from SiH_4 and Si_2H_6 ,' *Appl. Phys. Lett.* **60**, 53(1992).
- [56] S.H. Wolff, S. Wagner, J.C. Bean, R. Hull, and J.M. Gibson, 'Hydrogen surface coverage – raising the silicon epitaxial growth temperature,' *Appl. Phys. Lett.* **55**, 2017(1989).
- [57] D.P. Adams, S.M. Yalisove, and D.J. Eaglesham, 'Effect of hydrogen on surface roughening during Si homoepitaxial growth,' *Appl. Phys. Lett.* **63**, 3571(1993).
- [58] T. Vasek and M.G. Lagally, presented at the American Vacuum Society Meeting, Orlando, 1993.
- [59] D.J. Eaglesham, G.S. Higashi, and M. Cerullo, '370°C clean for Si molecular beam epitaxy using a HF dip,' *Appl. Phys. Lett.* **59**, 685(1991).
- [60] T. Ohmi, T. Ichikawa, H. Iwabuchi, and T. Shibata, 'Formation of device-grade epitaxial silicon films at extremely low temperatures by low energy bias sputtering,' *J. Appl. Phys.* **66**, 4756(1989).

- [61] C.-C. Chen, D.L. Smith, G.B. Anderson, and S.B. Hagstrom, 'Low temperature epitaxy on H-passivated Si(100) by sputter deposition,' *Mat. Res. Soc. Symp. Proc.* **259**, 443(1992).
- [62] F.A. Smidt, 'Use of ion beam-assisted deposition to modify the microstructure and properties of thin films,' *Int. Met. Rev.* **35**, 61(1990).
- [63] W.-X. Ni, J. Knall, M.A. Hasan, G.V. Hansson, J.-E. Sundgren, S.A. Barnett, L.C. Markert, and J.E. Greene, 'Kinetics of dopant incorporation using a low-energy antimony ion beam during growth of Si(100) films by molecular beam epitaxy,' *Phys. Rev. B* **40**, 10449(1989).
- [64] P. Bedrossian, J.E. Houston, J.Y. Tsao, E. Chason, and S.T. Picraux, 'Layer-by-layer sputtering and epitaxy of Si(100),' *Phys. Rev. Lett.* **67**, 124(1991).
- [65] C.J. Tsai and H.A. Atwater, 'Suppression of island formation during initial stages of Ge/Si(100) growth by ion-assisted molecular beam epitaxy,' *Mat. Res. Soc. Symp. Proc.* **268**, 127(1992); *J. Vac. Sci. Technol.*, to be published.
- [66] C.H. Choi, R. Ai, and S.A. Barnett, 'Suppression of 3-dimensional island nucleation during GaAs growth on Si(100),' *Phys. Rev. Lett.* **67**, 2826(1991).
- [67] H.A. Atwater, 'Low energy ion-surface interactions during epitaxial growth,' *Sol. St. Phen.* **27**, 67(1992).
- [68] P.C. Zalm and L.J. Beckers, 'Ion-beam epitaxy of silicon on Ge and Si at temperatures of 400 K,' *Appl. Phys. Lett.* **41**, 167(1982).

- [69] R.A. Zuhr, B.R. Appleton, N. Herbots, B.C. Larson, T.S. Noggle, and S.J. Pennycook, 'Low temperature epitaxy of Si and Ge by direct ion beam deposition,' J. Vac. Sci. Technol. A5, 2135(1987).
- [70] K.G. Orrman-Rossiter, A.H. Al Bayati, D.G. Armour, S.E. Donnelly, and J.A. Van den Berg, 'Ion beam deposited epitaxial thin silicon films,' Nucl. Instr. Meth. B59, 197(1991).
- [71] G.K. Wehner, R.M. Warner, Jr., P.D. Wang, and Y.H. Kim, 'Substituting low energy (< 30 eV) ion bombardment for elevated temperature in silicon epitaxy,' J. Appl. Phys. 64, 6754(1988).
- [72] C.J. Tsai, P. Rozenak, H.A. Atwater, and T. Vreeland, 'Strain modification by ion-assisted molecular beam epitaxy in the $\text{Si}_x\text{Ge}_{1-x}$ alloy system - a kinetic analysis,' J. Cryst. Gr. 111, 931(1991).
- [73] E. Chason, P. Bedrossian, K.M. Horn, J.Y. Tsao, and S.T. Picraux, 'Ion beam enhanced epitaxial growth of Ge(001),' Appl. Phys. Lett. 57, 1793(1990).

Chapter 2

LOW TEMPERATURE SILICON MOLECULAR BEAM EPITAXY

When you follow two separate chains of thought, Watson, you will find some point of intersection that should approximate to the truth.

– *Sherlock Holmes*, The Disappearance of Lady Frances Carfax

Sir Arthur Conan Doyle

2.1 The Molecular Beam Epitaxy System

The silicon films were deposited in a custom-built molecular beam epitaxy (MBE) system. Figure 2.1 shows a view of the ultra-high vacuum (UHV) chamber. A schematic is shown in Fig. 2.2. The chamber is pumped with a 330 l/s turbomolecular pump and a 1600 l/s cryogenic pump. The base pressure in the chamber was around 10^{-7} Pa. Pressure was measured using a nude-ion guage. The ion gauge is normally calibrated for nitrogen. The gas

correction factors were taken as 0.71 for argon and 6.04 for helium [1]. A mass spectrometer was used for monitoring the residual gas and leak checking. The residual gas was mostly composed of H_2 , CO and H_2O . The silicon wafers were introduced into the chamber through a load lock, thus preventing the need to bring the chamber up to air each time. The chamber is equipped with several valves and shutters to isolate the appropriate parts of the system.

The silicon wafers were held by tantalum clips onto a molybdenum block. Molybdenum has a negligible vapor pressure and does not react with silicon at the temperatures of interest ($T < 700^\circ\text{C}$). The substrate manipulator allows angular and azimuthal rotation as well as translation in two orthogonal directions. The substrate temperature was monitored by a thermocouple attached to the side of the substrate heater block. An optical pyrometer, which gives more reliable measurements above 300°C , was occasionally used. The thermocouple was calibrated using the pyrometer measurements and temperatures below 300°C were obtained by an extrapolation of the pyrometer readings.

The UHV chamber is equipped with two electron guns. They have copper crucibles with 7 cc pockets to hold the source material. One of these was used to deposit silicon. The silicon used as source material was obtained from a high purity silicon ingot. The dopant density in the source was less than 10^{15} cm^{-3} . Silicon was placed in the 7 cc pocket and also in the region surrounding the pocket to prevent contamination from the copper crucible [2]. The distance from the source to substrate was about 60 cm. The source was outgassed extensively before depositing the films. The pressure during growth was typically 10^{-6} Pa and mainly composed of H_2 . A quartz crystal

sensor was used to record the growth rate. The sensor was calibrated by cross section transmission electron microscopy (XTEM). The copper crucible in the electron gun and the quartz crystal sensor were water-cooled during operation.

For low energy ion beams, two ion sources were employed. A Kaufman source was used for generating Ar^+ ions. The chamber was backfilled with argon to a pressure of 3×10^{-3} Pa during operation. An electron cyclotron resonance (ECR) source was used to generate He^+ ions. The starting purity of both Ar and He gas was better than 99.999%. The gas was passed through a purifier just before introduction into the ion source. The gas purifier was rated to give a purity of 10 ppb. The distance from either ion source to the substrate was about 20 cm. The ion guns were oriented so that the ions were incident at a 45° angle with respect to the surface normal when the sample was horizontal.

The sample surface morphology was monitored *in situ* by reflection high energy electron diffraction (RHEED) using a 12 keV beam. The RHEED beam was incident typically at a grazing angle of $0 - 2^\circ$. A 50 l/s turbo-molecular pump was used to differentially pump the RHEED gun so that it could be used while working at relatively high pressures such as during ion irradiation of the substrates.

The silicon wafers used in the experiments were of the (001) orientation with a miscut of less than 1° . They were either n- or p-type with a resistivity of 10 - 50 Ω -cm.

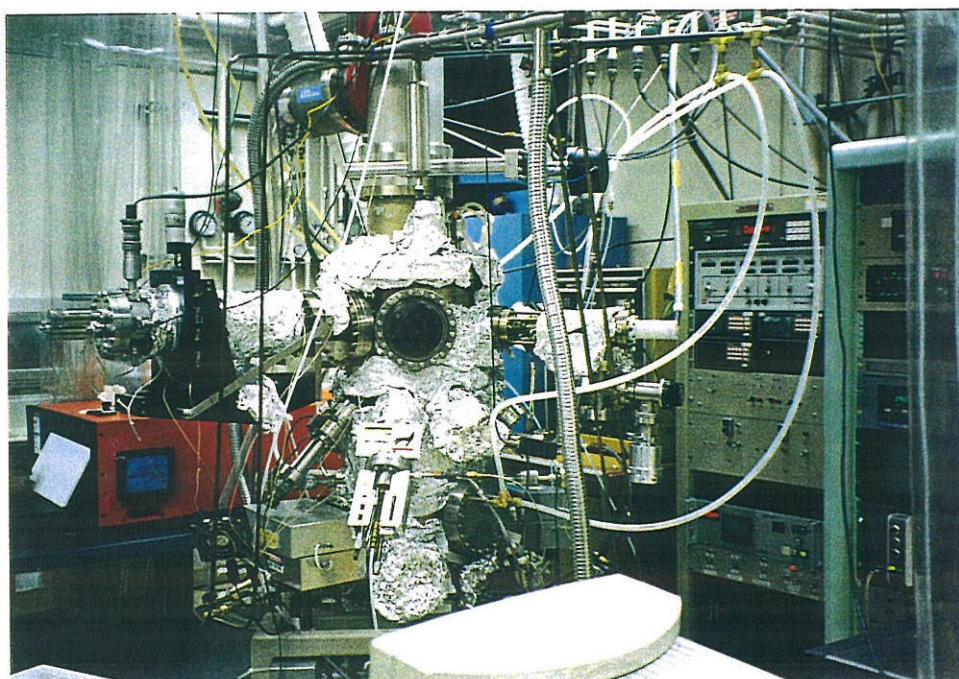


Figure 2.1: The molecular beam epitaxy system.

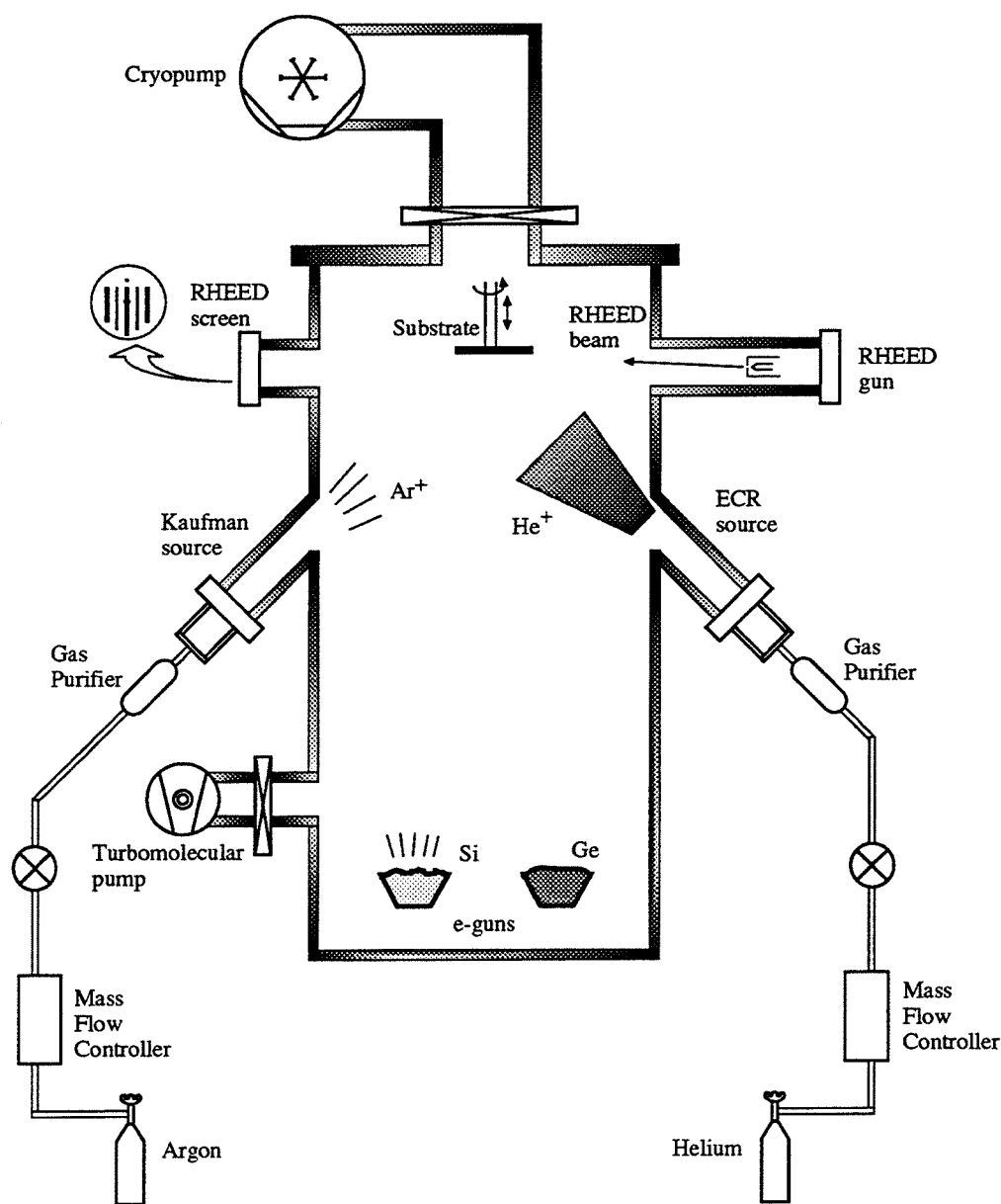


Figure 2.2: A schematic of the molecular beam epitaxy system. The drawing is not to scale.

2.2 Sample Preparation

Silicon forms a thin (1 – 2 nm) native oxide when exposed to atmosphere. The surface may also contain metal and organic contaminants. The wafers were cleaned in chemical solutions before transferring to the UHV chamber.

The procedure used for chemical cleaning of Si wafers is taken from Ref. [3]. The wafer cleaning procedure is also listed in Appendix A for convenience. All ratios mentioned below are by volume and the chemicals are of the appropriate concentrations available commercially (except HF for which the actual concentration is given) [4]. The native oxide is first removed by a dilute HF ($\sim 1:20$ HF : H₂O) dip. The wafer is then placed for 5 minutes in a hot alkaline peroxide solution composed of NH₄OH : H₂O₂ : H₂O in a 1:1:5 ratio. The resulting oxide is then etched by a dilute HF dip and the process repeated three times. This step removes organic contaminants and some metals from the surface [5]. The wafer is then placed for 5 minutes in a hot acidic peroxide solution composed of HCl : H₂O₂ : H₂O in a 1:1:5 ratio. The resulting oxide is again etched by a dilute HF dip and the process repeated three times. This step removes metal contaminants from the surface [5]. In the final step, the Si wafer is dipped in dilute HF for 50 to 60s [6]. This results in a nominally dihydride-terminated Si(001) surface. There are significant fractions of monohydride and trihydride species on such surfaces indicating that it is microscopically rough [7]. The wafer is transferred to the load lock within three minutes after the last step. On the dihydride-terminated Si(001) surface, hydrogen atoms saturate the dangling bonds of Si atoms. This passivates the Si surface from oxidation and chemisorption

of impurities. In fact, such surfaces have been shown to resist oxidation for as long as 12 hours in the laboratory atmosphere [8].

The silicon wafer so cleaned may still contain physisorbed contaminants. Prior to epitaxy, the samples were baked at 200 – 250°C for one or more hours. It has been shown that this low temperature bake removes any physisorbed hydrocarbons on the surface [9]. The samples are then heated above 500°C to desorb the hydrogen and obtain a clean, reconstructed Si(001)-2×1 surface.

2.3 Silicon Molecular Beam Epitaxy – A Reflection High-Energy Electron Diffraction Study

Reflection high-energy electron diffraction (RHEED) is an *in situ* technique for obtaining information about the sample surface morphology. In our experiments, a 12 keV electron beam was incident at a grazing angle of 0 – 2° on the sample. The corresponding wavelength of 0.011 nm is seen to be smaller than the typical bond length of 0.2 nm. This allows one to obtain structural information about the surface through elastic scattering. The mean free path of electrons is about 5 nm at 10 keV [10]. Since the electrons are incident at $\sim 1^\circ$, most of the electrons are scattered within a 1 nm region near the surface. This makes RHEED a strong surface sensitive probe. The incident electrons typically undergo multiple scattering which makes the interpretation of intensities difficult. Kikuchi lines and other non-kinematic features in the RHEED pattern can be easily located [11]. However, the elastic scatter-

ing features can be readily identified and are used here to obtain qualitative information about the surface morphology.

If the assumption of scattering only from the uppermost surface layer is made, the reciprocal lattice consists of rods. Since the electron wavelength $\lambda \ll a$, the unit cell lattice parameter, the Ewald sphere diameter is large compared to the rod spacing. If the rods were infinitesimally narrow and the instrumental broadening small, a spotty pattern would be obtained from an atomically smooth surface. However, in most practical situations nonidealities such as steps and islands result in broadening and streakiness of the rods. This gives rise to the streaks seen in RHEED patterns, particularly at very glancing incident angles.

The surface unit cell of the unreconstructed Si(001) is a square lattice with a lattice constant of 0.384 nm as shown in Fig. 2.3(a) [12]. The corresponding reciprocal lattice is shown in Fig. 2.4(a). Each Si atom on the surface has two dangling bonds. In vacuum, a clean Si(001) surface reconstructs to form the structure shown in Fig. 2.3(b). Two Si atoms on the surface move closer together to form a bond. There is also some inward relaxation of the surface layer atoms. Now the unit cell is rectangular and the reciprocal lattice shows extra half-order rods. On a vicinal surface, i.e., a wafer with a slight misorientation, the (2×1) reconstruction rotates by 90° at a monatomic step. Thus both (1×2) and (2×1) domains are present on the surface giving rise to half-order rods in both orthogonal $\langle 110 \rangle$ directions.

The RHEED pattern of a reconstructed Si(001)- 2×1 surface along the $\langle 110 \rangle$ azimuth is shown in Fig. 2.5(a). The $(0, \pm \frac{1}{2})$ and $(0, \pm \frac{3}{2})$ lines can be seen clearly. The RHEED pattern of the same surface at different incidence

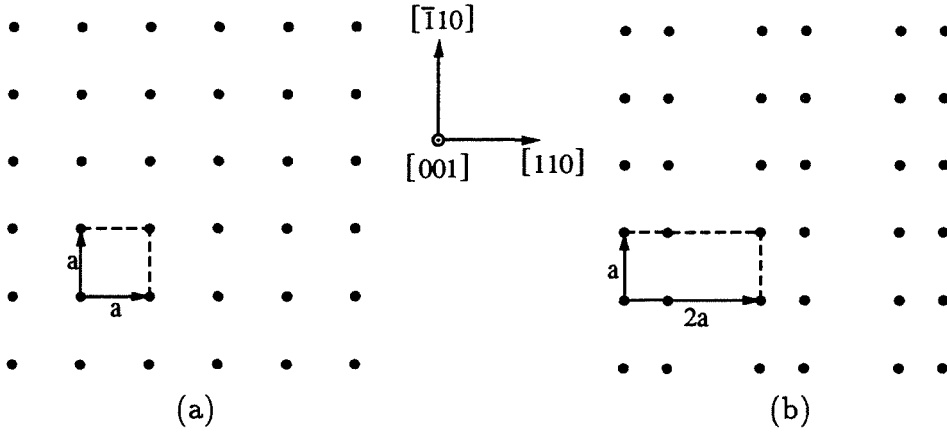


Figure 2.3: The surface net of the (a) unreconstructed Si(001), and (b) (2×1) reconstructed Si(001). The (2×1) reconstruction is shown in the x -direction.

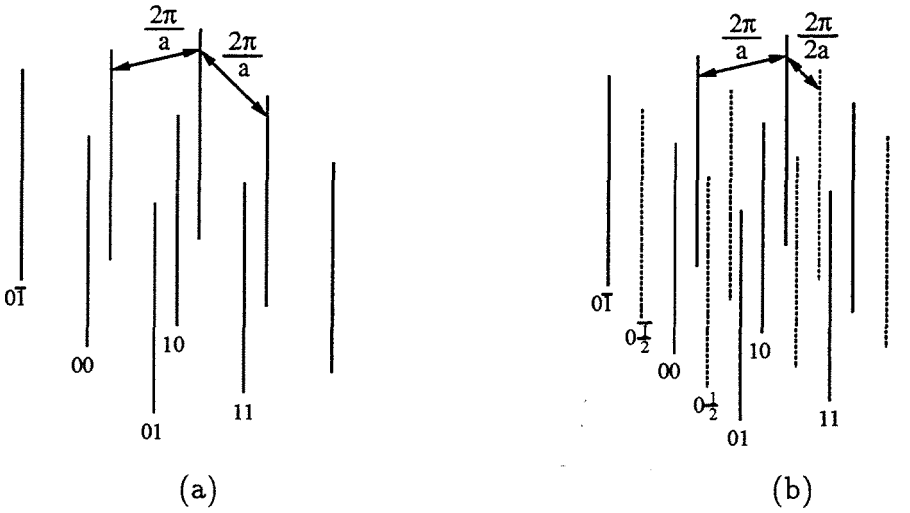


Figure 2.4: The reciprocal lattice corresponding to the (a) unreconstructed Si(001), and (b) (2×1) reconstructed Si(001) in the previous figure.

angles is shown in Fig. 2.5(b)–(c). We see that the streaks decrease with increasing angle of incidence. The RHEED pattern was monitored along the $\langle 110 \rangle$ azimuth during the experiments because it gives information about the reconstruction of the surface.

After the chemical cleaning of the silicon wafer as described in the preceding section, we obtain a nominally dihydride-terminated $\text{Si}(001)\text{-}1\times 1$ surface. The RHEED pattern from such a surface is shown in Fig. 2.6(a). The hydrogen coverage is nominally 2 monolayers (ML). The surface changes to a (2×1) monohydride structure (hydrogen coverage 1 ML) following partial hydrogen desorption at $350 - 400^\circ\text{C}$. Complete hydrogen desorption occurs above 500°C and Fig. 2.6(b) shows the diffraction pattern from a clean, reconstructed $\text{Si}(001)\text{-(}2\times 1\text{)}$ surface after heating to 550°C . A buffer layer was deposited at this temperature. The silicon growth rate was set to 0.09 nm/s . In Fig. 2.6(c), the RHEED pattern after 0.5 nm growth of Si is shown. A spotty pattern indicative of three-dimensional island growth is observed. This is due to small amounts ($\sim 1 - 5\%$ of a ML) of carbon and oxygen impurities at the starting surface and is further discussed in Section 2.7.2. From a thermodynamic view [13], one would expect a homoepitaxial film to completely wet the substrate because the surface energy of both film and substrate is the same (and interface energy is zero). The islanding is illustrative of the important role that adsorbates play in silicon homoepitaxy. The C and O impurities are buried upon further growth and the surface begins to become smooth. This can be seen in Fig. 2.6(d) which shows the RHEED pattern after 30 nm deposition. A smooth (2×1) pattern with Kikuchi lines can be seen in Fig. 2.6(e) after the growth of a 110 nm buffer layer. At this point,

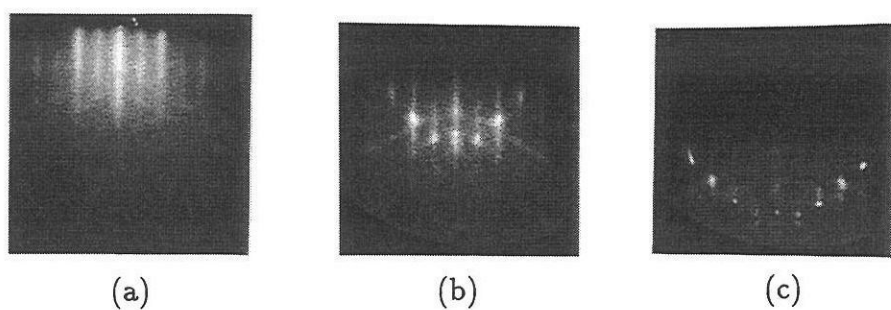


Figure 2.5: The RHEED pattern of a Si(001)-2 \times 1 surface along the $\langle 110 \rangle$ azimuth with the electron beam incident at (a) 0.6°, (b) 1.5°, and (c) 2.1° grazing angle.

growth was interrupted and the substrate temperature dropped to 300°C for low temperature growth. The cooldown time was about 15 minutes. The RHEED pattern after 60 nm growth at 300°C is shown in Fig. 2.6(f). There are no reconstruction lines and the spotty pattern indicates a rough three-dimensional surface morphology. In addition, extra spots are seen in the diffraction pattern. This is due to twinning and a complete picture of all the observed spots is shown in Fig. 2.6(g). During low temperature growth the twin spots appear suddenly during the course of deposition. Further growth results in a complete transformation to amorphous silicon deposition. The ring pattern characteristic of amorphous materials is shown in Fig. 2.6(h). This was after 200 nm film deposition.

In situ observation of the RHEED pattern shows that growth at low temperatures starts epitaxially. As the film thickness increases, the RHEED pattern becomes increasingly spotty which is indicative of three-dimensional islanding. Nucleation of twin boundaries occurs suddenly after a certain thickness as judged from the appearance of extra spots. The intensity of the twin spots increases and a ring pattern characteristic of amorphous silicon is soon visible. Further growth results in a complete transformation to amorphous silicon. At very low temperatures ($T < 150^{\circ}\text{C}$), the transformation to amorphous silicon is direct and twin spots are not observed. This phenomenon has been studied using a wide variety of techniques to understand more about the nature of the film and the growing surface, and is the topic of the next several sections.

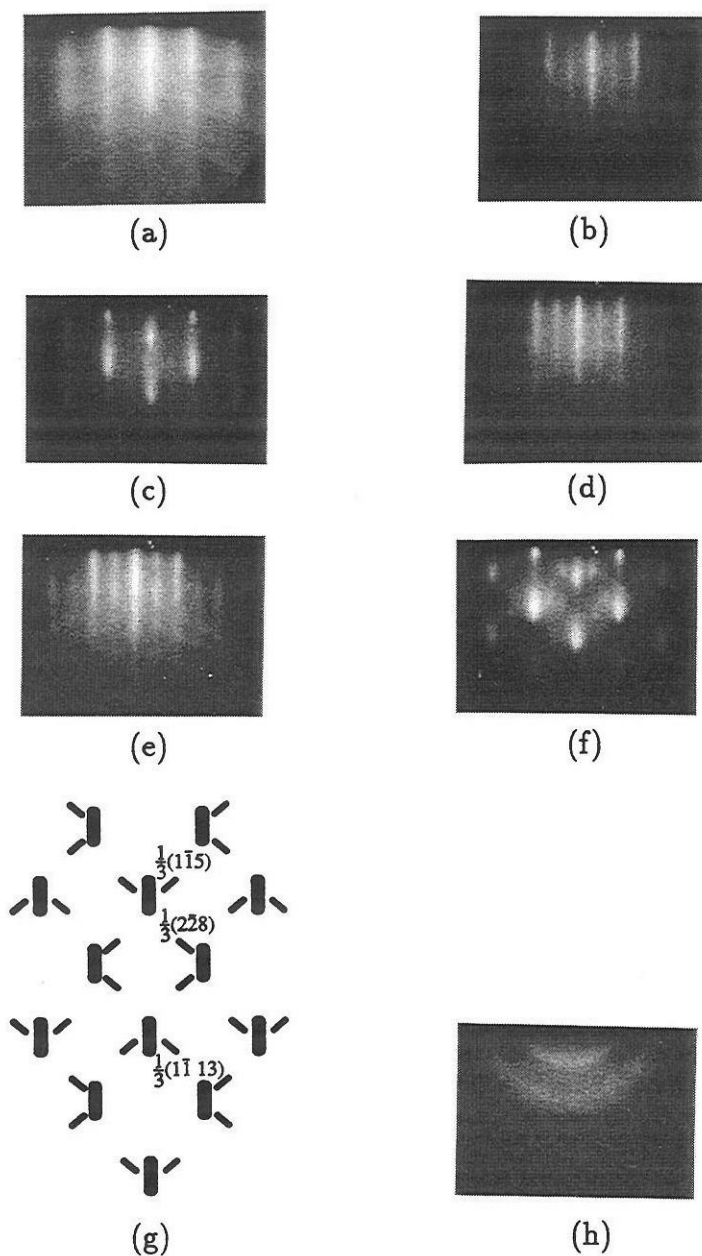


Figure 2.6: A sequence of RHEED patterns illustrating substrate preparation and Si MBE at high and low temperatures. RHEED pattern after (a) chemical cleaning; and (b) complete hydrogen desorption at 550°C. *High temperature buffer layer*. RHEED patterns after (c) 0.5 nm; (d) 30 nm; and (e) 110 nm deposition at 550°C. *Low temperature growth*. RHEED patterns after (f) 60 nm deposition; (g) identification of diffraction spots (only twin spots) in (f); and (h) 200 nm deposition at 300°C.

2.4 Conventional Molecular Beam Epitaxy – A Transmission Electron Microscopy Study

Transmission electron microscopy (TEM) was performed using a Phillips EM430 microscope operated at 300 kV. The point-to-point resolution of 0.23 nm is sufficient to obtain lattice-resolved images of silicon. The threshold energy of electrons for production of point defects in silicon is about 200 keV. The incident electron energy of 300 keV was slightly higher, and imaging was performed before causing any noticeable damage to the specimen.

Cross section specimens were prepared by polishing the wafers on a silicon-carbide paper to $\sim 100\ \mu\text{m}$ thickness followed by dimpling to create a perforation. Ion milling was subsequently performed to thin the specimens down to electron transparency. The maximum temperature during the entire process did not exceed 200°C . This is well below the solid phase epitaxy temperature and any annealing of defects in the film may be considered negligible.

Before describing the observations, it is appropriate to define the concept of epitaxial thickness, h_{epi} . This is defined as the thickness up to which the film is defect free. While the region of view is limited in a cross section transmission electron microscopy (XTEM) specimen (typically $1\ \mu\text{m}$ long), the large number of nucleation sites of the defects makes this a reasonable definition. This definition also provides an answer to the crystal grower's question, "How thick a film can one grow ensuring that it is defect free?" Other definitions have been used in the literature such as the thickness at

which half of the deposited material is amorphous [14].

Figure 2.7 shows an XTEM image of a 220 nm film deposited by conventional MBE at 370°C. It is a bright field image taken under multibeam conditions in the $\langle 110 \rangle$ projection. The film growth rate was 0.09 nm/s. The film/buffer layer interface is visible in some regions due to the contrast from small amount of impurities accumulated during the growth interrupt. These impurities are described in more detail in Section 2.7.2. The film appears defect free up to a thickness, h_{epi} , of about 83 nm. The film above that is highly disordered. The presence of twins can be inferred from the moiré fringes with a spacing of three $\{111\}$ planes. The high density of twins gives rise to the extra spots in the RHEED pattern described in the previous section.

A high resolution image of a twinned region is shown in Fig. 2.8(a). Although not from the above film, this is a typical defect in the disordered region. The moiré fringes can be seen with a periodicity of three $\{111\}$ planes. In addition to twins, isolated planar defects are also visible in the disordered region. These have been identified as stacking faults and “hydrogen platelets.” A through-focus series of images showed that some defects did not show the contrast typical of a stacking fault or a dislocation. We believe these are “hydrogen platelet” defects (see Fig. 2.8(b)). Such defects have been observed after hydrogen plasma-etching of silicon [15, 16, 17]. One model for the hydrogen-platelets involves breaking Si–Si bonds between neighboring $\{111\}$ planes and terminating the Si atoms with H atoms [18].

A high resolution transmission electron microscope (HRTEM) image of a 110 nm film deposited by conventional MBE at 240°C and 0.09 nm/s is

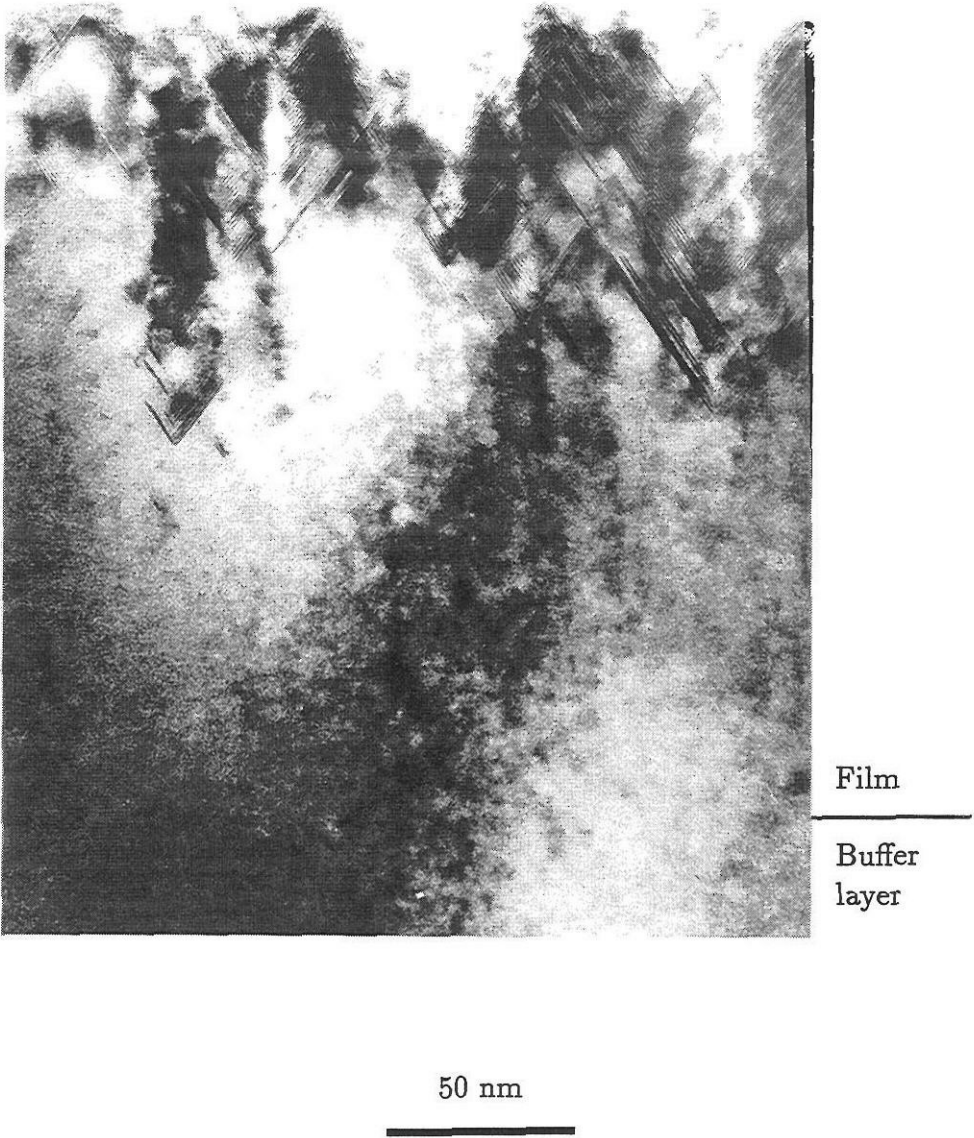
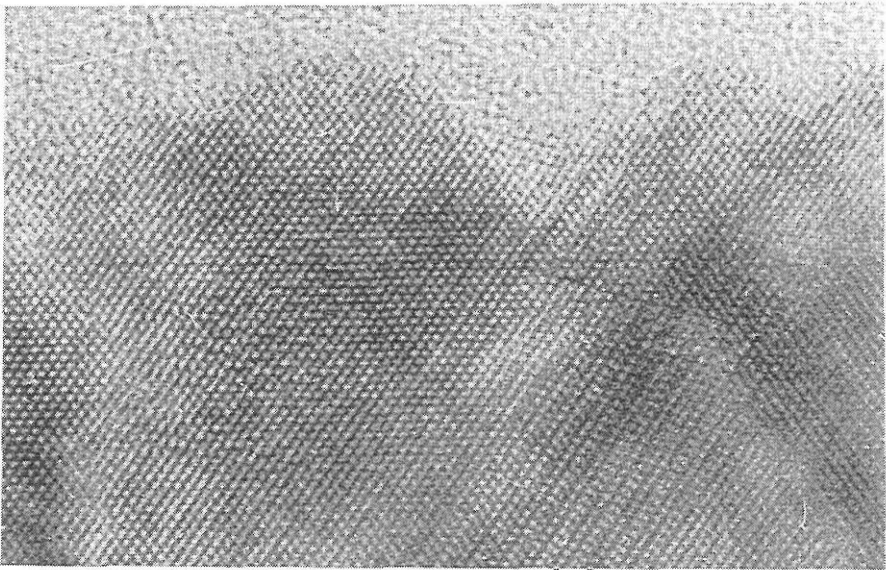
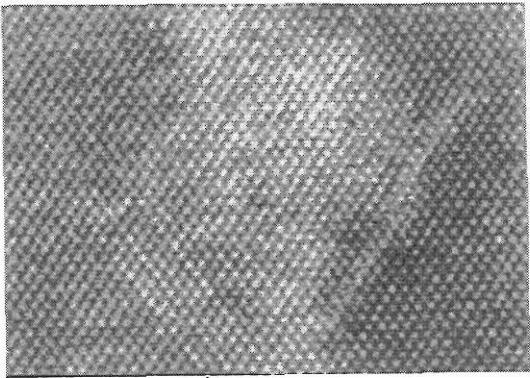


Figure 2.7: Bright field image of a 220 nm film deposited by conventional MBE at 370°C. The image was taken under multibeam conditions in the $\langle 110 \rangle$ projection. The epitaxial thickness, h_{epi} , is estimated to be 83 nm.



0.94 nm

(a)



(b)

Figure 2.8: (a) High resolution image of a twinned region. (b) A planar defect believed to be a “hydrogen-platelet.”

shown in Fig. 2.9. The epitaxial thickness is about 25 nm. The crystalline-to-amorphous transition is seen to be quicker compared to Fig. 2.7.

2.5 The Breakdown of Epitaxy at Low Temperatures

The transition from single crystal silicon to amorphous silicon deposition is a characteristic of low temperature silicon molecular beam epitaxy. This transition is abrupt and occurs on a local scale. As seen in the preceding section, there is a disordered region with a high density of twin planes between the regions of single crystal and complete amorphous silicon deposition. As the temperature is reduced, this disordered region gets smaller and the transition is quicker.

A possible pathway to the nucleation of amorphous silicon is as follows. Amorphous silicon has short range order but no long range order. The continuous random network models of amorphous silicon show that besides six-member rings, it also consists of five- and seven-member rings [19]. Due to lower diffusivity of Si atoms at low temperatures, growth on Si(001) surfaces leads to 3D islanding and the formation of {111} facets. This is shown schematically in Fig. 2.10(a). Now, $\Sigma 3$ coherent twin boundaries can form on such planes as they cost relatively little energy. At a twin boundary, the six-member ring structure of silicon is preserved. It is only the third (and higher) nearest neighbor atoms that are now at a different position. Figure 2.10(b) shows a (111) twin boundary in a wireframe model. While investi-

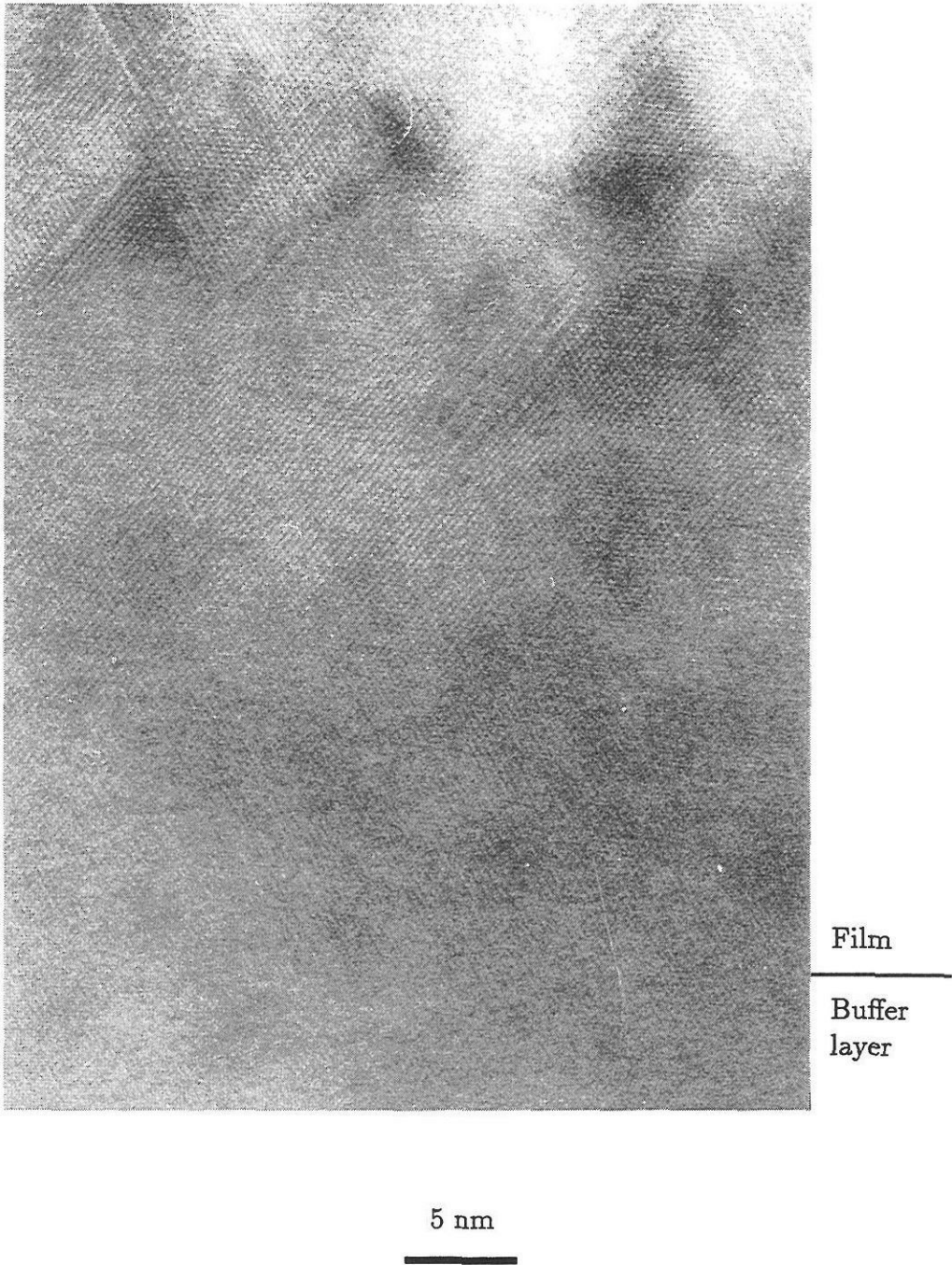


Figure 2.9: High resolution image of a 110 nm film deposited by conventional MBE at 240°C. The image was taken in the $\langle 110 \rangle$ projection. The epitaxial thickness, h_{epi} , is estimated to be 25 nm.

gating Si(111) homoepitaxy by chemical vapor deposition, it was suggested in Ref. [20] that twin boundaries can nucleate by adatoms clustering in the wrong sites. One only needs to take this postulate to its logical conclusion. When a twinned region grows and meets a different $\{111\}$ or $\{001\}$ plane of the perfect crystal, it inevitably leads to the formation of five- and seven-member rings. This is shown in Fig. 2.10(b). At very low temperatures ($T \lesssim 150^\circ\text{C}$) this rapidly leads to a transformation to amorphous silicon deposition. At more moderate temperatures ($150 \lesssim T \lesssim 450^\circ\text{C}$), a crystalline film continues to grow after the formation of a grain boundary because a crystalline network (plus a grain boundary) still has lower energy than an amorphous network. Eventually the density of defects grows very high, leading to a transition to amorphous silicon deposition. We will refer to this mechanism as the twin-boundary/facet (TBF) mechanism. The breakdown of epitaxy at the edge of a stacking fault or twin boundary has been reported several times in the past [21, 22].

It was widely believed that semiconductor growth resulted in crystalline films above a certain “epitaxial temperature” and amorphous films below that temperature [23]. This epitaxial temperature was estimated by different authors to be between 0 and 200°C [24]. Recently, it was shown that the concept of an epitaxial temperature does not describe semiconductor epitaxy well. Instead, it was proposed that the epitaxial thickness was a more fundamental parameter [6]. It was shown that growth on Si(001) always proceeds epitaxially up to a certain thickness followed by a crystal-state — amorphous-state transition [6]. This raised the important question of the relative role of surface roughness and adsorbates such as carbon, hydrogen and oxygen in

this transition. It has also been observed that energetic beam techniques such as ion beam-assisted molecular beam epitaxy, direct ion beam deposition and sputter deposition produce thicker epitaxial films at very low temperatures. These important issues in low temperature Si MBE are addressed in the rest of this chapter.

2.6 Ion Beam-Assisted Molecular Beam Epitaxy

Low energy ion beams have been used to modify semiconductor film growth for several different applications. Heavily doped silicon films have been deposited at low temperatures with the use of energetic beams of dopants [25]. The surface segregation problem is overcome by incorporating the dopant atom in a sub-surface site. Ion beam-assisted molecular beam epitaxy has been used to modify the strain in $\text{Si}_{1-x}\text{Ge}_x$ films deposited on Si(001) [26]. This was achieved without introducing dislocations. Ion irradiation has also been used to suppress 3-D island nucleation during the early stages of epitaxy of Ge [27] and GaAs [28] on Si(001). Energetic silicon ions have been used to deposit silicon films [29, 30]. In this case, the deposited atoms themselves carry the energy and the process is referred to as direct ion beam deposition. Films with improved crystallinity have been obtained by this process compared to conventional MBE. A chief problem has been the rather low deposition rates (~ 0.01 nm/s) due to the difficulties in generating mass separated low energy beams. Sputter deposition has also been reported to

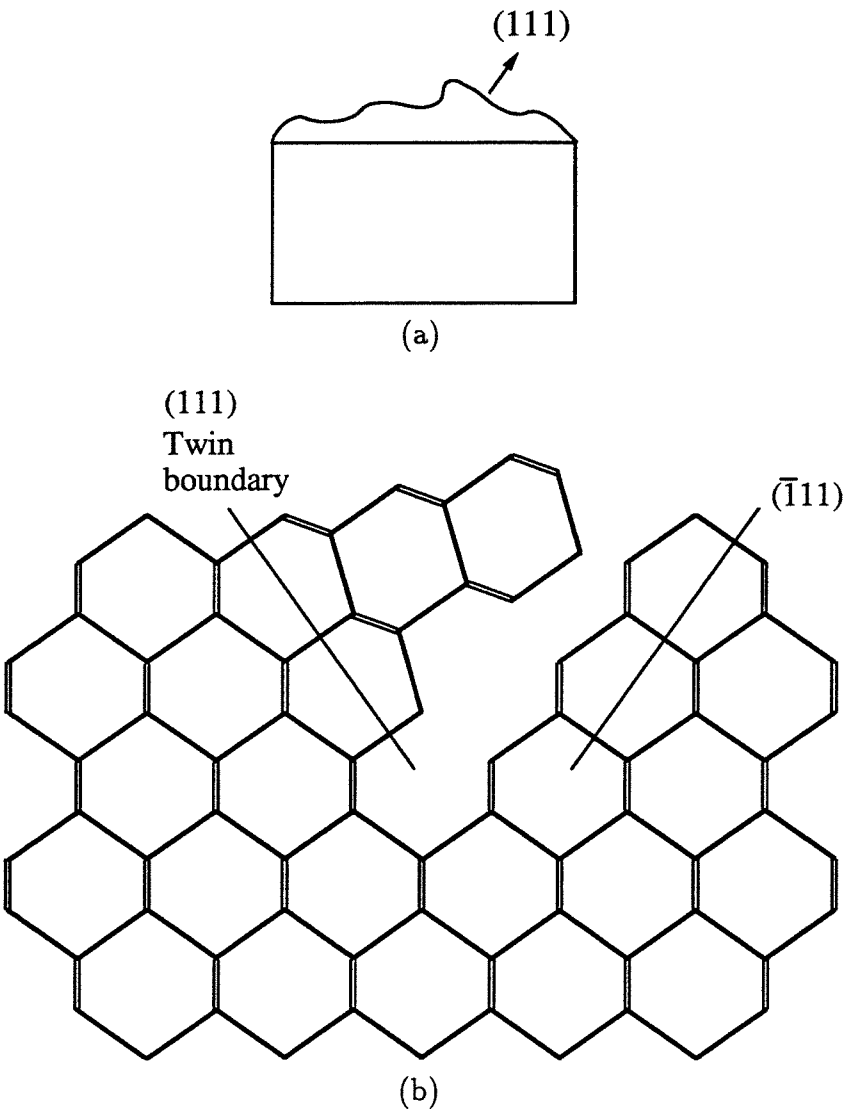


Figure 2.10: A possible pathway to the breakdown of epitaxy. (a) Low temperature growth results in three-dimensional islanding with some $\{111\}$ oriented facets. (b) A wireframe model illustrating the pathway to amorphous silicon. It is postulated that a $\Sigma 3$ coherent twin boundary is formed on a (111) plane. When this twinned region grows and meets a different plane, say $(\bar{1}11)$, the atoms do not line up. This necessarily leads to the formation of five- and seven-member rings and acts as a nucleation site for amorphous silicon.

produce good quality epitaxial films [31, 32, 33]. The sputtered particles carry a few eV of energy which produces a dramatic improvement in the film morphology. Closer to our work is the use of Xe^+ ions to modify the surface morphology in Ge(001) homoepitaxy [34, 35]. It was observed that growth alone or ion bombardment alone led to an increase in surface roughness. However, concurrent ion irradiation during growth resulted in a smooth surface. It was suggested that this smoothing was a consequence of the annihilation of ion-induced vacancy-like defects and growth-induced adatoms and small islands.

To understand the influence of ion irradiation, it is necessary to systematically investigate the role of ion energy in the modification of surface kinetics. We have used noble gas ions (Ar^+ and He^+) because only the physical effects are important. Concurrent ion irradiation during film growth was employed to study its effect on surface morphology and film microstructure.

The Ar^+ ions were generated by a Kaufman source. The ions were incident at 45° to the substrate normal along the $\langle 100 \rangle$ azimuth. Two different ion energies, 50 and 70 eV, were employed.

A HRTEM image of a 200 nm film deposited by ion beam-assisted molecular beam epitaxy (IAMBE) at 370°C is shown in Fig. 2.11(a). The Ar^+ ion energy was 50 eV and the ion-to-atom flux ratio was about 0.06. The film growth rate was 0.09 nm/s. When compared to the conventional MBE film under similar conditions (see Fig. 2.7), we see that the epitaxial thickness, h_{epi} , of 130 nm for the IAMBE film is higher. The defects are, again, mostly twin boundaries and stacking faults. An enlarged view of the surface is shown in Fig. 2.11(b). A $\{311\}$ facet is marked on the surface. Both $\{311\}$

and $\{111\}$ facets were observed at the growing front.

The epitaxial thickness for conventional MBE estimated by two methods, XTEM and RHEED observations, is shown as a function of inverse temperature in Fig. 2.12. The $h_{\text{epi}}^{\text{RHEED}}$ for RHEED observations is the thickness at which twin spots became visible. We see that the $h_{\text{epi}}^{\text{RHEED}}$ values are a little higher than the XTEM values. At the breakdown of epitaxy, the surface is faceted and contains amorphous and crystalline regions. As the RHEED pattern only gives areal-averaged information on $\sim 1 \text{ mm}^2$ of the surface, it is difficult to pinpoint the time of transition from RHEED observations alone. However, it does allow a quick determination of the epitaxial thickness.

The variation in h_{epi} with temperature for IAMBE films is compared with conventional MBE in Fig. 2.13. Two different Ar^+ ion energies of 50 and 70 eV with ion-to-atom flux ratios of about 0.06 and 0.09, respectively, were employed. The film growth rate was about 0.09 nm/s for all films. We see that above a certain temperature, there is an increase in the epitaxial thickness. However, below 300°C , concurrent ion irradiation resulted in a decrease in the epitaxial thickness. This suggests that annealing of ion damage is incomplete at these temperatures.

Qualitatively, similar results were observed with IAMBE as in Ref. [34]. Concurrent ion irradiation during growth results in a smoother surface as observed in RHEED patterns. Ion beam-assisted molecular beam epitaxy thus produces films with an improved crystalline quality at low temperatures. The data also suggest that Ar^+ ion energies lower than 50 eV are required for improvement in the crystalline quality of films deposited below 250°C .

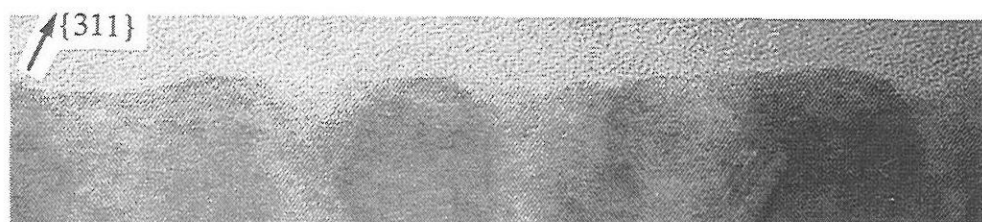
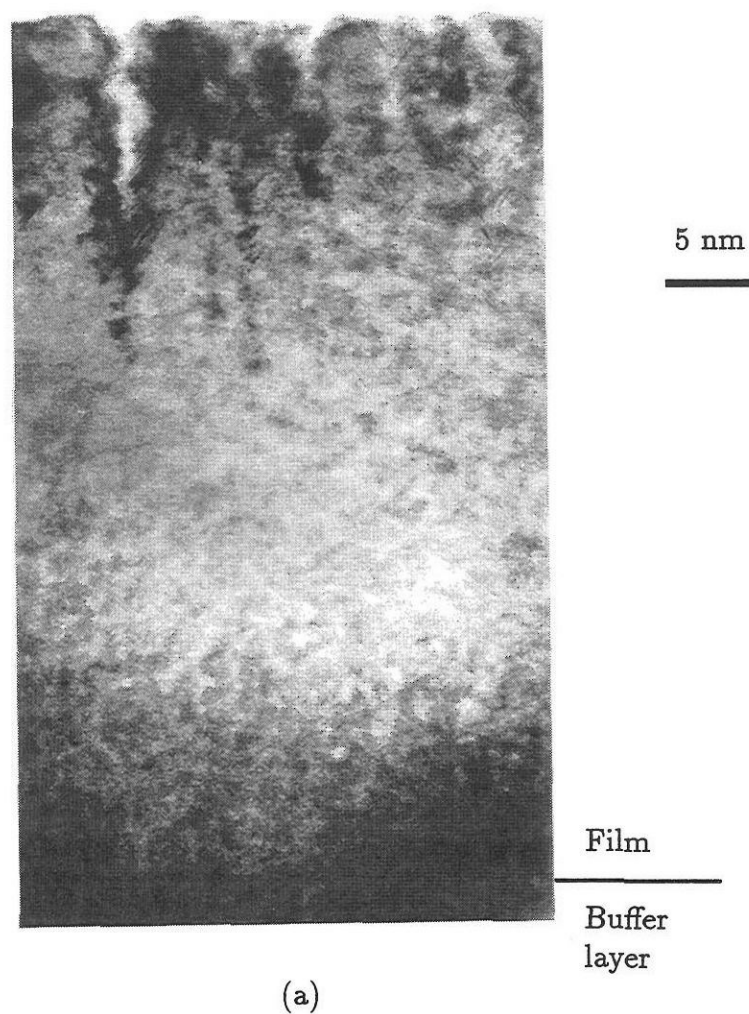


Figure 2.11: (a) High resolution TEM image of an IAMBE film deposited at 370°C and 0.09 nm/s. The Ar^+ ion energy was 50 eV and the ion-to-atom flux was about 0.06. The image was taken in the $\langle 110 \rangle$ projection. (b) An enlarged view of the surface showing a $\{311\}$ facet. Both $\{311\}$ and $\{111\}$ facets were observed on the growing front.

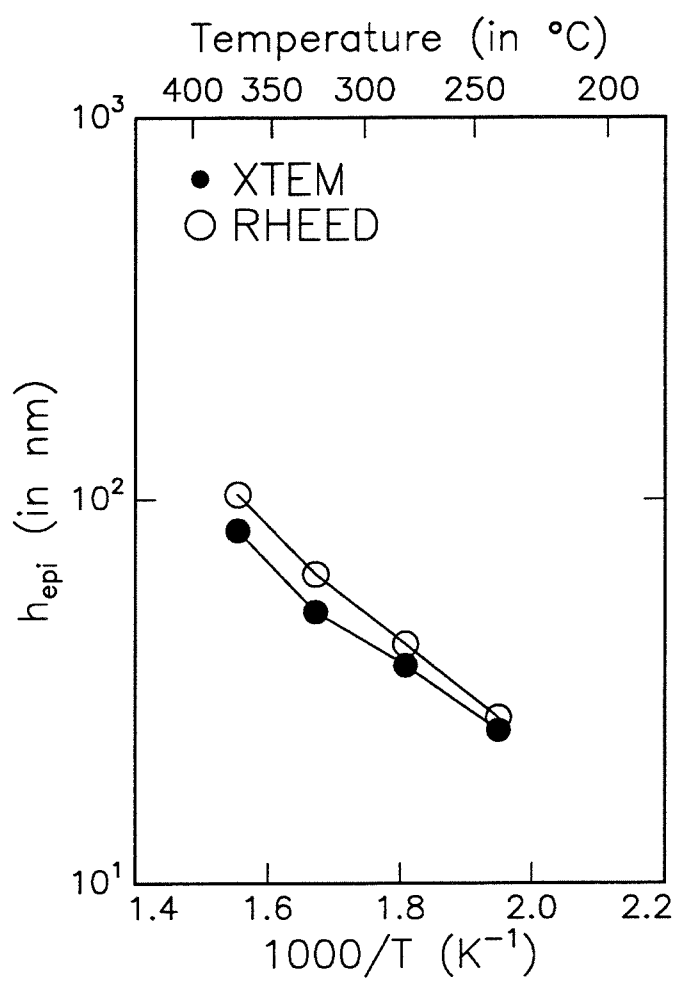


Figure 2.12: Epitaxial thickness vs. inverse temperature for conventional MBE films measured by (a) • cross section transmission electron microscopy, and (b) ○ RHEED observations.

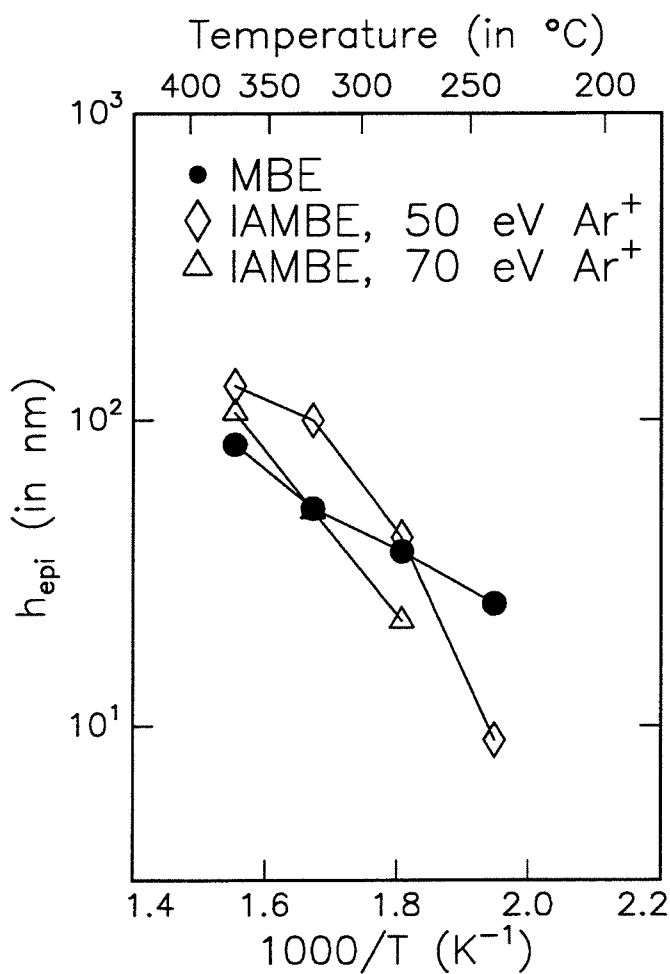


Figure 2.13: Epitaxial thickness vs. inverse temperature for (a) • Conventional MBE, (b) ◊ 50 eV Ar⁺ IAMBE, and (c) △ 70 eV Ar⁺ IAMBE. The epitaxial thickness was measured by cross section transmission electron microscopy.

2.7 Other Thin Film Characterization Techniques

2.7.1 Rutherford Backscattering and Channeling

The XTEM images of low temperature films show that they are free of extended defects up to the epitaxial thickness. A Rutherford backscattering/channeling analysis was performed to check the quality of these layers. The He^{++} ions were incident normally on the surface and the solid state detector was at a 170° backscattering angle. With 2 MeV He^{++} ions, the minimum yield χ_{\min} from a Si(001) wafer for this geometry is about 0.03 [36]. A χ_{\min} value of 0.03 was indeed obtained with a dilute HF-dipped Si(001) wafer. Figure 2.14(a) shows the random and (001) aligned spectra from a 50 nm film deposited by conventional MBE at 370°C . The deposition conditions were identical to the one shown in Fig. 2.7. The χ_{\min} value of 0.03 clearly indicates a film with a low defect density. It is noted that about 75% of the signal from the low temperature film lies within the surface peak. Figure 2.14(b) shows the result of a similar analysis on an 80 nm IAMBE film deposited at 370°C . Again, a 0.03 minimum yield indicates that low energy ion irradiation does not result in the generation of dechanneling defects.

The RBS spectrum of the IAMBE film did not show any Ar peak indicating that the Ar concentration is less than the detection limit of about 0.1%.

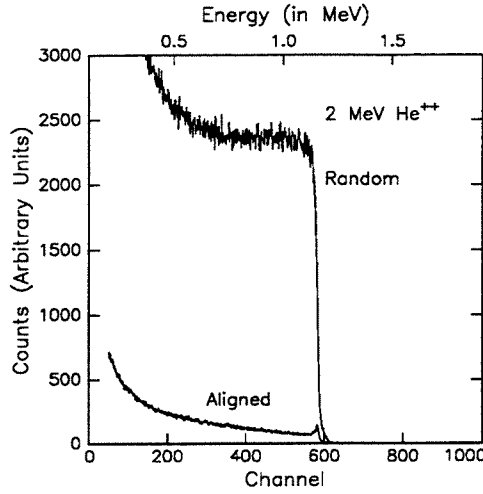
In Ref. [37], positron annihilation spectroscopy was used to show that low temperature Si films have a very low concentration of point defects. The

authors concluded that the density of point defects was not sufficient to explain the breakdown of epitaxy. While channeling yield is not sensitive to low concentrations of defects, the analysis nevertheless indicates that the breakdown of epitaxy is an abrupt phenomenon and not caused by a continuous increase in the defect density.

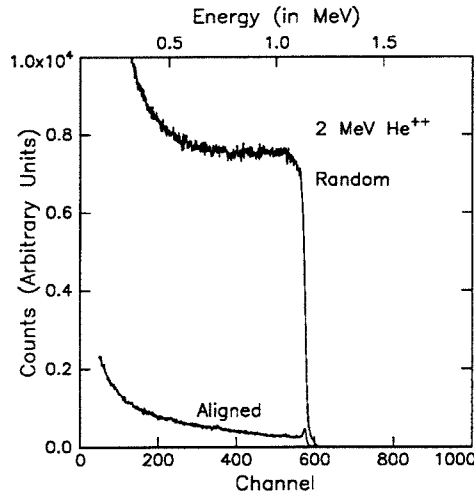
2.7.2 Secondary Ion Mass Spectrometry

There are several sources of contamination in an MBE chamber. A typical pressure during growth was 10^{-6} Pa. This corresponds to a monolayer time, i.e., the time required to build up one monolayer of contaminants, of about 100 s. Fortunately, the contamination rates are much lower because the sticking coefficients of most residual gases on silicon are low. Hydrogen is the main residual gas and comes from extensive outgassing of the source and surrounding regions. Molecular hydrogen does not react with silicon but atomic hydrogen which may be produced by cracking of hydrogen and hydrocarbons at hot filaments and silicon melt has almost unity sticking coefficient. The next most abundant gases are carbon monoxide, carbon dioxide and water.

Secondary ion mass spectrometry (SIMS) was performed on a CAMECA IMS-3f system. The carbon and oxygen profiles were obtained with a 14.5 keV Cs^+ beam and the hydrogen profiles were obtained with a 10.5 keV O_2^+ beam. The sample bias was held at 4.5 keV and the ions were incident nominally at 30° . The sample bias causes a slight deviation in the incident beam which can be estimated [38]. For the Si signal, the counts of the ^{30}Si isotope were



(a)



(b)

Figure 2.14: Rutheford backscattering/channeling spectra from (a) a 50 nm film deposited by conventional MBE at 370°C, and (b) an 80 nm film deposited by IAMBE. The substrate temperature was 370°C for both films. The minimum yield $\chi_{\min} = 0.03$ for the (001) aligned spectra in both cases. It is noted that about (a) 75% and (b) 50% of the signal from the low temperature film falls within the surface peak.

monitored. The secondary ion yields were converted to atomic densities using

$$N_A = \frac{I_A}{I_s} A_s \text{ RSF}_A \quad (2.1)$$

where N_A is the atomic density of the element A, I_A and I_s are the yields of the element A and the ^{30}Si isotope, A_s is the relative abundance of the ^{30}Si isotope and RSF_A is the relative sensitivity factor of the element A. The relative sensitivity factors have been experimentally determined for a number of elements in the Si matrix [38]. The RSF of C and O for the 14.5 keV Cs^+ beam were taken as 2.4×10^{22} and $4.8 \times 10^{22} \text{ cm}^{-3}$ respectively [38]. Since the RSF of H atoms with 10.5 keV O_2^+ ions was not readily available, the value from Ref. [38] of $6.2 \times 10^{24} \text{ cm}^{-3}$ for 8 keV ions was used. The relatively modest base pressure of 10^{-6} Pa in the SIMS analysis chamber limited the sensitivity of the method. A high sputtering rate of $\sim 1 \text{ nm/s}$ was used to improve the detection limit. The depth scale was obtained by using the sputtering rates from previous data [38].

Figure 2.15(a) shows the SIMS profiles of C, H and O from the film deposited at 370°C by conventional MBE. The C and O profiles show two peaks at the buffer layer/substrate and film/buffer layer interfaces. This corresponds to contamination at the initial wafer surface and the contaminants accumulated during the growth interrupt after buffer layer deposition. The total amount of carbon at the buffer layer/substrate and film/buffer layer interfaces is about 0.02 ML ($1 \text{ ML} \equiv 6.78 \times 10^{14} \text{ cm}^{-2}$) and 0.005 ML respectively; the corresponding numbers for oxygen are 0.06 and 0.02 ML respectively. These impurities play an extremely important role in the evolution of surface morphology. The observation of islanding in the initial stages

of growth (see Section 2.3) can be correlated to these impurities. One way in which impurities can cause film growth in the Volmer-Weber mode is by decreasing the surface energy [13]. The islanding in this case, however, seems to be due to kinetic effects. The extent of islanding can be reduced by going to slower deposition rates.

The SIMS profiles from the IAMBE film deposited at 370°C are shown in Fig. 2.15(b). Again, a small amount of C and O is observed at the buffer layer/substrate interface. The double peak in Fig. 2.15(b) is due to a growth interrupt during buffer layer deposition. One can also infer a similar contamination peak at the film/buffer layer interface. In addition, the C and O content in the low temperature film is seen to be higher than the corresponding conventional MBE film. This is probably due to contamination from the ion beam. Since h_{epi} for the IAMBE films was higher, this provides some evidence that C and O contamination is not the direct cause of breakdown of epitaxy. Another experiment showing that C and O do not directly cause the crystalline-to-amorphous transition is discussed in Section 2.8.

The hydrogen peak is not observed at either of the two interfaces. This is not surprising since hydrogen (for coverage < 1 ML) is known to segregate on the surface during growth [39].

The concentration of all three elements increases toward the surface. This rise coincides with the observation of defects in these films. The disordered region of the film contains a high density of dangling bonds. This probably causes the increase in the impurity incorporation by the diffusion of impurities after exposure to atmosphere and enhanced sticking during growth. The delayed rise in the H, C and O concentrations in the IAMBE film com-

pared to the conventional MBE film is consistent with the increased epitaxial thickness for the IAMBE film.

The SIMS analysis has thus shown that small amounts of C and O are accumulated during growth interrupts. These impurities can be correlated with the observation of islanding in the initial stages of Si homoepitaxy. The increased C and O contamination observed in the IAMBE films is a concern for the use of ion beams in depositing device quality films.

2.7.3 Atomic Force Microscopy

Even though low temperature growth starts on a planar surface, the surface does not remain planar during growth. RHEED observations of films deposited at different temperatures indicate that the increase in surface roughness strongly correlates with the epitaxial thickness. A scanning probe technique such as atomic force microscopy (AFM) can provide quantitative information about the surface roughness.

Atomic force microscopy was performed *ex situ* using the Digital Instruments, Nanoscope III. The samples were imaged with a metal tip on a Si_3N_4 cantilever. The force constant of the cantilever was 0.58 N/m. Images were obtained in the contact mode under constant force conditions. A few samples were imaged with different tips to check for tip artifacts. Similar results were obtained with the different tips. An atomically resolved image was not observed.

The Si surface gets oxidized immediately on exposure to atmosphere. This oxide was removed with a dilute HF dip just prior to imaging. While

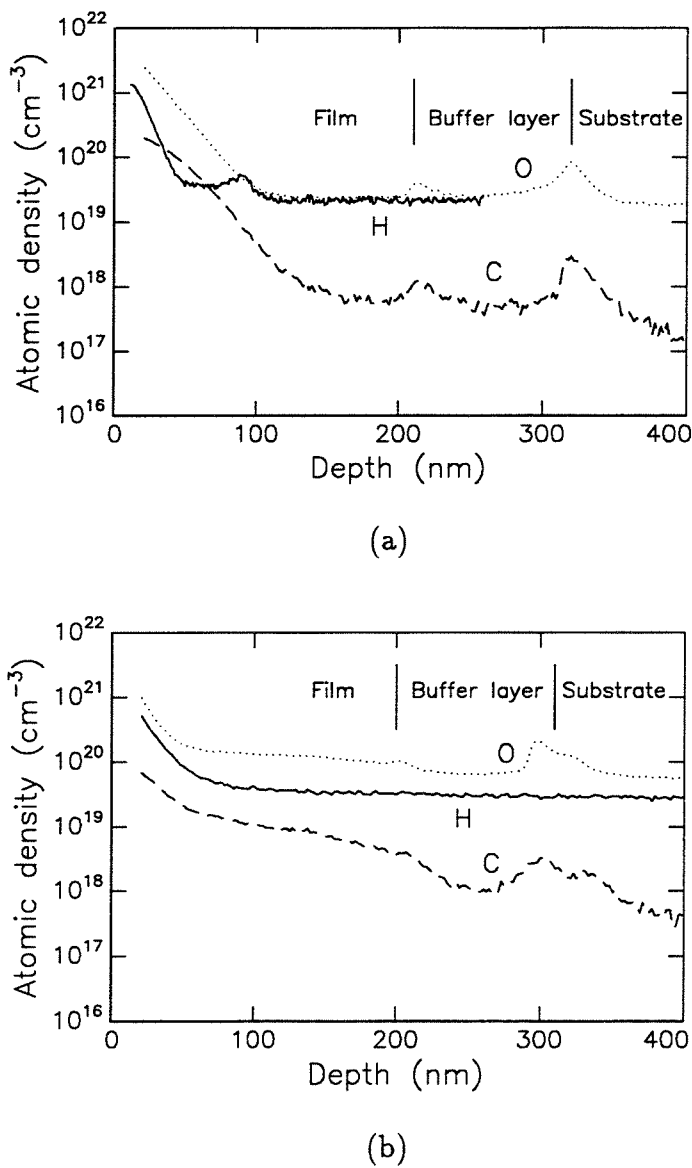


Figure 2.15: The SIMS profiles of H, C and O in (a) conventional MBE film and (b) IAMBE film. Both films were deposited at 370°C and 0.09 nm/s. C and O profiles were obtained with a 14.5 keV Cs⁺ beam; the H profile was obtained with a 10.5 keV O₂⁺ beam. Note that the background levels of H and O are different for (a) and (b).

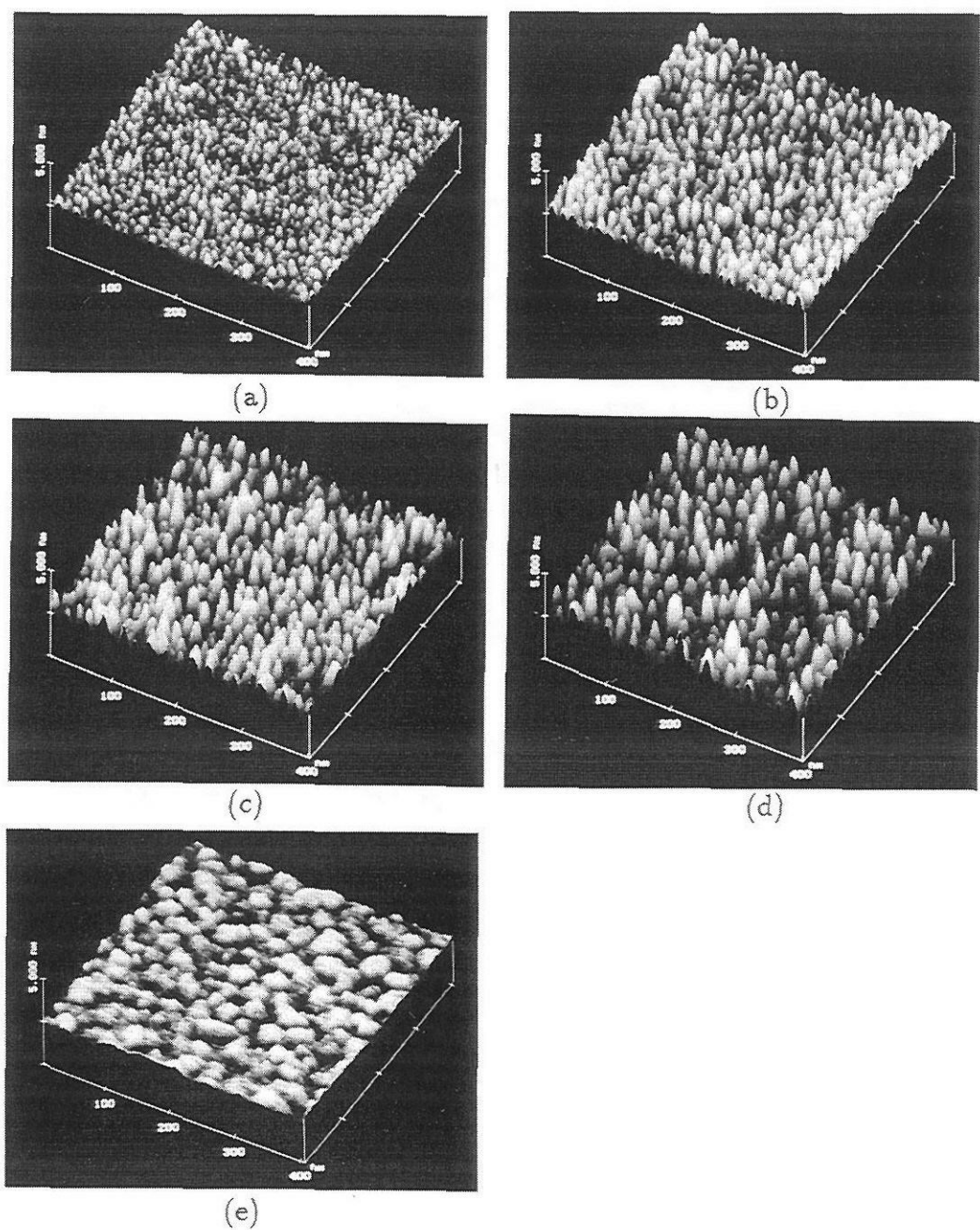


Figure 2.16: AFM images after (a)20, (b)40, (c)60, and (d)80 nm film deposited at 325°C by conventional MBE. The growth rate was 0.09 nm/s. (e) AFM image of an IAMBE film after 40 nm deposition at 325°C. The Ar^+ ion energy was 50 eV and the ion-to-atom flux ratio was about 0.06. The horizontal and vertical scales are 100 nm/division and 2.5 nm/division, respectively.

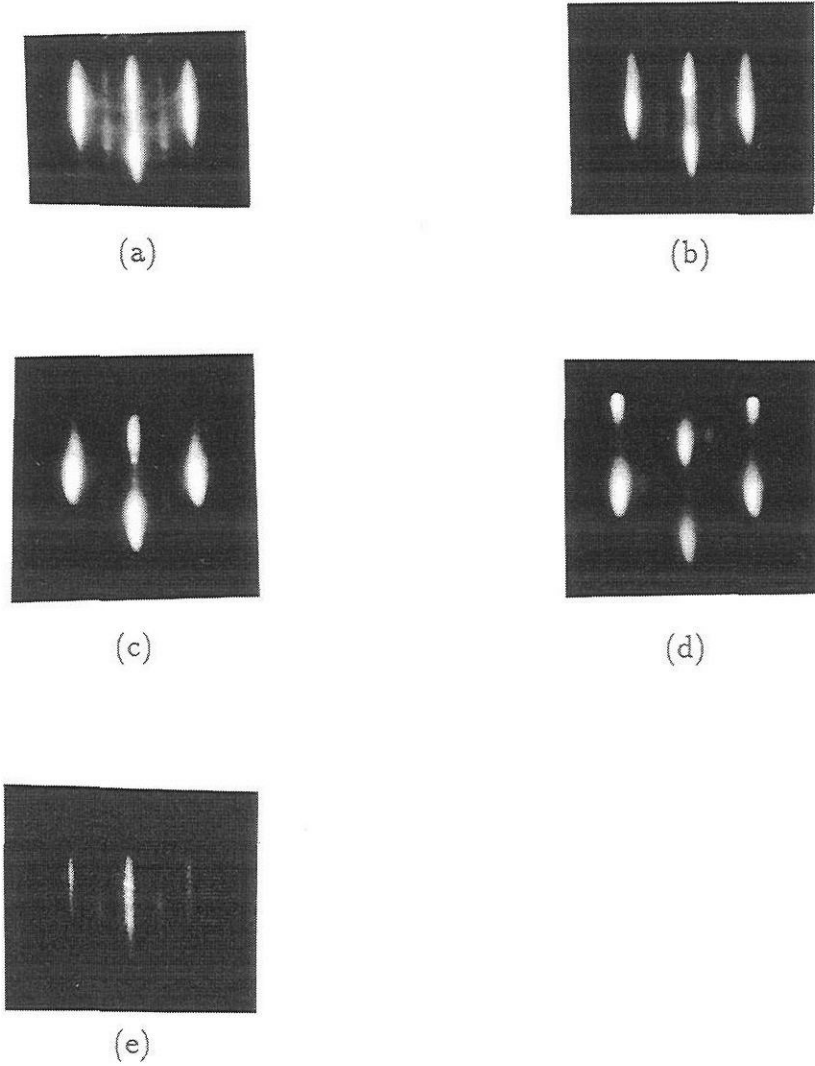


Figure 2.17: RHEED patterns after (a)20, (b)40, (c)60, and (d)80 nm film deposited at 325°C. (a) RHEED pattern from an IAMBE film after 40 nm deposition at 325°C. These RHEED patterns correspond to the AFM images in the previous figure.

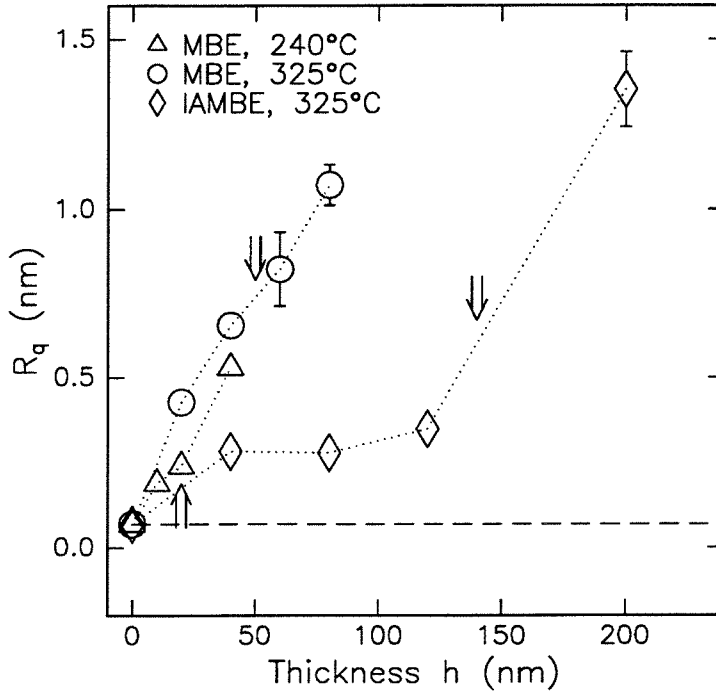


Figure 2.18: The rms surface roughness vs. film thickness for different growth conditions. The roughness was measured over a $300 \times 300 \text{ nm}^2$ area at three separate points on each specimen. Conventional MBE at (a) \triangle , 240°C , (b) \circ , 325°C , and IAMBE at (c) \diamond , 325°C . The arrows indicate the epitaxial thickness estimated from the RHEED patterns. The dashed line is the measured roughness of a high-temperature buffer layer.

this process may change some features on the surface, it does not significantly affect the conclusions drawn here. This is because the tip-surface convolution rounds off all the sharp features. While the tip size can introduce artifacts, it is noted that most of the islands observed in the images were much larger than the smallest feature observed.

Films of different thicknesses were deposited side by side at 240 and 325°C by conventional MBE. The substrate shutter was used to block a region of the substrate after depositing the desired thickness. The growth rate was 0.09 nm/s. The AFM images obtained from the films at 325°C are shown in Figs. 2.16(a)–(d). One can see 3D islanding even at the smallest thickness of 20 nm. An increase in surface roughness and island coalescence with film thickness can also be inferred from the images. The RHEED patterns from the corresponding surfaces are shown in Figs. 2.17(a)–(d). The width of the Bragg spots increases with the surface roughness, as expected. Twin spots were observed in the RHEED pattern after 50 nm deposition. Films were also deposited by IAMBE at 325°C and 0.09 nm/s using 50 eV Ar⁺ ions. These films were deposited separately, as it was not possible to simultaneously block the ion and growth fluxes in different regions. As a consequence, some sample variation is expected. Figure 2.16(e) shows the surface of an IAMBE film after 40 nm deposition. Comparison with Fig. 2.16(b) shows that Ar⁺ ion irradiation leads to surface smoothing. This is also evident from the RHEED patterns in Figs. 2.17(b) and (e).

The rms roughness R_q was measured over a $300 \times 300 \text{ nm}^2$ region at three different points on each specimen. This is plotted as a function of film thickness in Fig. 2.18. The arrows indicate the epitaxial thicknesses esti-

mated from the RHEED patterns. We see that the IAMBE film is much smoother than the conventional MBE film. The rms roughness for the film at 240°C is seen to rise more slowly than the film at 325°C. This is somewhat puzzling since surface roughness builds up more rapidly at lower temperatures. For conventional MBE, the ratio of the rms roughness at the epitaxial thickness $R_q(370^\circ\text{C})/R_q(240^\circ\text{C}) \approx 3$. The ratio of the diffusion lengths is $L_p(370^\circ\text{C})/L_p(240^\circ\text{C}) \approx 3$, assuming an activation energy and prefactor of 0.67 eV and $10^{-3} \text{ cm}^2/\text{s}$ for Si adatom diffusion [40]. We see that these ratios are approximately the same. Although neglecting the effects of adsorbates and the assumption of a single diffusion constant are oversimplifications, the ratio of the moments of the surface roughness and the diffusion length deserves a further study.

From Fig. 2.18, we can infer a kinetic roughening exponent $\beta \sim 1$ for conventional MBE. The continuum models that describe crystal growth give $\beta \leq 1/2$ [41] (see Section 1.5 for more discussion). If the arriving atoms are uncorrelated in space and time, and there is no surface diffusion, $\beta = 1/2$. Including surface diffusion only reduces the value of the exponent. Although one needs data at least over three orders of magnitude in film thickness to make a good comparison, it is nevertheless significant that the experiment indicates such a large value for the exponent. This was also noted in Ref. [42]. A possible explanation for this rather large value is the presence of adsorbates during growth. Adsorbates such as carbon and oxygen (Section 2.7.2) and hydrogen [43] can significantly accelerate the surface roughness. This must be taken into account in the continuum models. In a simple model for IAMBE, it was shown that $R_q \sim \ln h$ asymptotically [44]. For the IAMBE

film, we see that the rms roughness remains relatively low up to about 120 nm film thickness, in agreement with theory. Again, one would need more data to make a comparison with theory in this case. The rms roughness for the IAMBE film is seen to rise rapidly with the breakdown of epitaxy. A possible explanation is that once twins nucleate, adatoms move away from the positions (re-entrant corners) where they would be forced to form five- and seven-member rings, resulting in an acceleration of surface roughness.

2.8 Annealing Experiment

The SIMS analysis described in Section 2.7.2 showed that the rise of C,H and O profiles coincides with the breakdown of epitaxy. However, we believe the presence of these impurities is an effect and not a cause of the transition. The conclusive proof that C and O do not cause a breakdown of epitaxy comes from an annealing experiment first described in Ref. [14]. We have seen that growth at low temperature proceeds epitaxially up to a thickness h_{epi} followed by a crystalline-to-amorphous transition. It was found that by repeating the steps – (a) depositing the film up to h_{epi} , and (b) interrupting growth and annealing at 500°C for 1 min. – one can grow crystalline silicon indefinitely [14]. We found that a 450°C anneal for 10 min. has the same effect. Now, the temperature of 450°C is too low for desorption of C and O. A thin SiO layer requires at least 700°C for desorption and SiC, if formed, does not desorb until the melting point of Si. The RHEED pattern before and after annealing at 450°C is shown in Fig. 2.19. It is clear that there is remarkable

smoothing of the surface during the anneal due to island coarsening. The annealing temperature is also sufficiently high to desorb hydrogen, if the coverage exceeds 1 ML.

These experiments thus show that the breakdown of epitaxy is not directly caused by the presence of carbon or oxygen at the observed concentrations.

2.9 Voids in Low Temperature MBE Grown Silicon

The microstructure of the low temperature deposited silicon films discussed so far started with single crystal and transformed into amorphous silicon with an intermediate region consisting of planar defects. Figure 2.20(a) shows an XTEM image of a film deposited at 410°C and 0.11 nm/s by conventional MBE. We see that starting at a certain thickness, there is a trail of volume defects in the film. These defects were identified as voids in Refs. [45, 46] using positron annihilation spectroscopy. The voids range in size from 1 to 5 nm in diameter. The diffraction pattern from the film is shown in Fig. 2.20(b). The extra spots are twin spots and double diffraction spots.

Is the breakdown of epitaxy due to these volume defects, or voids? The above film differs from the other films in one important respect – the presence of defects at the interface, in this case the buffer layer/substrate interface. An enlarged view of one such defect is shown in Fig. 2.20(c). It appears that the initial surface of the wafer had some impurities, possibly SiO₂ or SiC, around which the film has grown. A twinned region can also be seen.

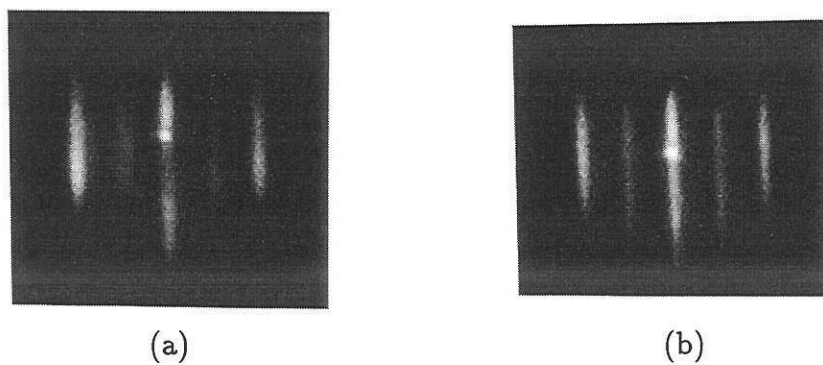


Figure 2.19: RHEED pattern along $\langle 110 \rangle$ azimuth. (a) After depositing 50 nm at 325°C , and (b) after 10 min. anneal at 450°C .

All reported observations of voids in low temperature silicon films [45, 46] have had such defects either at the film/buffer layer or buffer layer/substrate interface. This was also noted in Ref. [37]. This suggests that film growth on a surface with such impurities results in a morphological instability causing void formation. The cause of this morphological instability is not understood at present. The film morphology is similar to that observed in constitutional supercooling of binary alloys [47] although it is not clear how far one can stretch the analog.

It is thus clear that low temperature films can be grown without voids. The crystalline-to-amorphous transition still occurs and is independent of void formation.

2.10 Beam-Induced Desorption of Surface Hydrogen

Surface smoothing by low energy Ar^+ ions was shown to be an important effect in IAMBE films. Another effect of ion irradiation could be sputtering of impurities. This is indeed the case with surface hydrogen. A nominally dihydride-terminated $\text{Si}(001)\text{-}1\times 1$ surface was irradiated with 50 eV Ar^+ ions incident at 45° with respect to the substrate normal. The ion flux was $6.8\times 10^{12} \text{ /cm}^2\text{-s}$ ($\equiv 0.01 \text{ ML/s}$) and the substrate temperature was 190°C . Figure 2.21 shows the RHEED pattern after a dose of 22 ML. The surface is (2×1) reconstructed suggesting at least partial hydrogen desorption.

Epitaxy on hydrogen-terminated silicon surfaces and the beam-induced

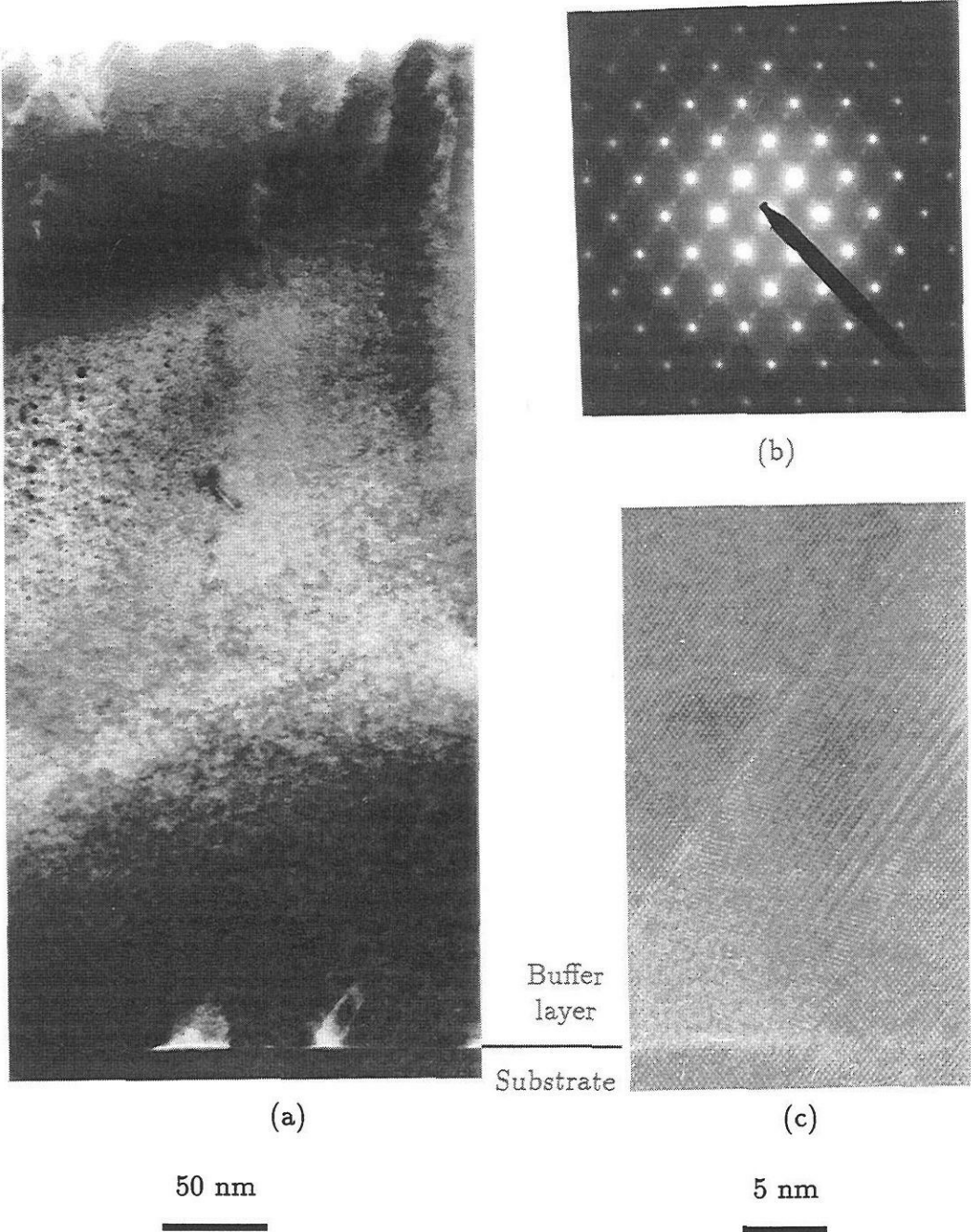


Figure 2.20: (a) Bright field image of a 140 nm buffer layer deposited at 530°C followed by a 340 nm film at 410°C. The image was taken under multibeam conditions in the $\langle 110 \rangle$ projection. A trail of voids can be seen in the film. (b) The diffraction pattern shows twin spots. (c) An enlarged view (high resolution) of a defect at the buffer layer/substrate interface.

reconstruction of silicon is the subject of Chapters 4 and 5. Some important observations are noted here. Silicon deposition on an initially dihydride-terminated Si(001)- 1×1 surface results in amorphous film growth. However, Si deposition on a surface after beam-induced reconstruction results in epitaxial films. It is also possible to grow an epitaxial silicon film on an initially monohydride-terminated Si(001)- 2×1 surface [6]. In a systematic study of the influence of hydrogen, it was shown that introduction of atomic hydrogen reduces the epitaxial thickness [42]. Thus a high coverage of hydrogen (> 1 ML) can cause a premature breakdown of epitaxy.

The beam-induced reconstruction experiment also suggested that the sputtering rate of H was rather low for the flux used. The ion-to-atom flux ratio in the IAMBE films was typically less than 0.1. The removal of surface hydrogen due to ion irradiation is thus expected to play a small role in the evolution of the film microstructure during ion-assisted growth.

2.11 Temperature Ramp Experiments

A clear picture of the difference in growth morphology at different temperatures can be seen from a temperature ramp experiment. The temperature is dropped during deposition at a constant rate starting at a high temperature, normally in the step flow growth mode. Such a study was first reported in Ref. [48]. They used an optical reflectivity technique to measure the crystalline-to-amorphous transition thickness (and hence the temperature). The transition temperature was a function of both the growth rate and the temperature ramp rate [48, 49]. Higher growth rates resulted in a quicker

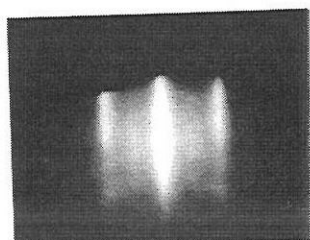


Figure 2.21: RHEED pattern showing low energy Ar^+ ion beam-induced reconstruction. The substrate temperature was 190°C .

breakdown of epitaxy.

Temperature ramp experiments were performed for both conventional MBE and IAMBE. A buffer layer was deposited at high temperature, typically 550°C. The temperature was then dropped at 9 K per minute. The appearance of twin spots in the RHEED pattern for the different film growth conditions is shown in Table 2.1. Both Ar^+ and He^+ ions were used in these experiments. For the growth rate of 0.09 nm/s, we see that the breakdown of epitaxy is delayed with the use of ion bombardment. In the case of conventional MBE, the breakdown temperatures are higher than the ones reported in Ref. [48]. This could be due to the different characterization techniques, substrate temperature measurement and also other factors such as contamination rates.

The ECR source was used to generate helium ions and the background pressure during growth was 7×10^{-2} Pa. A crude Langmuir probe measurement indicated ion energies in the range 10 – 30 eV. An XTEM image for the He^+ IAMBE is shown in Fig. 2.22. This image shows the first defects at an equivalent temperature of 300°C. The surface is seen to be highly faceted. To see the influence of any possible contaminants in the He gas, a film was deposited by conventional MBE in a background of He gas (7×10^{-2} Pa) and the XTEM image of the film is shown in Fig. 2.23. The first defects are observed at an equivalent temperature of 270°C. Helium ions, because of their lighter mass, can transfer energy better to the H atoms. Hence, if H atoms were responsible for the breakdown of epitaxy, one would have expected to see a significant effect on the transition temperature. This suggests that H accumulation is not causing the breakdown of epitaxy. However, we

Table 2.1: The results of temperature ramp experiments.

Growth Conditions	Temperature ramp rate (K/min.)	Growth rate (nm/s)	Observation of twin spots in RHEED	Ref. [49] Numbers in parentheses are temperature ramp rates
MBE	-9	0.09	350°C	190°C (-6)
IAMBE, 50 eV Ar ⁺	-9	0.09	290°C	—
IAMBE, 70 eV Ar ⁺	-9	0.09	310°C	—
MBE	-9	0.02	240°C	260°C (-3)
IAMBE, He ⁺	-9	0.02	250°C	—

do not have a good measure of the He⁺ ion flux and hence cannot be certain about this conclusion. (The He⁺ flux is estimated to be $5 \times 10^{13} \text{ cm}^{-2} \text{ s}^{-1}$ to within a factor of 3).

Temperature ramp experiments illustrate the abruptness of the breakdown of epitaxy at low temperatures. Film growth starts in a perfectly single crystal form at high temperatures and ends with amorphous deposition at low temperatures. Also, there is no buffer layer/film interface for contaminant accumulation since there is no growth interrupt. These experiments, however, are harder to interpret because of the different growth modes encountered in the different temperature regimes.

2.12 The Crystal-state—Amorphous-state Transition

Based on the above experiments, we can make some observations regard-

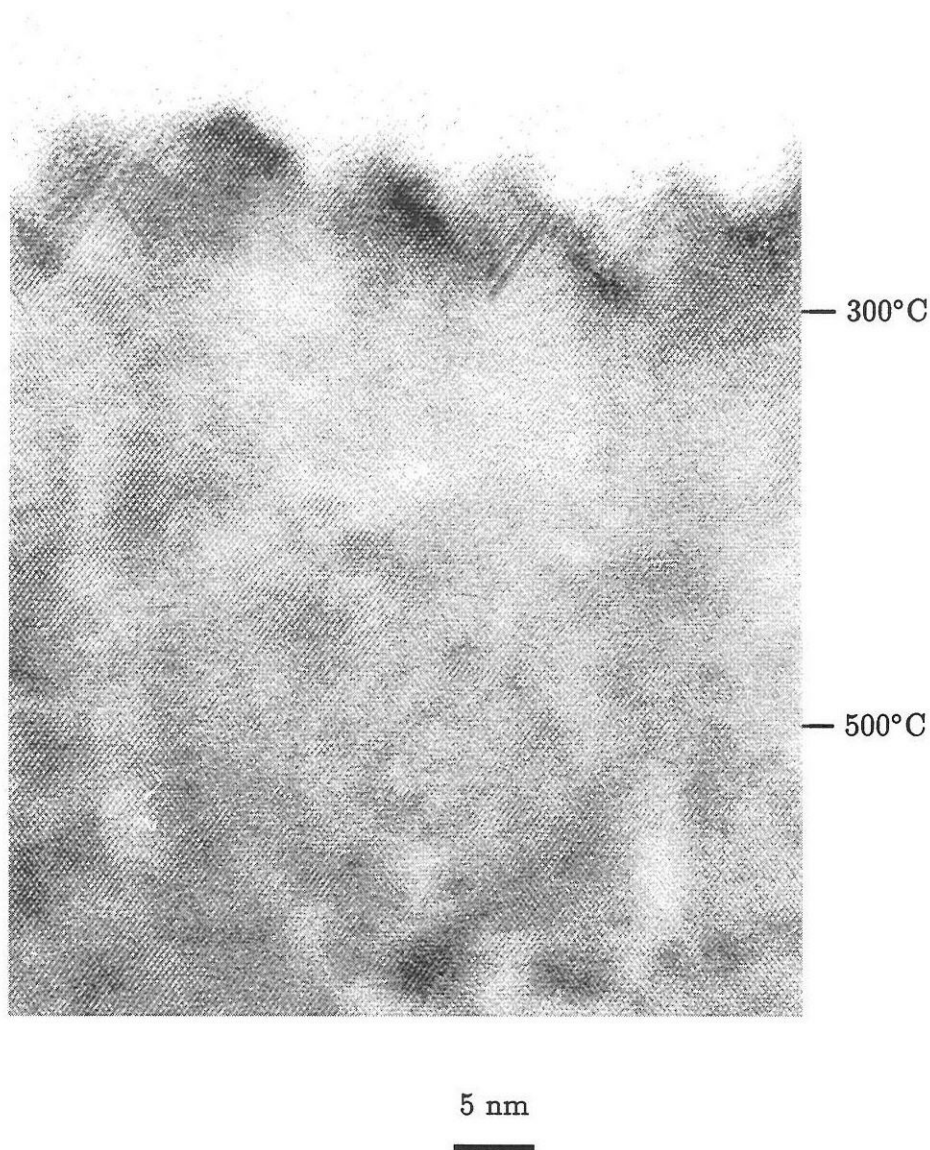


Figure 2.22: HRTEM image of a film deposited by He^+ IAMBE. The temperature was dropped at a rate of 9 K/min. starting at 500°C and the growth rate was 0.02 nm/s. The ECR source was operated at 130 W and 0.07 Pa He pressure.

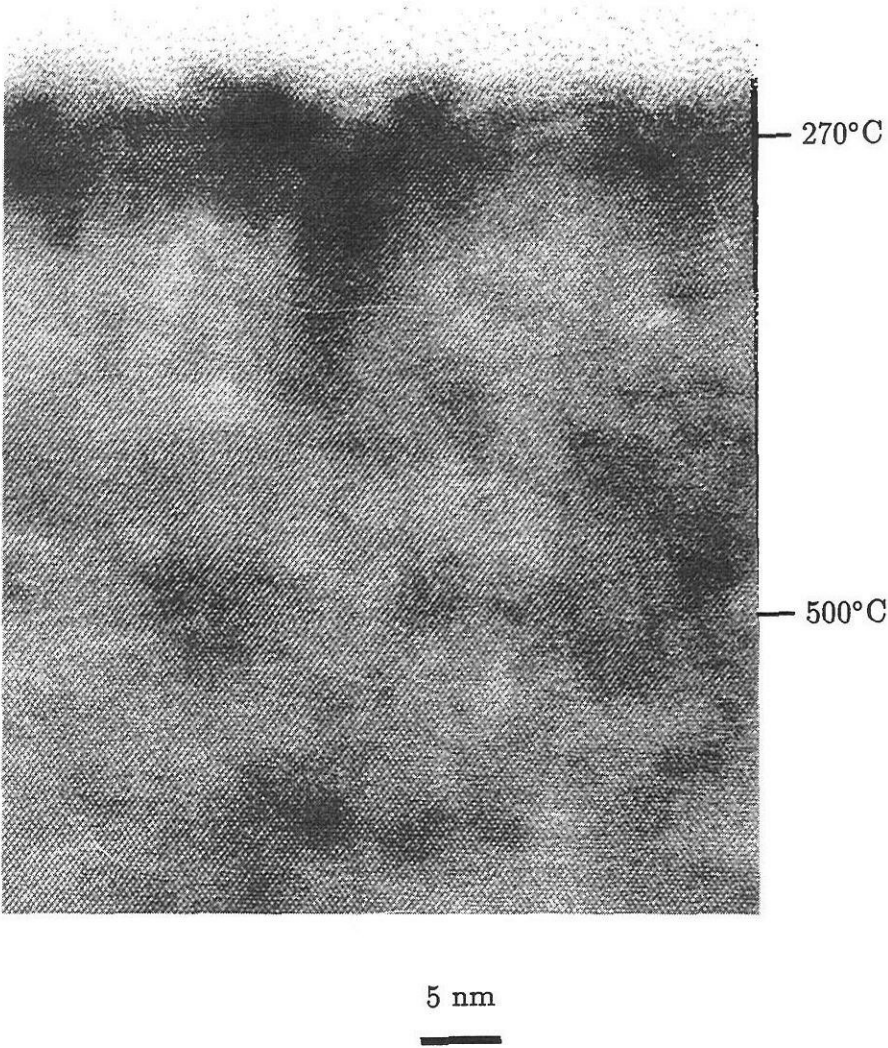


Figure 2.23: HRTEM image of a film deposited by conventional MBE in a background (0.07 Pa) of He gas. Temperature was dropped at a rate of 9 K/min. starting at 500°C and the growth rate was 0.02 nm/s.

ing the influence of various parameters on the crystal-state—amorphous-state transition.

The presence of voids, or volume defects, has been mentioned as a cause of the breakdown of epitaxy [33]. These voids are of sufficiently large size to be observable in XTEM images. We have correlated these voids with the presence of defects at the film/substrate interface. The formation of voids can be prevented by starting with a clean Si(001)-2×1 surface. In our experiments, the crystal-state—amorphous-state transition was observed to occur without voids. This agrees with the results of Ref. [37], where positron annihilation spectroscopy was used to show that the point (and volume) defect density in the epitaxial layer was too low to account for the crystalline-to-amorphous transition.

Consider roughness alone as a cause of the breakdown of epitaxy. Surface roughness has a positive correlation with the temperature dependence of the epitaxial thickness, h_{epi} . The roughness increases more rapidly at low temperatures due to lower adatom diffusivity. We have also observed through AFM images and RHEED patterns that concurrent low energy Ar^+ ion irradiation during deposition results in surface smoothing. The roughness mechanism can thus explain the observed increase in h_{epi} for ion beam-assisted MBE films. Thus it seems plausible that the twin-boundary/facet (TBF) mechanism described in Section 2.5 is the way the film deposition goes from being epitaxial to being amorphous.

It is noted that the values of the epitaxial thickness reported by different groups differ by an order of magnitude for similar growth conditions. Thus for conventional MBE at 325°C and 0.09 nm/s, we measured an epitaxial

thickness of about 50 nm. Epitaxial thicknesses of ~ 100 nm (~ 0.1 nm/s, 310°C) and ~ 500 nm (albeit with voids, 0.1 nm/s, 300°C) are reported in Refs. [50] and [45] respectively. This suggests that some other factor in addition to surface roughness is playing a role in the breakdown of epitaxy. This role is best filled by adsorbates. It was observed in SIMS analysis that C and O accumulate at the surface during a growth interrupt. The initial 3D islanding observed in silicon films (Section 2.7.2) was correlated with small amounts of these impurities. Recently it was shown using a scanning tunneling microscope that a small coverage of H can dramatically increase the Si island density during Si MBE [43]. Hence impurities can play an indirect role in the breakdown of epitaxy by accelerating the surface roughness. Do impurities such as H, C and O alone cause the crystalline-to-amorphous transition? From the annealing experiment described in Section 2.8 (and SIMS analysis), we have seen that a small coverage of C and O does not provide a site for the nucleation of amorphous silicon. A saturation coverage ($\sim 2\text{ML}$) of hydrogen can result in an amorphous silicon film even without any surface roughness. At coverages lower than 1 ML , it is known that hydrogen does not impede the growth of a crystalline film [14, 39]. An unknown quantity is the hydrogen coverage during growth. A difficulty with the viewpoint that hydrogen alone causes the breakdown of epitaxy is that hydrogen desorption is negligible below 350°C on the time scale of film growth. However, h_{epi} is observed to exhibit a strong dependence on temperature (Section 2.6 and Ref. [6]). An indirect role of the impurities is thus more consistent with the evolution of film morphology in low temperature silicon molecular beam epitaxy.

The TBF mechanism for the breakdown of epitaxy raises several interesting issues. It is known that five- and seven-member rings are present at the Si(001)- 2×1 and the Si(111)- 2×1 surface. However, they do not seem to act as nucleation sites for amorphous silicon. The important difference here is that the five- or seven-member ring is not *forced* into the film microstructure by these reconstructions. The rings open up when adatoms are in the vicinity. This is possibly why surface anti-phase domains seem to have no effect on the film microstructure. The (2×1) reconstruction of the Si(001) surface results in a lower symmetry (twofold) on the surface than in the bulk (fourfold). This can cause two independently nucleated islands to be out-of-phase creating an anti-phase boundary (APB) when they coalesce. Silicon growth in the 2D nucleation and growth regime will result in a high density of such APBs. Yet, single crystal can be grown indefinitely in this regime indicating that the five-member rings open up when adatoms are in the vicinity.

An alternative mechanism for the breakdown of epitaxy was proposed recently in a study of low temperature Ge(001) homoepitaxy [51]. The initial step was the increase in surface roughness and the formation of $\{111\}$ facets, just as in the TBF mechanism. Single adatoms dropped on the Si(111) surface stick in the T_4 or the H_3 site to increase their coordination. Calculations have shown that the T_4 site is the lowest energy site for an adatom on the (111) surface [52]. It was proposed that if the adatom did not have sufficient time to move out of the T_4 site into its bulk position, it would lead to a crystalline-to-amorphous transition. At present, I do not see a simple way to distinguish between the two mechanisms from the existing data. There is certainly evidence for twinning in the low temperature films. Whereas the TBF

is active at all temperatures, it is possible that the above mechanism and also other mechanisms such as the five-member rings on the reconstructed surfaces could become active at some lower temperature.

Is epitaxial thickness more fundamental than epitaxial temperature? It was noted in Ref. [6] that the finite h_{epi} on the Si(001) was due to the difficulty in nucleating the amorphous phase on this surface. This is borne by the TBF mechanism which suggests that it is the {111} surface which is required to initiate the breakdown of epitaxy. This leads us to the very interesting case of low temperature epitaxy on the Si(111) surface. Since there is an "infinite" area of the (111) oriented surface, epitaxy must be more difficult on this surface even if the surface diffusion is more rapid. This indeed seems to be the case. Using a Rutherford backscattering/channeling study, it was reported that the films deposited below 400°C on an initially Si(111)-7×7 surface had defects [21]. Another interesting observation is that the stacking fault in the (7×7) reconstruction (dimer-adatom-stacking fault model [53]) remains intact when Si is deposited at room temperature [22, 54]. Amorphous silicon starts right at the edge of the stacking fault, just as predicted by the TBF mechanism.

Bibliography

- [1] Perkin-Elmer ionization gauge manual.
- [2] M.A. Herman and H. Sitter, *Molecular Beam Epitaxy: Fundamentals and Current Status*, Springer-Verlag, Berlin, 1989.
- [3] A. Ishizaka and Y. Shiraki, 'Low temperature surface cleaning of silicon and its application to silicon MBE,' J. Electrochem. Soc. **133**, 666 (1986).
- [4] Both ammonium hydroxide and hydrogen peroxide were 30% solutions.
- [5] W. Kern and D.A. Puotinen, 'Chemical solutions based on hydrogen peroxide for use in silicon semiconductor technology,' RCA Rev. **31**, 187 (1970).
- [6] D.J. Eaglesham, G.S. Higashi, and M. Cerullo, '370°C clean for Si molecular beam epitaxy using a HF dip,' Appl. Phys. Lett. **59**, 685(1991).
- [7] Y.J. Chabal, G.S. Higashi, K. Raghavachari, and V.A. Burrows, 'Infrared spectroscopy of Si(111) and Si(100) surfaces after HF treatment: hydrogen termination and surface morphology,' J. Vac. Sci. Technol. A **7**, 2104(1989).

- [8] T. Takahagi, I. Nagai, A. Ishitani, H. Kuroda, and Y. Nagasawa, 'The formation of hydrogen passivated silicon single-crystal surfaces using ultraviolet cleaning and HF etching,' J. Appl. Phys. **64**, 3516(1988).
- [9] S. Nikzad, S.S. Wong, C.C. Ahn, A.L. Smith, and H.A. Atwater, '*In situ* reflection electron energy loss spectroscopy measurements of low temperature surface cleaning for Si molecular beam epitaxy,' Appl. Phys. Lett. **63**, 1414(1993).
- [10] L.C. Feldman and J.W. Mayer, *Fundamentals of Surface and Thin Film Analysis*, North-Holland, New York, 1986.
- [11] P.K. Larsen, P.J. Dobson, J.H. Neave, B.A. Joyce, B. Bolger, and J. Zhang, 'Dynamic effects in RHEED from MBE grown GaAs(001) surfaces,' Surf. Sci. **169**, 176(1986).
- [12] C. Kittel, *Introduction to Solid State Physics*, 6th ed., Wiley, New York, 1986.
- [13] J.Y. Tsao, *Materials Fundamentals of Molecular Beam Epitaxy*, Academic Press, Boston, 1993.
- [14] D.J. Eaglesham, H.-J. Gossmann, and M. Cerullo, 'Limiting thickness h_{epi} for epitaxial growth and room temperature Si growth on Si(100),' Phys. Rev. Lett. **65**, 1227(1990).
- [15] N.M. Johnson, F.A. Ponce, R.A. Street, and R.J. Nemanich, 'Defects in single-crystal silicon induced by hydrogenation,' Phys. Rev. **B35**, 4166(1987).

- [16] H.P. Strunk, H. Cerva, and E.G. Mohr, 'Damage to the silicon lattice by reactive ion etching,' J. Electrochem. Soc. **135**, 2876(1988).
- [17] S.J. Jeng, G.S. Oehrlein, and G.J. Scilla, 'Hydrogen plasma induced defects in silicon,' Appl. Phys. Lett. **53**, 1735(1988).
- [18] S.B. Zhang and W.B. Jackson, 'Formation of extended hydrogen complexes in silicon,' Phys. Rev. B **43**, 12142(1991).
- [19] See, for example, F. Wooten, K. Winer, and D. Weaire, 'Computer-generation of structural models of amorphous Si and Ge,' Phys. Rev. Lett. **54**, 1392(1985).
- [20] G.R. Booker and R. Stickler, 'Crystallographic imperfections in epitaxially grown silicon,' J. Appl. Phys. **33**, 3281(1962).
- [21] B.E. Weir, B.S. Freer, R.L. Headrick, D.J. Eaglesham, G.H. Gilmer, J. Bevk, and L.C. Feldman, 'Low temperature homoepitaxy on Si(111),' Appl. Phys. Lett. **59**, 204(1991).
- [22] J.M. Gibson, H.-J. Gossmann, J.C. Bean, R.T. Tung, and L.C. Feldman, 'Preservation of a 7×7 periodicity at a buried amorphous-Si/Si(111) interface,' Phys. Rev. Lett. **56**, 355(1986).
- [23] J.A. Venables and G.L. Price in *Epitaxial Growth*, ed. J.W. Matthews, Academic Press, New York, 1975.
- [24] For a survey of estimates of epitaxial temperature, see H.-J. Gossmann and E.F. Schubert, 'Delta doping in silicon,' Crit. Rev. Sol. St. Mat. Sci. **18**, 1(1993).

- [25] See, for example, W.X. Ni, J. Knall, M.A. Hasan, G.V. Hansson, J.E. Sundgren, S.A. Barnett, L.C. Markert, and J.E. Greene, 'Kinetics of dopant incorporation using a low energy antimony ion beam during growth of Si(100) films by molecular beam epitaxy,' *Phys. Rev. B* **40**, 449(1989).
- [26] C.J. Tsai, P. Rozenak, H.A. Atwater, and T. Vreeland, 'Strain modification by ion-assisted molecular beam epitaxy in the $\text{Si}_x\text{Ge}_{1-x}$ alloy system – a kinetic analysis,' *J. Cryst. Gr.* **111**, 931(1991).
- [27] C.J. Tsai and H.A. Atwater, 'Suppression of island formation during initial stages of Ge/Si(100) growth by ion-assisted molecular beam epitaxy,' *Mat. Res. Soc. Symp. Proc.* **268**, 127(1992); *J. Vac. Sci. Technol.*, to be published.
- [28] C.H. Choi, R. Ai, and S.A. Barnett, 'Suppression of 3-dimensional island nucleation during GaAs growth on Si(100),' *Phys. Rev. Lett.* **67**, 2826(1991).
- [29] R.A. Zuhr, B.R. Appleton, N. Herbots, B.C. Larson, T.S. Noggle, and S.J. Pennycook, 'Low temperature epitaxy of Si and Ge by direct ion beam deposition,' *J. Vac. Sci. Technol. A* **5**, 2135(1987).
- [30] K.G. Orrman-Rossiter, A.H. Al Bayati, D.G. Armour, S.E. Donnelly, and J.A. Van den Berg, 'Ion beam deposited epitaxial thin silicon films,' *Nucl. Instr. Meth. B* **59**, 197(1991).

- [31] G.K. Wehner, R.M. Warner, Jr., P.D. Wang, and Y.H. Kim, 'Substituting low energy (< 30 eV) ion bombardment for elevated temperature in silicon epitaxy,' J. Appl. Phys. **64**, 6754(1988).
- [32] T. Ohmi, T. Ichikawa, H. Iwabuchi, and T. Shibata, 'Formation of device-grade epitaxial silicon films at extremely low temperatures by low energy bias sputtering,' J. Appl. Phys. **66**, 4756(1989).
- [33] D.L. Smith, C.-C. Chen, G.B. Anderson, and S.B. Hagstrom, 'Enhancement of low temperature critical epitaxial thickness of Si(100) with ion beam sputtering,' Appl. Phys. Lett. **62**, 570(1993).
- [34] E. Chason, P. Bedrossian, K.M. Horn, J.Y. Tsao, and S.T. Picraux, 'Ion beam enhanced epitaxial growth of Ge(001),' Appl. Phys. Lett. **57**, 1793(1990).
- [35] E. Chason, J.Y. Tsao, K.M. Horn, S.T. Picraux, and H.A. Atwater, 'Surface roughening of Ge(001) during 200 eV Xe ion bombardment and Ge molecular beam epitaxy,' J. Vac. Sci. Technol. **A8**, 2507(1990).
- [36] W.K. Chu, J. W. Mayer, and M.A. Nicolet, *Backscattering Spectrometry*, Academic Press, New York, 1978.
- [37] H.-J. Gossmann, P. Asoka-Kumar, T.C. Leung, B. Nielsen, K.G. Lynn, F.C. Unterwald, and L.C. Feldman, 'Point defects in Si thin films grown by molecular beam epitaxy,' Appl. Phys. Lett. **61**, 540(1992).
- [38] R.G. Wilson, F.A. Stevie, and C.W. Magee, *Secondary Ion Mass Spectrometry: A Practical Handbook for Depth Profiling and Bulk Impurity Analysis*, Wiley, New York, 1989.

- [39] M. Copel and R.M. Tromp, 'H-Coverage dependence of Si(001) homoepitaxy,' Phys. Rev. Lett. **72**, 1236(1994).
- [40] Y.W. Mo, J. Kleiner, M.B. Webb, and M.G. Lagally, 'Activation energy for surface diffusion of Si on Si(001) - a scanning tunneling microscopy study,' Phys. Rev. Lett. **66**, 1998(1991).
- [41] J. Villain, 'Continuum models of crystal growth from atomic beams with and without desorption,' J. Phys. I **1**, 19(1991).
- [42] D.P. Adams, S.M. Yalisove, and D.J. Eaglesham, 'Effect of hydrogen on surface roughening during Si homoepitaxial growth,' Appl. Phys. Lett. **63**, 3571(1993).
- [43] T. Vasek and M.G. Lagally, presented at the American Vacuum Society Meeting, Orlando, 1993.
- [44] A. Zangwill, private communication.
- [45] D.D. Perovic, G.C. Weatherly, P.J. Simpson, P.J. Schultz, T.E. Jackman, G.C. Aers, J.P. Noël, and D.C. Houghton, 'Microvoid formation in low temperature molecular beam epitaxy grown silicon,' Phys. Rev. **B43**, 4257(1991).
- [46] H. Schut, A. Van Veen, G.F.A. VandeWalle, and A.A. Vangorkum, 'Positron beam defect profiling of silicon epitaxial layers,' J. Appl. Phys. **70**, 3003(1991).
- [47] D.P. Woodruff, *The Solid-Liquid Interface*, Cambridge University Press, London, 1973.

- [48] H. Jorke, H.J. Herzog, and H. Kibbel, 'Kinetics of ordered growth of Si on Si(100) at low temperatures,' *Phys. Rev. B* **40**, 2005(1989).
- [49] H. Jorke, H. Kibbel, F. Schaffler, and H.J. Herzog, 'Low temperature kinetics of Si(100) MBE growth,' *Thin Sol. Fi.* **183**, 307(1989).
- [50] D.J. Eaglesham, F.C. Unterwald, H. Luftman, D.P. Adams, and S.M. Yalisove, 'Effect of H on Si molecular beam epitaxy,' *J. Appl. Phys.* **74**, 6615(1993).
- [51] G. Xue, H.Z. Xiao, M.A. Hasan, J.E. Greene, and H.K. Birnbaum, 'Critical epitaxial thickness for low temperature (20 – 100°C) Ge(100)-2×1 growth by molecular beam epitaxy,' *J. Appl. Phys.* **74**, 2512(1993).
- [52] E. Kaxiras and J. Erlebacher, 'Adatom diffusion by orchestrated exchange on semiconductor surfaces,' *Phys. Rev. Lett.* **72**, 1714(1994); E. Kaxiras, private communication.
- [53] K. Takayanagi, Y. Tanishiro, S. Takahashi, and M. Takahashi, 'Structure analysis of Si(111)-7×7 reconstructed surface by transmission electron diffraction,' *Surf. Sci.* **164**, 367(1985).
- [54] H. Nakahara and A. Ichimiya, 'Structural study of Si growth on a Si(111)7×7 surface,' *Surf. Sci.* **241**, 124(1991).

Chapter 3

LOW ENERGY ION IRRADIATION OF SILICON – A MOLECULAR DYNAMICS INVESTIGATION

And here – ah, now, this really is something a little recherché.

– Sherlock Holmes, The Musgrave Ritual

Sir Arthur Conan Doyle

3.1 Introduction

An atomistic view of film growth, ion-solid interactions or any other physical process has always been an important goal of condensed matter physics. A lot of knowledge regarding atomic structure and dynamics has been gained over

the years through techniques such as X-ray diffraction, electron microscopy, ion scattering, and infrared and microwave spectroscopies. With the advent of the scanning tunneling microscope and other scanning probe techniques, this knowledge base has rapidly increased. This serves as a base both for constructing models and verifying theoretical predictions.

There are a whole range of computational techniques which one can use to study a given problem. These include kinetic Monte Carlo simulations where the atoms are allowed to move between sites with certain rates, classical molecular dynamics where the atomic motion is governed by a classical potential and techniques which treat the electronic structure of atoms at various levels of approximation – tight binding approximation, local density approximation and *ab initio* theory. Here, we are primarily interested in determining the mechanisms of film growth and the influence of low energy ion irradiation. These processes occur on a time scale and crystal size scale that is beyond the scope of a first principles calculation on today's computers. A classical molecular dynamics technique seems the best approach to understand the physics of these processes.

Molecular dynamics simulations are generally limited to small ensembles ($10^3 - 10^4$) of atoms and short durations, typically a few picoseconds. To compare the simulation results with an experiment, one must average over all variables that are also averaged by a given experiment or measurement. These include the impact parameter, energy and angular spread in the incident beam for an ion-solid collision.

3.2 Interatomic Potential for Silicon

3.2.1 The Tersoff Potential

In classical molecular dynamics, the atoms are considered as point masses whose trajectories are obtained by solving Newton's equations of motion. The atoms respond to an interatomic potential which may be a function of the distance between atoms, angle between a pair of bonds, etc. The set of differential equations can be written as

$$\frac{d\mathbf{r}_i(t)}{dt} = \mathbf{v}_i(t) \quad (3.1)$$

$$M_i \frac{d\mathbf{v}_i(t)}{dt} = \mathbf{F}_i(\mathbf{r}_i(t)) \quad (3.2)$$

where

$$\mathbf{F}_i = -\nabla \left(\sum_{i < j} \Phi_{ij} \right) \quad (3.3)$$

and Φ_{ij} is the potential energy between the pair of atoms i and j . Here, $\mathbf{r}_i(t)$ and $\mathbf{v}_i(t)$ are the position and velocity of atom i at time t . The force \mathbf{F}_i on atom i is given by the gradient of the interatomic potential.

Silicon has the diamond cubic structure with strongly directional bonding. A two-body potential $V(r)$ depending only the separation r between atoms cannot be used to describe such a structure. For a two-body interatomic potential, the hexagonal close-packed (hcp) structure has the minimum energy. Hence, an interatomic potential to describe silicon must at least have a

three-body term. Several interatomic potentials have been developed to describe silicon and other semiconductors. These include the Keating potential [1, 2], the Biswas-Hamann potential [3], the Stillinger-Weber potential [4], the Dodson potential [5] and the Tersoff potential [6]. The Keating potential expresses the potential energy in terms of the elastic constants. It has been used with considerable success to study the ordering in III-V alloy semiconductors [7]. Since the potential uses the harmonic oscillator approximation, deviations far from the equilibrium position are not well described.

A central feature of cascade dynamics is the numerous overcoordinated and undercoordinated configurations in which the atoms are found. The chosen interatomic potential must be able to describe not only the atomic interactions near the equilibrium position, but also the low- and high-density regions occurring in a collision cascade. The other potentials mentioned above were developed by fitting to positions far from equilibrium such as point defects, polytypes and surfaces.

For the molecular dynamics simulations described here, the Tersoff potential [6] was used to describe silicon. The potential energy between a pair of atoms is written as

$$V = \sum_{i < j} \Phi_{ij} \quad (3.4)$$

$$\Phi_{ij} = \{ A \exp(-\lambda_1 r_{ij}) - B_0 \exp(-\lambda_2 r_{ij})(1 + \beta^\eta \zeta_{ij}^\eta)^{-\delta} \} f_c(r_{ij}) \quad (3.5)$$

where

$$\zeta_{ij} = \sum_{k \neq i,j} f_c(r_{ik}) \left[1 + \frac{c^2}{d^2} - \frac{c^2}{d^2 + (h - \cos\theta_{jik})^2} \right] \exp[\alpha(r_{ij} - r_{ik})^3] \quad (3.6)$$

and

$$f_c(r_{ij}) = \begin{cases} 1 & , r_{ij} < R - D \\ \frac{1}{2} - \frac{1}{2} \sin\left(\pi \frac{r_{ij} - R}{2D}\right) & , R - D < r_{ij} < R + D \\ 0 & , r_{ij} > R + D \end{cases} \quad (3.7)$$

The interatomic potential thus consists of a many-body term attached to a Morse-type potential [8]. The potential energy between atoms i and j thus depends on their separation r_{ij} and on the position of a third atom k through the r_{ik} and θ_{jik} terms. Note that the potential is not symmetric, $\Phi_{ij} \neq \Phi_{ji}$. It can be made symmetric by defining $\overline{\Phi}_{ij} = (\Phi_{ij} + \Phi_{ji})/2$. Also, the potential has a many-body term and not a three-body term. The potential energy is cutoff at a distance of $R + D = 3.00 \text{ \AA}$ so that an atom interacts only with its first nearest neighbors. This is necessary to speed up the computation. The parameters in the potential are listed in Table 4.1 in Section 4.2.

3.2.2 Description of Silicon

The interatomic potential (eq. 3.4 – 3.7) was fitted to the various high pressure phases of silicon based on the pseudopotential calculations in Ref. [9]. The diamond structure has the minimum energy among all the phases. The cohesive energy per atom and the bond length are 4.63 eV and 2.35 Å respectively, in agreement with experimental values [10]. The radial distribution function of the amorphous state is also in good agreement with experiment.

The (2×1) reconstruction on the Si(001) surface is well described. The atomic rearrangement due to the reconstruction is shown in Fig. 3.1. The top layer relaxes inward by about 15% and the dimer bond length is 2.37 Å. The dimer bond length has been estimated as 2.51 Å in *ab initio* cluster calculations [11]. The energies of the vacancy and some interstitial sites are close to the first principles calculations.

There are limitations to the potential, some of which are mentioned here. The various reconstructions (2×1 , 5×5 and 7×7) on the Si(111) surface are not well described. The potential predicts that the unreconstructed (1×1) surface has the minimum energy whereas a 7×7 structure is observed experimentally after a high temperature anneal. Due to the neglect of interactions beyond the first nearest neighbor, the energy of a stacking fault (and also $\Sigma 3$ coherent twin boundaries) is zero. Therefore, the energy of both the diamond cubic structure and the wurtzite structure is the same. The melting point of silicon is predicted as 2550 K [12] whereas the experimental value is 1685 K [10].

The size and shape of small clusters is also not well described. The bond length in the Si_2 dimer is 2.30 Å whereas first principles calculations give a value of 2.24 Å [13]. Another example is the Si_4 cluster which has been shown (experimentally) to be planar in the shape of a rhombus [14].

Overall, the Tersoff potential does a fairly good job of describing silicon. One can obtain a qualitative picture of a phenomenon using the potential.

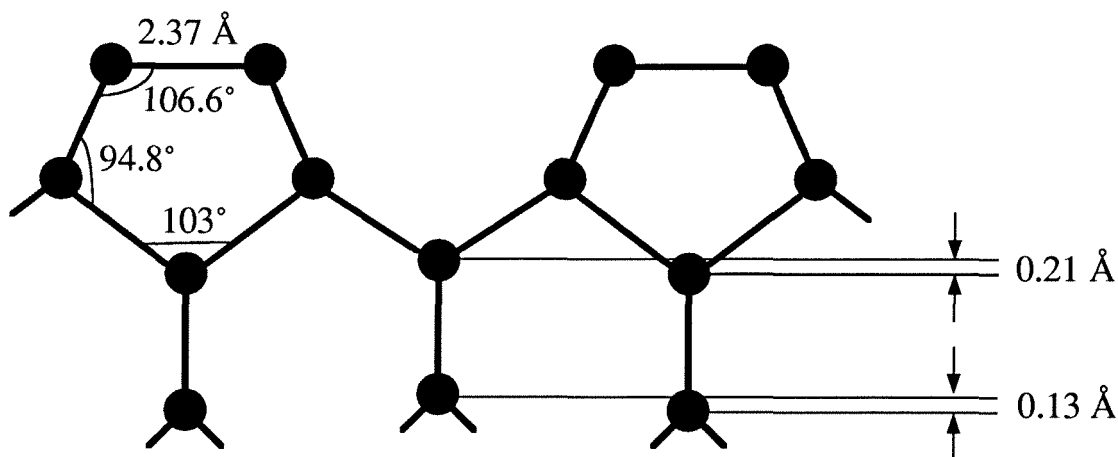


Figure 3.1: The (2×1) reconstructed Si(001) surface viewed along the $\langle 110 \rangle$ axis according to the Tersoff potential.

3.3 Numerical Methods

3.3.1 The Algorithm

The equations of motion (eq. 3.1 – 3.2) have to be solved numerically. A flow chart of the algorithm is shown in Fig. 3.2. The main aspects of the algorithm are a technique for determining all the neighbors of an atom, computation of forces on all atoms and a numerical method for solving the differential equations. The neighbors of an atom were determined by the link cell method. The Runge-Kutta-Nyström method [15] was used to solve the differential equations. An adaptive step size was used to achieve the optimal speed. These are discussed in more detail in the subsequent subsections.

The computer program SIH for molecular dynamics simulations of Si and H atoms was written in the C language and is listed in Appendix C. Two workstations, a DEC3100 and an IBM RS6000/340, were used for performing

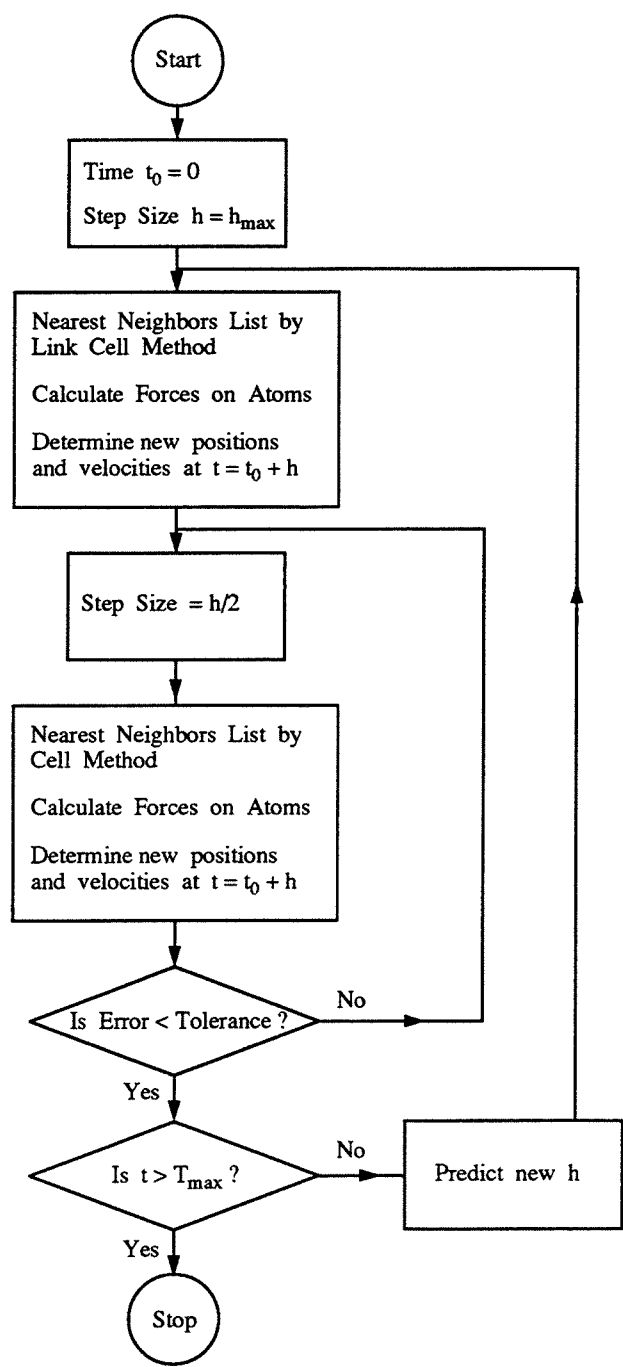


Figure 3.2: Flow chart showing the major steps in the molecular dynamics code.

Table 3.1: The speed of operation of molecular dynamics codes.

Machine	Speed of operation (ms/atom-timestep)	No. of function evaluations/timestep	Ref.
DEC3100	8.60	5	this work
RS6000/340	1.70	5	this work
CRAY YMP C90	0.08	1	[16]
Special Purpose Computer	0.40	1	[17]

the simulations. The speed of a program is best described by specifying the time required per atom per timestep. This is listed in Table 3.1. An optimum speed of 1.7 ms/atom-timestep was achieved on the RS6000/340 workstation with the Tersoff interatomic potential. The speed dropped to about 1.9 ms/atom-timestep when the Si-H and H-H interatomic potentials were included. These are compared to the values of 0.08 ms/atom-timestep in Ref. [16] on the Cray YMP and 0.40 ms/atom-timestep in Ref. [17] on a special purpose computer. Both of these references used the Stillinger-Weber potential [4]. It is noted that the Runge-Kutta-Nyström method with the adaptive step size used in our simulations requires five function evaluations per timestep whereas the Refs. [16] and [17] used a 4th order predictor-corrector method and the Verlet method [18] respectively which requires only one function evaluation per timestep. If this factor is included, it is seen that the speed of the code on the RS6000 compares favorably with the Cray YMP and the special purpose computer which are inherently faster machines.

3.3.2 The Runge-Kutta-Nyström Method

There are several techniques for solving a system of ordinary differential equations, and the method chosen is usually a compromise between accuracy and speed. The accuracy is determined by the order of the method. A higher order method gives more accuracy but also requires more function (in our case, forces on atoms) evaluations.

There are three classes of methods for solving ordinary differential equations numerically — Runge-Kutta methods, predictor-corrector methods and extrapolation methods [15]. For a given order of the method, predictor-corrector methods require the minimum number of function evaluations. However, there are two problems with these methods. For an n^{th} order method, the knowledge of the atom positions over the past n steps is required. Typically in a molecular dynamics simulation, one only knows the positions and velocities at the start, $t = 0$. This can be overcome by using the Runge-Kutta method to generate the first n values. The other problem with these methods is that it is rather hard to develop an adaptive step size. We will see that this is an important attribute of a numerical method. With Runge-Kutta methods, one only needs the positions and velocities at $t = 0$ to predict the corresponding values at $t = h$. This is done by evaluating the function at several strategic points. An adaptive step size can be easily developed for these methods. However, for a given order of integration, these methods require higher number of function evaluations.

The third order Runge-Kutta-Nyström (RKN) method was used to solve the differential equations [15]. This was combined with Richardson extrapo-

lation to achieve adaptive step size control [15, 19]. The RKN method takes advantage of the fact that the potential is velocity- and time-independent. The third order is achieved with just two function evaluations. This method is described here for a simple second order differential equation [15]:

$$y''(t) = f(y) \quad (3.8)$$

The position (y) and velocity (y') are known at time $t = t_0$. This information is used to evaluate the new values at $t = t_0 + h$ as follows:

$$k_1 = \frac{2}{3}y'(t_0) + \frac{2}{9}y''(t_0)h \quad (3.9)$$

$$k_2 = y'(t_0) + \frac{1}{4}(y''(t_0) + y''(t_0 + k_1h))h \quad (3.10)$$

$$l_1 = \frac{1}{4}y''(t_0) + \frac{3}{4}y''(t_0 + k_1h) \quad (3.11)$$

$$y(t_0 + h) = y(t) + k_2h \quad (3.12)$$

$$y'(t_0 + h) = y'(t) + l_1h \quad (3.13)$$

Adaptive step size control is achieved by estimating the error in the above calculation. Since the RKN method is of third order, an expansion of the form

$$y^*(t_0 + h) = y(t_0 + h) + a_3(t_0)h^3 + a_4(t_0)h^4 + \dots \quad (3.14)$$

holds where the error has been expanded in a Taylor series. Here, $y^*(t_0 + h)$ and $y(t_0 + h)$ are the true and estimated values of $y(t)$ at $t = t_0 + h$. The error is estimated by calculating the value of $y(t_0 + h)$ in two ways: the first, y_1 , with a step size of h and the second, y_2 , with two steps of size $h/2$. Now, we assume that the error ϵ is dominated by the $a_3 h^3$ term and hence is given by

$$\epsilon = \left| \frac{y_2 - y_1}{7} \right| \quad (3.15)$$

If this error is below a certain preset tolerance, the present step size is accepted. Otherwise, the step size is halved to $h/2$ and the procedure repeated. If the step is successful, the next step size is *predicted* using the value of ϵ [19]:

$$h^{\text{new}} = \max \left\{ h \left(\frac{\theta h \tau}{\epsilon} \right)^{\frac{1}{p}}, h_{\min} \right\} \quad (3.16)$$

where τ is the tolerance per unit step and θ is a constant. The minimum step size is taken as h_{\min} . For a system of differential equations, the maximum value of ϵ is used. Frequently, one also limits the maximum value of the step size. In our case, we could keep the step size below a quarter of the fundamental vibrational period of the atoms.

Finally, this can also be used to get an improved estimate of $y(t_0 + h)$, often called *active extrapolation* [19]:

$$y^{\text{new}}(t_0 + h) = y_2 + \frac{y_2 - y_1}{7} \quad (3.17)$$

Note that this correction makes the RKN method with Richardson extrapolation a fourth-order method.

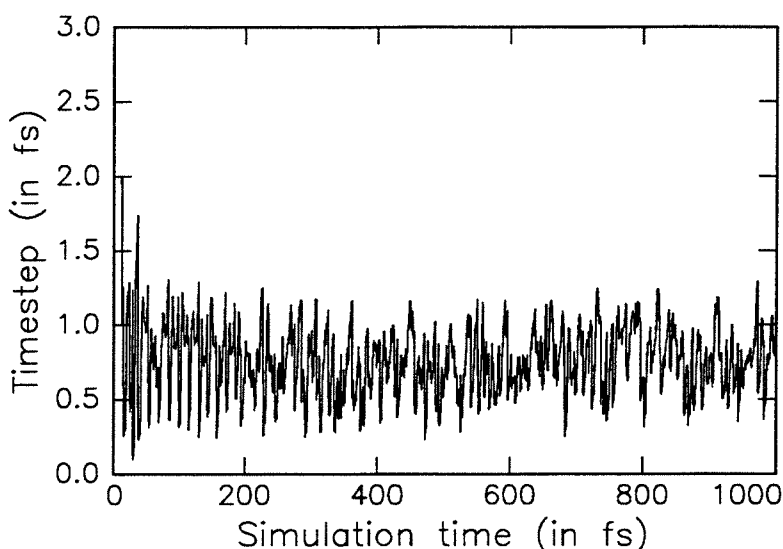


Figure 3.3: The variation in step size during a simulation of a 10 eV Si atom incident on a dihydride-terminated Si(001) surface.

In the molecular dynamics simulations with the many-body interatomic potential, a value of $\theta = 0.7$ was found to give a reasonable prediction of the step size without being too optimistic. A high value of θ can result in an increased rejection of the step size resulting in more computation time.

The RKN method with Richardson extrapolation thus requires five function evaluations per timestep. Since this is 2-1/2 times larger than the RKN method alone, this is profitable only if the step size variations during a simulation are large. This was indeed the case in many ion-solid collisions. The step size variation during a 1 ps simulation of a 10 eV Si atom incident on a dihydride-terminated Si(001) surface is shown in Fig. 3.3. We see that the step size changes significantly during a simulation.

3.3.3 The Link Cell Method

For determining the potential energy or interatomic forces, all the neighbors of an atom within the cutoff distance must be known. A direct way of making such a list is to compute the distance to all atoms and compare it with the cutoff distance. This method, sometimes called the Verlet method [18], is of $O(N^2)$ where N is the number of atoms.

An alternate way is to divide the space into cubes, each side equal to the cutoff distance. Each atom is assigned the address of the cube in which it resides. Then, an atom will interact only with other atoms in the same cube and the nearest neighbor cubes. This reduces the search to a great extent. This method is of $O(N)$.

For many-body potentials, it is essential to store the location of all the atoms within the cutoff distance of a given atom in an array. After the computation of the two-body terms, one can use the stored information for calculating the three- and many-body terms.

3.3.4 The Cutoff Function

The interatomic potential is usually terminated at a certain distance to speed up the computation. A cutoff function, $f_c(r)$, is used to make the potential vanish after a certain distance. The cutoff function in eq. 3.7 is frequently used. This function is continuous and has a continuous first derivative at the boundaries, $r = R - D$ and $R + D$. It was observed that a better energy and momentum conservation could be achieved by going to a higher order cutoff

function.

$$f_c(r) = \begin{cases} 1 & , r < R - D \\ \frac{1}{2} - \frac{9}{16}\sin(\pi\frac{r-R}{2D}) + \frac{1}{16}\sin(3\pi\frac{r-R}{2D}) & , R - D < r < R + D \\ 0 & , r > R + D \end{cases} \quad (3.18)$$

This function with two sinusoidal terms has a continuous third derivative at the cutoff points. The additional computational expense is minimal, since at any given time the fraction of atom pairs within the cutoff region is quite low.

A general n^{th} order cutoff function $g_n(x)$ can be obtained from

$$g_n(x) = 1 - \int_0^x \sin^n t \, dt \quad (3.19)$$

This gives a function between 0 and π and can be scaled and translated to the desired region. It is noted that the cutoff function introduces an artificial barrier centered at $x = R$, and this becomes more pronounced as the order of the function increases.

3.3.5 Boundary Conditions

The number of atoms used to describe a crystal is limited by the computing resources available. Typically, $10^3 - 10^4$ atoms are used in a simulation of low energy ion-solid interactions. For silicon, this corresponds to a cube of side 3 – 5 nm. A small size of the crystallite can introduce artifacts such as reflection of energy at the edges and surfaces, distortion due to reconstruction and relaxation of the surfaces, etc. The distortion of the crystallite

is circumvented by using periodic boundary conditions in the transverse directions. The bottom two layers of the crystal were also held rigid in some simulations. The size of the crystallite was chosen to be sufficiently large to reduce the influence of energy reflections.

3.4 Low Energy Ar^+ Ion Irradiation of Smooth and Rough Silicon Surfaces

3.4.1 Energy Loss of Ions

There is no detailed information available about how ion irradiation affects the surface kinetics. The energy loss of ions in solids is frequently divided, for sake of convenience, into electronic and nuclear energy losses. For ion energies exceeding a few keV, there are “universal” expressions for the energy loss which give reasonable predictions of the range and straggle for most ion-target combinations [20]. Scattering of the ion is considered in the binary collision approximation, in which the ion interacts with one target atom at a time. Two commonly used programs are TRIM [21, 22] and MARLOWE [23]. The binary collision approximation cannot be applied at low energies where many-atom collisions become important. A molecular dynamics (MD) simulation where the interaction of each atom with all other atoms is taken into account can provide a better description of the collision cascade. At present there are no good models to determine what fraction of the ion energy is channeled into the electronic energy loss, even though several inelastic or

electronic events can occur in a low energy ion-solid collision. Events such as neutralization of the incident ion, atom excitation, secondary and Auger electron emission, surface and bulk plasmon excitation and electron-hole pair creation are considered to be electronic energy loss components. Energy loss by creation of phonons is also considered as an electronic energy loss component. Atomic displacements in the surface and bulk, and sputtering, are considered as nuclear energy loss components. It should be mentioned that such classification is only for convenience. An example where such a classification becomes difficult is chemical sputtering, i.e., an enhancement in the sputtering yield with the use of a reactive ion beam. The computation of electronic energy loss of ions requires a first principles calculation. With classical molecular dynamics simulations, one can only study the damage produced by the ions and the energy loss to lattice vibrations (“heat”) or phonons. Nevertheless, this provides a qualitative picture of the influence of ion bombardment.

3.4.2 Simulation Description

A growing Si film does not remain smooth at low temperatures. Surface roughness was one of the central features in low temperature silicon homoepitaxy and is especially clear from the AFM images and RHEED patterns in Section 2.7.3. It was also shown that the principal effect of concurrent low energy Ar^+ ion irradiation during growth was surface smoothing.

Previous MD studies of silicon include initial stages of epitaxy [24], direct ion-beam deposition [25], sputtering by keV range Ar^+ ions [26] and obser-

vation of surface channeling on Si(111) [27]. These studies have employed idealized atomically smooth (001) or (111) surfaces. For real surfaces subject to ion bombardment at energies near the displacement threshold, some or all of the effects of ion bombardment could occur preferentially at certain surface “defect” structures. These include ledges, kinks, dimer strings and 3D islands with different facets (i.e., local surface orientations). A better understanding of the principal effects of ion bombardment can be gained by studying the interactions of the ion with a surface containing the above-mentioned structures.

Ion beam-induced defect production was estimated from a smooth (2×1) reconstructed Si(001) surface, a dimer pair and the center and the edge of a dimer string placed on Si(001). The choice of these structures was guided by the scanning tunneling microscope images of reconstructed Si(001) surfaces [28]. There are, in principle, several choices for the position of these defect structures on the Si(001) surface. The positions shown in Fig. 3.4 correspond to configurations with minimum energy calculated using the Tersoff potential and these were used for studying the effects of ion bombardment.

Recent experimental [29] and theoretical [30, 31, 32, 33] studies indicate that single adatoms are highly mobile at $T \geq 300$ K. Adatom diffusion is also highly anisotropic, the fast direction being along the dimer rows. The activation energy and prefactor for single adatom diffusion have been estimated to be 0.67 eV and 10^{-3} cm²/s respectively [29]. Two atoms, as in a dimer pair, form a stable cluster on Si(001) [28]. At typical ion fluxes employed in experiments ($\sim 10^{13} - 10^{16}$ cm⁻²s⁻¹), the interarrival time of ions is very large compared to the lifetime of an adatom. During ion irradiation, the

probability of striking an adatom becomes significant only at $T \leq 300$ K.

The Tersoff potential (Section 3.2.1) was used to model silicon. For the simulations described below, a sharp cutoff at 3.20 \AA was used ($f_c(r) = 1$, $r < 3.20 \text{ \AA}$ and $f_c(r) = 0$, $r > 3.20 \text{ \AA}$). The Ar-Si interaction was taken to be purely repulsive,

$$V_{\text{Ar-Si}} = A \exp(-\lambda r) \quad (3.20)$$

with $A = 1830.8 \text{ eV}$ and $\lambda = 2.00 \text{ \AA}^{-1}$. The potential had a sharp cutoff at 4.00 \AA . Note that the value of A is the same as that of the Tersoff potential and the value of λ_1 has been scaled to approximately reflect the radius of the Ar^+ ion. The principal idea was to impart some energy to the surface through an ion and study its evolution.

In the simulations, ions were incident at 45° with respect to the substrate normal and along the $[110]$, $[\bar{1}10]$ and $[100]$ directions as indicated by the arrows in Fig. 3.4. Five different ion energies – 10, 15, 20, 35 and 50 eV were employed. A total of 102 simulations were carried out for each energy with each structure. The incident ion impact points were chosen at random within the rectangle drawn around each structure in Fig. 3.4. For the smooth Si(001) surface, the impact parameter range is the (2×1) unit cell. The average and the standard deviation of the impact parameter along with the size of the simulation crystallite for each of the structures is shown in Table 3.2. We see that these are sufficiently close to make a fair comparison. The initial substrate temperature was 0 K and simulations were carried out for a period of 1.0 ps.

In the simulation results described below, the layer containing the atoms

Table 3.2: Impact parameters used with different surface defect structures.

Surface structure	Crystallite size (in unit cells)	Average (nm)	Impact parameter	
			Standard deviation (nm)	Measured with respect to atoms in the
Smooth Si(001)	6×6×6	0.116	0.056	(2×1) cell
Dimer pair	6×6×6	0.130	0.064	placed dimer
Dimer string edge	8×8×6	0.112	0.052	placed dimers
Dimer string center	8×8×6	0.115	0.059	placed dimers

placed on the (2×1) surface is referred to as layer 0, the (2×1) surface is referred to as layer 1, the one below it as layer 2, and so on up to layer 24.

3.4.3 Simulation Results

The typical events observed in a collision cascade include production of atomic displacements, interstitials and sputtered atoms. Our criterion for an atomic displacement is met if there is no Si atom within the hard sphere radius, i.e., a sphere of radius equal to half the equilibrium Si-Si bond length, within the original lattice site. Figure 3.5 shows the evolution of total displacement yield with time for 10–50 eV ions incident on smooth Si(001)-2×1 surface. The displacement yield rises rapidly in the initial stages and then falls, first rapidly and then gradually due to replacement collisions and atoms getting back into their original positions. Figure 3.6 shows the total displacement yield observed at different ion energies for the different structures. The results here are all averaged over 102 simulations. With 10 eV ions, the yields from the different ions are spread over a wide range. At higher energies, sur-

face displacements constitute a smaller fraction of the total displacements and the surface defect structure is expected to have a smaller effect on the collision cascade. This results in a steady decline in the difference in yield between the different defect structures with increase in energy. The bulk displacement yield E_D for Si is often taken to be 14 eV. The large spread in the calculated displacement yields for the different structures at 10 eV is consistent with this estimate.

Figure 3.7(a) – (d) shows the depth distribution of displacements in the crystal. With 10 eV ions, the displacements are almost exclusively confined to the defect layer (layer 0). For ions incident on smooth Si(001), displacement yields greater than 0.05 were observed up to the third, fourth and fifth layers with 20, 35 and 50 eV ions, respectively. It should be noted that the number of displacements in layer 0 can be at most two for the dimer pair. Also, these displacement yields were observed at the end of the simulation period of 1 ps. The substrate temperature will determine the annealing dynamics and, hence, any observable defect generation on a laboratory timescale [34]. The calculated difference in yields from the different defect structures at low energies indicate that surface displacement yields are site specific, and any experimental determination of threshold energies must account for this fact.

Sputtering of silicon atoms was not observed from any of the structures in the energy range considered. An extrapolation of the experimental values of the sputtering yield of silicon with argon ions gives a value of ~ 0.01 for 50 eV ions [35]. In Chapter 4, we will see that the sputtering yield from a hydrogen-terminated silicon surface can be very different.

A useful figure-of-merit for the effect of ion irradiation is the surface-to-

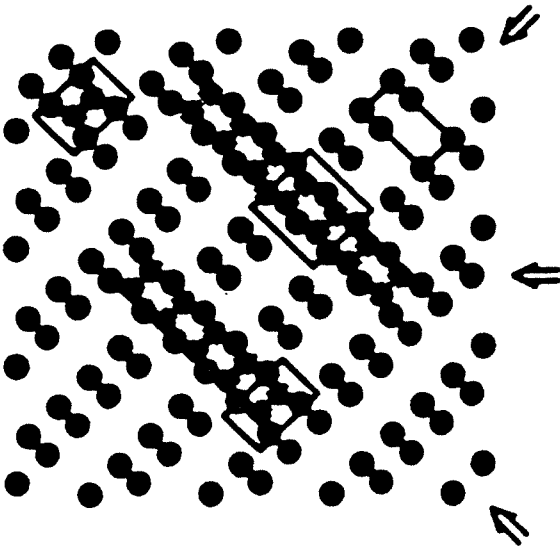


Figure 3.4: The three defect structures placed on the Si(001) surface. The rectangles drawn around each structure indicate the area in which the ions were incident. All ions were incident at 45° with respect to the surface normal and the arrows indicate the azimuths.

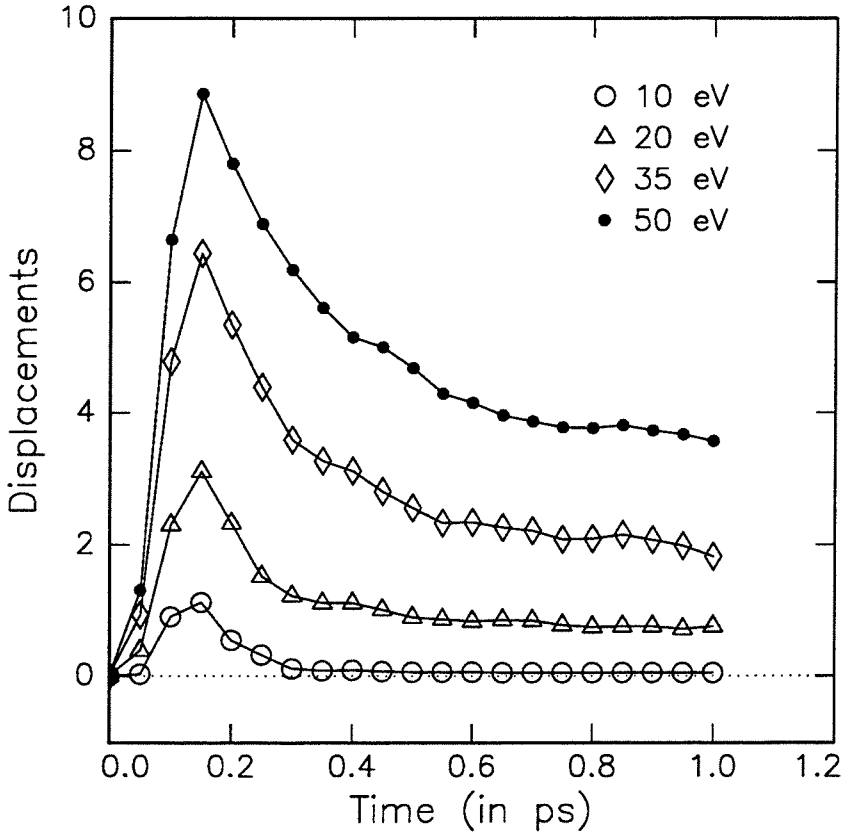


Figure 3.5: The time evolution of displacement yield for argon ions incident on smooth Si(001)-2x1 surface. The lines are spline fits to guide the eye.

bulk displacement ratio, R [36]. Here, the surface is taken as layer 0 and the rest of the crystal is taken as the bulk. Figure 3.8(a) shows the ratio R from the different defect structures. The ratio changes from about 2 – 3 for 20 eV ions to 0.6 – 0.8 for 50 eV ions. In Fig. 3.8(b), the number of broken dimers (only from the placed dimers) is shown for the different energies. A surface-to-bulk displacement ratio greater than unity is observed with ion energies less than 35 eV. The absolute number of displacements with 10 and 15 eV ions was too low to give a value of R without a large error.

A large surface-to-bulk displacement ratio is desirable because it may allow modification of surface kinetics without causing bulk damage. In Chapter 2, an increase in the epitaxial thickness was observed with the use of 50 and 70 eV Ar^+ ions. Better results were observed with 50 eV ions. The observed improvement in the crystalline quality was also a strong function of the substrate temperature. These observations suggest that at lower temperatures and higher energies, there is inadequate annealing of the “damage” produced by the ions. As mentioned in Chapter 2, RBS/channeling measurements and XTEM images have shown that the IAMBE films are free of extended defects. At very low temperatures, ions can amorphize the surface region. This is discussed in more detail in Chapter 5. Recently, successful epitaxy has been reported at temperatures around 300°C on both clean [37] and hydrogen-terminated [38] Si(001) surfaces by low energy bias sputtering. The best quality films were obtained with ion energies less than 30 eV.

In the simulations, observations of Si atom recoils show that, on average, they move only a lattice site or two from their original position after an ion impact. Comparison of the recoil atom trajectories and STM-derived kinetic

data on adatom diffusion [29] clearly show that the thermal migration of single adatoms dominates any ion induced migration at $T \geq 300$ K. This suggests that ion irradiation does not enhance the migration component of diffusion except for ion incidence along special surface channeling directions [27]. The most important effect of ion irradiation is the beam-induced creation of single adatoms, which corresponds to the provision of the adatom formation energy (ledge-terrace desorption energy or dimer-breaking energy). This can produce smoother surfaces if adatoms produced by breaking 2D and 3D islands can migrate to the step edge. The simulations and the AFM images in Chapter 2 are suggestive of such a mechanism in ion beam-assisted molecular beam epitaxy.

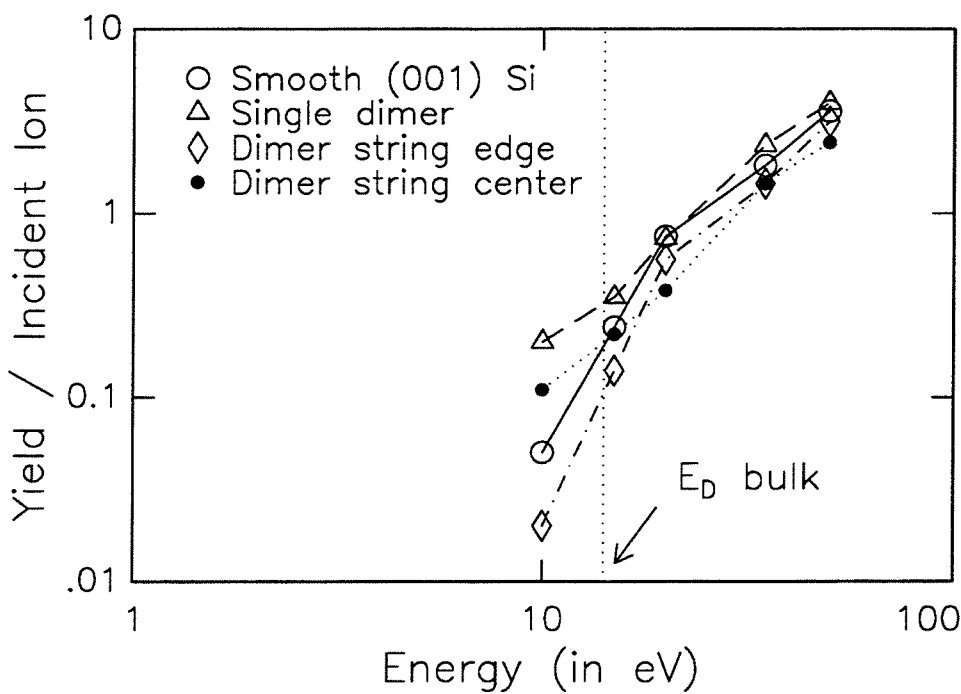


Figure 3.6: The total displacement yield vs. energy for the defect structures. The lines are spline fits to guide the eye.

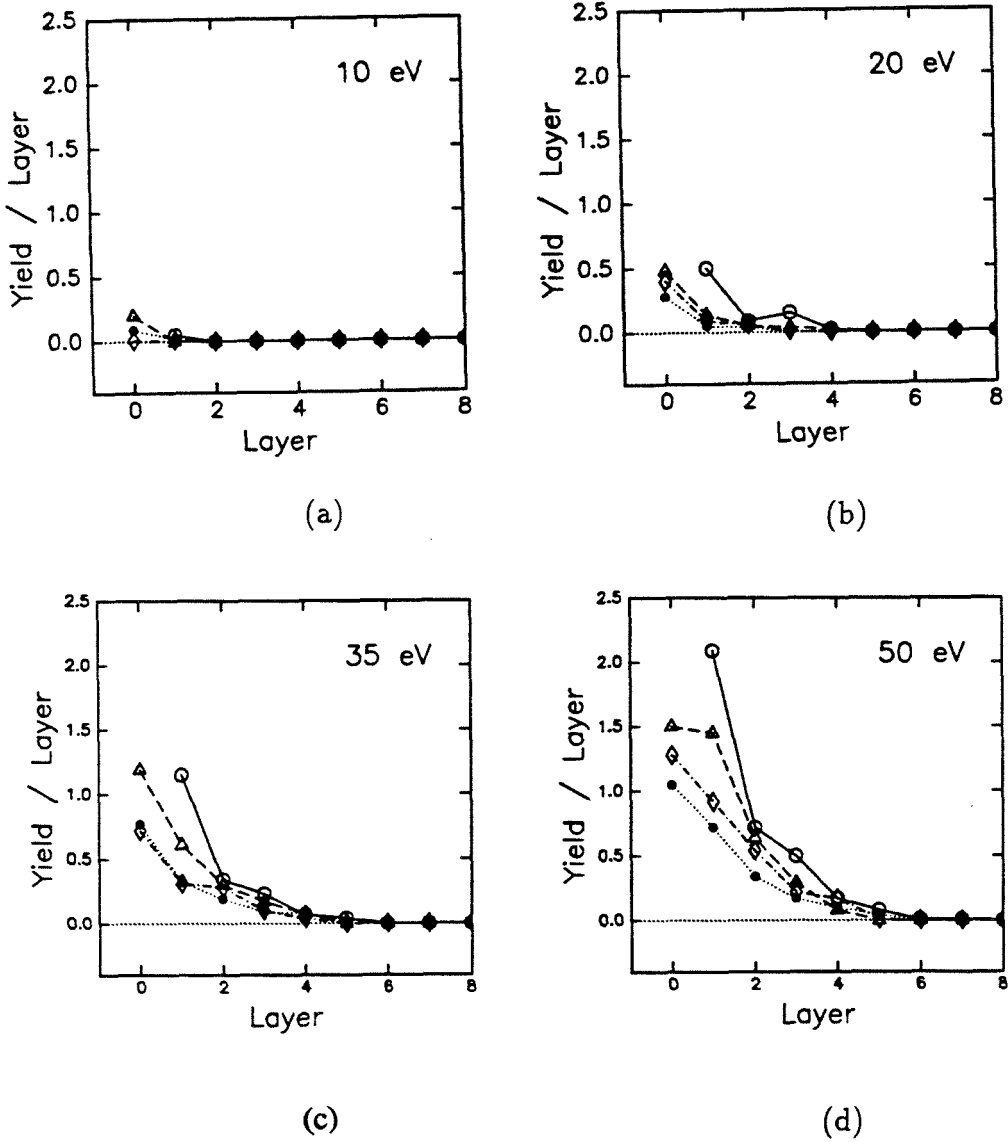


Figure 3.7: The distribution of displacements in the substrate at (a) 10 eV, (b) 20 eV, (c) 35 eV, and (d) 50 eV. The four symbols refer to smooth Si(001) (\circ), dimer pair (Δ), dimer string edge (\diamond), and dimer string center (\bullet). Displacements in layer 0 are those from the defect placed on the surface.

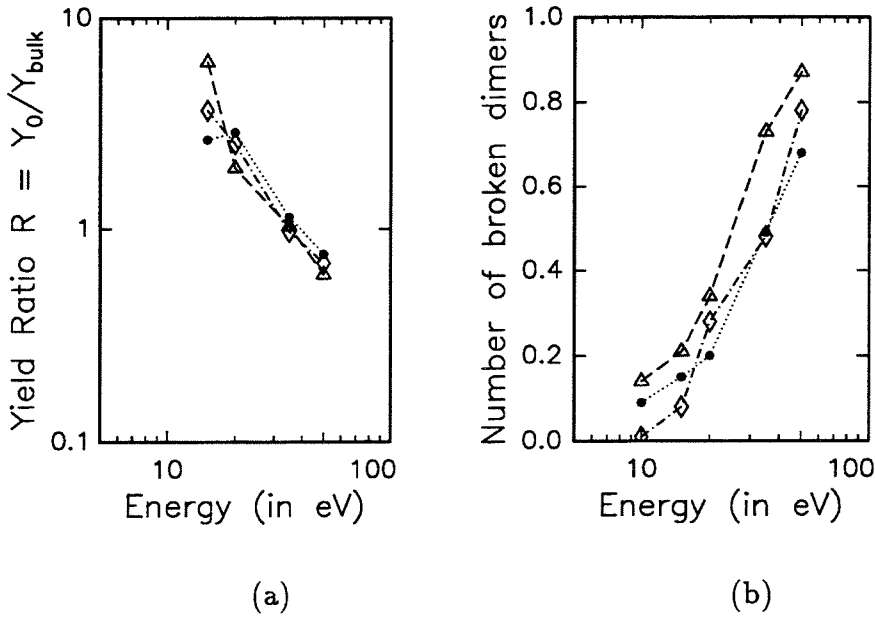


Figure 3.8: (a) The surface-to-bulk displacement ratio R and (b) the average number of broken dimers per incident ion (only from the placed dimers) for the different defect structures. The results are for the dimer pair (\triangle), dimer string edge (\diamond), and dimer string center (\bullet).

Bibliography

- [1] P.N. Keating, 'Effect of invariance requirements on the elastic strain energy of crystals with application to the diamond structure,' Phys. Rev. **145**, 637(1966).
- [2] R.M. Martin, 'Elastic properties of ZnS structure semiconductors,' Phys. Rev. **B1**, 4005(1970).
- [3] R. Biswas and D.R. Hamann, 'Interatomic potentials for silicon structural energies,' Phys. Rev. Lett. **55**, 2001(1985).
- [4] F.H. Stillinger and T.A. Weber, 'Computer simulation of local order in condensed phases of silicon,' Phys. Rev. **B31**, 5262(1985).
- [5] B.W. Dodson, 'Development of a many-body Tersoff-type potential for silicon,' Phys. Rev. **B35**, 2795(1987).
- [6] J. Tersoff, 'Empirical interatomic potential for silicon with improved elastic properties,' Phys. Rev. **B38**, 9902(1988).
- [7] J.Y. Tsao, *Materials Fundamentals of Molecular Beam Epitaxy*, Academic Press, Boston, 1993.
- [8] I.M. Torrens, *Interatomic Potentials*, Academic Press, New York, 1972.

- [9] M.T. Yin and M.L. Cohen, 'Theory of static structural properties, crystal stability, and phase transformations: application to Si and Ge,' *Phys. Rev. B* **26**, 5668(1982).
- [10] C. Kittel, *Introduction to Solid State Physics*, 6th ed., Wiley, New York, 1986.
- [11] Y.J. Chabal, G.S. Higashi, K. Raghavachari, and V.A. Burrows, 'Infrared spectroscopy of Si(111) and Si(100) surfaces after HF treatment — hydrogen termination and surface morphology,' *J. Vac. Sci. Technol.* **A7**, 2104(1989).
- [12] S.J. Cook and P. Clancy, 'Comparison of semi-empirical potential functions for silicon and germanium,' *Phys. Rev. B* **47**, 7686(1993).
- [13] S.D. Peyerimhoff and R.J. Buenker, 'Potential energy curves and transition moments for the low-lying electronic states of the Si₂ molecule,' *Chem. Phys.* **72**, 111(1982).
- [14] See, for example, E.C. Honea, A. Ogura, C.A. Murray, K. Raghavachari, W.O. Sprenger, M.F. Jarrold, and W.L. Brown, 'Raman-spectra of size-selected silicon clusters and comparison with calculated structures,' *Nature* **366**, 42(193).
- [15] C.W. Gear, *Numerical Initial Value Problems in Ordinary Differential Equations*, Prentice-Hall, New Jersey, 1971.
- [16] M.-J. Caturla, T.D. de la Rubia, and G.H. Gilmer, *Mat. Res. Soc. Symp. Proc.* **316**, 141(1994).

- [17] A.F. Bakker, G.H. Gilmer, M.H. Grabow, and K. Thompson, 'A special purpose computer for molecular dynamics calculations,' J. Comput. Phys. **90**, 313(1990); G.H. Gilmer, private communication.
- [18] L. Verlet, 'Computer "experiments" on classical fluids. I. Thermodynamical properties of Lennard-Jones molecules,' Phys. Rev. **159**, 98(1967).
- [19] G. Dahlquist and A. Björck, *Numerical Methods*, Prentice-Hall, New Jersey, 1974.
- [20] L.C. Feldman and J.W. Mayer, *Fundamentals of Surface and Thin Film Analysis*, North-Holland, New York, 1986.
- [21] J.F. Ziegler, J.P. Biersack, and U. Littmark, *The Stopping and Range of Ions in Solids*, Pergamon Press, New York, 1985.
- [22] J.P. Biersack and L.G. Haggmark, Nucl. Instr. Meth. **174**, 257(1980).
- [23] I.M. Torrens and M.T. Robinson, Phys. Rev. **139**, 5008(1974).
- [24] D.W. Brenner and B.J. Garrison, 'Microscopic mechanisms of reactions associated with silicon MBE – a molecular dynamics investigation,' Surf. Sci. **198**, 151(1988).
- [25] M. Kitabatake, P. Fons, and J.E. Greene, 'Molecular dynamics simulations of low energy particle bombardment effects during vapor phase crystal growth — 10 eV Si atoms incident on Si(001)-2×1 surfaces,' J. Vac. Sci. Technol. A **8**, 3726(1990).

- [26] R. Smith, D.E. Harrison, and B.J. Garrison, 'KeV particle bombardment of semiconductors — a molecular dynamics simulation,' *Phys. Rev. B* **40**, 40(1989).
- [27] B.W. Dodson, 'Molecular dynamics simulation of low energy beam deposition of silicon,' *J. Vac. Sci. Technol. B* **5**, 1393(1987).
- [28] M.G. Lagally, *Kinetics of Ordering and Growth at Surfaces*, Plenum, New York, 1990.
- [29] Y.-W. Mo, J. Kleiner, M.B. Webb, and M.G. Lagally, 'Activation energy for surface diffusion of Si on Si(001) - a scanning tunneling microscopy study,' *Phys. Rev. Lett.* **66**, 1998(1991).
- [30] G. Brocks, P.J. Kelly, and R. Car, 'Binding and diffusion of a Si adatom on the Si(100) surface,' *Phys. Rev. Lett.* **66**, 1729(1991).
- [31] C. Roland and G.H. Gilmer, 'Epitaxy on surfaces vicinal to Si(001). 1. Diffusion of silicon adatoms over the terraces,' *Phys. Rev. B* **46**, 13248(1992).
- [32] D. Srivastava and B.J. Garrison, 'The dynamics of surface rearrangements in Si adatom diffusion on the Si(100)(2×1) surface,' *J. Chem. Phys.* **95**, 6885(1991).
- [33] T. Miyazaki, H. Hiramoto, and M. Okazaki, '*Ab initio* study of elementary processes in silicon homoepitaxy – adsorption and diffusion on Si(001),' *Jpn. J. Appl. Phys.* **29**, L1165(1990).

- [34] S.T. Picraux, D.K. Brice, K.M. Horn, J.Y. Tsao, and E. Chason, 'Near-threshold energy dependence of Xe-induced displacements on Ge(001),' Nucl. Instr. Meth. B48, 414(1990).
- [35] N. Matsunami, Y. Yamamura, Y. Itikawa, N. Itoh, Y. Kazumata, S. Miyagawa, K. Morita, R. Shimizu, and H. Tawara, 'Energy dependence of the ion-induced sputtering yields of monatomic solids,' At. Data Nucl. Data Tables 31, 1(1984).
- [36] D.K. Brice, J.Y. Tsao, and S.T. Picraux, 'Partitioning of ion-induced surface and bulk displacements,' Nucl. Instr. Meth. B44, 68(1989).
- [37] G.K. Wehner, R.M. Warner, Jr., P.D. Wang, and Y.H. Kim, 'Substituting low energy (< 30 eV) ion bombardment for elevated temperature in silicon epitaxy,' J. Appl. Phys. 64, 6754(1988).
- [38] T. Ohmi, T. Ichikawa, H. Iwabuchi, and T. Shibata, 'Formation of device-grade epitaxial silicon films at extremely low temperatures by low energy bias sputtering,' J. Appl. Phys. 66, 4756(1989).

Chapter 4

EPITAXY ON HYDROGEN-TERMINATED SILICON SURFACES

"Is there any point to which you would wish to draw my attention?"

(Inspector Gregory)

"To the curious incident of the dog in the night-time."

"The dog did nothing in the night-time."

"That was the curious incident," remarked Sherlock Holmes.

– Silver Blaze

Sir Arthur Conan Doyle

4.1 Introduction

Adsorbates play an important role in low temperature silicon homoepitaxy. Even a small coverage (0.01 – 0.1 ML) of adsorbates can change the evolution of surface morphology and hence the film microstructure. The common adsorbates in an ultrahigh vacuum system are carbon, hydrogen and oxy-

gen. In a TEM study of silicon films deposited using a silane beam, it was shown that exposure of a Si(111)- 7×7 surface to ethylene (prior to deposition) changed the growth mode from layer-by-layer to 3-D island nucleation and growth [1, 2]. A similar conclusion was drawn in Section 2.7.2 for small coverages (~ 0.01 ML) of carbon and oxygen through *in situ* RHEED observations and *ex situ* SIMS analysis. Surface hydrogen has received a lot of attention in recent years. Introduction of atomic hydrogen leads to a premature breakdown of epitaxy [3]. At the same time, it is interesting to note that epitaxial silicon films can be deposited by MBE on a surface covered with 1 ML of hydrogen atoms [4]. Furthermore, sputter deposition results in epitaxial films even on a nominally dihydride-terminated Si(001) surface [5, 6]. What makes these results extraordinary is that there are no dangling bonds at the surface and hence apparently no adsorption sites. In the only atomically resolved study (using STM) of MBE on a hydrogen-terminated Si(001) surface, it was observed that even a small coverage (< 0.1 ML) of hydrogen atoms could dramatically increase the Si island density [7]. This was interpreted as hydrogen atoms impeding the diffusion of silicon atoms.

We have used molecular dynamics simulations to understand the atomistics of the growth process. The calculations were performed using the Si-Si, Si-H and H-H interatomic potentials described in Chapter 3. One can envision different models for epitaxy on hydrogen-terminated silicon surfaces. For example, the incident Si atom could (a) cause the surface hydrogen atoms to desorb and thus create an adsorption site, (b) recoil implant the surface hydrogen atoms and create an adsorption site, or (c) “subplant” itself, i.e., get implanted one layer below the surface. We will show through molecu-

lar dynamics simulations that mechanism (c) is the pathway for epitaxy on hydrogen-terminated Si(001) surfaces.

4.2 An Empirical Interatomic Potential for Si–H Interactions

We have noted the important role of hydrogen in low temperature silicon homoepitaxy. Hydrogen and silicon interact in many ways and in many important processes of device fabrication. Hydrogen plays an important role in the overall chemical vapor deposition growth mechanism from precursors such as silane and disilane. Hydrogen in bulk silicon can passivate dopants and deep level defects. In our work, hydrogen-termination of the surface has been an important issue. Hydrogen-termination of silicon surfaces prior to epitaxy in ultra-high vacuum has become increasingly popular due to the relatively low desorption temperature of the passivation layer. Epitaxial silicon layers have been deposited on hydrogen-terminated surfaces [5, 6, 4]. A low temperature Ar^+ ion beam-induced (2×1) reconstruction from an initially dihydride-terminated Si(001) surface is discussed in Chapter 5. Many of these processes occur on a time scale and crystal size scale which is beyond the scope of a first principles approach but which can be described with empirical force constants. An empirical Si–H potential is described here for molecular dynamics simulations of the hydrogen-terminated silicon surfaces and various gas-surface interactions.

Before proceeding to develop a potential, it is pertinent to ask whether

a classical description of the silicon-hydrogen system is reasonable. A look at the various configurations of silicon and hydrogen provides a good start. The Si-H bonding in gas phase molecules and radicals is varied. Saturated molecules such as SiH_4 and Si_2H_6 contain sp^3 -type bonds whereas p-type bonds are found in SiH and SiH_2 . The molecule Si_2H_4 exhibits π -bonding. Hydrogen adsorption on a silicon surface can result in different reconstructions depending on coverage. The hydrogen atoms on the surface are quite localized even at low coverages. Scanning tunneling microscope images at low coverages reveal the location of hydrogen atoms [8] (or more precisely, the unpaired electron opposite the hydrogen atom). This is in contrast to some metals where a delocalized state of the proton has been observed at low coverages [9]. The properties of hydrogen in bulk silicon depend on its charge state [10]. An important position is the bond-centered site of atomic hydrogen where it is bonded to two silicon atoms [11]. It is clear from this brief description that some aspects, such as the dependence on charge state, do not allow for a simple solution within a classical adiabatic framework. Other aspects such as the different types of Si-H bonds and the multiple bonding of hydrogen in the bond-centered site can be modeled, particularly by making a special case for them. Finally, the strongly localized bonding of hydrogen on silicon surfaces and the directional bonds on both the surface and in molecules are features which readily permit a classical description. It is clear from the above that this range of silicon-hydrogen interactions provides a formidable challenge.

Empirical expressions for the Si-H potential have been developed previously [12, 13]. However, these potentials were not tested over a sufficiently

wide range of configurations to determine their usefulness and limitations. A classical potential with an expression similar to the one described here was reported recently [14]. An earlier version of the potential described here can be found in Ref. [15]. As described in Section 3.2.1, several interatomic potentials have been developed to model silicon-silicon interactions [16, 17]. The strong directional bonding in silicon is described by a many-body term attached to a Morse-type potential. The Si potential in Ref. [17] gives a good description of the different allotropes of silicon and the Si(001) surface. This has been extended to germanium and carbon [18] and has also been used to describe the C-H interactions in hydrocarbons [19]. We have chosen this form to model the Si-H interactions. The total potential energy is written as a sum over pairs:

$$V = \sum_{i < j} \Phi_{ij} \quad (4.1)$$

$$\Phi_{ij} = \{ AF_1(N) \exp(-\lambda_1 r_{ij}) - B_o F_2(N) \exp(-\lambda_2 r_{ij}) (1 + \zeta_{ij}^\eta)^{-\delta} \} f_c(r_{ij}) \quad (4.2)$$

$$\zeta_{ij} = \sum_{k \neq i,j} f_c(r_{ik}) [c + d \{H(N) - \cos \theta_{jik}\}^2] \exp[\alpha \{ (r_{ij} - R_{ij}^{(e)}) - (r_{ik} - R_{ik}^{(e)}) \} \beta] \quad (4.3)$$

The valency of hydrogen is set by the parameters α , β and H in the many-body part of the potential. A high value of α and $\beta = 1$ gives a monovalent nature to hydrogen while $\alpha = 0$ and $H = -1$ in the presence of two Si atoms describes the bond-centered site in bulk Si. Here, F_1 , F_2 and H are functions of the coordination N_H^i and N_{Si}^i of the i^{th} Si atom. To obtain a continuous function for the coordination, we write [19]

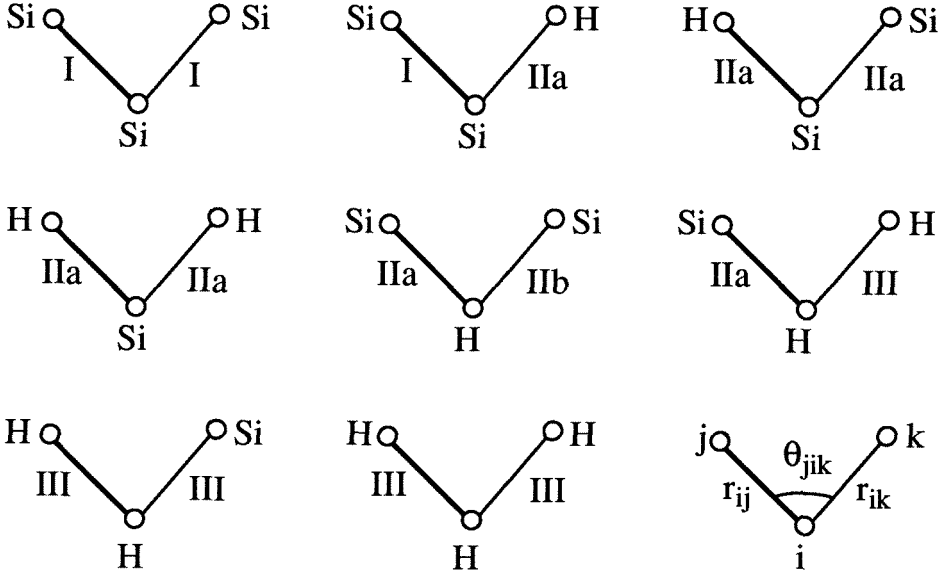


Figure 4.1: The combination of the potentials used for different triples. I is the Si-Si potential, IIa and IIb are parts of the Si-H potential and III is the H-H potential.

$$N_H^{i=(\text{Si})} = \sum_{j=(\text{H})} f_c(r_{ij}), \quad N_{\text{Si}}^{i=(\text{Si})} = \sum_{j=(\text{Si})} f_c(r_{ij}) \quad \text{and} \quad N = N_H^{i=(\text{Si})} + N_{\text{Si}}^{i=(\text{Si})} \quad (4.4)$$

$$f_c(r_{ij}) = \begin{cases} 1 & , r_{ij} < R - D \\ \frac{1}{2} - \frac{9}{16} \sin(\pi \frac{r_{ij}-R}{2D}) + \frac{1}{16} \sin(3\pi \frac{r_{ij}-R}{2D}) & , R - D < r_{ij} < R + D \\ 0 & , r_{ij} > R + D \end{cases} \quad (4.5)$$

A piecewise linear fit was used to compute the values of F_1 , F_2 and H for non-integral values of N . Numerical values for the parameters were obtained by fitting the potential to the various silicon hydride molecules and interstitial hydrogen sites in bulk silicon. For Si-Si and H-H interactions, the potentials of Ref. [17] (Section 3.2.1) and Ref. [19] (potential I) were used, respectively.

A combination of the three potentials is used to determine the potential energy and forces for the different triples such as Si-Si-H, H-Si-H, etc., as shown in Fig. 4.1. One could, in principle, derive a separate set of coefficients for each of the triples. It was found that a single Si-H potential gives a reasonable description in most situations, the exception being the Si-H-Si triple. The Si-H bond energy of 3.42 eV for silane was obtained from the heat of formation at 0 K [20], the values of 4.63 eV for Si cohesive energy [21] and 2.375 eV for hydrogen [20], neglecting the zero point energy correction. The Si-H bond length for silane was taken [22] as 1.476 Å. The parameters were also adjusted to give a reasonable fit to the stretch and bend modes of various silicon hydride molecules. The value of δ was taken to be the same as that of the H-H potential [19]. The potential was cutoff at 2.00 Å. The parameters of the Si-H potential along with the Si-Si [17] and H-H [19] potentials are listed in Table 4.1. The interstitial sites of atomic hydrogen in bulk Si were used to determine the values of the parameters in column IIb of Table 4.1. It is noted that the parameters in the potential were not systematically optimized.

The bond lengths, angles and some vibrational wave numbers for the Si_mH_n molecules and radicals are shown in Table 4.2. The properties explicitly fitted to the Si-H potential have been indicated. The properties of the Si_2 dimer and the H_2 molecule are also included. The geometry and vibronic properties of most molecules are fairly well reproduced. The bond length in disilane is 0.07 Å higher than the experimental value of 2.33 Å [24]. Due to the neglect of long-range interactions, the potential does not distinguish between eclipsed and staggered forms of disilane. The experimental value

Table 4.1: The parameters used in the Si-H interatomic potential along with the Si-Si and H-H potentials.

Parameter	Si-Si I (Ref. [17])	Si-H		H-H III (Ref. [19])
		IIa	IIb	
A (eV)	1830.8	323.54	—	80.07
B ₀ (eV)	471.18	84.18	—	31.38
λ_1 (\AA^{-1})	2.4799	2.9595	—	4.2075
λ_2 (\AA^{-1})	1.7322	1.6158	—	1.7956
α (\AA^{-1} or \AA^{-3})	5.1975	4.00	0.00	3.00
β	3	3	—	1
R ^(e) (\AA)	2.35	1.475	—	0.74
c	—	0.0216	0.70	4.00
d	0.160	0.27	1.00	—
h	-0.59826	—	-1.00	—
R (\AA)	2.85	1.85	—	1.40
D (\AA)	0.15	0.15	—	0.30
η	0.78734	1.00	—	1.00
δ	0.635	0.80469	—	0.80469
F ₁ (1)	—	1.005	—	—
F ₁ (2)	—	1.109	—	—
F ₁ (3)	—	0.953	—	—
F ₁ (n), n>4	—	1.000	—	—
F ₂ (1)	—	0.930	—	—
F ₂ (2)	—	1.035	—	—
F ₂ (3)	—	0.934	—	—
F ₂ (n), n>4	—	1.000	—	—
H(1)	—	-0.040	—	—
H(2)	—	-0.040	—	—
H(3)	—	-0.276	—	—
H(n), n>4	—	-0.470	—	—

for the rotation barrier is about 0.05 eV [25]. The predicted wave number of the torsion mode therefore vanishes, for which a small value of 91 cm^{-1} has been estimated [22]. The energy differences for the decomposition reactions of disilane are listed in Table 4.3. The values for the Si_2H_4 and SiH_3SiH decomposition reactions deviate by about 0.7 and 0.4 eV respectively. There is reasonable agreement between the values calculated from the potential and the experimental/theoretical estimated values for the other reactions. It is noted that these are the energy differences between the products and disilane and not the activation energies for the reactions. The Si-Si bond length in disilene is also larger than the experimental value. The π -bonding in this molecule accounts for this large difference. The bond angle and the inversion barrier in SiH_3 are 106° and 0.21 eV respectively. The corresponding experimental values are 110.5° and 0.23 eV respectively [29]. Most of the vibrational wave numbers are within 15% of the experimental values.

Hydrogen termination of the silicon surface results in different reconstructions depending on coverage as shown in Fig. 4.2. A clean $\text{Si}(001)$ surface exhibits a (2×1) reconstruction with the dimer bond along the $\langle 110 \rangle$ direction. The Si-Si interatomic potential gives a dimer bond length of 2.37 Å. For a hydrogen coverage of 1 monolayer (ML), the surface retains the (2×1) reconstruction with hydrogen atoms terminating the dangling bonds of silicon. The Si-Si dimer length increases to 2.43 Å. A similar lengthening of the dimer bond was also reported in the semi-empirical [31] and *ab initio* cluster calculations [32]. The H-Si-Si bond angle was found to be 112.4° compared to the values of 110.2° [33] and 114.7° [31] reported in the literature. The wave number of the symmetric stretch mode was 2144 cm^{-1} compared to the

Table 4.2: Properties of some Si_mH_n molecules. Vibrational wave numbers in cm^{-1} . The bond energy of H_2 includes the zero-point energy. Asterisk (*) indicates a theoretically calculated value. The Si-H potential was explicitly fitted to the properties marked by the † sign.

Si-H Expt./ Ref. Potential Theory				Si-H Expt./ Ref. Potential Theory			
SiH₄				SiH			
$a_{\text{Si-H}}$	1.475 Å	1.48 Å	[20] †	$a_{\text{Si-H}}$	1.51 Å	1.51 Å	[22] *†
$E_{\text{Si-H}}$	3.42 eV	3.42 eV	[20] †	$E_{\text{Si-H}}$	3.10 eV	3.14 eV	[23] †
$\theta_{\text{H-Si-H}}$	109.5°	109.5°	[20] †	ν_1	2034	2042	[23]
ν_1	2100	2186	[23] †	SiH₂			
ν_2	985	972	[23]	$a_{\text{Si-H}}$	1.51 Å	1.51 Å	[22] *†
ν_3	2151	2189	[23]	$E_{\text{Si-H}}$	3.42 eV	3.49 eV	[20] †
ν_4	913	913	[23] †	$\theta_{\text{H-Si-H}}$	92.3°	92.1°	[28] †
Si₂H₆				A_1 sym stretch	2136	2032	[28]
$a_{\text{Si-H}}$	1.48 Å	1.49 Å	[24]	A_1 bend	878	1004	[28]
$a_{\text{Si-Si}}$	2.40 Å	2.33 Å	[24]	SiH₃			
$\theta_{\text{H-Si-Si}}$	109.4°	110.3°	[24]	$a_{\text{Si-H}}$	1.48 Å	1.48 Å	[22] *†
A_{1g} Si-H stretch	2110	2163	[25]	$E_{\text{Si-H}}$	3.21 eV	3.25 eV	[20] †
A_{1g} SiH ₃ bend	894	920	[25]	$\theta_{\text{H-Si-H}}$	106°	110.5°	[29]
A_{1g} Si-Si stretch	387	432	[25]	Inv. barrier	0.21 eV	0.23 eV	[29] †
A_{1u} torsion	0	91	[22] *	ν_1	2051	1955	[28]
E_g Si-H stretch	2150	2155	[25]	H₂			
Si₂H₄				$a_{\text{H-H}}$	0.74 Å	0.74 Å	[20]
$a_{\text{Si-H}}$	1.48 Å	1.48 Å	[22] *	$E_{\text{H-H}}$	4.75 eV	4.75 eV	[20]
$a_{\text{Si-Si}}$	2.36 Å	2.17 Å	[22] *	ν_1	4400	4400	[30]
$\theta_{\text{H-Si-Si}}$	106.0°	118.9°	[22] *	SiH₃SiH			
$\theta_{\text{H-Si-H}}$	106.0°	112.8°	[22] *	$a_{\text{Si-Si}}$	2.37 Å	2.39 Å	[22] *
Si₂				$a_{\text{Si-H}} (1)$	1.48 Å	1.48 Å	[22] *
$a_{\text{Si-Si}}$	2.30 Å	2.24 Å	[26] *	$a_{\text{Si-H}} (2)$	1.51 Å	1.51 Å	[22] *
$E_{\text{Si-Si}}$	2.66 eV	3.13 eV	[20]	$\theta_{\text{H-Si-Si}} (1)$	109.5°	114.2°	[22] *
ν_1	469	518	[27]	$\theta_{\text{H-Si-Si}} (2)$	92.3°	89.1°	[22] *

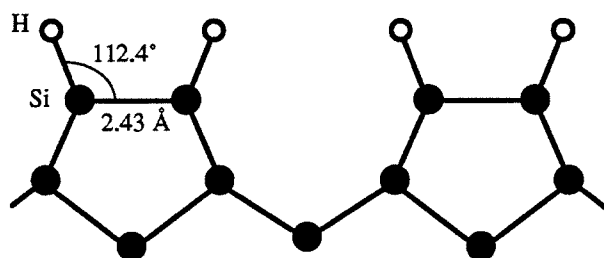
Table 4.3: The energy differences ΔH for disilane decomposition. The asterisk (*) indicates a theoretically estimated value.

Reaction	Potential	Literature	Reference
$\text{Si}_2\text{H}_6 \rightarrow 2 \text{SiH}_3$	3.27 eV	3.21 eV	[20]
$\text{Si}_2\text{H}_6 \rightarrow \text{Si}_2\text{H}_5 + \text{H}$	3.73 eV	3.78 eV	[20]
$\text{Si}_2\text{H}_6 \rightarrow \text{Si}_2\text{H}_4 + \text{H}_2$	2.70 eV	2.04 eV	[22] *
$\text{Si}_2\text{H}_6 \rightarrow \text{SiH}_3\text{SiH} + \text{H}_2$	1.91 eV	2.32 eV	[22] *
$\text{Si}_2\text{H}_6 \rightarrow \text{SiH}_4 + \text{SiH}_2$	2.03 eV	2.17 eV	[22] *

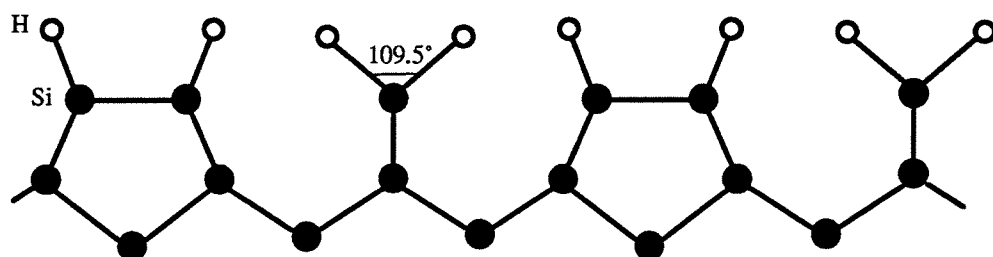
experimental value of 2099 cm^{-1} [32]. At a coverage of 1.33 ML, a (3×1) reconstructed surface consisting of alternate monohydride and dihydride units is obtained [8, 34]. The H-Si-H angle in the dihydride units was found to be 109.5° in agreement with the first principles calculations [35]. At a coverage of 2 ML, the surface reverts to a (1×1) structure. There is strong repulsion between H atoms bonded to neighboring Si atoms. A canted-row structure was found to have a lower energy than the symmetric dihydride structure. The H-Si-H angle in the canted-row structure is about 106° compared to 100° in the symmetric structure. The Si surface atoms are displaced by about 0.16 \AA from their bulk positions in the canted-row structure. Although the difference of $0.02 \text{ eV}/(1 \times 1)$ pair is small, it is significant that a symmetry-breaking displacement produces a structure close in energy to the symmetric structure. Such a canted-row structure was shown to have a lower energy using the local density approximation [35]. A somewhat larger difference of $0.18 \text{ eV}/(1 \times 1)$ pair and a Si surface atom displacement of 0.6 \AA was reported in these calculations. Experimentally, dihydride-terminated Si(001)- 1×1 surfaces are found to be rough on an atomic scale, presumably

due to H-H repulsion [8]. At low hydrogen coverages, hydrogen atoms have been observed experimentally to pair up [8]. The difference in energy between an isolated H atom and an H atom in a dimer pair was found to be 0.015 eV, with the isolated atom having lower energy. This difference, albeit small, is contrary to the experimental observation. Using the configuration interaction method, it was shown in Ref. [33] that the H atom in a dimer pair had a lower energy by ~ 0.05 eV. The driving force for pairing of H atoms thus appears to be small. A 1 ML hydrogen coverage on the Si(111)- 1×1 surface gave a Si-H bond length of 1.48 Å and the stretch mode of 2137 cm^{-1} . The experimental value for the stretch mode is 2084 cm^{-1} [32]. An interesting result is the possibility of formation of a bond-centered Si-H-Si site on the surface. Although this has never been observed for silicon, such a bridge-bonded site was recently observed experimentally on the GaAs surface [36]. *It is noted that none of the surface properties were fitted to the Si-H potential and the above results may be considered as predictions of the potential.*

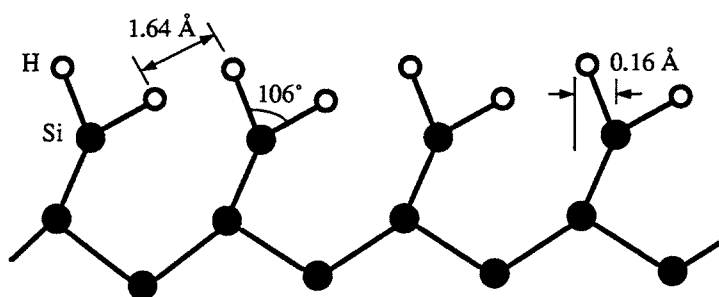
The interstitial positions of hydrogen in silicon have been studied extensively using first principles techniques. The important sites of atomic hydrogen can be found in Ref. [37]. All the energies mentioned below are with respect to H atoms in free space and bulk Si atoms. The minimum energy site has been shown to depend on the charge state of hydrogen [10]. For both neutral H and H^+ , the bond-centered (BC) site is the minimum energy site [10, 11]. The set of parameters (labeled IIb in Table 4.1) in the potential were adjusted to produce a minimum energy of atomic H at the BC site. The Si-H bond length in this site is 1.54 Å and the second nearest neighbor atoms are displaced by 0.10 Å. The bridged Si-H bond length in



(a)



(b)



(c)

Figure 4.2: The different hydrogen-induced reconstructions of the silicon surface. (a) The (2×1) monohydride structure with a hydrogen coverage $\theta = 1 \text{ ML}$, (b) the (3×1) structure with alternate monohydride and dihydride units at $\theta = 1.33$, and (c) the (1×1) dihydride structure with $\theta = 2 \text{ ML}$. The dimensions and angles are according the Si-H potential.

the radical $\text{H}_3\text{Si}-\text{H}-\text{SiH}_3$ is 1.58 Å. This increase is due to the free motion of the SiH_3 units in the outward direction.

The Si-H bond lengths of 1.58 Å and 1.72 Å were obtained in the BC site and the radical, respectively in *ab initio* cluster calculations [11]. The energy at the BC site is 1.26 eV compared to 1.05 eV in Ref. [38]. A site near C (on the line between C and T) was found to be 0.2 eV higher in energy compared to the BC site. This site was reported to be the saddle point for H diffusion between BC sites [10] with an activation energy of about 0.2 eV. Among the other sites, the antibonding site AB was not a metastable site. At both the tetrahedral interstitial T and the hexagonal interstitial H sites, the H atom did not interact with any Si atoms. While this is clearly an oversimplification, *ab initio* calculations have shown that there is very little relaxation of Si atoms when an H atom is placed at these sites [11, 39]. In the H_2 molecule oriented in the $\langle 100 \rangle$ direction at the tetrahedral interstitial site, the H atoms were too far from the Si atoms to interact. The energy per H atom was therefore 2.38 eV, same as in the free H_2 molecule. A value of 1.92 eV per H atom and an increase of 0.03 Å in the H-H bond length for the H_2 molecule was reported with the local density approximation [38]. The energy per H atom in the H_2^* complex (H atoms in adjacent BC and AB positions) was 1.50 eV compared to 1.65 eV in Ref. [38].

There are several dynamic situations where one could apply the classical potential described here. A brief analysis of the strengths and weaknesses of the potential is thus appropriate. An area of considerable interest is the low temperature chemical vapor deposition of silicon from precursors such as SiH_4 and Si_2H_6 . The potential might be used to study the dissociative

adsorption of these molecules on the Si(001) surface. However, one must be more cautious with the dissociation of these molecules in the gas phase because of the inadequate description of the Si_2H_4 molecule and the presence of ionized species. Hydrogen-terminated silicon surfaces are fairly well described by the potential. Thus the potential may be used to study various physical vapor deposition techniques such as molecular beam epitaxy and sputter deposition of silicon. Another area of application might be modeling of hydrogenated amorphous silicon. This seems reasonable, since the Si-H bond lengths and the stretching and bending modes in hydrogenated amorphous silicon are not very different from those of the SiH_4 molecule and the hydrogen-terminated silicon surface [40].

This potential is used here to study epitaxy of silicon on hydrogen-terminated silicon surfaces and the beam-induced reconstruction of silicon in Chapter 5.

4.3 Epitaxy on a Dihydride-Terminated Si(001)- 1×1 Surface

Figure 4.3 shows a HRTEM image of a film deposited by conventional MBE on a nominally dihydride-terminated Si(001) surface. The growth rate was 0.09 nm/s. The substrate preparation involved the chemical cleaning described in Appendix A ending with the HF dip. This was followed by baking overnight in the UHV chamber at the growth temperature of 190°C. The deposited film is completely amorphous. Epitaxial silicon films have

been deposited on a similar surface by bias sputtering at 300°C [5] and ion beam sputtering at 210°C [6]. In Ref. [5], both the Si target and substrate were biased and rf excitation was used to generate an Ar plasma. In Ref. [6], a 750–1000 eV Ar^+ beam was incident on a Si target and the sputtered Si was used to form the film. The main difference between conventional MBE and sputter deposition is the incident particle energy. In MBE, Si atoms are effused out at the temperature of the source and have an energy of ~ 0.2 eV. In sputter deposition, the incident particle energy is ~ 5 eV.

In the molecular dynamics simulations, silicon atoms were incident normally on a dihydride-terminated $\text{Si}(001)\text{-}1\times 1$ surface. The canted-row structure (see Figure 4.2) was used as it corresponds to the minimum energy configuration. The substrate had 24 Si layers with 100 atoms/layer. Periodic boundary conditions were used in the transverse directions and the bottom two layers were held rigid. The substrate temperature was held at 0 K and the simulations were followed for 1 ps. The incident atom energies ranged from 0.25 to 10 eV.

The results of two simulations are shown in Figs. 4.4 and 4.5. These atomic positions are at the end of 1 ps. In Fig. 4.4, the incident particle energy was 0.25 eV, typical of conventional MBE. The incident Si atom was not able to penetrate the layer of H atoms due to steric constraints. In Fig. 4.5, the incident particle energy was 4 eV, typical of sputter deposition. In this case, the incident Si atom is “subplanted,” i.e., implanted one layer below the surface in the lattice. It not only penetrates the layer of H atoms but also pushes a surface Si atom upward.

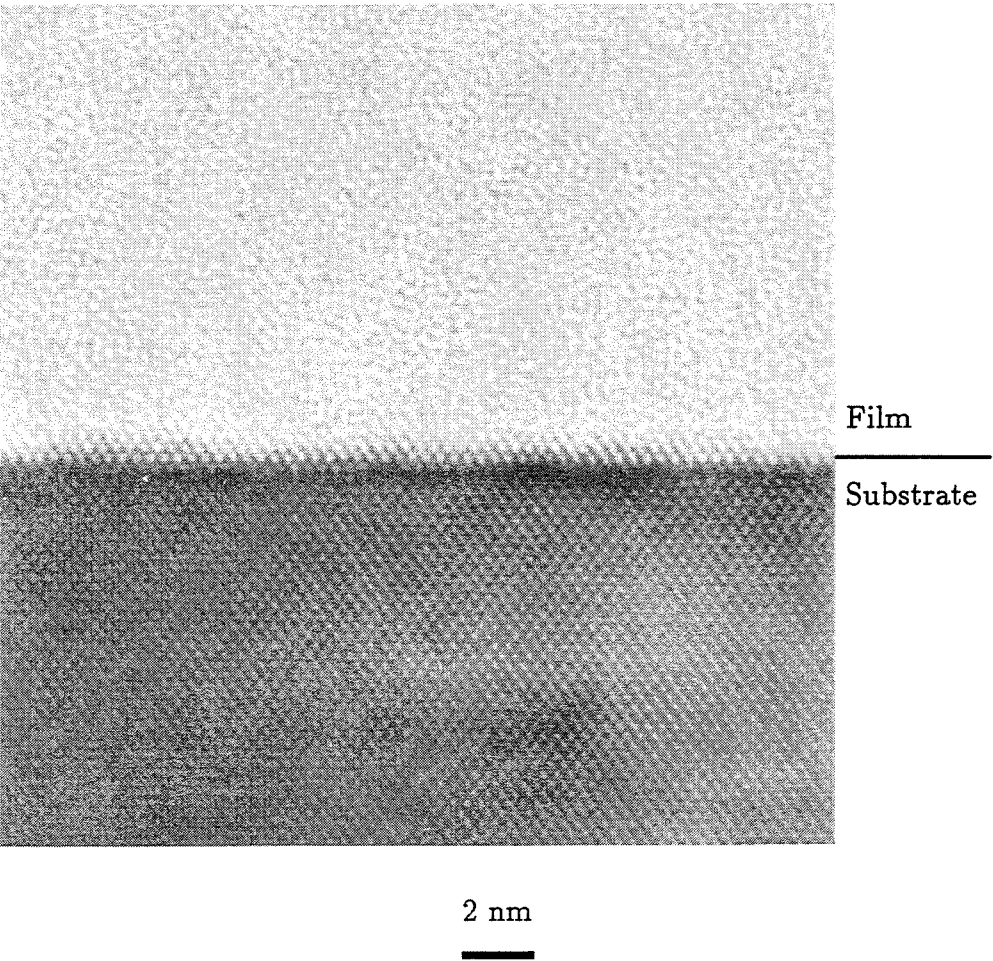
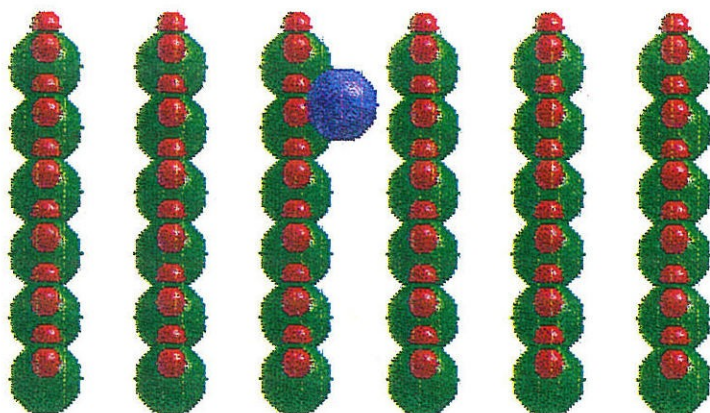
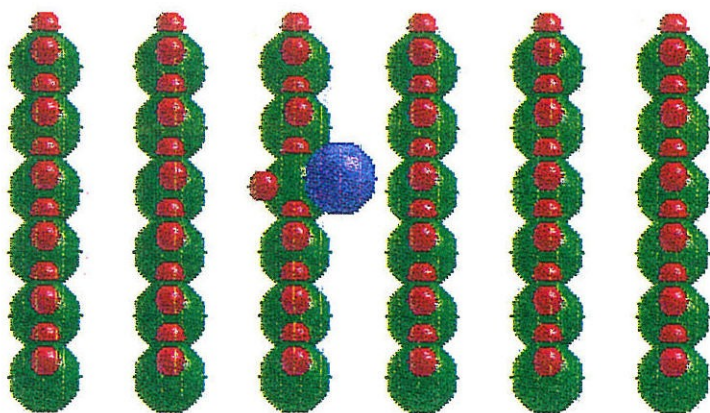


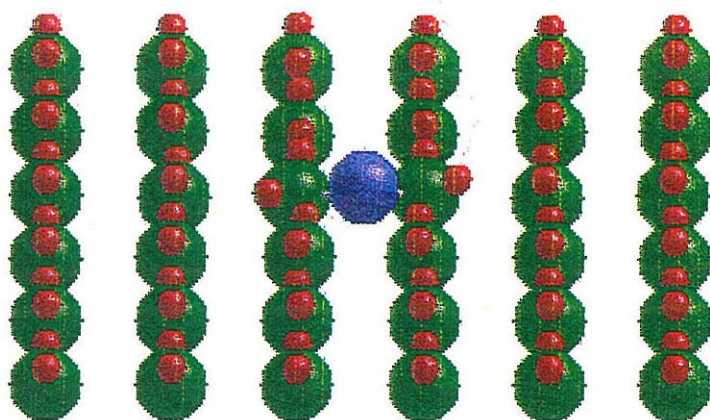
Figure 4.3: HRTEM image of a silicon film deposited on an initially dihydride-terminated Si(001)-1 \times 1 surface. The substrate temperature was 190°C and the growth rate was 0.09 nm/s. The film is amorphous.



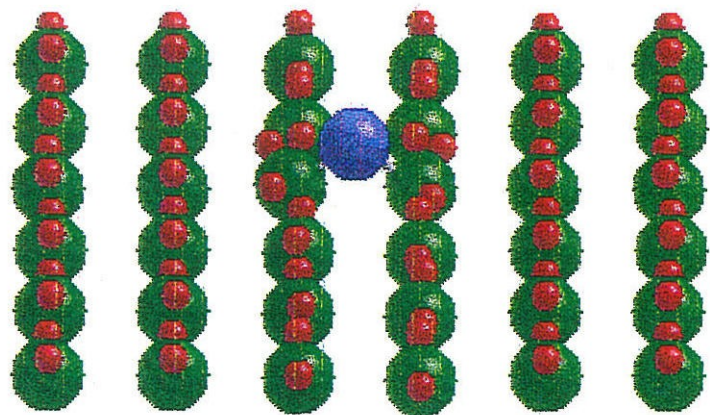
(a)



(b)

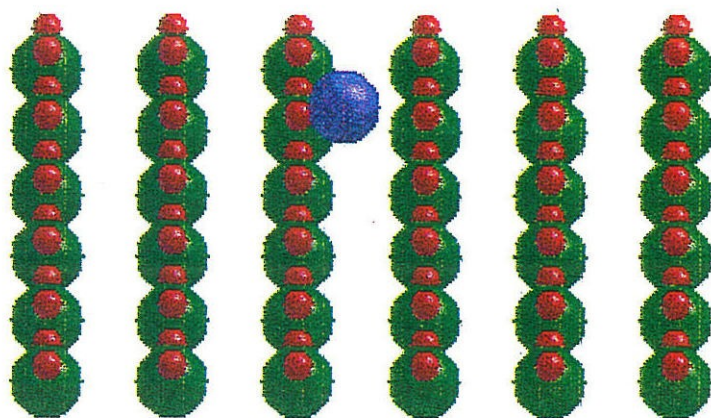


(c)

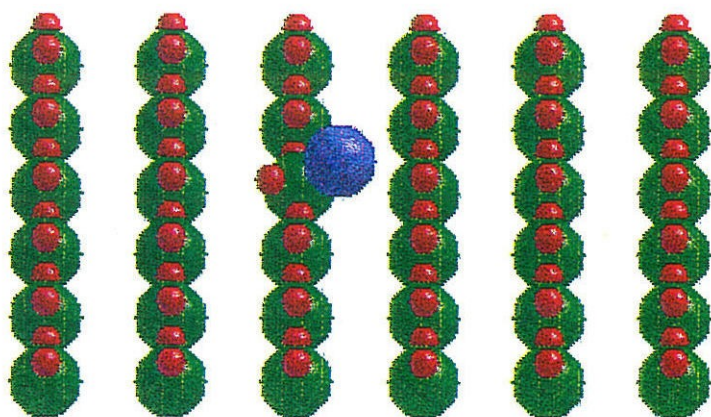


(d)

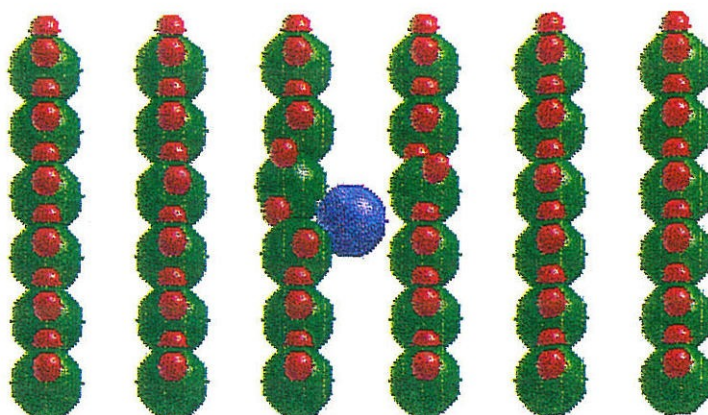
Figure 4.4: Molecular dynamics simulation of a 0.25 eV Si atom (blue) incident on a dihydride-terminated Si(001)-1 \times 1 surface. The atomic positions are at (a) 0 ps, i.e. start of the simulation, (b) 0.15 ps, (c) 0.30 ps, and (d) 1 ps into the simulation. Only the top layer of silicon atoms (green) and hydrogen atoms (red) in the region of interest are shown.



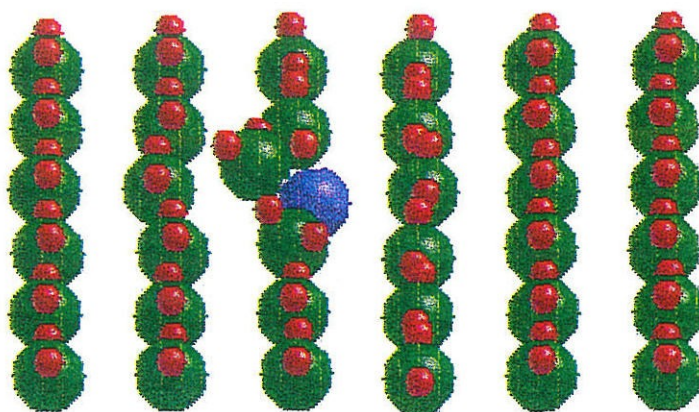
(a)



(b)



(c)



(d)

Figure 4.5: Molecular dynamics simulation of a 4 eV Si atom (blue) incident on a dihydride-terminated Si(001)-1 \times 1 surface. The atomic positions are at (a) 0 ps, i.e. start of the simulation, (b) 0.05 ps, (c) 0.10 ps, and (d) 1 ps into the simulation. Only the top layer of silicon atoms (green) and hydrogen atoms (red) in the region of interest are shown.

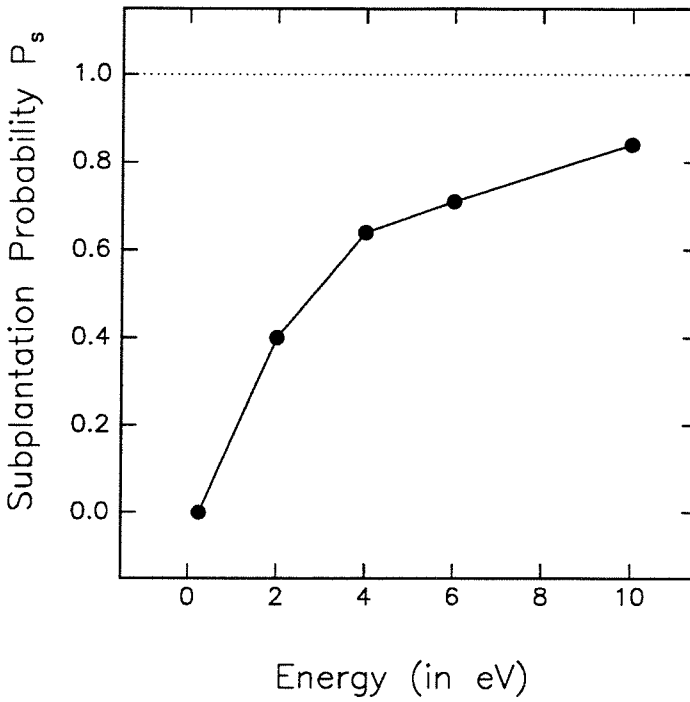


Figure 4.6: The subplantation probability P_s versus incident silicon atom energy.

The subplantation probability P_s is plotted as a function of incident particle energy in Fig. 4.6. The results shown are averages over 50 simulations at each energy. An incident particle is considered subplanted if at the end of 1 ps it is below a surface Si atom. We see that P_s rises very rapidly with incident particle energy. At 4 eV, which corresponds to the peak in the sputtered particle energy distribution [41], almost two-thirds of the incident particles are subplanted. At 0.25 eV, none of the incident Si atoms were subplanted. Note that these probabilities are at the end of 1 ps and their values may be different on the time scale of growth ($\sim 0.01 - 10$ s). A small amount of hydrogen sputtering was also observed and the results are summarized in Table 4.4.

Table 4.4: Hydrogen sputtering events during energetic silicon atom deposition on a dihydride-terminated Si(001) surface.

Incident silicon atom energy (eV)	Number of simulations	Number of hydrogen atoms sputtered
0.25	50	0
2.0	50	0
4.0	50	0
6.0	50	1
10.0	50	4

The simulations suggest that in conventional MBE, the incident particle is not able to penetrate the layer of hydrogen atoms. There is no good epitaxial site at the level of the hydrogen atoms. A silicon atom deposited in the first monolayer will form a stronger bond with the arriving Si atoms than with the substrate Si atoms. This will result in a randomly networked structure, or amorphous silicon. In sputter deposition, the SiH₂ unit segregates to the surface. How do these results compare with experimental observations? In Ref. [5], a (1×1) surface was observed in RHEED during the entire growth of a 200 nm film whereas in Ref. [6], (2×1) spots were observed in low energy electron diffraction (LEED) after ~ 10 nm deposition. While the results after deposition of several layers are different in the two cases, it can be concluded that the surface is (1×1) in the initial stages of growth. This, together with the observation that the surface remains smooth on an atomic scale [5, 6], is strongly indicative of surface segregation of hydrogen. The simulations suggest that the surface Si-H bonds are not broken and it is the entire SiH₂ unit that segregates to the surface. A small amount of hydrogen loss by sputtering was observed in the simulations and this could result in

a gradual transformation to a (2×1) structure as reported in Ref. [6]. The rate of hydrogen loss in an experiment would be quite sensitive to the tail of the sputtered particle energy distribution and the flux of energetic Ar recoils from the target.

In the simulations, the incident Si atom does not always end up in an epitaxial position. It is usually in an interstitial position to maximize the number of bonds. This is expected since more than one atom would have to be deposited to get an epitaxial layer. Finally, it is noted that these simulations only suggest a mechanism for the initial stages of epitaxy. Sputter deposition also produces epitaxial films at low temperatures and high growth rates compared to conventional MBE. The energy of the incident particles thus also serves to smooth the surface during growth.

4.4 Epitaxy on a Monohydride-Terminated Si(001)- 2×1 Surface

Figure 4.7 shows a HRTEM image of a silicon film deposited at 380°C by conventional MBE on an initially monohydride-terminated Si(001)- 2×1 surface. The growth rate was 0.02 nm/s . The substrate preparation involved the chemical cleaning described in Appendix A ending with the HF dip. The substrate was then heated and maintained at 380°C for 30 minutes to get the dihydride-to-monohydride transition. Since complete hydrogen desorption occurs at a much higher temperature ($T \sim 450 - 500^\circ\text{C}$), the surface coverage is believed to be close to 1 ML. The XTEM image of the film is

quite typical of low temperature deposited silicon films. There is an initial region of epitaxial growth followed by the breakdown of epitaxy. A twinned region can be seen near the surface. The important observation, however, is that the initial growth is epitaxial even with 1 ML coverage of hydrogen.

Epitaxial silicon films on a monohydride-terminated Si(001) surface (at 370°C) were first reported in Ref. [4]. More recently, it was observed that Si films were epitaxial when deposited above 200°C [42]. It was also shown that hydrogen atoms segregate to the surface during growth [42].

Molecular dynamics simulations similar to the one described in the previous section were employed to study the atomistics of the growth process. The substrate size and boundary conditions were the same as in the previous section. The geometry of the (2×1) surface is shown in Fig. 4.2. The initial substrate temperature was 0 K. The incident Si atoms had a kinetic energy of 0.25 eV.

The atomic positions after 1 ps in two simulations are shown in Fig. 4.8. In Fig. 4.8(a), the incident Si atom is subplanted in the lattice whereas in Fig. 4.8(b), the Si atom is in the same layer as the H atoms. Here, the subplantation is driven in large part enthalpy difference (4.63 eV) between a vapor phase and a solid phase silicon atom. The incident atom accelerates toward the surface as it gains its binding energy and is occasionally subplanted. The simulations suggest that it is the SiH unit that segregates to the surface. The subplantation probability was 0.1 averaged over 50 simulations. While this is rather small, it is possible that simulation at a higher substrate temperature and for a longer time might result in a subplantation probability consistent with efficient SiH segregation and Si epitaxy. These

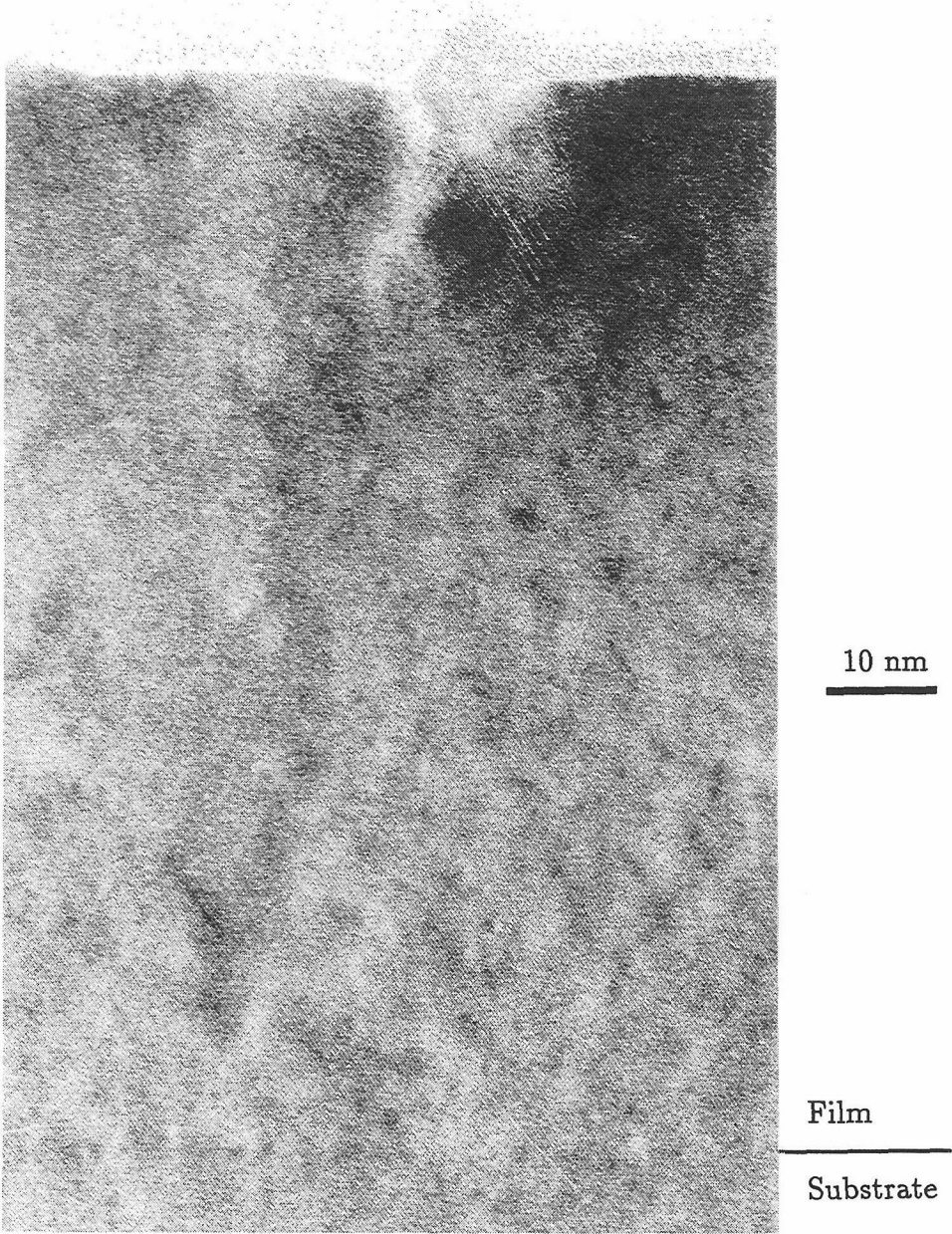
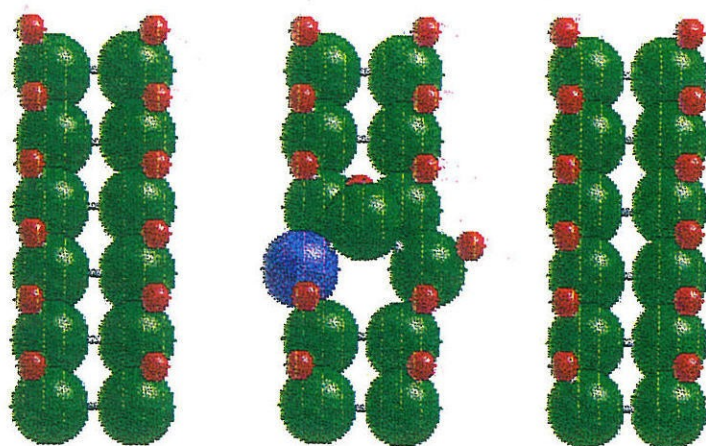
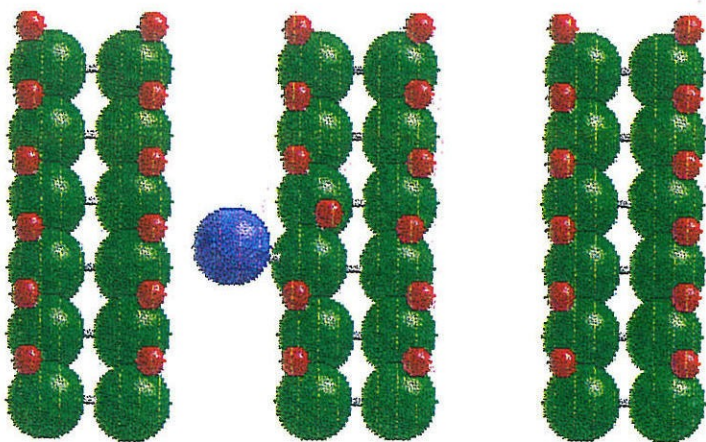


Figure 4.7: Epitaxial silicon film deposited on an initially monohydride-terminated $\text{Si}(001)\text{-}2\times 1$ surface. The substrate temperature was 380°C and the growth rate was 0.02 nm/s .



(a)



(b)

Figure 4.8: The atomic positions after 1 ps of simulation for two different impact points of the incident silicon atom. The incident atom (blue) is subplanted in (a) but remains at the level of hydrogen atoms in (b). The incident atom had a kinetic energy of 0.25 eV. Only the top layer of silicon atoms (green) and hydrogen atoms (red) in the region of interest are shown.

results also do not rule out the possibility of an adatom breaking a surface dimer bond followed by the transfer of a hydrogen atom to the adatom. This would only result in H segregation but not the SiH unit.

4.5 Discussion

Introduction of atomic hydrogen during low temperature Si MBE can cause an early breakdown of epitaxy [3]. However, conventional MBE results in epitaxial films even with a uniform surface coverage of 1 ML [4]. These results appear to be contradictory but can be explained as follows. At low surface coverages, hydrogen atoms act as diffusion barriers which results in a dramatic increase in Si island density [7]. This accelerates the increase in surface roughness and causes an early breakdown of epitaxy. Our molecular dynamics simulations have provided some insight into the mechanism of epitaxy at large hydrogen coverages. The simulations suggest that the incident silicon atom is subplanted during epitaxy on hydrogen-terminated Si(001) surfaces. On the dihydride-terminated surface, it appears that the SiH₂ unit segregates on the surface which is in agreement with the experimental observations [5, 6]. The subplantation probability was found to rise very rapidly with the incident particle energy. On the monohydride-terminated surface, the results are less conclusive. It appears that the SiH unit segregates to the surface at least on some occasions. This would be consistent with the observed surface segregation of hydrogen [42].

It is instructive to compare these results with the case of epitaxy on a

clean Si(001)- 2×1 surface. Molecular dynamics simulations have shown the opening of a dimer when an adatom is in the vicinity [43]. Subplantation of the incident Si atom has also been observed occasionally [44, 45] in MD simulations. However, for epitaxial growth it is not necessary for the incident atom to be subplanted. On a hydrogen-terminated silicon surface (with high coverage), there are no good epitaxial sites at the level of hydrogen atoms. It appears that (at least on the dihydride-terminated surface) epitaxial layers are produced by subplanting the incident silicon atom.

It was mentioned earlier that both the monohydride- and dihydride-terminated Si(001) surfaces have no dangling bonds. This makes these surfaces extremely unreactive. A dihydride-terminated surface can resist oxidation for as long as 12 hours in a laboratory atmosphere [46]. A monohydride-terminated surface remains (2×1) reconstructed even after exposure to air for a few minutes [47]. The possibility of doing epitaxy on such surfaces with sputter deposition is therefore extremely interesting. A problem with sputter deposition is the implantation of energetic Ar recoils in the film. This can be overcome with techniques such as pulsed laser deposition which produce a hyperthermal beam of silicon atoms. One might then be able to deposit epitaxial silicon films even under high vacuum conditions.

Bibliography

- [1] B.A. Joyce, J.H. Neave, and B.E. Watts, 'The influence of substrate surface conditions on the nucleation and growth of epitaxial silicon films,' *Surf. Sci.* **15**, 1(1969).
- [2] J.M. Charig and D.K. Skinner, 'Carbon contamination of Si(111) surfaces,' *Surf. Sci.* **15**, 277(1969).
- [3] D.P. Adams, S.M. Yalisove, and D.J. Eaglesham, 'Effect of hydrogen on surface roughening during Si homoepitaxial growth,' *Appl. Phys. Lett.* **63**, 3571(1993).
- [4] D.J. Eaglesham, G.S. Higashi, and M. Cerullo, '370°C clean for Si molecular beam epitaxy using a HF dip,' *Appl. Phys. Lett.* **59**, 685(1991).
- [5] T. Ohmi, T. Ichikawa, H. Iwabuchi, and T. Shibata, 'Formation of device-grade epitaxial silicon films at extremely low temperatures by low energy bias sputtering,' *J. Appl. Phys.* **66**, 4756(1989).
- [6] C.-C. Chen, D.L. Smith, G.B. Anderson, and S.B. Hagstrom, 'Low temperature epitaxy on H-passivated Si(100) by sputter deposition,' *Mat. Res. Soc. Symp. Proc.* **259**, 443(1992).

- [7] T. Vasek and M.G. Lagally, presented at the American Vacuum Society Meeting, Orlando, 1993.
- [8] J.J. Boland, 'Scanning tunneling microscopy of the interaction of hydrogen with silicon surfaces,' *Adv. Phys.* **42**, 129(1993).
- [9] C. Astaldi, A. Bianco, S. Modesti, and E. Tosatti, 'Vibrational spectra of atomic H and D on Cu(110) — evidence for H quantum delocalization,' *Phys. Rev. Lett.* **68**, 90(1991).
- [10] C.G. Van de Walle, P.J.H. Denteneer, Y. Bar-Yam, and S.T. Pantelides, 'Theory of hydrogen diffusion and reactions in crystalline silicon,' *Phys. Rev. B* **39**, 1079(1989).
- [11] S. Estreicher, 'Equilibrium sites and electronic structure of interstitial hydrogen in Si,' *Phys. Rev. B* **36**, 9122(1987).
- [12] I. Kwon, R. Biswas, and C.M. Soukoulis, 'Molecular dynamics simulations of defect formation in hydrogenated amorphous silicon,' *Phys. Rev. B* **45**, 3332(1992).
- [13] P.M. Agrawal, D.L. Thompson, and L.M. Raff, 'Computational studies of $\text{SiH}_2 + \text{SiH}_2$ recombination reaction dynamics on a global potential surface fitted to *ab initio* and experimental data,' *J. Chem. Phys.* **88**, 5948(1988).
- [14] T. Ohira, presented at the Materials Research Society Conference, San Francisco, 1994.

- [15] M.V.R. Murty and H.A. Atwater, 'Empirical interatomic potential for Si-H interactions,' *Mat. Res. Soc. Symp. Proc.* **317**, 1993.
- [16] F.H. Stillinger and T.A. Weber, 'Computer simulation of local order in condensed phases of silicon,' *Phys. Rev.* **B31**, 5262(1985).
- [17] J. Tersoff, 'Empirical interatomic potential for silicon with improved elastic properties,' *Phys. Rev.* **B38**, 9902(1988).
- [18] J. Tersoff, 'Modeling solid-state chemistry — interatomic potentials for multicomponent systems,' *Phys. Rev.* **B39**, 5566(1989).
- [19] D.W. Brenner, 'Empirical potential for hydrocarbons for use in simulating the chemical vapor deposition of diamond films,' *Phys. Rev.* **B42**, 9458(1990).
- [20] *Handbook of Chemistry and Physics*, CRC Press, 72nd ed., 1991-92.
- [21] C. Kittel, *Introduction to Solid State Physics*, 6th ed., Wiley, New York, 1986.
- [22] M.S. Gordon, T.N. Truong, and E.K. Bonderson, 'Potential primary pyrolysis processes for disilane,' *J. Am. Chem. Soc.* **108**, 1421(1986).
- [23] *JANAF Thermochemical Tables*, 3rd ed., Dow Chemical Company, 1985.
- [24] B. Beagley, A.R. Conrad, J.M. Freeman, J.J. Monaghan, B.G. Norton, and G.C. Holywell, 'Electron diffraction studies of the hydrides Si_2H_6 and P_2H_4 ,' *J. Molec. Struct.* **11**, 371(1972).

- [25] J.R. Durig and J.S. Church, 'Vibrational spectra of crystalline disilane and disilane-d₆, barrier to internal rotation and some normal coordinate calculations on H₃SiSiH₃, H₃SiNCO, and H₃SiNCS,' J. Chem. Phys. **73**, 4784(1980).
- [26] S.D. Peyerimhoff and R.J. Buenker, 'Potential energy curves and transition moments for the low-lying electronic states of the Si₂ molecule,' Chem. Phys. **72**, 111(1982).
- [27] R.D. Verma and P.A. Warsop, 'The adsorption spectrum of the Si₂ molecule,' Can. J. Phys. **41**, 152(1963).
- [28] D.E. Milligan and M.E. Jacox, 'Infrared and ultraviolet spectra of the products of the vacuum-ultraviolet photolysis of silane isolated in an argon matrix,' J. Chem. Phys. **52**, 2594(1970).
- [29] C. Yamada and E. Hirota, 'Detection of the silyl radical SiH₃ by infrared diode-laser spectroscopy,' Phys. Rev. Lett. **56**, 923(1986).
- [30] P.W. Atkins, *Molecular Quantum Mechanics*, 2nd ed., Oxford University Press, New York, 1983.
- [31] B.I. Craig and P.V. Smith, 'The structure of the Si(100)2×1-H surface,' Surf. Sci. **226**, L55(1990).
- [32] Y.J. Chabal, G.S. Higashi, K. Raghavachari, and V.A. Burrows, 'Infrared spectroscopy of Si(111) and Si(100) surfaces after HF treatment — hydrogen termination and surface morphology,' J. Vac. Sci. Technol. **A7**, 2104(1989).

- [33] C.J. Wu and E.A. Carter, 'Adsorption of hydrogen atoms on the Si(100)- 2×1 surface — implications for the H_2 desorption mechanism,' *Chem. Phys. Lett.* **185**, 172(1991).
- [34] Y.J. Chabal and K. Raghavachari, 'New ordered structure for the H-saturated Si(100) surface — the (3×1) phase,' *Phys. Rev. Lett.* **54**, 1055(1985).
- [35] J.E. Northrup, 'Structure of Si(100)-H — dependence on the H chemical potential,' *Phys. Rev. B* **44**, 1419(1991).
- [36] H.H. Qi, P.E. Gee, and R.F. Hicks, 'Infrared study of hydrogen adsorbed on $c(2\times 8)$ and (2×6) GaAs(100),' *Phys. Rev. Lett.* **72**, 250(1994).
- [37] S.M. Myers, M.I. Baskes, H.K. Birnbaum, J.W. Corbett, G.G. DeLeo, S.K. Estreicher, E.E. Haller, P. Jena, N.M. Johnson, R. Kirchheim, S.J. Pearton, and M.J. Stavola, 'Hydrogen interactions with defects in crystalline solids,' *Rev. Mod. Phys.* **64**, 559(1992).
- [38] C.G. Van de Walle, 'Energies of various configurations of hydrogen in silicon,' *Phys. Rev. B* **49**, 4579(1994).
- [39] *Hydrogen in Semiconductors*, ed. J.I. Pankove and N.M. Johnson, *Semiconductors and Semimetals Vol. 34*, Academic Press, 1991.
- [40] R.A. Street, *Hydrogenated Amorphous Silicon*, Cambridge University Press, New York, 1991.
- [41] P.C. Zalm, 'Ion-beam assisted etching of semiconductors,' *Vacuum* **36**, 787(1986).

- [42] M. Copel and R.M. Tromp, 'H-Coverage dependence of Si(001) homoepitaxy,' *Phys. Rev. Lett.* **72**, 1236(1994).
- [43] D.W. Brenner and B.J. Garrison, 'Microscopic mechanisms of reactions associated with silicon MBE – a molecular dynamics investigation,' *Surf. Sci.* **198**, 151(1988).
- [44] D. Srivastava, B.J. Garrison, and D.W. Brenner, 'Anisotropic spread of surface dimer openings in the initial-stages of the epitaxial-growth of Si on Si(100),' *Phys. Rev. Lett.* **63**, 302(1989).
- [45] C. Roland and G.H. Gilmer, 'Epitaxy on surfaces vicinal to Si(001). 1. Diffusion of silicon adatoms over the terraces,' *Phys. Rev. B* **46**, 13248(1992).
- [46] T. Takahagi, I. Nagai, A. Ishitani, H. Kuroda, and Y. Nagasawa, 'The formation of hydrogen passivated silicon single-crystal surfaces using ultraviolet cleaning and HF etching,' *J. Appl. Phys.* **64**, 3516(1988).
- [47] M. Hirose, private communication.

Chapter 5

LOW TEMPERATURE ION BEAM-INDUCED Si(001)-2×1 SURFACE RECONSTRUCTION

What one man can invent another can discover.

– *Sherlock Holmes*, The Adventure of the Dancing Men

Sir Arthur Conan Doyle

5.1 Introduction

Surface cleaning of silicon is a recurring theme during VLSI processing. A passivating surface layer is always present to protect the underlying silicon from contaminants. The choice of the passivation layer depends on the processing step. The chemical oxide is used prior to the gate oxidation step in

MOS device fabrication, formation of refractory metal silicides such as WSi_2 , and Ti-W barrier layers. Hydrogen termination is used prior to the deposition of transition metals to form silicides such as CoSi_2 . The choice of the passivation layer to form the metal silicides is related to the ability of the metal atoms to reduce the oxide [1].

A clean silicon wafer is immediately covered with an oxide when exposed to atmosphere. This native oxide grows to a thickness of $\sim 1 - 2$ nm and passivates the underlying silicon. The surface also frequently contains hydrocarbons and metal contaminants. A chemical oxide prepared by oxidation in an alkaline or acidic peroxide solution is frequently preferred over the native oxide. Another common way of passivating the silicon surface is to terminate the surface dangling bonds with hydrogen. This is usually achieved by a dilute HF dip which etches the oxide and terminates the surface with hydrogen atoms.

For silicon homoepitaxy, the passivation layer is removed to obtain a clean, reconstructed $\text{Si}(001)\text{-}2\times 1$ surface. Thermal desorption of the oxide requires heating to 800°C [2]. Alternatively, the oxide can be removed by using an ion beam of silicon or a noble gas such as argon. Cleaning with a silicon beam reduces the desorption temperature to about 700°C [3]. Sputtering with Ar^+ ions can be done at $\sim 500^\circ\text{C}$ but a high temperature anneal is frequently required to remove the ion damage. Complete thermal desorption of hydrogen occurs at $\sim 500^\circ\text{C}$ [4].

A number of techniques are being developed to reduce the processing temperature in epitaxy, oxidation and doping. A method for the preparation of clean $\text{Si}(001)\text{-}2\times 1$ surfaces at low temperatures is needed to complement

these processes. In this chapter, a method analogous to the sputtering of the SiO_x layer with noble gas ions is described to remove the hydrogen from the surface. Reconstructed $\text{Si}(001)\text{-}2\times 1$ surfaces have been prepared even at room temperature ($\sim 50^\circ\text{C}$) in this way. Silicon films were deposited after ion irradiation as a test of the cleaning process.

5.2 Beam-Induced Reconstruction of Silicon

5.2.1 Sample Preparation

The chemical cleaning of the silicon wafers is described in Appendix A. After the dilute HF dip, a hydrophobic, unreconstructed and nominally dihydride-terminated $\text{Si}(001)$ surface is obtained. The wafer was then loaded into the UHV chamber and baked overnight at the desired ion irradiation temperature.

The Kaufman source was used to generate Ar^+ ions. The Ar^+ ion energy was 50 eV in all experiments, and the ions were incident along the $\langle 100 \rangle$ azimuth within 5° . The incident angle of the beam was varied in some cases to study the effects. An electron cyclotron resonance source was used to generate He^+ ions. The source was operated at 130 W and a pressure of 0.07 Pa. The substrate was oriented at 45° with respect to the axis of the ECR ion source. Both argon and helium were passed through a gas purifier rated to give a purity of 10 ppb. The surface morphology was monitored *in situ* using RHEED during ion irradiation and subsequent film growth.

5.2.2 Reflection High-Energy Electron Diffraction

The RHEED pattern along the $\langle 110 \rangle$ azimuth from an as-inserted Si(001) wafer is shown in Fig. 5.1(a). A (1×1) pattern characteristic of a dihydride-terminated Si(001) surface is observed. The surface was then irradiated with an ion beam. During ion irradiation, the half-order lines appear gradually indicating the loss of surface hydrogen. The RHEED pattern after a dose of 1.5×10^{16} Ar⁺ ions/cm² and an incidence angle of 45° is shown in Fig. 5.1(b). The substrate temperature was 190°C. The ion flux was $\sim 5 \times 10^{12}$ /cm²-s.

At 150°C and below, we were unable to obtain reconstructed Si(001) surfaces with 50 eV Ar⁺ ions incident at 45°. The surfaces gradually became amorphous upon ion bombardment. However, a more grazing angle of 65° with respect to the surface normal resulted in a (2×1) reconstructed surface. A (2×1) surface prepared at 100°C with an Ar⁺ flux of 2×10^{13} ions/cm²-s for 10 min. is shown in Fig. 5.1(c). The same process at 60°C resulted in amorphization of the surface region. Thus, with 50 eV Ar⁺ ion irradiation, (2×1) reconstructed surfaces were observed at 100°C and above.

Exposure to a helium plasma, generated using an ECR source, also produced (2×1) surfaces. The ECR source was operated at 130 W and a pressure of 0.07 Pa. A crude Langmuir probe measurement indicated He⁺ ion energies in the range of 10 – 30 eV. (The He⁺ flux is estimated to be 5×10^{13} /cm²-s to within a factor of 3). RHEED patterns after He⁺ ion bombardment for 25 min. at 190°C and 20 min. at 50°C are shown in Fig. 5.1(d) and(e) respectively. To our knowledge, this is the first observation of a (2×1) reconstructed Si(001) surface produced at “room temperature.”

It is noted that reconstruction lines were clearly visible after a quarter of the total dose used in the above experiments. It is not possible to distinguish between a monohydride-terminated surface and a clean Si(001)- 2×1 surface from the geometrical features in a RHEED pattern. Molecular dynamics simulations described below suggest that the surfaces are almost free of hydrogen for the dose of ions used in these experiments.

5.2.3 Transmission Electron Microscopy of Silicon Films

Silicon films were deposited on the Si(001)- 2×1 surfaces produced by ion irradiation. The deposition temperature was the same as the ion irradiation temperature. Figures 5.2 and 5.3 show high resolution XTEM images of films grown on substrates prepared at 190°C by Ar⁺ and He⁺ ion beam-induced reconstruction respectively. The growth rates were 0.09 and 0.03 nm/s respectively. The film-substrate interface is visible presumably due to carbon and/or oxygen impurities. In both cases, the film growth starts out epitaxially. This is in sharp contrast to the film deposited on a dihydride-terminated surface (see Fig. 4.3) which is completely amorphous. The films, however, do contain some defects. A stacking fault is seen to originate at the film/substrate interface in Fig. 5.3. The crystal-state — amorphous-state transition is also seen in these films, as expected.

Figure 5.4 shows the high resolution XTEM image of a silicon film deposited at 100°C following Ar⁺ ion beam-induced reconstruction. The film-substrate interface proved hard to locate due to the thickness fringes. The

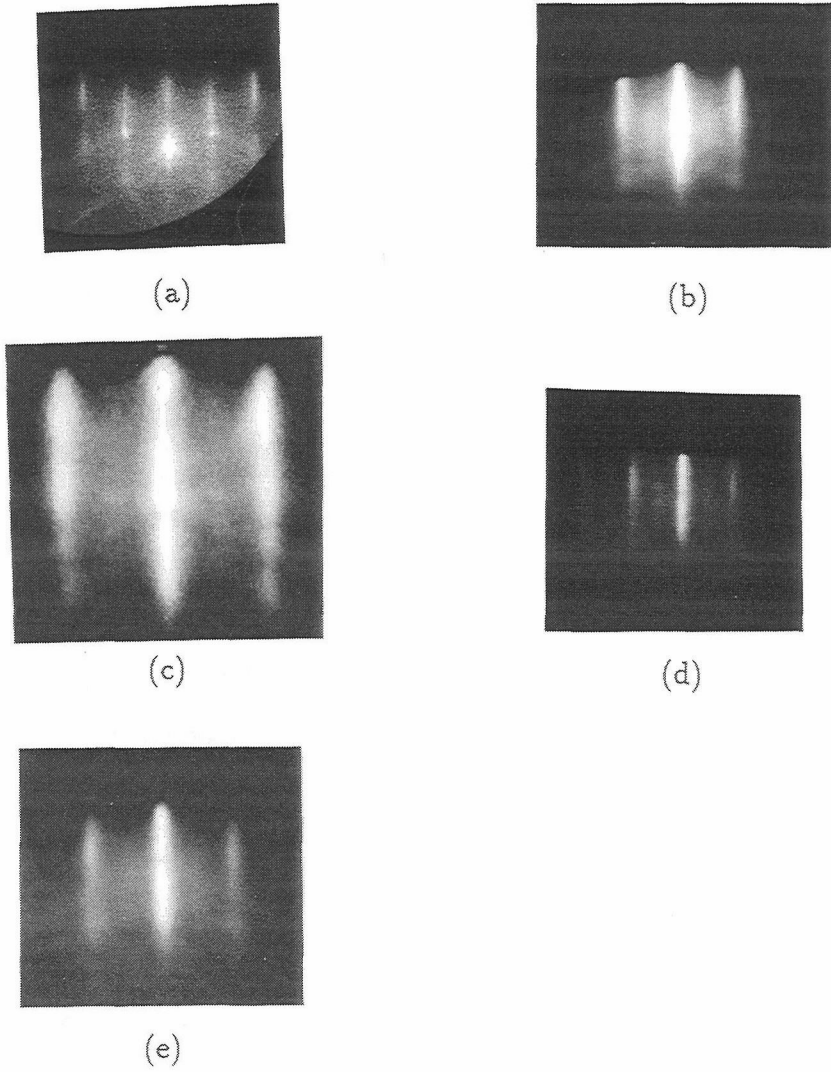


Figure 5.1: RHEED pattern (a) immediately after HF dip; after 50 eV Ar^+ ion irradiation at (b) 190°C , and (c) 100°C ; and after exposure to He^+ ions at (d) 190°C , and (e) 50°C .

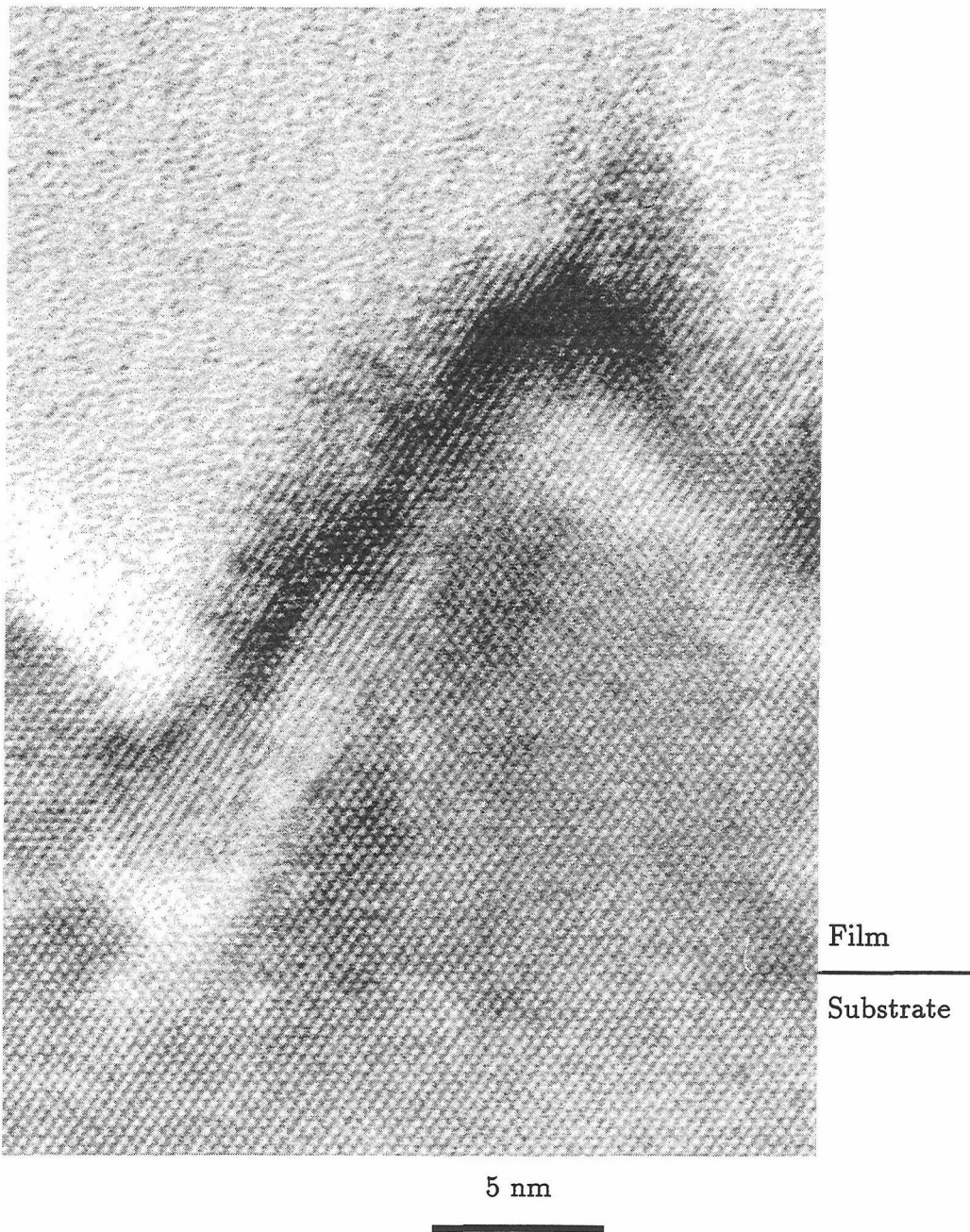


Figure 5.2: HRTEM image of a silicon film deposited after beam-induced reconstruction using 50 eV Ar^+ ions incident at 45° with respect to the substrate normal. The substrate temperature was 190°C and the growth rate was 0.09 nm/s.

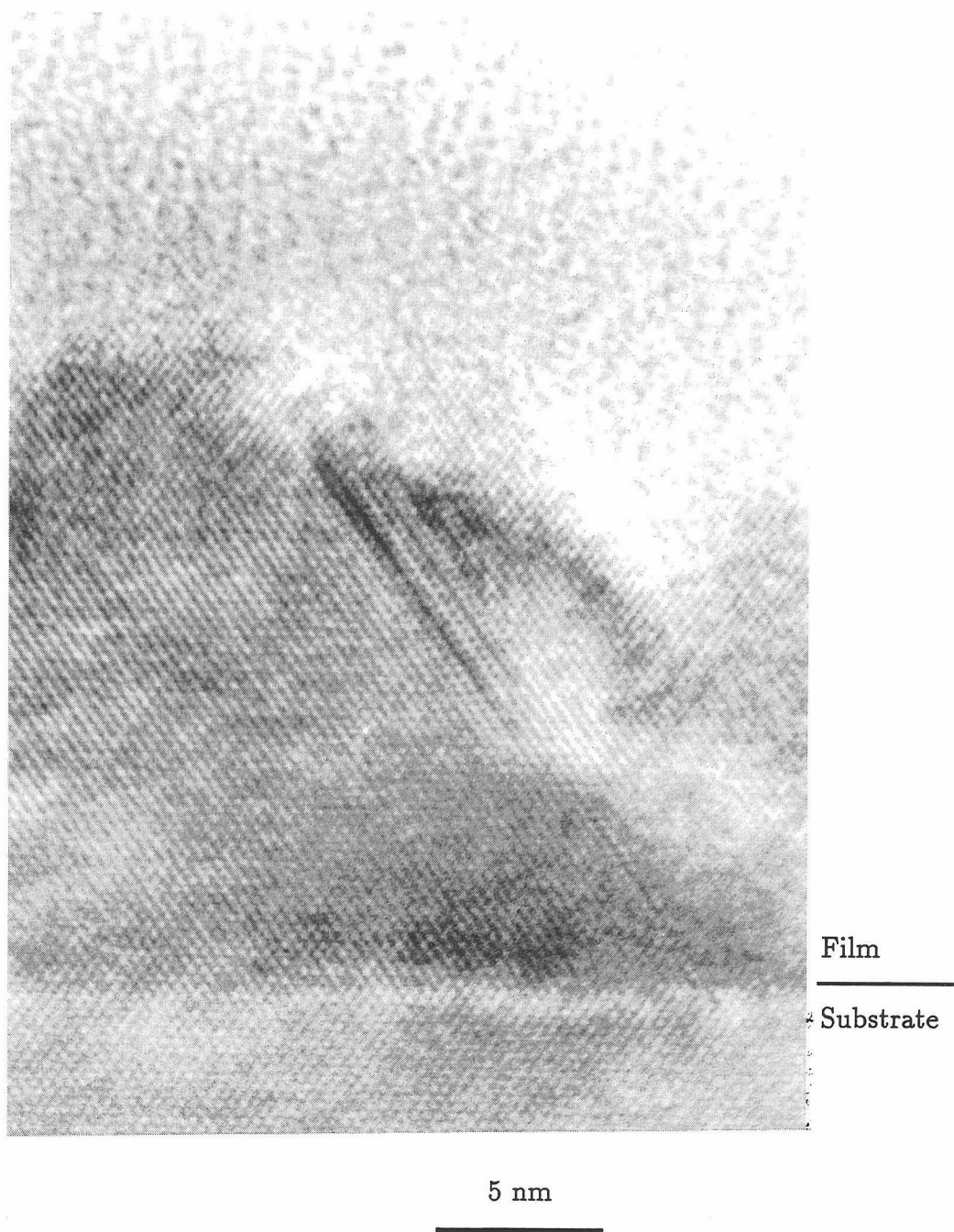


Figure 5.3: HRTEM image of a silicon film deposited after beam-induced reconstruction using He^+ ions. The substrate temperature was 190°C and the growth rate was 0.03 nm/s .

film was judged to be epitaxial from the measured thickness on the quartz crystal monitor. The rough crystal-amorphous interface is also indicative of an initial regime of epitaxial growth. Figure 5.5 shows the XTEM image of a film deposited at 50°C after exposure to He⁺ ions. The very rapid transformation to amorphous film deposition at such low temperatures makes it difficult to say if the film is epitaxial. A faint contrast marked by arrows in Fig. 5 is suggestive of a film-substrate interface and an epitaxial thickness of about 0.5 – 1 nm.

5.3 Molecular Dynamics Simulations of the Beam-Induced Reconstruction

To understand the nature of the depletion of surface hydrogen, molecular dynamics simulations were used. The Si-Si, Si-H and H-H interatomic potentials were described in Chapter 3. The Ar-H and Ar-Si interactions were taken to be purely repulsive, with Born-Mayer type expressions:

$$V(r) = A \exp(-\lambda r) f_c(r) \quad (5.1)$$

For the Ar-Si potential, the Abrahamson parameters $A = 5941.7$ eV and $\lambda = 3.6641 \text{ \AA}^{-1}$ were used [5]. The potential was cutoff with $R = 3.25 \text{ \AA}$ and $D = 0.15 \text{ \AA}$. The parameters $A = 746.6$ eV and $\lambda = 4.1898 \text{ \AA}^{-1}$ for the Ar-H potential were likewise obtained by combining the repulsive part of the H-H potential [6] and the Ar-Ar potential [5]. The potential was cutoff with $R = 2.35 \text{ \AA}$ and $D = 0.15 \text{ \AA}$. The cutoff function, $f_c(r)$, has the form given in Eq. 3.18.

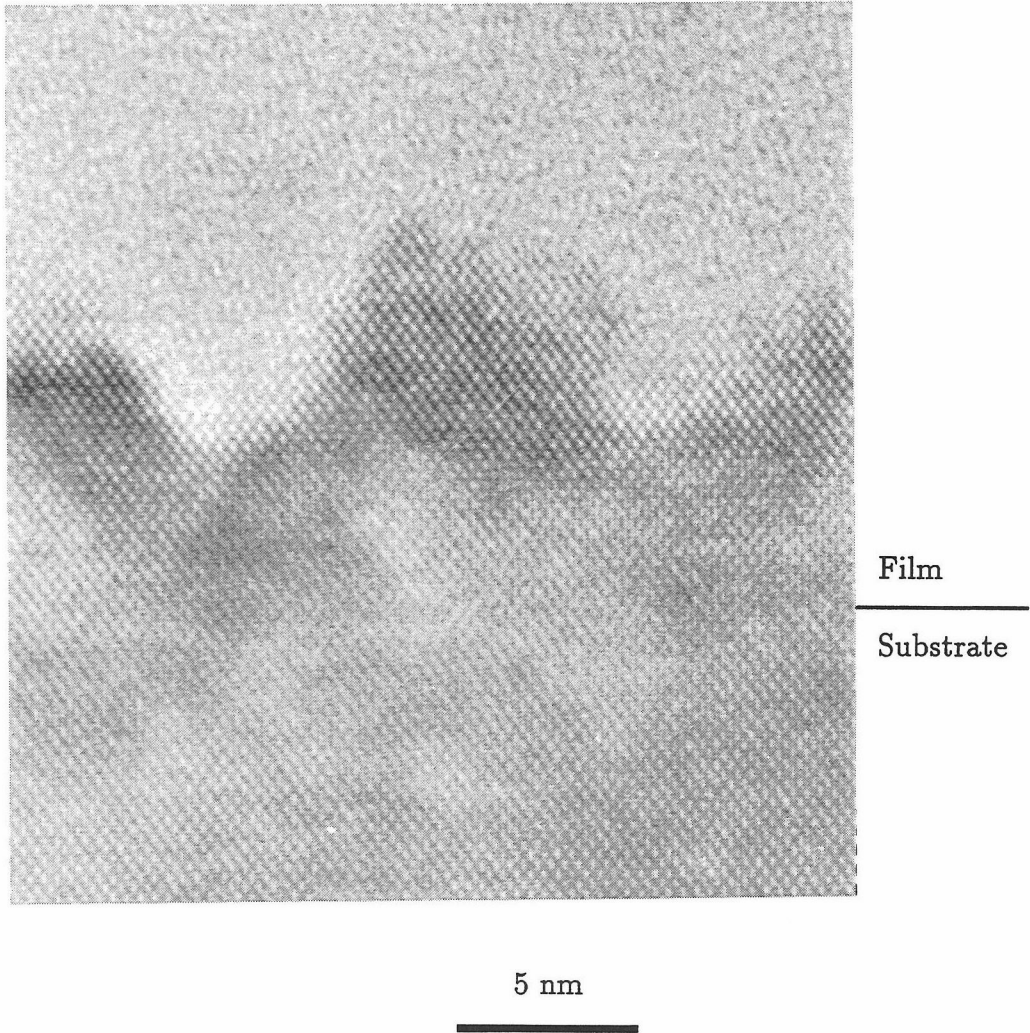


Figure 5.4: Silicon film deposited after beam-induced reconstruction using 50 eV Ar^+ ions incident at 65° with respect to the substrate normal. The substrate temperature was 100°C and the growth rate was 0.03 nm/s.

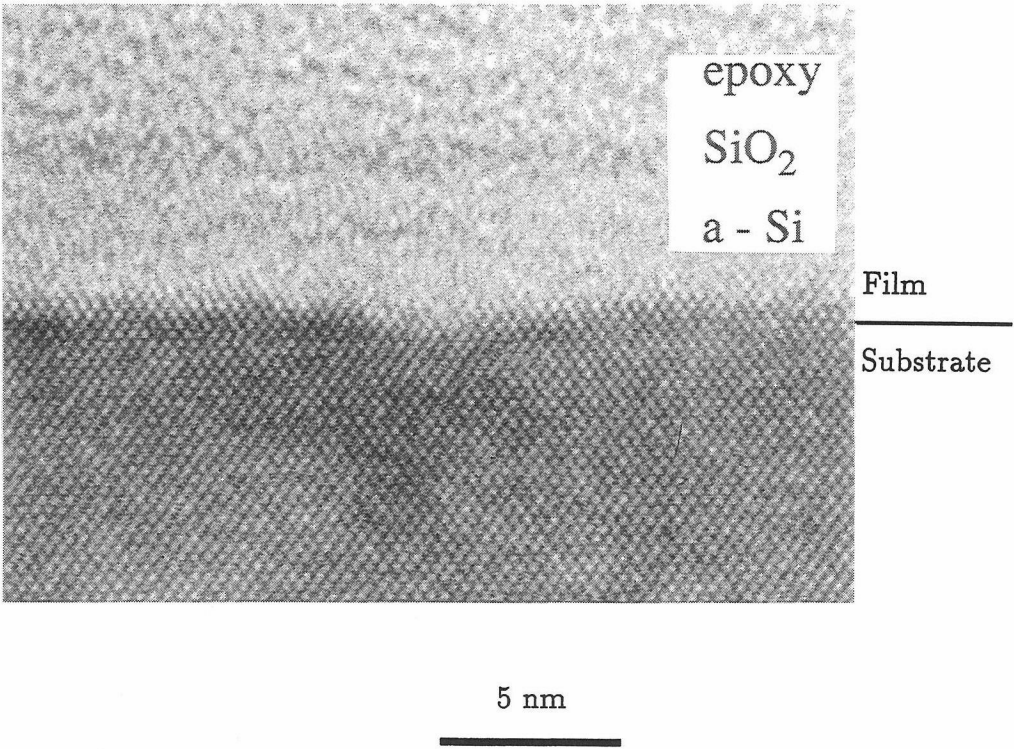


Figure 5.5: Silicon film deposited after beam-induced reconstruction using He^+ ions. The substrate temperature was 50°C and the growth rate was 0.03 nm/s . The thin oxide at the surface is also visible.

In the simulations, Ar ions were incident at 50° with respect to the surface normal and 5° from the $\langle 100 \rangle$ azimuth. There were a total of 24 Si layers with 100 atoms/layer in the substrate. The sputtering of H and Si atoms was estimated from both monohydride- and dihydride-terminated Si(001) surfaces. Periodic boundary conditions were used in the transverse directions and the bottom two layers were held rigid. The starting substrate temperature was 0 K and the simulations were carried out for 1 ps. The incident Ar ion energy ranged from 15 to 50 eV. The results presented below are all averaged over 50 simulations at each energy.

On both dihydride- and monohydride-terminated surfaces, hydrogen was removed by both sputtering and implantation. The hydrogen sputtering and implantation yield are shown in Figs. 5.6 and 5.7 for the dihydride- and monohydride-terminated Si(001) surfaces. The sputtered species observed were atomic H, H_2 , and SiH_2 . If sputtering were independent of the bonding of hydrogen atoms, one would expect the yield from the dihydride surface to be twice that from the monohydride surface. The hydrogen sputtering yield from the dihydride surface is seen to be much more than twice that of the monohydride surface. At 25 eV and below, the sputtering yield from the monohydride surface is seen to be negligible whereas that from the dihydride surface is finite. The implantation yields are seen to be comparable to the sputter yields. Due to the short time period of the simulations, it is not clear whether the implanted hydrogen would diffuse into the bulk or toward the surface. Even if all the hydrogen is lost only by sputtering, the calculated yields suggest that almost all the surface hydrogen was removed by ion irradiation in the experiments described in Section 5.2.2. It was reported in

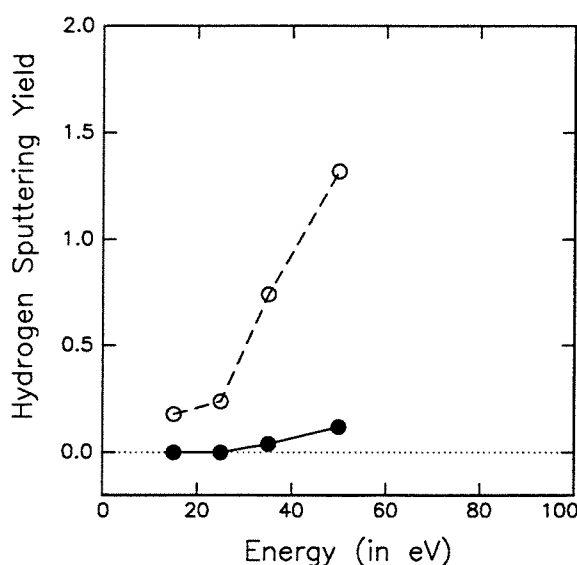


Figure 5.6: The sputtering yield of hydrogen versus Ar ion energy from (a) \circ dihydride-terminated Si(001)- 1×1 surface, and (b) \bullet monohydride-terminated Si(001)- 2×1 surface. The lines are spline fits to guide the eye.

Ref. [7] that Si films deposited on a monohydride-terminated surface were only epitaxial above 200°C (for a growth rate of 1 ML/min). The growth of epitaxial films after beam-induced reconstruction (Section 5.2.3) suggests that most of the surface hydrogen was removed.

A surprising result was the sputtering yield of silicon which is shown in Fig. 5.8. On dihydride-terminated surfaces, there is strong repulsion between H atoms bonded to neighboring Si atoms. This gives rise to a rather low threshold for the sputtering of the SiH_2 unit. The onset of SiH_2 sputtering can be seen at about 25 eV incident ion energy. It is noted that the sputtering yield of silicon from a clean surface is negligible ($< 1\%$) at these energies [8]. This may be, therefore, considered as a case of chemically-enhanced physical sputtering of silicon.

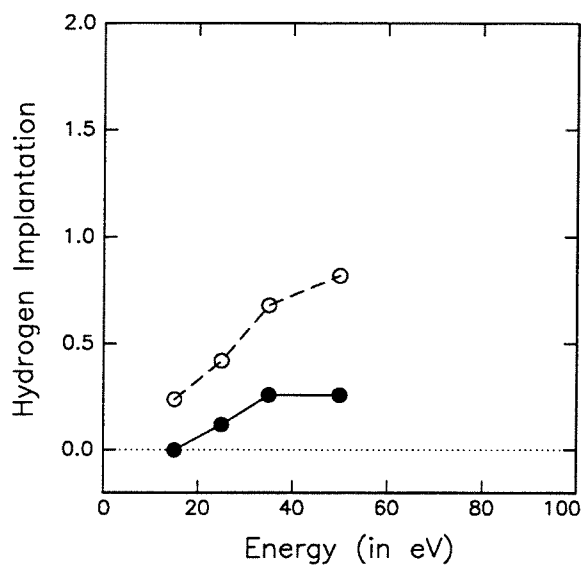


Figure 5.7: The implantation of surface hydrogen atoms versus Ar ion energy from (a) \circ dihydride-terminated Si(001)- 1×1 surface, and (b) \bullet monohydride-terminated Si(001)- 2×1 surface. The lines are spline fits to guide the eye.

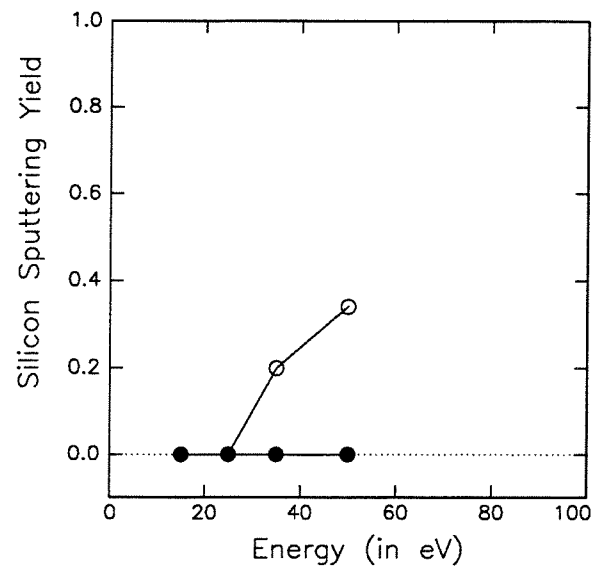


Figure 5.8: The silicon sputtering yield from (a) \circ dihydride-terminated Si(001)- 1×1 surface, and (b) \bullet monohydride-terminated Si(001)- 2×1 surface. The lines are spline fits to guide the eye.

5.4 Discussion

Ion bombardment also results in atomic displacements in the silicon substrate. The surface can be amorphized if the beam flux is too high and insufficient time is available for annealing. At a more moderate beam flux, the surface roughens but does not become amorphous. The broadened Bragg rods in Fig. 5.1(b) and (c) are indicative of rough surfaces. Significant surface and sub-surface atomic displacements can occur with the use of 50 eV Ar^+ ions as seen in Section 3.4. Helium ion bombardment produces more smoother surfaces compared to argon ions. For a two-body collision, the energy transfer from an incident atom of mass M_1 to a target atom of mass M_2 is determined by the $\gamma = 4M_1M_2/(M_1 + M_2)^2$ factor. Helium ions with $\gamma = 0.64$ can transfer energy much more efficiently to hydrogen atoms compared to argon ions with $\gamma = 0.12$. The helium beam-induced reconstructed surface shown in Fig. 5.1(d) looks similar to a (2×1) surface obtained by thermal desorption of hydrogen. The “room temperature” surface shown in Fig. 5.1(e), however, shows some broadening of the Bragg rods. The improvement in the surface morphology by going to more grazing angles of incidence can be attributed to the increased energy loss of the ions at the surface.

After an HF dip, the surface frequently has some amount of physisorbed hydrocarbons [9]. At the extremely low temperatures used in the experiments above, these contaminants may not be desorbed during the bake before ion irradiation. It is remarkable that (2×1) surfaces could still be obtained. It is possible that small amounts of physisorbed hydrocarbons can also be

removed by the ion beam.

Surface cleaning with remote hydrogen and helium plasmas was reported at temperatures 250°C and higher in Refs. [10, 11]. A (3×1) reconstructed surface was obtained after exposure to a remote hydrogen plasma which changed to a (2×1) structure after exposure to a remote He plasma. The use of a hydrogen beam had the added advantage of reducing the C and O contamination at the substrate surface.

The beam-induced reconstruction results suggest that low energy ion beams can be used to control the hydrogen coverage on the surface. The preferential removal of dihydride-units can be used to keep the H surface coverage below 1 ML, which is beneficial for the growth of epitaxial films by MBE. Another application is the low temperature chemical vapor deposition of silicon where growth rates are rather low and limited by the hydrogen desorption from the surface [12]. Hydrogen removal with low energy ion beams can increase the growth rate tremendously.

In conclusion, the removal of surface hydrogen at low temperatures without causing damage to the silicon substrate has been demonstrated. The use of low energy ions incident at a grazing angle helps to keep most of the atomic displacements in the top layer(s). Both argon and helium ions have been used successfully for the beam-induced reconstruction, although helium ions gave slightly better results. The (2×1) surfaces thus prepared were suitable for silicon homoepitaxy. High resolution TEM images of silicon films have occasionally shown defects originating at the film/substrate interface indicating some ion damage. Molecular dynamics simulations have shown that sputtering of hydrogen from dihydride units was much higher than monohy-

drude units. A chemically-enhanced physical sputtering of silicon was also observed on hydrogen-adsorbed surfaces.

The phenomenon of beam-induced reconstruction deserves a further study. The use of lower energy ions and more grazing angles of incidence need to be investigated. The damage produced by the ions on scales larger than that observable in an XTEM image will have to be established for any application.

Bibliography

- [1] A.H. Reader, A.H. van Ommen, P.J.W. Weijs, R.A.M. Wolters, and D.J. Oostra, 'Transition-metal silicides in silicon technology,' Rep. Prog. Phys. **56**, 1397(1993).
- [2] A. Ishizaka and Y. Shiraki, 'Low temperature surface cleaning of silicon and its application to silicon MBE,' J. Electrochem. Soc. **133**, 666(1986).
- [3] M. Tabe, 'Etching of SiO₂ films by Si in ultrahigh vacuum,' Jpn. J. Appl. Phys. Part 1, **21**, 534(1982).
- [4] G. Schulze and M. Henzler, 'Adsorption of atomic hydrogen on clean cleaved silicon (111),' Surf. Sci. **124**, 336(1983).
- [5] A.A. Abrahamson, 'Born-Mayer type interatomic potential for neutral ground state atoms with $Z = 2$ to $Z = 105$,' Phys. Rev. **178**, 76(1969).
- [6] D.W. Brenner, 'Empirical potential for hydrocarbons for use in simulating the chemical vapor deposition of diamond films,' Phys. Rev. B **42**, 9458(1990).
- [7] M. Copel and R.M. Tromp, 'H-Coverage dependence of Si(001) homoepitaxy,' Phys. Rev. Lett. **72**, 1236(1994).

- [8] N. Matsunami, Y. Yamamura, Y. Itikawa, N. Itoh, Y. Kazumata, S. Miyagawa, K. Morita, R. Shimizu, and H. Tawara, 'Energy dependence of the ion-induced sputtering yields of monatomic solids,' *At. Data Nucl. Data Tables* **31**, 1(1984).
- [9] S. Nikzad, S.S. Wong, C.C. Ahn, A.L. Smith, and H.A. Atwater, 'In situ reflection electron energy loss spectroscopy measurements of low temperature surface cleaning for Si molecular beam epitaxy,' *Appl. Phys. Lett.* **63**, 1414(1993).
- [10] T. Hsu, L. Breaux, B. Anthony, S. Banerjee, and A. Tasch, 'Defect microstructure in low temperature epitaxial silicon grown by RPCVD,' *J. Elec. Mat.* **19**, 375(1990).
- [11] A. Mahajan, J. Irby, D. Kinosky, R. Qian, S. Thomas, S. Banerjee, A. Tasch, and T. Picraux, 'Si atomic layer epitaxy based on Si_2H_6 and remote He plasma bombardment,' *Thin Sol. Fi.* **225**, 177(1993).
- [12] S.M. Gates and S.K. Kulkarni, 'Hydrogen coverage during Si growth from SiH_4 and Si_2H_6 ,' *Appl. Phys. Lett.* **60**, 53(1992).

Chapter 6

SUMMARY

“That is final,” said Lestrade.

“Yes, that is final,” I (Watson) involuntarily echoed.

“It is final,” said Holmes.

– The Adventure of the Norwood Builder

Sir Arthur Conan Doyle

6.1 Silicon Molecular Beam Epitaxy

Historically, advancing integrated circuit technology and understanding the physics of thin film growth have served as two motivating factors for studying semiconductor epitaxy. Silicon epitaxy has particularly benefitted from the concurrence of these factors. This has led to the development of many different schemes for silicon film deposition. The optimum ambient conditions for growing defect-free epitaxial films have been studied in great detail. There

has also been a very consistent drive toward lower growth temperatures. Molecular beam epitaxy made it possible to grow Si films at temperatures as low as 500°C. Although not used in the integrated circuit industry because of low throughput and excessive maintenance costs, the possibility of fabricating layered structures with exceptional control down to the monolayer level made it popular as a research tool. It also allowed one to control the different variables associated with thin film growth. As a result, many of the phenomena associated with the surface and growth at temperatures greater than about 400°C are known at the atomic scale.

Molecular beam epitaxy at temperatures lower than 400°C proceeds by the now familiar crystal-state—amorphous-state transition. It was the discovery of this phenomenon [1, 2] which renewed interest in the physics of low temperature silicon MBE. As discussed in Chapter 1, the number of variables influencing atom migration on the surface are staggering. Nowhere are these more important than in low temperature epitaxy. It was the objective of this work to explain their influence on the film microstructure. The following chapter summarizes the current understanding of silicon molecular beam epitaxy at low temperatures and issues that need to be further addressed.

6.2 Summary of Results

An atomistic model, the twin-boundary/facet mechanism, has been proposed for the crystal-state—amorphous-state transition observed in low temperature silicon molecular beam epitaxy. The increase in surface roughness

during film growth has been directly tied to the breakdown of epitaxy. Adsorbates such as carbon and oxygen can dramatically increase the surface roughness even at small coverages (~ 0.01 ML). They thus play an indirect role by accelerating the surface roughening rate, but do not directly induce the crystalline-to-amorphous transition on the smooth starting surface, for coverages of interest here ($0 < \theta < 0.2$ ML).

Films with improved crystalline quality were deposited by ion beam-assisted molecular beam epitaxy. Atomic force microscopy revealed that the main effect of low energy Ar^+ ion irradiation was surface smoothing.

Molecular dynamics simulations suggest that epitaxy on hydrogen-terminated silicon surfaces (at high hydrogen coverage) proceeds by subplantation of the incident Si atom and segregation of SiH_x units. The remarkable success of sputter deposition in growing epitaxial films on a dihydride-terminated $\text{Si}(001)$ surface is explained by the very rapid rise in the subplantation probability with the incident Si atom energy.

An empirical interatomic potential has been developed to describe Si-H interactions. This can be used, with caution, for molecular dynamics investigations of hydrogen-terminated silicon surfaces, chemical vapor deposition of silicon and hydrogenated amorphous silicon.

A technique for low temperature $\text{Si}(001)\text{-}2\times 1$ substrate preparation was developed to complement the various low temperature processes that are being developed for device fabrication. This was achieved by low energy noble gas ion (Ar^+ or He^+) irradiation of a nominally dihydride-terminated $\text{Si}(001)\text{-}1\times 1$ surface. Reconstructed $\text{Si}(001)\text{-}2\times 1$ surfaces were prepared at temperatures as low as 100°C . Silicon films deposited on such surfaces were

epitaxial.

6.3 The Crystal-state—Amorphous-state Transition

6.3.1 The Role of Surface Roughness

We will begin with the central issue of low temperature silicon homoepitaxy, namely, the crystal-state—amorphous-state transition. The twin-boundary/facet mechanism (Section 2.5) accounts for most of the observations regarding the breakdown of epitaxy. The evolution of surface morphology plays a key role in this transition. Due to limited surface diffusion at low temperatures, adatoms are not able to reach a step edge. Formation of islands on top of islands, i.e., 3-D islanding, is thus a consequence of limited adatom mobility. The sequence of atomic force microscope images (see Fig. 2.16) of a film at different thicknesses clearly shows the surface roughening. This can also be inferred from the broadening of the Bragg rods and the appearance of a transmission-like pattern in RHEED (see Fig. 2.17). This roughening is due to kinetic effects although some low index orientations such as the $\{111\}$ and $\{311\}$ will be favored by their lower surface energies. Such facets can be identified in XTEM images (Fig. 2.11). Now, twin boundaries can nucleate on $\{111\}$ oriented surfaces since they cost relatively little energy. A twin boundary is a mirror image along a $\{111\}$ plane. The crystal is still composed of even-member rings after the formation of a twin

boundary (which accounts for its low energy). However, when a twinned region grows and meets a different surface of the perfect crystal, it inevitably results in the formation of five- and seven-member rings. At intermediate temperatures ($150 \lesssim T \lesssim 400^\circ\text{C}$), crystalline silicon continues to grow after the formation of a grain boundary because a crystalline network (plus a grain boundary) has lower energy than an amorphous network. This can be seen in the XTEM images of films at 240 and 370°C (Section 2.4). Eventually, the number of such grain boundaries increases and there is a gradual transition to amorphous silicon deposition. At low temperatures ($T \lesssim 150^\circ\text{C}$), the transition to amorphous silicon seems to be direct (Section 5.2.3). This could be due to the nucleation and growth of amorphous silicon very rapidly after the formation of a twin boundary. It is noted that the breakdown of epitaxy in other semiconductors such as Ge and GaAs can be understood in an analogous way.

A fundamental difference between crystalline and amorphous silicon is in the type of ring structures formed by silicon atoms. Crystalline silicon contains only even-membered rings. The continuous random network models of amorphous silicon show that it consists of five- and seven-member rings in addition to six-membered rings (and higher odd and even-membered rings). A mechanism for the breakdown of epitaxy must therefore provide a way for the nucleation of odd-membered rings. The TBF mechanism leads to the *forced* formation of five- and seven-member rings. An alternate mechanism involving the trapping of an adatom at the T_4 site on a $\{111\}$ facet was proposed recently [3]. I do not see a simple way to distinguish between the two mechanisms from the current data. The low temperature Si films definitely

show twinning. We speculate that the TBF is operative at all temperatures and the other mechanism becomes active at some lower temperature.

At this point, it is appropriate to consider some of the remarks that have been made regarding low temperature silicon homoepitaxy. It was noted in Ref. [4] that epitaxy on Si(111) breaks down at the edge of a twin boundary. Molecular dynamics simulations also showed the breakdown of epitaxy at the edge of a stacking fault [4]. In Refs. [5, 6], it was observed that the stacking fault was preserved during room temperature epitaxy on Si(111)- 7×7 . Amorphous silicon starts right at the edge of the stacking fault, just as expected from the TBF mechanism. It has also been remarked that the reason for the finite epitaxial thickness on clean Si(001) is due to the difficulty of nucleating amorphous silicon on this surface [2]. This is borne by the TBF mechanism which requires the formation of a faceted surface to initiate the breakdown of epitaxy.

6.3.2 The Role of Low Energy Ion Irradiation

The TBF mechanism is an intrinsic mechanism, i.e., it predicts the breakdown of epitaxy even in the absence of any adsorbates. Thus, if one wants to deposit epitaxial silicon films on Si(001) at low temperatures, the surface roughening, and specifically, faceting must be prevented. Concurrent low energy ion irradiation during growth is one way to reduce the surface roughening. Films with increased epitaxial thickness were obtained with ion beam-assisted molecular beam epitaxy compared to conventional MBE. Argon ions with 50 eV gave slightly better results compared to 70 eV ions.

Improvement in the crystalline quality of the films was only observed above $\sim 300^\circ\text{C}$. This suggests that the dynamic annealing of ion damage was insufficient at the lower temperatures.

Ion bombardment can influence the evolution of surface morphology and film microstructure in a number of ways. We have observed two effects of low energy Ar^+ ion irradiation – surface smoothing and the removal of surface hydrogen. Surface smoothing can be clearly seen in the AFM images (Fig. 2.16) and RHEED patterns (Fig. 2.17) comparing the results of conventional MBE and IAMBE. The improvement in epitaxial thickness during IAMBE is thus explained by the surface smoothing effect of low energy argon ions. The removal of surface hydrogen is discussed later in this chapter.

Silicon films have now been deposited at low temperatures using energetic beam techniques in several different configurations. Direct silicon ion beam deposition has produced films with improved crystallinity [7, 8, 9]. However, the use of mass separated low energy beams results in rather low deposition rates ($\sim 0.01\text{ nm/s}$). Another concern is the C,O and N contamination in the film from CO and N_2 (both of mass 28 amu) in the beam. In fact, films deposited with ^{30}Si have been reported to be superior (in crystal quality) compared to films with ^{28}Si [8, 9]. Our investigation of IAMBE helped in determining the most important effect of ion irradiation, namely surface smoothing. These experiments were also limited by the ion flux and energy to some extent. Lower beam energies and higher fluxes may produce better films. Such a beam could be generated with, for example, an electron cyclotron source. By far, maximum improvement in crystal quality has been reported with low energy bias sputtering [10, 11] and ion beam sputtering

[12]. Sputtering produces Si atoms with hyperthermal energies (few eV) and this seems to be the optimum energy for surface smoothing.

While we have made significant progress toward gaining an atomistic view of the breakdown of epitaxy, the prediction of surface roughening is still an open and challenging problem. A prediction of the intrinsic epitaxial thickness, h_{epi} , would require such an effort. Experiments (Section 2.7.3 and [19]) suggest a value of β closer to 1 (see Section 1.5 for a discussion of kinetic roughening). If the roughening were only due to the random arrival of incident atoms, the maximum value of β would be $1/2$. Thus, for describing practical situations, the effects of adsorbates must be incorporated into the continuum/Monte Carlo models. The variation in the rms surface roughness for the IAMBE film was consistent with a simple model which predicted $R_q \sim \ln h$ asymptotically [13]. However, we had data spanning only one decade in the thickness h . It would be interesting to see if this were valid for a larger range of film thicknesses. Almost all the continuum models do not allow for overhangs. This is usually done to prevent h from being multiply-valued. However, low temperature Si growth can lead to void formation under certain conditions (Section 2.9 and [14, 15]). This suggests that one must allow for overhangs in a complete theory for Si growth.

6.3.3 The Role of Adsorbates

How do adsorbates such as carbon, oxygen and hydrogen influence epitaxy? Quite a few experiments in the 1960s were done in high vacuum conditions. As a result, even films deposited at high temperatures ($\sim 1000^\circ\text{C}$) often con-

tained defects [16]. It was later shown that deliberate carbon contamination of the surface results in a change from layer-by-layer growth to 3-D island nucleation and growth [17, 18]. A similar conclusion was drawn from RHEED observations during low temperature MBE and SIMS analysis (see Section 2.7.2). The SIMS analysis and the annealing experiment (see Section 2.8) also showed that carbon and oxygen contamination is not the direct cause of breakdown of epitaxy at low temperatures. However, even a small coverage (~ 0.01 ML) of carbon or oxygen can accelerate the rise in surface roughness and hence cause a premature breakdown of epitaxy.

The role of hydrogen is more complex. On one hand, introduction of atomic hydrogen can lead to an early crystal-state—amorphous-state transition [19]. On the other hand, conventional MBE gives epitaxial films even with a uniform surface coverage of 1 ML (Ref. [20] and Fig. 4.7). Finally, on a smooth, nominally dihydride-terminated Si(001)- 1×1 surface, an amorphous film is produced (Fig. 4.3). These results might seem contradictory but can be explained as follows. At low surface coverages, hydrogen atoms act as diffusion barriers which results in a dramatic increase in Si island density [21]. This, in turn, leads to an early breakdown of epitaxy [19]. Our molecular dynamics simulations have provided some insight into the mechanism of epitaxy with large hydrogen coverages. It appears that epitaxial films are obtained by subplantation, i.e., implantation of the incident Si atom one layer below the surface. On the monohydride-terminated Si(001)- 2×1 surface, the subplantation is driven in large part by the enthalpy difference (4.63 eV) between a vapor phase and a solid phase silicon atom. The predicted subplantation probability (0.1) was rather small. It is possible that calculations at a fi-

nite substrate temperature and for a longer time might yield values that are consistent with epitaxial growth. On the dihydride-terminated Si(001)- 1×1 surface, the subplantation probability was observed to increase very rapidly with the incident particle energy. At thermal energies (0.25 eV), the incident Si atom is not able to penetrate the layer of hydrogen atoms due to steric constraints. However, at 4 eV almost two-thirds of the incident atoms were subplanted at the end of 1 ps of simulation. Thus, the remarkable success of epitaxial films on a dihydride-terminated surface by sputter deposition [11, 22] can be understood in terms of subplantation probabilities. The simulations suggest that the SiH and SiH₂ units segregate during epitaxy on the monohydride- and dihydride-terminated Si(001) surfaces. This is in agreement with the observations of hydrogen segregation during epitaxy on the monohydride-terminated surface [23] and the (1×1) RHEED pattern and a smooth growing front during the initial stages of epitaxy on the dihydride-terminated surface [11, 22].

The molecular dynamics simulations suggest that the surface Si atom also segregates during epitaxial growth on hydrogen-terminated surfaces. It would be interesting to see if this is true experimentally. This could be done by using an isotope of silicon. Such an experiment would tell whether the surface hydrogen atom remains bonded to the original Si atom or it bonds to the incoming Si atom.

The ability to grow epitaxial films on hydrogen-terminated silicon surfaces has significant advantages. These surfaces are extremely unreactive because there are no dangling bonds. While sputter deposition has been very successful, a chief problem is the embedding of energetic Ar (or any

other primary ion) recoils in the film and production of Si interstitials. This can be overcome with techniques like laser ablation which produce a hyper-thermal beam of silicon atoms. This could alleviate the need for ultra high vacuum conditions.

6.4 Other Results

6.4.1 Surface Cleaning of Silicon

Surface cleaning of silicon has always received a lot of attention because of potential consequences on further processing steps. The usual procedure is to generate a surface passivation layer to protect the underlying silicon. The two common passivation layers are a thin oxide grown chemically and hydrogen passivation. For some processes, the passivation layer has to be removed just prior to the process. Low energy ion beam-induced reconstruction is a promising technique for the production of Si(001)- 2×1 surfaces at extremely low temperatures. Starting with a nominally dihydride-terminated Si(001)- 1×1 surface, both argon and helium ions were successfully used to remove the surface hydrogen. Helium ions gave somewhat better results presumably due to less energy transfer to the substrate silicon atoms. Better results were also obtained when ions were incident at grazing angles. This is due to the less energy transfer to atoms in the subsurface layers. Silicon films deposited after ion irradiation were epitaxial as judged from XTEM images (Section 5.2.3). Molecular dynamics simulations suggest that the ratio of sputtering

yields of hydrogen from dihydride-terminated surface to the monohydride-terminated surface is much higher than two (with argon ions). This could be used to preferentially remove dihydride units from the surface.

The phenomenon of beam-induced reconstruction should be studied in more detail. Ions with even lower energy and more grazing angles of incidence may produce better results. Besides noble gas ions, the effects of hydrogen and halogen ions should also be investigated. Hydrogen ions can also remove C and O impurities from the surface [24]. The damage produced by the ions on a scale larger than observable in an XTEM image will have to be established for any possible application.

6.4.2 Empirical Si-H Interatomic Potential

An empirical interatomic potential was developed to describe silicon-hydrogen interactions. The Si-H potential gives a reasonably good description of the various gas phase Si_mH_n molecules, hydrogen adsorbed on the silicon surface and interstitial sites of atomic hydrogen in bulk silicon. The interatomic potential can be further characterized by determining the barriers to surface diffusion of hydrogen and desorption. The potential may be used to study a multitude of problems such as chemical vapor deposition from silanes, processing of hydrogen-terminated silicon surfaces, and hydrogenated amorphous silicon. However, a note of caution is added since classical potentials are only a crude approximation to the complete quantum mechanical solution.

Finally, one might ask if low temperature silicon epitaxy will ever be used in a widespread manner for device fabrication. And if so, will the technique be molecular beam epitaxy? The answer to the first question definitely seems to be yes. Epitaxy at temperatures as low as 500°C is being used in some integrated circuits [25]. However, these Si (and $\text{Si}_{1-x}\text{Ge}_x$) films are being deposited by UHVCVD. Molecular beam epitaxy systems have low throughput and are expensive to maintain and it appears that deposition by CVD is going to be preferred. Molecular beam epitaxy allows one to precisely control the process parameters and hence is a very good tool for understanding the physics of film growth. It helps to understand the more complicated events during chemical vapor deposition.

Bibliography

- [1] H. Jorke, H.J. Herzog, and H. Kibbel, 'Kinetics of ordered growth of Si on Si(100) at low temperatures,' Phys. Rev. B **40**, 2005(1989).
- [2] D.J. Eaglesham, H.-J. Gossmann, and M. Cerullo, 'Limiting thickness h_{epi} for epitaxial growth and room temperature Si growth on Si(100),' Phys. Rev. Lett. **65**, 1227(1990).
- [3] G. Xue, H.Z. Xiao, M.A. Hasan, J.E. Greene, and H.K. Birnbaum, 'Critical epitaxial thickness for low temperature (20 – 100°C) Ge(100)-2×1 growth by molecular beam epitaxy,' J. Appl. Phys. **74**, 2512(1993).
- [4] B.E. Weir, B.S. Freer, R.L. Headrick, D.J. Eaglesham, G.H. Gilmer, J. Bevk, and L.C. Feldman, 'Low temperature homoepitaxy on Si(111),' Appl. Phys. Lett. **59**, 204(1991).
- [5] J.M. Gibson, H.-J. Gossmann, J.C. Bean, R.T. Tung, and L.C. Feldman, 'Preservation of a 7×7 periodicity at a buried amorphous-Si/Si(111) interface,' Phys. Rev. Lett. **56**, 355(1986).
- [6] H. Nakahara and A. Ichimiya, 'Structural study of Si growth on a Si(111)7×7 surface,' Surf. Sci. **241**, 124(1991).

- [7] P.C. Zalm and L.J. Beckers, 'Ion-beam epitaxy of silicon on Ge and Si at temperatures of 400 K,' Appl. Phys. Lett. **41**, 167(1982).
- [8] R.A. Zuhr, B.R. Appleton, N. Herbots, B.C. Larson, T.S. Noggle, and S.J. Pennycook, 'Low temperature epitaxy of Si and Ge by direct ion beam deposition,' J. Vac. Sci. Technol. A **5**, 2135(1987).
- [9] K.G. Orrman-Rossiter, A.H. Al Bayati, D.G. Armour, S.E. Donnelly, and J.A. Van den Berg, 'Ion beam deposited epitaxial thin silicon films,' Nucl. Instr. Meth. B **59**, 197(1991).
- [10] G.K. Wehner, R.M. Warner, Jr., P.D. Wang and Y.H. Kim, 'Substituting low energy (< 30 eV) ion bombardment for elevated temperature in silicon epitaxy,' J. Appl. Phys. **64**, 6754(1988).
- [11] T. Ohmi, T. Ichikawa, H. Iwabuchi, and T. Shibata, 'Formation of device-grade epitaxial silicon films at extremely low temperatures by low energy bias sputtering,' J. Appl. Phys. **66**, 4756(1989).
- [12] D.L. Smith, C.-C. Chen, G.B. Anderson, and S.B. Hagstrom, 'Enhancement of low temperature critical epitaxial thickness of Si(100) with ion beam sputtering,' Appl. Phys. Lett. **62**, 570(1993).
- [13] A. Zangwill, private communication.
- [14] D.D. Perovic, G.C. Weatherly, P.J. Simpson, P.J. Schultz, T.E. Jackman, G.C. Aers, J.P. Noël, and D.C. Houghton, 'Microvoid formation in low temperature molecular beam epitaxy grown silicon,' Phys. Rev. B **43**, 4257(1991).

- [15] H. Schut, A. Van Veen, G.F.A. VandeWalle, and A.A. Vangorkum, 'Positron beam defect profiling of silicon epitaxial layers,' *J. Appl. Phys.* **70**, 3003(1991).
- [16] B.A. Joyce, 'The growth and structure of semiconducting thin films,' *Rep. Prog. Phys.* **37**, 3639(1974).
- [17] B.A. Joyce, J.H. Neave, and B.E. Watts, 'The influence of substrate surface conditions on the nucleation and growth of epitaxial silicon films,' *Surf. Sci.* **15**, 1(1969).
- [18] J.M. Charig and D.K. Skinner, 'Carbon contamination of Si(111) surfaces,' *Surf. Sci.* **15**, 277(1969).
- [19] D.P. Adams, S.M. Yalisove, and D.J. Eaglesham, 'Effect of hydrogen on surface roughening during Si homoepitaxial growth,' *Appl. Phys. Lett.* **63**, 3571(1993).
- [20] D.J. Eaglesham, G.S. Higashi, and M. Cerullo, '370°C clean for Si molecular beam epitaxy using a HF dip,' *Appl. Phys. Lett.* **59**, 685(1991).
- [21] T. Vasek and M.G. Lagally, presented at the American Vacuum Society Meeting, Orlando, 1993.
- [22] C.-C. Chen, D.L. Smith, G.B. Anderson, and S.B. Hagstrom, 'Low temperature epitaxy on H-passivated Si(100) by sputter deposition,' *Mat. Res. Soc. Symp. Proc.* **259**, 443(1992).
- [23] M. Copel and R.M. Tromp, 'H-Coverage dependence of Si(001) homoepitaxy,' *Phys. Rev. Lett.* **72**, 1236(1994).

- [24] A. Mahajan, J. Irby, D. Kinosky, R. Qian, S. Thomas, S. Banerjee, A. Tasch, and T. Picraux, 'Si atomic layer epitaxy based on Si_2H_6 and remote He plasma bombardment,' *Thin Sol. Fi.* **225**, 177(1993).
- [25] B.S. Meyerson, 'UHV CVD growth of Si and Si-Ge alloys – chemistry, physics, and device applications,' *IEEE Proc.* **80**, 1592(1992).

Appendix A

Chemical Cleaning of Silicon Wafers

The procedure used for chemical cleaning of Si wafers is taken from Ref. [1]. All ratios mentioned below are by volume. The resistivity of H_2O was 15–18 $\text{M}\Omega\text{-cm}$.

Dilute HF dip. The Si(001) wafer is first dipped in a dilute HF solution ($\text{HF} : \text{H}_2\text{O}$ 1:20) for 10 – 15 s to etch the native oxide and then followed with an H_2O rinse (15 – 30 s).

Alkaline peroxide solution. The wafer is then placed for 5 minutes in a hot alkaline peroxide solution composed of $\text{NH}_4\text{OH} : \text{H}_2\text{O}_2 : \text{H}_2\text{O}$ in a 1:1:5 ratio. Both NH_4OH and H_2O_2 are 30% solutions. The temperature was $70 \pm 10^\circ\text{C}$. The resulting oxide is then etched by a dilute HF dip (10 – 15s) and followed by an H_2O rinse (15 – 30s). This sequence was repeated three times. This step removes organic contaminants and some metals from the surface [2].

Acidic peroxide solution. The wafer is then placed for 5 minutes in a hot acidic peroxide solution composed of $\text{HCl} : \text{H}_2\text{O}_2 : \text{H}_2\text{O}$ in a 1:1:5 ratio. The temperature was again $70 \pm 10^\circ\text{C}$. The resulting oxide is again etched by a dilute HF dip (10 – 15 s) and followed by an H_2O rinse (15 – 30s). This sequence was repeated three times. This step removes metal contaminants from the surface [2].

Dilute HF dip. In the final step, the Si wafer is dipped in dilute HF for 50 to 60 s [3]. This results in a nominally dihydride-terminated $\text{Si}(001)$ surface.

The wafer is transferred to the load lock within three minutes after the last step. On the dihydride-terminated $\text{Si}(001)$ surface, hydrogen atoms saturate the dangling bonds of Si atoms. This passivates the Si surface from oxidation and chemisorption of impurities. In fact, such surfaces have been shown to resist oxidation for as long as 12 hours in the laboratory atmosphere [4].

Bibliography

- [1] A. Ishizaka and Y. Shiraki, 'Low temperature surface cleaning of silicon and its application to silicon MBE,' J. Electrochem. Soc. **133**, 666 (1986).
- [2] W. Kern and D.A. Puotinen, 'Chemical solutions based on hydrogen peroxide for use in silicon semiconductor technology,' RCA Rev. **31**, 187 (1970).
- [3] D.J. Eaglesham, G.S. Higashi, and M. Cerullo, '370°C clean for Si molecular beam epitaxy using a HF dip,' Appl. Phys. Lett. **59**, 685(1991).
- [4] T. Takahagi, I. Nagai, A. Ishitani, H. Kuroda, and Y. Nagasawa, 'The formation of hydrogen passivated silicon single-crystal surfaces using ultraviolet cleaning and HF etching,' J. Appl. Phys. **64**, 3516(1988).

Appendix B

Elastic Recoil Spectrometry

B.1 Introduction

Hydrogen has always been a hard element to detect. Conventional core loss techniques such as X-ray photoelectron (XPS) and Auger electron spectroscopies (AES) cannot be used because hydrogen has only one electron which is involved in bonding. Nevertheless, there are several techniques to measure hydrogen concentrations — some specific to the Si-H system and some that are based on physical techniques and are more general. Some methods specific to the silicon-hydrogen system are infrared spectroscopy (IR) [1] and high resolution electron energy loss spectroscopy (HREELS) [2]. These techniques are based on the excitation or absorption of Si-H vibrational modes. This makes them rather sensitive to the chemical environment of the hydrogen atom. While this may be useful for distinguishing various configurations of H on the surface, it makes it difficult to measure absolute coverages because one has to monitor all possible vibrational modes. Hydrogen can also be detected by physical techniques such as secondary ion mass spectrometry (SIMS), time-of-flight medium energy ion scattering

(TOF-MEIS) [3] and nuclear reaction analysis (NRA). Secondary ion mass spectrometry is a destructive method as it relies on analysis of sputtered particles. The cross sections for most nuclear reactions are rather small. A commonly used reaction is the $^{19}\text{F}(\text{p},\alpha)^{16}\text{O}$ with a cross section of about 0.5 mb/sr at an incident particle energy of 1.25 MeV [4].

Elastic recoil spectrometry (ERS) is a physical technique for the detection of atoms lighter than the incident ion. After filtering out the forward scattered incident beam, the scattered atoms are energy analyzed to determine their absolute concentration and depth distribution. This technique is also known as forward recoil spectrometry (FRS) and elastic recoil detection analysis (ERDA) and is basically an extension of the Rutherford backscattering spectrometry (RBS). Typically, incident ions with a few MeV are used. For the detection of hydrogen and its isotopes, ions with atomic number 2 or higher can be used. Heavy ions such as $^{28}\text{Si}^+$ or $^{40}\text{Ar}^+$ can be used to measure C and O profiles but cause significant damage to the substrate. The damage with MeV He^+ ions is comparatively lower, and several μC can be deposited before any noticeable damage. This allows one to obtain many spectra from the same sample. The cross sections for elastic scattering are also large. A typical number is 320 mb/sr for a 2 MeV He^+ ion and a scattering angle of 25° [5]. There is also a resonance with deuterium at about 2.14 MeV [6]. The forward scattered He^+ ions can be separated from the protons either with a thin Mylar or Al foil or by magnetic deflection. Separation with the stopper foil depends on the larger stopping cross sections for larger Z particles. A 2 MeV He^+ ion is completely stopped with a 8 μm Al foil whereas a 1 MeV H^+ loses only about 400 keV. The straggling in the stopper foil restricts the

depth resolution to about 50 nm. A good reference for the optimization of scattering geometry and the stopper foil for best depth resolution is Ref. [7]. The technique does suffer from rather large data collection times. With a 5 nA beam it takes about 20 minutes to build up good statistics. It is possible to detect as little as 0.01 ML although practical considerations restrict the limit to about 0.1 ML. Since the cross sections for light ion scattering are well known, ERS is one of the best techniques for obtaining absolute concentrations.

B.2 The Elastic Recoil Spectrometry System

The elastic recoil spectrometry system is designed to measure hydrogen coverage and profiles in thin films and on surfaces. A schematic of the end station is shown in Fig. B.1. A base pressure of about 2×10^{-7} Pa is achieved in the end station when it is isolated from the Pelletron. The chamber is pumped with an ion pump and two turbomolecular pumps. During operation, the pressure rises to about 8×10^{-7} Pa due to the N_2 stripper gas used for ionizing He atoms in the Pelletron. The pressure in the Pelletron is typically 10^{-3} Pa. An ion gauge is used to measure the pressure and a mass spectrometer is used to monitor the residual gas. The ERS system is connected to the accelerator beam line through a 4 mm diameter aperture. This serves as a differential pumping port and helps isolate the high pressure side (the accelerator) from the ERS system. The He^+ beam enters through this aperture

and is incident on the substrate at about 78° with respect to the substrate normal. This angle is obtained by tilting the part of the chamber containing the sample with respect to the beam axis. The He^+ beam enters the end station off-axis to avoid hitting the wall of the chamber. This off-axis displacement is achieved using a bellows arrangement. Solid state detectors are used to detect the scattered particles. The detectors are bakeable to 200°C . However, the maximum baking temperature is limited to about 150°C by the electrical connectors used on the detectors. The samples are inserted through a load lock. This helps maintain a good vacuum in the chamber for surface studies. Substrates can be heated for adsorption-desorption studies and film growth. A reflection high-energy electron diffraction (RHEED) gun is used (not shown in Fig. B.1) to monitor the surface morphology. An electron beam deposition source, an effusion cell, an ion gun or an atomic hydrogen source can be connected at a line-of-sight port shown in Fig. B.1 (marked by the letter A). The effects of exposing the substrate to different processing conditions can be investigated. A schematic of the electronics for processing the signals from the detectors is shown in Fig. B.2.

The scattering geometry for hydrogen coverage measurements is shown in Fig. B.3. The He^+ beam is incident at 78° with respect to the surface normal. The nominal backscattering angle is 102° and the solid angle of the detector is about 2.66 msr. An $8\text{ }\mu\text{m}$ Al foil [8] is used to block the forward scattered He beam from reaching the forward scattering detector. The nominal forward scattering angle is 24° and the solid angle of the the detector is 3.60 msr. The detectors (ORTEC Model U-012-050-100) are circular with an active area of 50 mm^2 . For optimum depth resolution, a rectangular slit should be used in

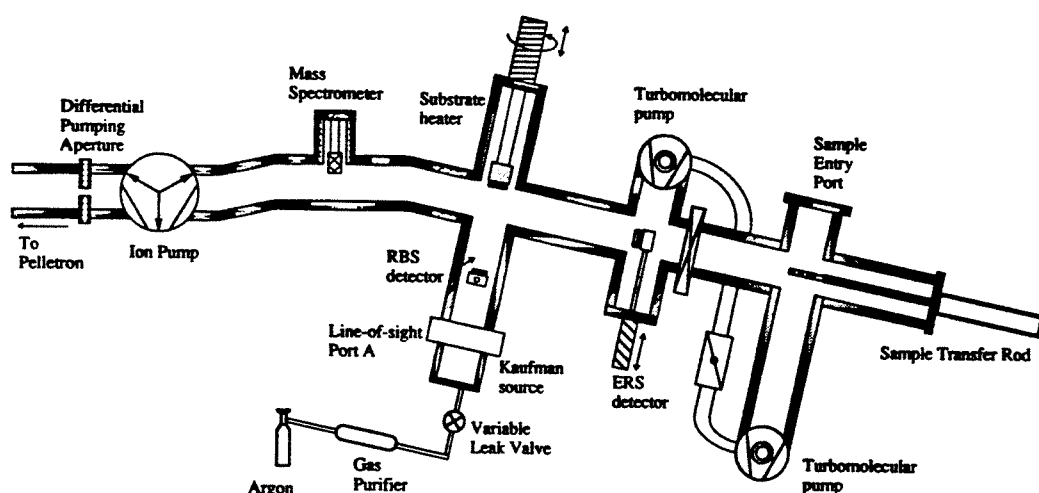


Figure B.1: A schematic of the elastic recoil spectrometry system. The line-of-sight port to the substrate is marked by the letter A. A Kaufman ion source is shown connected at this port. The drawing is not to scale.

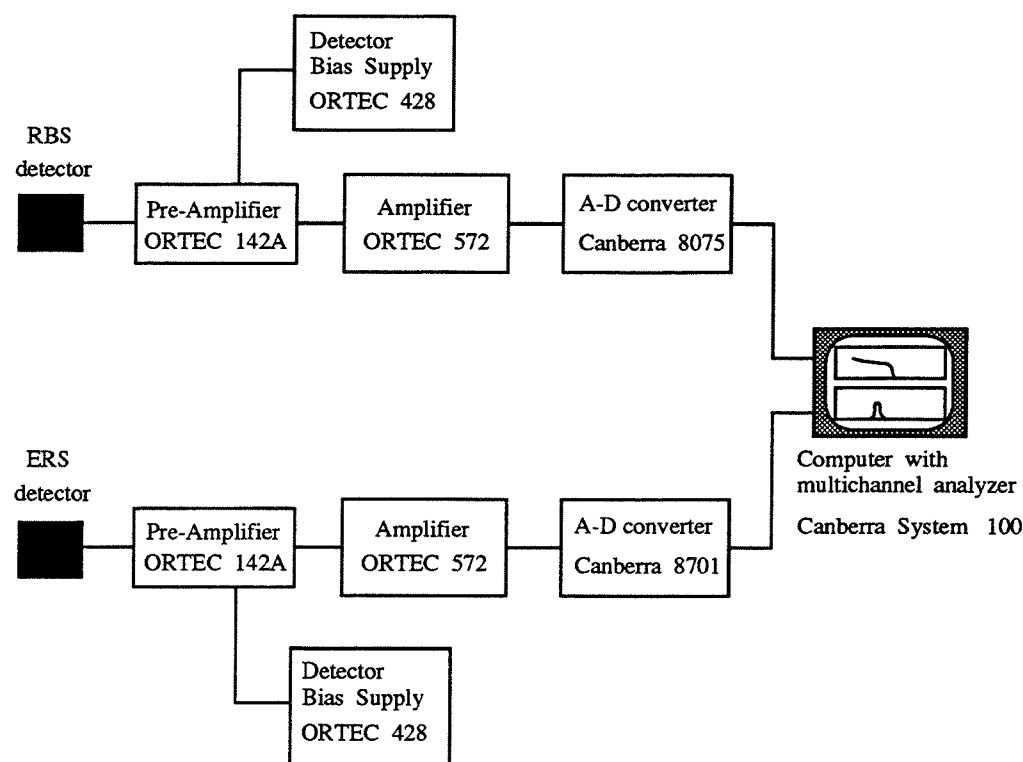


Figure B.2: The electronics used for the detection of alpha particles and protons. Both RBS and ERS spectra can be collected simultaneously on a single computer.

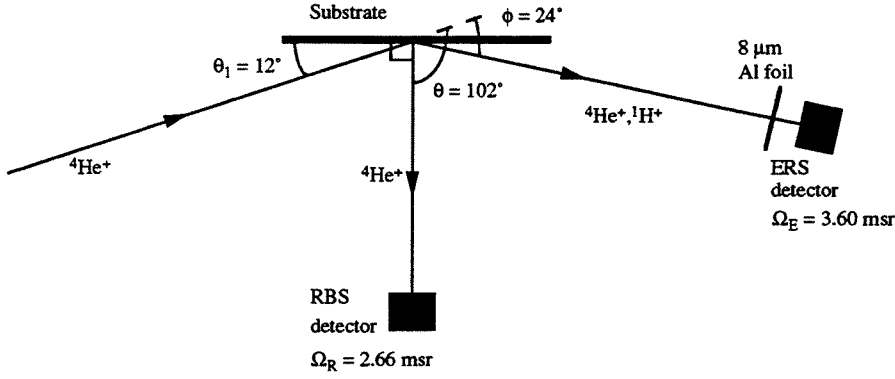


Figure B.3: The scattering geometry used in the experiments.

front of the ERS detector [9]. This decreases the dispersion in the kinematic factor of the H atoms. However, we have used the complete detector area to maximize the counting rate. This gives a measure of the total amount of hydrogen at the substrate on the surface and in the bulk. The RBS and ERS spectra are collected simultaneously. The hydrogen counts are thus referred to a substrate peak and this eliminates the need to measure the incident beam current. Care must be taken to ensure that the He^+ beam is not incident along a channeling direction in the substrate.

The analysis described below is for hydrogen on a silicon surface. Such surfaces can be prepared by an HF dip or exposing a clean silicon surface to an atomic hydrogen beam. The yield per channel for backscattering from the Si substrate is expressed in terms of the incident beam dose Q_R , solid angle Ω_R , scattering cross section σ_{Si} , energy per channel \mathcal{E} and the stopping cross section factor $[\varepsilon_o]$ [10]:

$$H_{\text{Si}} = \frac{Q_R \Omega_R \sigma_{\text{Si}} \mathcal{E}}{[\varepsilon_o] \cos(\theta_1)} \quad (\text{B.1})$$

The stopping cross section factor at the surface, the kinematic factor and the

scattering cross section are in turn given by [10]

$$[\varepsilon_o] = \frac{K_{Si}\varepsilon(E_0)}{\cos(\theta_1)} + \frac{\varepsilon(K_{Si}E_0)}{\cos(\theta_2)} \quad (B.2)$$

$$K = \left(\frac{M_{He}\cos\theta + \sqrt{M_{Si}^2 - M_{He}^2\sin^2\theta}}{M_{He} + M_{Si}} \right)^2 \quad (B.3)$$

$$\sigma_{Si} = \left(\frac{Z_{He}Z_{Si}e^2}{4\pi\epsilon_0(4E_0)} \right)^2 \left(\frac{1}{\sin^4(\theta/2)} - 2 \left(\frac{M_{He}}{M_{Si}} \right)^2 \right) \quad (B.4)$$

The Rutherford scattering cross section is assumed for scattering from the silicon atoms. Here, $\epsilon(E)$ is the stopping cross section for He^+ ions with energy E in silicon.

The He^+ ions recoil scatter protons from the substrate, some of which are detected by the forward scattering detector. Protons, being lighter than helium, are only scattered in the forward direction ($\phi < 90^\circ$). The total number of protons scattered into the forward detector can be expressed in terms of the incident beam dose Q_E , solid angle Ω_E , scattering cross section σ_H and the surface density (atoms/cm²) of hydrogen atoms N_H :

$$Y_H = \frac{Q_E\Omega_E\sigma_H N_H}{\cos(\theta_1)} \quad (B.5)$$

The energy transferred to the protons in the collision is given by

$$E_1 = \frac{4M_{He}M_H}{(M_{He} + M_H)^2} \cos^2\phi \quad (B.6)$$

Typically, 1.9 MeV He^+ ions are used in the experiments and the protons on the surface emerge in the direction of the detector with an energy of

1.01 MeV. Both helium ions and protons are scattered in the forward direction and have to pass through the Al foil to reach the detector. The energy loss of light ions (of energy E) is proportional to $M_1 Z_1^2$. The range of 1.9 MeV He^+ ions, 1 MeV protons and 1.7 MeV deuterons in Al is about $7 \mu\text{m}$, $14 \mu\text{m}$ and $22 \mu\text{m}$ respectively [11]. A TRIM91 simulation [12] with 1000 He ions incident on a $7 \mu\text{m}$ Al foil gave a range and straggle of $6.40 \mu\text{m}$ and $0.17 \mu\text{m}$, respectively. The helium ions are thus completely stopped in the Al foil. A simple calculation assuming Rutherford scattering cross section shows that the probability of backscattering of 1 MeV protons incident on the the Al foil is about 0.0002. The protons (and deuterons) lose energy on their way through the foil but retain sufficient energy to be detected. A TRIM91 simulation with 10000 protons gave a transmission coefficient of 0.9998. The Al foil thus allows us to separate the forward scattered protons from the He ions. The surface hydrogen density can be obtained from the eqs. B.1 and B.5 as

$$N_H = \frac{Q_R}{Q_E} \frac{\Omega_R}{\Omega_E} \frac{\sigma_{Si}}{\sigma_H} \frac{\mathcal{E}}{[\epsilon_l]} \frac{Y_H}{H_{Si}} \quad (\text{B.7})$$

Since the two spectra are collected simultaneously, the quantity Q_R/Q_E is close to unity, except for a minor correction factor. The two electronics chains might have different dead times depending on the arrival rate of the scattered ions. This is taken into account by replacing Q_R/Q_E by t_R/t_E where t_R and t_E are the actual collection times (true time - dead time) of the two chains. Note that this is only a first order correction since the dead time is not a strictly linear function of the number of ions incident on the detector. A variation of incident beam current with time will result in non-

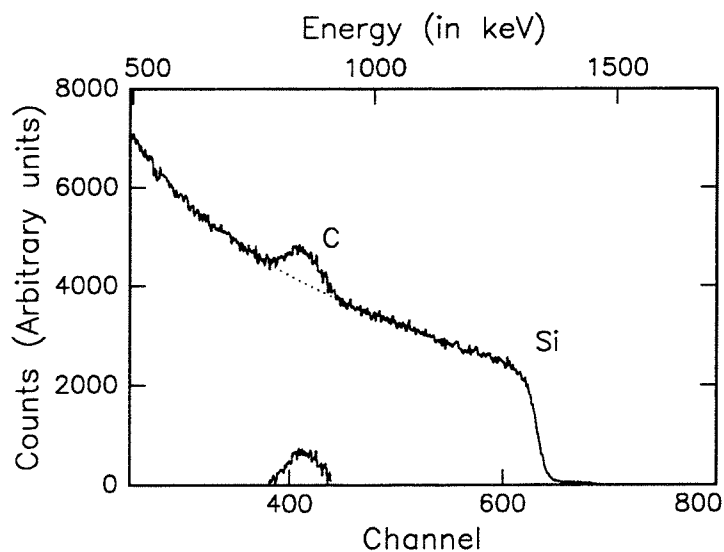
trivial corrections factors. Fortunately, this factor is close to unity in most cases and does not introduce a significant error. With this correction, eq. B.7 becomes

$$N_H = \frac{t_R}{t_E} \frac{\Omega_R}{\Omega_E} \frac{\sigma_{Si}}{\sigma_H} \frac{\mathcal{E}}{[\varepsilon_l]} \frac{Y_H}{H_{Si}} \quad (\text{B.8})$$

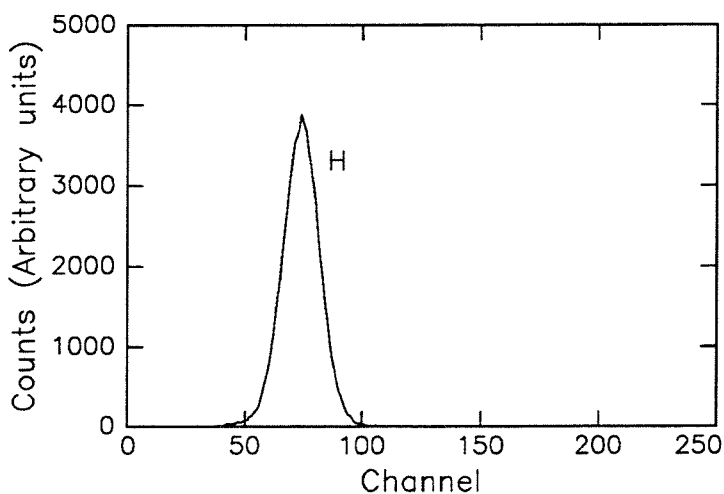
B.3 Calibration

To calculate the hydrogen coverage with eq. B.8, two quantities need to be determined — the energy per channel, \mathcal{E} in the RBS spectrum and the ratio of the solid angles, Ω_R/Ω_E . The quantity \mathcal{E} is determined using a sample consisting of Au, Rh and Co marker layers. This helps establish the energy versus channel relation for the RBS spectrum. The ratio of the solid angles is obtained from a 100 nm $(C_8H_8)_n$ (polystyrene) film (on Si substrate) consisting of C and H in a stoichiometric ratio of unity. The RBS and ERS spectra from such a sample are shown in Fig. B.4. The measured ratio, Ω_R/Ω_E , is about 0.76 ± 0.05 . This is close to the value of 0.74 estimated from geometry.

As only one sample can be inserted at a time in the chamber, it is not possible to do a calibration for each sample. Instead, calibration is done once in a while to check for any changes in the values of \mathcal{E} and Ω_R/Ω_E . The variations in their values are usually small.



(a)



(b)

Figure B.4: The (a) backscattering and (b) forward scattering spectra from a 100 nm film of $(C_8H_8)_n$ (polystyrene) on Si. The background subtracted carbon peak is also shown in the RBS spectrum. Both spectra were collected simultaneously. The incident He^+ ion energy was 2.0 MeV.

B.4 Error Analysis

Hydrogen coverage can be measured with quite high accuracy by elastic recoil spectrometry. The technique is based on a purely physical process, namely the transfer of energy in a high-energy collision. This makes it independent of the bonding environment of the H atoms. Still several factors can introduce errors in the measurement. These include the variation of the position of the incident beam spot, the sample and detector positions, sample misorientation, and the knowledge of scattering and stopping cross sections. It is useful to distinguish between different types of error when interpreting the results – (a) absolute error, the ultimate confidence that one can place in the measured values and (b) relative error, the variation in or the ratio of the measured values from sample to sample, or different spectra from the same sample.

The hydrogen coverage is expressed in eq. B.8 in terms of the ratio of solid angles Ω_R/Ω_E , the ratio of scattering cross sections σ_{Si}/σ_H and the stopping cross section factor $[\varepsilon_o]$.

The scattering cross sections for hydrogen and deuterium have been determined experimentally by using calibrated samples. The values usually differ from the Rutherford scattering cross sections for MeV alpha particles. This is expected since the distance of closest approach between a proton and a MeV alpha particle is comparable to the diameter of a nucleus ($\sim 10^{-15}$ m). In our calculations, we have used the hydrogen scattering cross sections from Ref. [5] and the deuterium scattering cross sections from Ref. [6]. These values are probably accurate to within 10%.

Sample misorientation (deviation in the angle θ_1 in Fig. B.3) is a major source of error. A 1° misorientation can result in about 8% change in the stopping cross section factor $[\epsilon_o]$. It is possible to check for sample misorientation by comparing a spectrum with one obtained after a 180° rotation of the sample. The ratio of solid angles Ω_R/Ω_E is probably known within 5%. It can be shown that if the sample and the detector are within 1 mm of their positions, the errors incurred are less than 4%. Another factor is the large incident beam spot size (typically $2 \times 10 \text{ mm}^2$) and its exact location on the sample. Overall, the errors due to small variations in the geometry is estimated to be about 10%.

The relative error when comparing spectra from two different samples is estimated to be about 10%. When comparing spectra from the same sample, the errors are probably less than 5% because the sample misorientation and the detector and sample positions are also the same. The absolute error in the measured concentration of hydrogen should be about 20%.

B.5 Hydrogen on Silicon Surface

Figure B.5 shows the backscattering and forward scattering spectra from a Si(001) wafer after a dilute ($\sim 5\%$) HF dip. This corresponds to a hydrogen coverage of 5.0 ML. This is an unusually high value. The saturation coverage of hydrogen on Si(001) is close to 2.0 ML. A saturation value of $1.85 \pm 0.18 \text{ ML}$ was reported in Ref. [13] after exposing a clean Si(001) wafer to atomic hydrogen under UHV conditions. This indicates that the

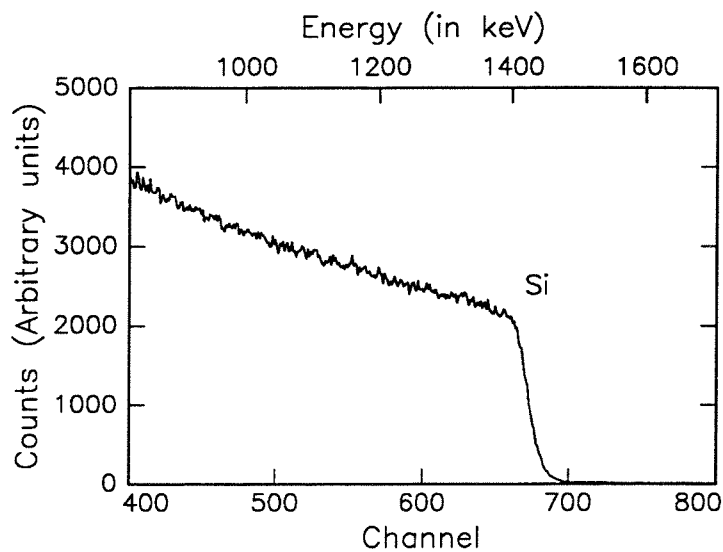
Table B.1: Hydrogen coverage after annealing a dilute HF dipped Si(001) wafer.

Process	Hydrogen coverage (ML)
as inserted	7.4
100°C, 15 min. anneal	6.8
150°C, 15 min. anneal	6.7
200°C, 15 min. anneal	4.9
200°C, overnight anneal	4.8

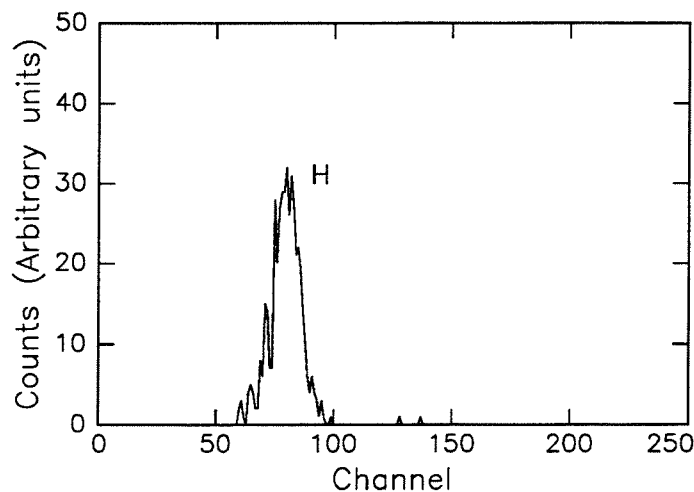
surface has a high density of physisorbed hydrocarbons (or any other H containing species). The wafer was exposed to atmosphere for about 10 minutes after the HF dip and before transfer to the load lock. It is possible that hydrocarbons accumulate on the surface when the wafer is pulled out of the HF solution and during the finite time needed to transfer the wafer to the vacuum system. Performing an RCA clean (see Appendix A) before the dilute HF dip did not seem to effect the hydrogen coverage. In all cases, a sharp (1×1) RHEED pattern was observed along the <110> azimuth.

The hydrocarbon coverage does decrease when the wafer is heated. The results of one experiment are shown in Table B.1. The hydrogen coverage goes down from 7.0 ML at room temperature to about 4.8 ML at 200°C. It has been shown that a low temperature bake can remove hydrocarbons from the Si(001) surface [14]. Our results are thus consistent with this observation. Unfortunately, we could not go to higher temperatures to follow the evolution of hydrogen coverage.

A silicon wafer can be terminated with deuterium atoms by dipping in a dilute solution ($\sim 1\%$) of HF in D₂O. Deuterium fractions higher than



(a)



(b)

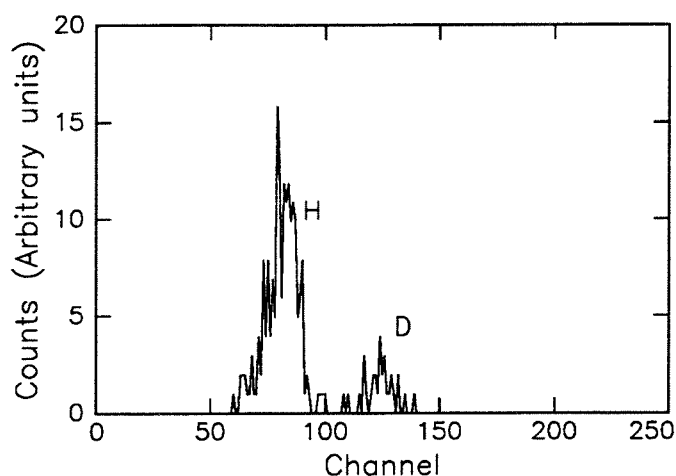
Figure B.5: The (a) backscattering and (b) forward scattering spectra from a Si(001) wafer after a dilute ($\sim 5\%$) HF dip. Both spectra were collected simultaneously. The incident He^+ ion energy was 2.0 MeV.

80% were reported in Ref. [15] after such a treatment. Fig. B.6(a) shows a forward scattering spectrum of a Si(001) wafer dipped in a $\sim 1\%$ solution of HF in D₂O for two minutes followed by an overnight anneal at 200°C. We see two peaks corresponding to H and D atoms. They correspond to a coverage of about 3.0 ML H and 0.26 ML D atoms. At various times, the deuterium coverage measured after such a treatment varied between 0.2 and 0.7 ML.

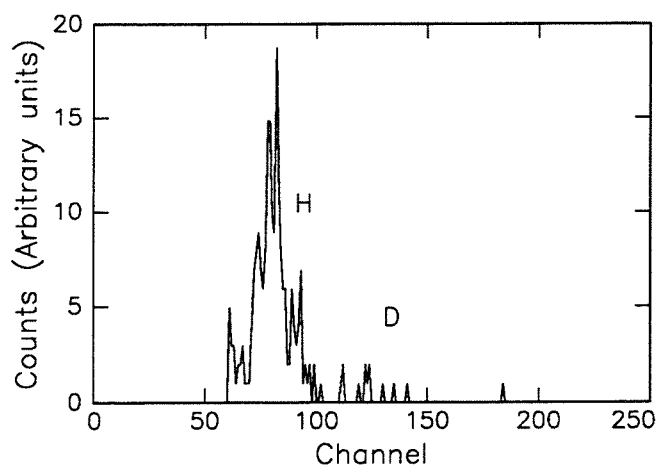
We have seen (Chapter 5) that low energy Ar⁺ ion irradiation can remove hydrogen from a Si(001) surface. The ERS spectrum after a ~ 1 ML dose of 50 eV Ar⁺ ions on a HF + D₂O dipped Si(001) wafer is shown in Fig. B.6(b). The substrate temperature during ion irradiation was 200°C. The spectra in Fig. B.6(a) and (b) are normalized with respect to the incident He⁺ dose. Although we have poor statistics, we see that the deuterium coverage has decreased significantly (from 0.26 to about 0.11 ML). One would have expected a similar drop in the ¹H coverage. But the ¹H coverage increases from 3.0 to 3.3 ML. This is presumably due to hydrogen adsorption from the ambient.

B.6 Conclusion

The elastic recoil spectrometry system can be used to measure hydrogen concentrations in thin films and substrates with quite high accuracy. It is possible to study the effects of different processes on the hydrogen concentration on the substrate. For surface studies, an improvement in vacuum conditions is desirable. This is particularly true when the surface is exposed



(a)



(b)

Figure B.6: (a) The ERS spectrum from a Si(001) wafer dipped in a $\sim 1\%$ HF + D₂O solution for two minutes followed by an overnight anneal at 200°C. The hydrogen coverage is about 3.0 ML and the deuterium coverage is about 0.26 ML. (b) The ERS spectrum after a 1 ML dose of 50 eV Ar⁺ ions at a substrate temperature of 200°C. The hydrogen coverage is about 3.3 ML and the deuterium coverage is about 0.11 ML. The spectra in (a) and (b) are normalized with respect to the incident He⁺ dose. The incident He⁺ ion energy was 2.0 MeV.

for several hours while studying the effects of different processes.

Bibliography

- [1] See, for example, Y.J. Chabal, G.S. Higashi, K. Raghavachari, and V.A. Burrows, 'Infrared spectroscopy of Si(111) and Si(100) surfaces after HF treatment: hydrogen termination and surface morphology,' J. Vac. Sci. Technol. A7, 2104(1989).
- [2] See, for example, J.A. Schaefer, 'Electronic and structural properties of hydrogen on semiconductor surfaces,' Physica B170, 45(1991).
- [3] See, for example, M. Copel and R.M. Tromp, 'H-Coverage dependence of Si(001) homoepitaxy,' Phys. Rev. Lett. 72, 1236(1994).
- [4] L.C. Feldman and J.W. Mayer, *Fundamentals of Surface and Thin Film Analysis*, North-Holland, New York, 1986.
- [5] J.E.E. Baglin, A.J. Kellock, M.A. Crockett, and A.H. Shih, 'Absolute cross section for hydrogen forward scattering,' Nucl. Instr. Meth. B64, 469(1992).
- [6] F. Besenbacher, I. Stensgaard, and P. Vase, 'Absolute cross section for recoil detection of deuterium,' Nucl. Instr. Meth. B15, 459(1986).
- [7] A. Turos and O. Meyer, 'Depth profiling of hydrogen by detection of recoiled protons,' Nucl. Instr. Meth. B232, 92(1984).

- [8] The 8 μm Al foils were obtained from Goodfellow Corporation.
- [9] B.L. Doyle and D.K. Brice, 'The analysis of elastic recoil detection data,' Nucl. Instr. Meth. **B35**, 301(1988).
- [10] W.K. Chu, J. W. Mayer, and M.A. Nicolet, *Backscattering Spectrometry*, Academic Press, New York, 1978.
- [11] J.F. Ziegler, J.P. Biersack, and U. Littmark, *The Stopping and Range of Ions in Solids*, Pergamon Press, New York, 1985.
- [12] J.P. Biersack and L.G. Haggmark, Nucl. Instr. Meth. **174**, 257(1980).
- [13] K. Oura, J. Yamane, K. Umezawa, M. Naitoh, F. Shoji, and T. Hanawa, 'Hydrogen adsorption on Si(100)-2 \times 1 surfaces studies by elastic recoil detection analysis,' Phys. Rev. **B41**, 1200(1990).
- [14] S. Nikzad, S.S. Wong, C.C. Ahn, A.L. Smith, and H.A. Atwater, 'In situ reflection electron energy loss spectroscopy measurements of low temperature surface cleaning for Si molecular beam epitaxy,' Appl. Phys. Lett. **63**, 1414(1993).
- [15] V.A. Burrows, Y.J. Chabal, G.S. Higashi, K. Raghavachari, and S.B. Christman, 'Infrared spectroscopy of Si(111) surfaces after HF treatment: hydrogen termination and surface morphology,' Appl. Phys. Lett. **53**, 998(1988).

Appendix C

Algorithm for Molecular Dynamics Simulations

The following is a description of the computer program SIH used for molecular dynamics simulations. The Si and H atoms respond to the Si-Si, Si-H and H-H interatomic potentials described in Chapter 3. A general discussion of the numerical methods is also given in Section 3.3. Briefly, the Runge-Kutta-Nyström method with Richardson extrapolation is used to solve the system of differential equations 3.1 – 3.2. The nearest neighbors of an atom are determined using the cell method. Two workstations, DEC3100 and RS6000/340, were used for the simulations. The computation time is about 9.6 ms/atom-timestep and 1.9 ms/atom-timestep on the DEC3100 and RS6000/340 workstations, respectively.

The program is written in the C language. A brief description of the various subroutines and some important variables is given below followed by the source code.

Subroutines:

- params* : Reads data in the input file “params.dat.”
- lattice* : Reads data the input file “lattice.dat.”
- energy* : Computes the total kinetic and potential energy of a configuration of atoms.
- func* : Computes the accelerations of all atoms for any given configuration.
- periodic* : Applies periodic boundary conditions in the transverse directions (x and y) of the crystallite.
- RKA* : The Runge-Kutta-Nyström method for the numerical solution of the system of differential equations.

Input files:

- params.dat : Contains information about the size of the crystallite, duration of simulation and other variables controlling the flow of the program. An example is give below.
- lattice.dat : Contains the initial positions, velocities and mass of atoms.
This is contained in seven columns as
- | | | | | | | |
|---|---|---|-------|-------|-------|------|
| x | y | z | v_x | v_y | v_z | mass |
|---|---|---|-------|-------|-------|------|

Output files:

- out.dat : The position and velocity of atoms (with $z < z_{save}$) is stored at regular time intervals specified in the input file “params.dat.”
- final.dat : The position and velocity of atoms is stored at regular time intervals specified in the input file “params.dat.”

Units:

The units for distance, mass and time are Å ($= 10^{-10}$ m), fs ($= 10^{-15}$ s) and amu ($= 1.67 \times 10^{-27}$ kg), respectively.

A sample input file *params.dat*.

```

auto
2601
1
1000.0
100.0
10.0
0.01
5.4310
10
10
6
-5.00
29.50
10.0
17.00      17.00      -3.00      0.00      0.00      0.20      28.0

```

Line 1 : There are two possible specifications. Using *auto* leads to a simulation with adaptive step size control. Using *relx* leads to a relaxation of the lattice to a minimum energy configuration. For relaxation, a simple algorithm is used which sets the velocity to zero whenever velocity and acceleration are in opposite directions.

- Line 2 : Number of atoms (including the incident atom) in the simulation.
- Line 3 : Use 0 if there is no incident atom and 1 if there is an incident atom.
- Line 4 : Duration of the simulation (in fs).
- Line 5 : Time-interval at which the atomic coordinates and velocities are stored.
- Line 6 : The maximum step size allowed (in fs).
- Line 7 : Tolerance (\AA or $\text{\AA}/\text{fs}$ per picosecond).
- Line 8 : Lattice constant of silicon (in \AA).
- Line 9,10,11 : Size of the crystallite in unit cells. The primitive cell dimensions are 3.84, 3.84 and 5.43 \AA in the x, y and z directions respectively. The x-direction must be [110] and the z-direction must be [001].
- Line 12,13 : Atoms with initial z-coordinates less (more) than the value in line 12 (13) are held rigid.
- Line 14 : Only atoms with initial z-coordinate less the value in line 14 are stored in the output file "out.dat."
- Line 15 : If there is an incident atom, its position (x,y,z), velocity (v_x, v_y, v_z) and mass are specified here.

```

#include "stdio.h"
#include "math.h"

FILE *parf, *latf, *outf, *finf, *warf, *ranf;

#define MAX 5600
#define MID 2700
#define NN 10
#define SIDEX 30
#define SIDEY 30
#define SIDEZ 15
#define CUBES 13500

short int s, mode, score[CUBES], rigid[MID], zs[MID], tpe[MAX];
int ma, mb, mc, atom, ion;
int m, n, enc[27], val[MAX];
int zone[CUBES][10], code[MAX];
int SYZ, STD, cu, stor[MAX][NN];
double A, Bo[NN], lda1, lda2[NN], b, c, d, Re[NN], eta, R, D;
double dlta, alpha, H;
double Al, Bl, Hl, As[MAX], Bs[MAX], Hs[MAX];
double Au[10], Bu[10], Hu[10], dAs[MAX], dBs[MAX], dHs[MAX];
double T, interval, hmax, tol, cutoff, sqcut;
double tme, la, rmin, est, zmax, dAq[MAX], dBq[MAX], dHq[MAX];
double sl, sr, sn, sf, delx, dely, zmin, zsave;
double mass[MID], rx[MAX][NN];
double x[MAX][3], vx[MID][3];
double u2[MAX][3], v2[MAX][3];
double f[MAX][3], vy[MAX][3];
double u1[MID][3], v1[MID][3], w2[MAX][3];
double t1[NN][NN], t2[NN][NN], t3[NN][NN];
double g1[NN][NN], g2[NN][NN], g3[NN][NN];

/* ----- */

void params (void)
{
    char c1, c2, c3, c4;
    short int ch1, ch2, ch3, ch4, ch5;
    int dim;
    double xoff, yoff, zoff;

    parf = fopen ("params.dat", "r");

    do {
        fscanf (parf, "%c", &c1);
        ch1 = ((c1 == 'A') || (c1 == 'a'));
        ch2 = ((c1 == 'R') || (c1 == 'r'));
    } while ((ch1 == 0) && (ch2 == 0));

    if (ch1 != 0) {
        fscanf (parf, "%c%c%c", &c2, &c3, &c4);
        ch3 = ((c2 == 'U') || (c2 == 'u'));
        ch4 = ((c3 == 'T') || (c3 == 't'));
        ch5 = ((c4 == 'O') || (c4 == 'o'));
        mode = 0;
    };

    if (ch2 != 0) {
        fscanf (parf, "%c%c%c", &c2, &c3, &c4);
        ch3 = ((c2 == 'E') || (c2 == 'e'));
        ch4 = ((c3 == 'L') || (c3 == 'l'));
        ch5 = ((c4 == 'X') || (c4 == 'x'));
        mode = 1;
    };
};

```

```

s = 0;
if ((ch3 == 0) || ((ch4 == 0) || (ch5 == 0))) {
    printf (" Line 1 must be      AUTO : automatic step control\n");
    printf ("                      RELX : getting a relaxed lattice\n");
    return;
};

fscanf (parf,"%d",&n);
if (n > MID) {
    printf (" Number of allowed lattice points = %d\n",MID);
    return;
};

fscanf (parf,"%d",&ion);
if (ion > 1) {
    printf (" Only one incident ion is allowed.\n");
    return;
};

fscanf (parf,"%lf",&T);
fscanf (parf,"%lf",&interval);
fscanf (parf,"%lf",&hmax);
fscanf (parf,"%lf",&tol);
fscanf (parf,"%lf",&la);
fscanf (parf,"%d",&ma);
fscanf (parf,"%d",&mb);
fscanf (parf,"%d",&mc);
fscanf (parf,"%lf",&zmin);
fscanf (parf,"%lf",&zmax);
fscanf (parf,"%lf",&zsave);

if (ion) {
    fscanf (parf,"%lf %lf %lf %lf %lf %lf %lf",&x[n-1][0],&x[n-1][1],
        &x[n-1][2],&vx[n-1][0],&vx[n-1][1],&vx[n-1][2],&mass[n-1]);
};
printf (" n = %d  T = %f\n",n,T);
fclose (parf);
s = 1;
}

/* ----- */

void lattice (void)
{
    register int  i;

    latf = fopen ("lattice.dat","r");
    for (i=0; i<n-ion; i++) {
        fscanf (latf,"%lf %lf %lf %lf %lf %lf %lf",&x[i][0],&x[i][1],&x[i][2],
            &vx[i][0],&vx[i][1],&vx[i][2],&mass[i]);
    };
    printf(" Over \n");
    fclose (latf);
}

/* ----- */

void energy (void)
{
    register int  p,q;

    short int  qa,qb,qc,rs,sum;
    short int  ja,value,l,yard[NN];
    int        i,j,r,decode,encode,stare[NN];
    double      dxij,dyij,dzij,rsqij,rij;

```

```

double      dxik,dyik,dzik,rik,nH,nS;
double      e,zij[NN],zijn,oc,z,tfc;
double      df,df3,bij,bijn,rq,gx,ua,u1,u3,du1,du3;
double      xx[NN],yy[NN],zz[NN],fc[NN];
double      PE,KE,EN,vsq,st,px,py,pz,rxe[NN];

PE = 0.0;
KE = 0.0;
px = 0.0;
py = 0.0;
pz = 0.0;

for (i=0; i<CUBES; i++) score[i] = 0;

for (i=0; i<m; i++) {
    qa = floor ((x[i][0] + 12.00)/cutoff);
    qb = floor ((x[i][1] + 12.00)/cutoff);
    qc = floor ((x[i][2] + 12.00)/cutoff);

    encode = qa*SYZ + qb*SIDEZ + qc;

    if ((qa < 0) || (qb < 0) || (qc < 0)) encode = 0;

    p = score[encode];
    zone[encode][p] = i;
    score[encode]++;
    code[i] = encode - STD;
};

for (i=0; i<n; i++) {
    if (tpe[i] == 0) {
        nS = 0.00;
        nH = 0.00;

        for (ja=0; ja<27; ja++) {
            decode = code[i] + enc[ja];
            if ((decode >= 0) && (decode < CUBES)) {
                for (l=0; l < score[decode]; l++) {
                    j = zone[decode][l];

                    if (tpe[j] == 0) sqcut = 9.00;
                    if (tpe[j] == 1) sqcut = 4.00;

                    dxij = x[i][0] - x[j][0];
                    dyij = x[i][1] - x[j][1];
                    dzij = x[i][2] - x[j][2];
                    rsqij = dxij*dxij + dyij*dyij + dzij*dzij;

                    if ((rsqij < sqcut) && (rsqij > 0.10)) {
                        rij = sqrt(rsqij);

                        if (tpe[j] == 0) {
                            R = 2.85;
                            D = 0.15;
                        };
                        if (tpe[j] == 1) {
                            R = 1.85;
                            D = 0.15;
                        };

                        if (rij > R - D) {
                            ua = 0.5*3.14159*(1.0 + (rij - R)/D);

```



```

        u1 = cos(ua);
        u3 = cos(3.0*ua);
        tfc = 0.5 + 9.0*u1/16.0 - u3/16.0;
    } else {
        tfc = 1.00;
    };

    if (tpe[j] == 0) nS += tfc;
    if (tpe[j] == 1) nH += tfc;

};
};
};

r = floor(nH + nS);
if (r < 0) r = 0;
rq = nH + nS - 1.0*r;

As[i] = Au[r] + rq*(Au[r+1] - Au[r]);
Bs[i] = Bu[r] + rq*(Bu[r+1] - Bu[r]);
Hs[i] = Hu[r] + rq*(Hu[r+1] - Hu[r]);

};
};

for (i=0; i<n; i++) {
    ,value = 0;

    for (ja=0; ja<27; ja++) {

        decode = code[i] + enc[ja];
        if ((decode >= 0) && (decode < CUBES)) {

            for (l=0; l < score[decode]; l++) {
                j = zone[decode][l];

                rs = 2*tpe[i] + tpe[j];

                sqcut = -1.00;
                switch(rs + 1) {
                    case 1 : sqcut = 9.00;
                        break;
                    case 2 : sqcut = 4.00;
                        break;
                    case 3 : sqcut = 4.00;
                        break;
                    case 4 : sqcut = 2.89;
                };

                dxij = x[i][0] - x[j][0];
                dyij = x[i][1] - x[j][1];
                dzij = x[i][2] - x[j][2];
                rsqij = dxij*dxij + dyij*dyij + dzij*dzij;

                if ((rsqij < sqcut) && (rsqij > 0.10)) {
                    rij = sqrt(rsqij);

                    yard[value] = rs;

                    if (rs == 0) {
                        A = 1830.8;
                        lda1 = 2.4799;

```

```

    R = 2.85;
    D = 0.15;
    Re[value] = 2.35;
    Bo[value] = 471.18;
    lda2[value] = 1.7322;
};
if (rs == 1) {
    A = As[i];
    lda1 = 2.9595;
    R = 1.85;
    D = 0.15;
    Re[value] = 1.475;
    Bo[value] = Bs[i];
    lda2[value] = 1.6158;
};
if (rs == 2) {
    A = As[j];
    lda1 = 2.9595;
    R = 1.85;
    D = 0.15;
    Re[value] = 1.475;
    Bo[value] = Bs[j];
    lda2[value] = 1.6158;
};
if (rs == 3) {
    A = 80.07;
    lda1 = 4.2075;
    R = 1.40;
    D = 0.30;
    Re[value] = 0.74144;
    Bo[value] = 31.38;
    lda2[value] = 1.7956;
};

if (rij > R - D) {
    ua = 0.5*3.14159*(1.0 + (rij - R)/D);
    u1 = cos(ua);
    u3 = cos(3.0*ua);
    fc[value] = 0.5 + 9.0*u1/16.0 - u3/16.0;
} else {
    fc[value] = 1.00;
};

PE += A*exp(-lda1*rij)*fc[value];

stare[value] = j;
rxs[value] = rij;
xx[value] = dxi;
yy[value] = dyi;
zz[value] = dzi;
value++;
};
};
};

for (p=0; p < value; p++) zij[p] = 0.0;
for (p=0; p < value; p++) {
    j = stare[p];
    rij = rxs[p];

    for (q=0; q < value; q++) {
        if (q != p) {
            rik = rxs[q];

```

```

oc = (xx[p]*xx[q] + yy[p]*yy[q] + zz[p]*zz[q])/(rij*rik);
sum = yard[p] + yard[q];

if (sum == 0) {
    c = 1.1e-6;
    d = 0.1603;
    H = -0.59826;
    alpha = 5.1975;
    cu = 3;
};
if ((sum > 0) && (sum < 3)) {
    c = 0.0216;
    d = 0.27;
    alpha = 4.00;
    cu = 3;
    H = Hs[i];
};
if (sum == 4) {
    c = 0.70;
    d = 1.00;
    H = -1.00;
    alpha = 0.00;
    cu = 1;
};
if (sum > 4) {
    c = 4.00;
    d = 0.00;
    H = 0.00;
    alpha = 3.00;
    cu = 1;
};

e = c + d*(H - oc)*(H - oc);
df = (rij - Re[p]) - (rik - Re[q]);

if (cu == 3) {
    df3 = df*df*df;
    z = exp(alpha*df3);
} else {
    z = exp(alpha*df);
};

zij[p] += fc[q]*e*z;
};
};

if (value >= 2) {
    for (p=0; p<value; p++) {
        if (yard[p] == 0) {
            eta = 0.78734;
            dlta = -0.5/eta;
        } else {
            eta = 1.00;
            dlta = -0.80469;
        };
        zijn = pow(zij[p],eta);
        bij = 1.0 + zijn;
        bijn = pow(bij,dlta);
        st = Bo[p]*bijn*exp(-lda2[p]*rx[p]);
        PE -= st*fc[p];
    };
} else if (value == 1) {
    st = Bo[0]*exp(-lda2[0]*rx[0]);
    PE -= st*fc[0];
}

```

```

    };

};

PE /= 2.0;

for (i=0; i<n; i++) {
    vsq = vx[i][0]*vx[i][0] + vx[i][1]*vx[i][1] + vx[i][2]*vx[i][2];
    KE += vsq*mass[i];

    px += mass[i]*vx[i][0];
    py += mass[i]*vx[i][1];
    pz += mass[i]*vx[i][2];
};

KE *= 52.1986;
EN = PE + KE;

fprintf (outf, " E = %11.4f eV  PE = %11.4f eV  KE = %11.4f eV\n", EN, PE, KE);
fprintf (outf, " Time = %10.4f fs\n #\n", tme);
printf (" E = %11.4f eV  PE = %11.4f eV  KE = %11.4f eV\n", EN, PE, KE);
printf (" px = %8.4f py = %8.4f pz = %8.4f\n", px, py, pz);
}

/* ----- */

func (y,w)

double y[][3];
double w[][3];

{
    register int p,q;

    short int qa,qb,qc,rs,sum;
    short int ja,yard[NN];
    int i,j,k,l,r,s,decode,encode,min;
    double dxij,dyij,dzij,rsqij,rij;
    double dxik,dyik,dzik,rik,fz1,qx,rq;
    double Fr,fx,fy,fz,st,fac,stc,nH,nS,tfc;
    double zij[NN],oc,e,z,zijn,te,ez;
    double df,df2,df3,bij,bijn,vij[NN],vl;
    double sx[NN],sy[NN],sz[NN],fc[NN],dfc[NN];
    double tx[NN],ty[NN],tz[NN],ti,tm,tr,expo;
    double xcl,ycl,zcl,xc2,yc2,zc2,ua,u1,u3,dul,du3;
    double cx,cy,cz,xax,yay,zaz,fcx,dfcx;
    double xx[NN],yy[NN],zz[NN];

    for (i=0; i<CUBES; i++) score[i] = 0;

    for (i=0; i<m; i++) {

        qa = floor ((y[i][0] + 12.00)/cutoff);
        qb = floor ((y[i][1] + 12.00)/cutoff);
        qc = floor ((y[i][2] + 12.00)/cutoff);

        encode = qa*SYZ + qb*SIDEZ + qc;

        if ((qa < 0) || (qb < 0) || (qc < 0)) encode = 0;

        p = score[encode];
        zone[encode][p] = i;
        score[encode]++;
        code[i] = encode - STD;
    }
}

```

```

};

for (i=0; i<m; i++) {
    w[i][0] = 0.0;
    w[i][1] = 0.0;
    w[i][2] = 0.0;
};

for (i=0; i<m; i++) {
    p = 0;

    if (tpe[i] == 0) {
        nS = 0.00;
        nH = 0.00;

        for (ja=0; ja<27; ja++) {
            decode = code[i] + enc[ja];

            if ((decode >= 0) && (decode < CUBES)) {
                for (l=0; l<score[decode]; l++) {

                    j = zone[decode][l];
                    sqcut = -1.00;
                    if (tpe[j] == 0) sqcut = 9.00;
                    if (tpe[j] == 1) sqcut = 4.00;

                    dxij = y[i][0] - y[j][0];
                    dyij = y[i][1] - y[j][1];
                    dzij = y[i][2] - y[j][2];
                    rsqij = dxij*dxij + dyij*dyij + dzij*dzij;

                    if ((rsqij < sqcut) && (rsqij > 0.10)) {
                        rij = sqrt(rsqij);

                        stor[i][p] = j;
                        rx[i][p] = rij;

                        p++;

                        if (tpe[j] == 0) {
                            R = 2.85;
                            D = 0.15;
                        };
                        if (tpe[j] == 1) {
                            R = 1.85;
                            D = 0.15;
                        };

                        if (rij > R-D) {
                            ua = 0.5*3.14159*(1.0 + (rij - R)/D);
                            u1 = cos(ua);
                            u3 = cos(3.0*ua);
                            tfc = 0.5 + 9.0*u1/16.0 - u3/16.0;
                        } else {
                            tfc = 1.00;
                        };

                        if (tpe[j] == 0) nS += tfc;
                        if (tpe[j] == 1) nH += tfc;
                    };
                };
            };
        };
    };
};

```

```

r = floor(nH + nS);
if (r < 0) r = 0;
rq = nH + nS - 1.0*r;

As[i] = Au[r] + rq*(Au[r+1] - Au[r]);
dAs[i] = Au[r+1] - Au[r];

Bs[i] = Bu[r] + rq*(Bu[r+1] - Bu[r]);
dBs[i] = Bu[r+1] - Bu[r];

Hs[i] = Hu[r] + rq*(Hu[r+1] - Hu[r]);
dHs[i] = Hu[r+1] - Hu[r];
};

if (tpe[i] == 1) {
  for (ja=0; ja<27; ja++) {
    decode = code[i] + enc[ja];

    if ((decode >= 0) && (decode < CUBES)) {
      for (l=0; l<score[decode]; l++) {

        j = zone[decode][l];
        sqcut = -1.00;
        if (tpe[j] == 0) sqcut = 4.00;
        if (tpe[j] == 1) sqcut = 2.89;

        dxij = y[i][0] - y[j][0];
        dyij = y[i][1] - y[j][1];
        dzij = y[i][2] - y[j][2];
        rsqij = dxij*dxij + dyij*dyij + dzij*dzij;

        if ((rsqij < sqcut) && (rsqij > 0.10)) {
          rij = sqrt(rsqij);

          stor[i][p] = j;
          rx[i][p] = rij;

          p++;
        };
      };
    };
  };
  val[i] = p;
};

for (i=0; i<m; i++) {
  if (i >= n) {
    min = 1;

    for (p=0; p<val[i]; p++) if (stor[i][p] < n) min = 0;
    if (min) val[i] = 0;
  };

  for (p=0; p<val[i]; p++) {
    j = stor[i][p];
    rij = rx[i][p];

    xx[p] = (y[i][0] - y[j][0])/rij;
    yy[p] = (y[i][1] - y[j][1])/rij;
    zz[p] = (y[i][2] - y[j][2])/rij;
  }
}

```

```

rs = 2*tpe[i] + tpe[j];

if (rs == 0) {
    A = 1830.8;
    lda1 = 2.4799;
    R = 2.85;
    D = 0.15;
    Re[p] = 2.35;
    Bo[p] = 471.18;
    lda2[p] = 1.7322;
};

if (rs == 1) {
    A = As[i];
    lda1 = 2.9595;
    R = 1.85;
    D = 0.15;
    Re[p] = 1.475;
    Bo[p] = Bs[i];
    lda2[p] = 1.6158;
};

if (rs == 2) {
    A = As[j];
    lda1 = 2.9595;
    R = 1.85;
    D = 0.15;
    Re[p] = 1.475;
    Bo[p] = Bs[j];
    lda2[p] = 1.6158;
};

if (rs == 3) {
    A = 80.07;
    lda1 = 4.2075;
    R = 1.40;
    D = 0.30;
    Re[p] = 0.74144;
    Bo[p] = 31.38;
    lda2[p] = 1.7956;
};

yard[p] = rs;

if (rij > R-D) {
    ua = 0.5*3.14159*(1.0 + (rij - R)/D);
    u1 = cos(ua);
    u3 = cos(3.0*ua);
    du1 = 0.5*3.14159*sin(ua)/D;
    du3 = 1.5*3.14159*sin(3.0*ua)/D;
    fc[p] = 0.5 + 9.0*u1/16.0 - u3/16.0;
    dfc[p] = 9.0*du1/16.0 - du3/16.0;
} else {
    fc[p] = 1.00;
    dfc[p] = 0.00;
};

if (i<j) {
    expo = exp(-lda1*rij);
    st = A*expo;
    Fr = lda1*st*fc[p] + st*dfc[p];

    fx = Fr*xx[p];
    w[i][0] += fx;
    w[j][0] -= fx;
}

```

```

    fy = Fr*yy[p];
    w[i][1] += fy;
    w[j][1] -= fy;

    fz = Fr*zz[p];
    w[i][2] += fz;
    w[j][2] -= fz;

    if (rs == 1) s = i;
    if (rs == 2) s = j;

    if ((rs == 1) || (rs == 2)) {
        for (q=0; q<val[s]; q++) {

            k = stor[s][q];
            rik = rx[s][q];

            xax = (y[s][0] - y[k][0])/rik;
            yay = (y[s][1] - y[k][1])/rik;
            zaz = (y[s][2] - y[k][2])/rik;

            if (tpe[k] == 0) {
                R = 2.85;
                D = 0.15;
            } else {
                R = 1.85;
                D = 0.15;
            };

            if (rik > R-D) {
                ua = 0.5*3.14159*(1.0 + (rik - R)/D);
                du1 = 0.5*3.14159*sin(ua)/D;
                du3 = 1.5*3.14159*sin(3.0*ua)/D;
                dfcx = 9.0*du1/16.0 - du3/16.0;
            } else {
                dfcx = 0.00;
            };

            if (tpe[k] == 0) Fr = fc[p]*expo*dAs[s]*dfcx;
            if (tpe[k] == 1) Fr = fc[p]*expo*dAs[s]*dfcx;

            fx = Fr*xax;
            w[s][0] += fx;
            w[k][0] -= fx;

            fy = Fr*yay;
            w[s][1] += fy;
            w[k][1] -= fy;

            fz = Fr*zaz;
            w[s][2] += fz;
            w[k][2] -= fz;
        };
    };
};
};
};

for (p=0; p < val[i]; p++) {
    sx[p] = 0.0;
    sy[p] = 0.0;
    sz[p] = 0.0;
    tx[p] = 0.0;
    ty[p] = 0.0;
    tz[p] = 0.0;

```



```

zij[p] = 0.0;
vij[p] = 0.0;

for (q=0; q<val[i]; q++) {
    g1[p][q] = 0.0;
    g2[p][q] = 0.0;
    g3[p][q] = 0.0;
};

for (p=0; p<val[i]; p++) {
    rij = rx[i][p];

    dxij = xx[p];
    dyij = yy[p];
    dzij = zz[p];

    for (q=0; q<val[i]; q++) {
        if (q != p) {
            rik = rx[i][q];

            dxik = xx[q];
            dyik = yy[q];
            dzik = zz[q];

            oc = dxij*dxik + dyij*dyik + dzij*dzik;

            sum = yard[p] + yard[q];

            if (sum == 0) {
                c = 1.1e-6;
                d = 0.1603;
                H = -0.59826;
                alpha = 5.1975;
                cu = 3;
            };
            if ((sum > 0) && (sum < 3)) {
                c = 0.0216;
                d = 0.27;
                alpha = 4.00;
                cu = 3;
                H = Hs[i];
            };
            if (sum == 4) {
                c = 0.70;
                d = 1.00;
                H = -1.00;
                alpha = 0.00;
                cu = 1;
            };
            if (sum > 4) {
                c = 4.0;
                d = 0.00;
                H = 0.00;
                alpha = 3.00;
                cu = 1;
            };

            e = c + d*(H - oc)*(H - oc);
            df = (rij - Re[p]) - (rik - Re[q]);

            if (cu == 3) {
                df2 = df*df;
                df3 = df*df2;
                z = exp(alpha*df3);
            } else {

```

```

    z = exp(alpha*df);
};

ez = fc[q]*e*z;
fz1 = dfc[q]*e*z;

zij[p] += ez;

if (cu == 3) {
    v1 = 3.0*alpha*df2*ez;
} else {
    v1 = alpha*ez;
};

vij[p] += v1;

v1 += fz1;

g1[p][q] -= v1*dxik;
g2[p][q] -= v1*dyik;
g3[p][q] -= v1*dzik;

sx[p] += v1*dxik;
sy[p] += v1*dyik;
sz[p] += v1*dzik;

ti = fc[q]*z*2.0*d*(H - oc);

if ((sum == 2) || (sum == 1)) {
    for (r=0; r<val[i]; r++) {
        l = stor[i][r];
        if (tpe[l] == 1) tr = ti*dfc[r]*dHs[i];
        if (tpe[l] == 0) tr = ti*dfc[r]*dHs[i];

        g1[p][r] -= tr*xx[r];
        g2[p][r] -= tr*yy[r];
        g3[p][r] -= tr*zz[r];

        sx[p] += tr*xx[r];
        sy[p] += tr*yy[r];
        sz[p] += tr*zz[r];
    };
};

xc1 = dxik - oc*dxij;
yc1 = dyik - oc*dyij;
zc1 = dzik - oc*dzij;

tm = ti/rij;
tx[p] += tm*xc1;
ty[p] += tm*yc1;
tz[p] += tm*zc1;

xc2 = dxij - oc*dxik;
yc2 = dyij - oc*dyik;
zc2 = dzij - oc*dzik;

tm = ti/rik;
t1[p][q] = tm*xc2;
t2[p][q] = tm*yc2;
t3[p][q] = tm*zc2;
};
};

```

```

};

for (p=0; p<val[i]; p++) {
  j = stor[i][p];
  st = 0.0;
  te = 0.0;

  if (val[i] >= 2) {
    if (yard[p] == 0) {
      eta = 0.78734;
      dlta = -0.5/eta;
    } else {
      eta = 1.00;
      dlta = -0.80469;
    };
    zijn = pow(zij[p],eta);
    bij = 1.0 + zijn;
    bijn = pow(bij,dlta);
    expo = exp(-lda2[p]*rx[i][p]);
    st = Bo[p]*bijn*expo;
    stc = st*fc[p];
    te = - 0.5*stc*dlta*eta*zijn/(bij*zij[p]);
  } else if (val[i] == 1) {
    expo = exp(-lda2[p]*rx[i][p]);
    st = Bo[p]*expo;
    stc = st*fc[p];
    zijn = 0.00;
    bijn = 1.00;
  };

  for (q=0; q<val[i]; q++) {
    k = stor[i][q];
    cx = te*t1[p][q];
    cy = te*t2[p][q];
    cz = te*t3[p][q];
    w[k][0] += te*g1[p][q] - cx;
    w[k][1] += te*g2[p][q] - cy;
    w[k][2] += te*g3[p][q] - cz;
    w[i][0] += cx;
    w[i][1] += cy;
    w[i][2] += cz;
  };

  Fr = - stc*lda2[p]/2.0 - te*vij[p] - st*dfc[p]*0.5;

  cx = Fr*xx[p] + te*tx[p];
  w[i][0] += cx + te*sx[p];
  w[j][0] -= cx;

  cy = Fr*yy[p] + te*ty[p];
  w[i][1] += cy + te*sy[p];
  w[j][1] -= cy;

  cz = Fr*zz[p] + te*tz[p];
  w[i][2] += cz + te*sz[p];
  w[j][2] -= cz;

  if ((yard[p] == 1) || (yard[p] == 2)) {
    if (yard[p] == 1) s = i;
    if (yard[p] == 2) s = j;

    for (q=0; q<val[s]; q++) {
      k = stor[s][q];

      rik = rx[s][q];

```

```

xax = (y[s][0] - y[k][0])/rik;
yay = (y[s][1] - y[k][1])/rik;
zaz = (y[s][2] - y[k][2])/rik;

if (tpe[k] == 0) {
    R = 2.85;
    D = 0.15;
} else {
    R = 1.85;
    D = 0.15;
};

if (rik > R-D) {
    ua = 0.5*3.14159*(1.0 + (rik - R)/D);
    du1 = 0.5*3.14159*sin(ua)/D;
    du3 = 1.5*3.14159*sin(3.0*ua)/D;
    dfcx = 9.0*du1/16.0 - du3/16.0;
} else {
    dfcx = 0.00;
};

if (tpe[k] == 0) Fr = - fc[p]*expo*bijn*dBs[s]*dfcx*0.5;
if (tpe[k] == 1) Fr = - fc[p]*expo*bijn*dBs[s]*dfcx*0.5;

fx = Fr*xax;
w[s][0] += fx;
w[k][0] -= fx;

fy = Fr*yay;
w[s][1] += fy;
w[k][1] -= fy;

fz = Fr*zaz;
w[s][2] += fz;
w[k][2] -= fz;
};
};
};

for (i=0; i<n; i++) {
    fac = 9.5788e-3/mass[i];
    w[i][0] *= fac;
    w[i][1] *= fac;
    w[i][2] *= fac;
};

}

/* ----- */

periodic (r)

double r[][3];

{
    register int i,k;

    short int ta,tb,tc,td;

    k = n;
    for (i=0; i<n; i++) {
        ta = (r[i][0] < sl);
        tb = (r[i][0] > sr);

```

```

tc = (r[i][1] < sn);
td = (r[i][1] > sf);

if (ta) {
    r[k][0] = r[i][0] + delx;
    r[k][1] = r[i][1];
    r[k][2] = r[i][2];
    tpe[k] = tpe[i];
    k++;
    if (tc) {
        r[k][0] = r[i][0] + delx;
        r[k][1] = r[i][1] + dely;
        r[k][2] = r[i][2];
        tpe[k] = tpe[i];
        k++;
    };
    if (td) {
        r[k][0] = r[i][0] + delx;
        r[k][1] = r[i][1] - dely;
        r[k][2] = r[i][2];
        tpe[k] = tpe[i];
        k++;
    };
};
if (tb) {
    r[k][0] = r[i][0] - delx;
    r[k][1] = r[i][1];
    r[k][2] = r[i][2];
    tpe[k] = tpe[i];
    k++;
    if (tc) {
        r[k][0] = r[i][0] - delx;
        r[k][1] = r[i][1] + dely;
        r[k][2] = r[i][2];
        tpe[k] = tpe[i];
        k++;
    };
    if (td) {
        r[k][0] = r[i][0] - delx;
        r[k][1] = r[i][1] - dely;
        r[k][2] = r[i][2];
        tpe[k] = tpe[i];
        k++;
    };
};
if (tc) {
    r[k][0] = r[i][0];
    r[k][1] = r[i][1] + dely;
    r[k][2] = r[i][2];
    tpe[k] = tpe[i];
    k++;
};
if (td) {
    r[k][0] = r[i][0];
    r[k][1] = r[i][1] - dely;
    r[k][2] = r[i][2];
    tpe[k] = tpe[i];
    k++;
};
if (k > MAX - 4) {
    warf = fopen ("warn.dat", "w");
    fprintf (warf, " 2\n");
    fprintf (warf, " %5.1f\n", est);
    fprintf (warf, " k = %d\n", k);
    fclose (warf);
    exit(0);
}

```

```

    };
};
m = k;
/* printf (" Number of atoms = %d\n",m); */
}

/* ----- */
void RKA (void)
{
    register int i,j;

    short int  cond;
    int        steps,force;
    double      pre,sgn,h2,hm,hs,range,gy,vsq;
    double      third,h,hx,err,z,delta;
    double      w[MAX][3],y[MAX][3];
    double      u3[MID][3];
    double      v3[MID][3];

    est = 0.0;
    range = -10.00;
    rmin = 10.00;
    steps = 0;
    h = hmax;
    tme = 0.0;
    force = 0;
    cond = 1;

    for (i=0; i<n; i++) {
        rigid[i] = 0;
        zs[i] = 0;
        if (x[i][2] < zmin) rigid[i] = 1;
        if (x[i][2] > zmax) rigid[i] = 1;
        if (x[i][2] < zsave) zs[i] = 1;
        if (zs[i]) {
            fprintf (outf, " %6.2f %6.2f %6.2f %7.4f %7.4f %7.4f %5.1f\n",x[i][0],
                x[i][1],x[i][2],vx[i][0],vx[i][1],vx[i][2],mass[i]);
        };

        tpe[i] = 0;
        if (mass[i] < 3.0) tpe[i] = 1;
        if ((mass[i] > 5.0) && (mass[i] < 32.0)) tpe[i] = 0;
    };

    m = n;
    while ((fabs(T - tme) > 0.0001) && (tme < T)) {
/*
      _____
     /         \
    /           \
*/

        steps = steps + 1;
        periodic (x);
        if (cond == 1) {
            energy ();
            cond = 0;
        };
        func (x,f);

        hm = h/3.0;
        hs = hm*hm;
        h2 = h*h;
        for (i=0; i<3; i++) {

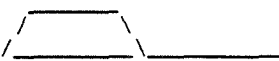
```

```

    for (j=0; j<n; j++) {
        y[j][i] = x[j][i] + 2.0*vx[j][i]*hm + 2.0*hs*f[j][i];
        if (rigid[j]) y[j][i] = x[j][i];
    };
};

periodic (y);
func (y,w);

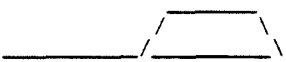
for (i=0; i<3; i++) {
    for (j=0; j<n; j++) {
        u1[j][i] = x[j][i] + vx[j][i]*h + (f[j][i] + w[j][i])*h2/4.0;
        v1[j][i] = vx[j][i] + (f[j][i] + 3.0*w[j][i])*h/4.0;
        if (rigid[j]) {
            u1[j][i] = x[j][i];
            v1[j][i] = vx[j][i];
        };
    };
};

/*
    
*/

do {
    hm = h/3.0;
    hs = hm*hm;
    h2 = h*h;
    for (i=0; i<3; i++) {
        for (j=0; j<n; j++) {
            y[j][i] = x[j][i] + 2.0*vx[j][i]*hm + 2.0*hs*f[j][i];
            if (rigid[j]) y[j][i] = x[j][i];
        };
    };

    periodic (y);
    func (y,w);

    for (i=0; i<3; i++) {
        for (j=0; j<n; j++) {
            u2[j][i] = x[j][i] + vx[j][i]*h + (f[j][i] + w[j][i])*h2/4.0;
            v2[j][i] = vx[j][i] + (f[j][i] + 3.0*w[j][i])*h/4.0;
            if (rigid[j]) {
                u2[j][i] = x[j][i];
                v2[j][i] = vx[j][i];
            };
        };
    };

    /*
        
    */

    periodic (u2);
    func (u2,w);

    for (i=0; i<3; i++) {
        for (j=0; j<n; j++) {
            y[j][i] = u2[j][i] + 2.0*v2[j][i]*hm + 2.0*w[j][i]*hs;
            if (rigid[j]) y[j][i] = x[j][i];
        };
    };
};

```

```

periodic (y);
func (y,w2);

for (i=0; i<3; i++) {
    for (j=0; j<n; j++) {
        u3[j][i] = u2[j][i] + v2[j][i]*h + (w[j][i] + w2[j][i])*h2/4.0;
        v3[j][i] = v2[j][i] + (w[j][i] + 3.0*w2[j][i])*h/4.0;
        if (rigid[j]) {
            u3[j][i] = x[j][i];
            v3[j][i] = vx[j][i];
        }
    }
};

delta = 0.002*h*tol;

err = 0.0;
for (i=0; i<3; i++) {
    for (j=0; j<n; j++) {
        z = fabs( u3[j][i] - u1[j][i] );
        if (z > err) err = z;
        z = fabs( v3[j][i] - v1[j][i] );
        if (z > err) err = z;
    }
};
err = err/7.0;
if ((err > delta) && (force == 0)) {
    h = h/2.0;
    for (i=0; i<3; i++) {
        for (j=0; j<n; j++) {
            u1[j][i] = u2[j][i];
            v1[j][i] = v2[j][i];
        }
    };
    printf ("failed\n");
};

if (force == 1) {
    err = 0.0;
    force = 0;
};

if (h < 0.0001) {
    force = 1;
};

} while ( err > delta );

force = 0;

for (i=0; i<3; i++) {
    for (j=0; j<n; j++) {
        x[j][i] = u3[j][i] + (u3[j][i] - u1[j][i])/7.0;
        vx[j][i] = v3[j][i] + (v3[j][i] - v1[j][i])/7.0;
    }
};

if ((ion) && (x[n-1][2] > range)) range = x[n-1][2];

if (h < 0.000001) {
    warf = fopen ("warn.dat","w");
    fprintf (warf," 3\n");
    fprintf (warf," %5.1f\n",est);
    fclose (warf);
    exit(0);
}

```



```

};
if (mode) {
    for (i=0; i<3; i++) {
        for (j=0; j<n; j++) {
            sgn = w[j][i]*vx[j][i];
            if (sgn < 0.00) vx[j][i] = 0.00;
        };
    };
};

h = 2.0*h;
printf (" Step %d",steps);
printf (" h = %7.4f ",h);
tme = tme + h;
pre = pre + h;
if (fabs(pre - interval) < 0.001) {
    pre = 0.0;
    cond = 1;
    for (i=0; i<n; i++) {
        if (zs[i]) {
            fprintf (outf, " %7.3f %7.3f %7.3f %9.6f %9.6f %9.6f %5.1f\n", x[i][0],
                x[i][1], x[i][2], vx[i][0], vx[i][1], vx[i][2], mass[i]);
        };
    };
    est = tme;
};
printf (" time = %7.2f fs\n", tme);
hx = delta/err;
h = 0.7*h*pow(hx,0.25);
if ((pre + h) > interval) h = interval - pre;
if (h > hmax) h = hmax;

};
periodic (x);
energy ();

if (ion) {
    range -= 0.1841;
    vsq = vx[n-1][0]*vx[n-1][0] + vx[n-1][1]*vx[n-1][1];
    vsq += vx[n-1][2]*vx[n-1][2];
    gy = 52.1986*vsq*mass[n-1];

    fprintf (ranf, " Range of incident ion : %6.2f\n", range);
    fprintf (ranf, " Distance of closest approach : %6.2f\n", rmin);
    fprintf (ranf, " Atom : %d\n", atom);
    fprintf (ranf, " %6.2f %6.2f (%d) %6.2f\n\n", range, rmin, atom, gy);
};

warf = fopen ("warn.dat", "w");
fprintf (warf, " 0\n");
fclose (warf);
}

/* ----- */
main() {

    int i;

    Au[0] = 1.005*323.54;
    Au[1] = 1.005*323.54;
    Au[2] = 1.109*323.54;
    Au[3] = 0.953*323.54;
    Au[4] = 1.00*323.54;
    Au[5] = 1.00*323.54;
    Au[6] = 1.00*323.54;
    Au[7] = 1.00*323.54;

```

```

Bu[0] = 0.930*84.18;
Bu[1] = 0.930*84.18;
Bu[2] = 1.035*84.18;
Bu[3] = 0.934*84.18;
Bu[4] = 1.00*84.18;
Bu[5] = 1.00*84.18;
Bu[6] = 1.00*84.18;
Bu[7] = 1.00*84.18;

Hu[0] = -0.040;
Hu[1] = -0.040;
Hu[2] = -0.040;
Hu[3] = -0.242;
Hu[4] = -0.47;
Hu[5] = -0.47;
Hu[6] = -0.47;
Hu[7] = -0.47;

SYZ = SIDEY*SIDEZ;
STD = SYZ + SIDEZ + 1;
for (i=0; i<3; i++) {
    enc[i] = i;
    enc[i+3] = i + SIDEZ;
    enc[i+6] = i + 2*SIDEZ;
};
for (i=0; i<9; i++) {
    enc[i+9] = enc[i] + SYZ;
    enc[i+18] = enc[i] + 2*SYZ;
};

params ();

cutoff = 3.00;

if (s == 0) printf ("error\n");
if (s == 1) {
/*    delx = la*ma;
    dely = la*mb;
    sl = 2.2*cutoff;
    sr = delx - 2.2*cutoff;
    sn = 2.2*cutoff;
    sf = dely - 2.2*cutoff; */

    delx = la*ma/sqrt(2.0);
    dely = la*mb/sqrt(2.0);
    sl = 2.6*cutoff;
    sr = delx - 2.6*cutoff;
    sn = 2.6*cutoff;
    sf = dely - 2.6*cutoff;

    if (mode == 0) printf (" Mode := AUTO\n");
    if (mode == 1) printf (" Mode := RELX\n");

    lattice ();

    outf = fopen ("out.dat","w");
    ranf = fopen ("range.dat","w");

    RKA ();

    fclose (outf);
    fclose (ranf);

```

```
    finf = fopen ("final.dat","w");  
    for (i=0; i<n; i++) {  
        fprintf (finf, " %11.7f %11.7f %11.7f %8.4f %8.4f %8.4f %5.1f\n",x[i][0],  
            x[i][1],x[i][2],vx[i][0],vx[i][1],vx[i][2],mass[i]);  
    };  
    fclose (finf);  
};  
}
```